

RICE UNIVERSITY

**Synthesis and design of nanocrystalline metal oxides for
applications in carbon nanotube growth and antioxidants**

by

Seung Soo Lee

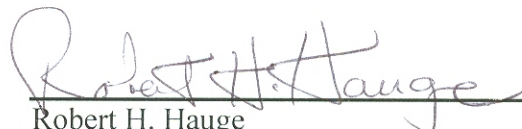
A THESIS SUBMITTED
IN PARTIAL FULFILLMENT OF THE
REQUIREMENTS FOR THE DEGREE

Doctor of Philosophy

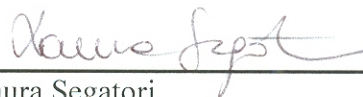
APPROVED, THESIS COMMITTEE



Vicki L. Colvin
Kenneth S. Pitzer-Schlumberger Professor of
Chemistry, Chair



Robert H. Hauge
Distinguished Faculty Fellow in
Chemistry



Laura Segatori
Assistant Professor of Chemical and
Biomolecular Engineering

HOUSTON, TEXAS
March 2013

ABSTRACT

Synthesis and design of nanocrystalline metal oxides for applications in carbon nanotube growth and antioxidants

by

Seung Soo Lee

Synthesis of size tunable nanomaterials creates distinct chemo-physical properties. Recently, the popularity of magnetic iron oxide and cerium oxide (CeO_2) nanocrystals enables researchers to use magnetic iron oxides (magnetite and ferrites) in size dependent magnetic separation and CeO_2 as an automobile exhaust gas catalyst. This research shows production of diameter-controlled monodisperse magnetic iron oxide (ranging from 3 to 40 nm in diameter) and CeO_2 (from 3 to 10 nm in diameter) nanocrystals with exceptional narrow diameter distribution ($\sigma < 10\%$). The morphology and composition of the nanocrystals were varied by use of diverse metal precursors, reaction temperature, time, cosurfactants, and molar ratio between metal salt and surfactant. Now the narrow diameter distributions of preformed magnetic iron oxide nanocrystals made it possible to grow diameter controlled uniform CNTs. The correlation between aluminum ferrite nanocrystal diameter and CNT diameter was nearly one. Additionally, we could synthesize the highest percentage (60%) of single walled CNTs from the smallest aluminum ferrite nanocrystals (4.0 nm). Because of the synthesis of uniform nanocrystalline CeO_2 , we could study diameter dependent antioxidant properties of nanocrystalline CeO_2 ; antioxidant capacity of CeO_2 was nine times higher than a known commercial

standard antioxidant, Trolox. In addition, the smallest CeO₂ nanocrystal (4 nm) decreased the oxidative stress of human dermal fibroblasts (HDF) exposed to hydrogen peroxide. These works suggest better understanding of monodisperse nanocrystal synthetic mechanism and potential uses of the materials, such as high quality CNT growth using magnetic iron oxides as precursor catalysts and the reduction of oxidative stress in cells using monodisperse CeO₂ nanocrystal as an antioxidant for reactive oxygen species in biological media.

Acknowledgments

I would like to thank Dr. Vicki L. Colvin, my PhD. advisor and chair of my thesis committee, for her advice, guidance, and generosity. Not only has she guided my academic career, but encouraged me to find myself and pushed me to pursue a broad range of scientific careers. I would also like to thank Dr. Robert H. Hauge, and Dr. Laura Segatori for participating as my thesis committee.

I would like to thank all my past and current group members: Dr. Huiguang Zhu, Dr. John T. Mayo, Dr. Arjun Prakash, Dr. Carolina Avendaño, Dr. Denise Benoit, Dr. William W. Yu, Dr. John Fortner, Dr. Zuzanna Lewicka, Dr. Feng Li, Dr. Elizabeth Quevedo-Contreras, Dr. Chris Jones, Dr. Minjung Cho, Hema Puppala, Natalia Gonzalez-Pech, Gabriella Escalera, Dr. Qingbo Zhang, Arash Bahloul, Nasim Taheri, Daniel Garcia, Adina Boyd, Erika Bryant, Dr. Tanya Peretyazhko, Camila Zies, Aniwai Lomeda, Jieying Jing, and Dr. Jing Li. I would also like to thank NSF REU student, Phuc Nguyen, who has contributed to nanocrystalline cerium oxide project.

I would like to thank some of my collaborators at Rice University: Chenguang Zhang in Dr. Robert H. Hauge group, and Wensi Song in Dr. Laura Segatori group. I would also like to thank all of those at Rice University that have given me significant guidance: Teresa Champion, Dr. Wenhua Guo, Dr. Bo Chen, Dr. Angelo Benedetto, Dr. Seunghyun Lee, Sangwoo Chung, Dr. Dongsuk Shin, Dr. Hoonkyung Lee, Dr. Ji Hee Kim, Dr. Seokjin Jun, SongI Han, and Hyun Seung Yang.

I would like to thank my parents for their help, support, and constant guidance throughout my entire life. I would specifically like to thank my loving wife, Minyoung Jo, for always understanding me and for encouraging me to finish my PhD. I am so grateful for her love and patience.

Contents

Acknowledgments	iv
Contents	vi
List of Figures	xii
List of Tables	xix
Nanocrystalline metal oxides: syntheses and applications	1
1.1. Introduction.....	1
1.2. Nanocrystal growth mechanism	2
1.3. Monodisperse nanocrystal synthesis	4
1.3.1. Iron oxide	4
1.3.1.1. Synthesis of iron oxide nanocrystals.....	4
1.3.2. Cerium oxide.....	8
1.3.2.1. Synthesis of cerium oxide nanocrystals	9
1.4. Applications of nanocrystals	12
1.4.1. Iron oxide for carbon nanotube growth	12
1.4.2. Cerium oxide as an antioxidant	15
1.5. Summary and outlook	18
Synthesis of magnetic metal oxide nanocrystals through non-hydrolytic route	22
2.1. Introduction.....	22
2.2. Experimental methods	24
2.2.1. Chemicals.....	24
2.2.2. Synthesis of iron oxide nanocrystals	24
2.2.2.1. Iron oleate synthesis	24
2.2.2.2. Nanocrystals from iron oleate	26
2.2.2.3. Nanocrystals from the mixture of iron oleate and oleyl alcohol.....	26
2.2.2.4. Nanocrystals from high monomer concentration	26
2.2.3. Synthesis of Ferrite nanocrystals.....	26
2.2.3.1. Nickel, manganese, and zinc oleate synthesis	26
2.2.3.2. Manganese iron oxide ($Mn_xFe_{3-x}O_4$)	27
2.2.3.3. Nickel iron oxide ($Ni_xFe_{3-x}O_4$)	27
2.2.3.4. Zinc iron oxide ($Zn_xFe_{3-x}O_4$)	27

2.2.3.5. Aluminum iron oxide ($\text{Al}_x\text{Fe}_{3-x}\text{O}_4$).....	27
2.2.3.6. Nickel aluminum iron oxide (NiAlFeO_4)	28
2.2.3.7. Manganese zinc iron oxide ($\text{Mn}_x\text{Zn}_{x-1}\text{Fe}_2\text{O}_4$).....	28
2.2.3.8. Manganese aluminum iron oxide (MnAlFeO_4)	28
2.2.3.9. Manganese zinc aluminum iron oxide ($\text{Mn}_{x-1}\text{Zn}_x\text{AlFeO}_4$).....	29
2.3. Results and discussion.....	29
2.3.1. Diameter control of iron oxide nanocrystals.....	29
2.3.2. Diameter control of ferrite nanocrystals.....	36
2.4. Conclusion	40
Synthesis of monodisperse aluminum ferrite nanocrystals.....	41
3.1. Introduction.....	41
3.2. Experimental Methods.....	43
3.2.1. Chemicals.....	43
3.2.2. Instrumentation.....	43
3.2.2.1. Transmission electron microscope (TEM).....	43
3.2.2.2. X-ray diffraction (XRD), and X-ray photoelectron spectroscopy (XPS)	44
3.2.2.3. Inductively coupled plasma atomic emission spectroscopy (ICP-AES).....	44
3.2.3. Synthesis of nanocrystalline iron oxide (magnetite)	44
3.2.3.1. Iron oxide nanocrystals prepared by Goethite (FeOOH)	44
3.2.3.2. Iron oxide nanocrystals prepared by iron oleate.....	45
3.2.4. Synthesis of nanocrystalline aluminum ferrite.....	45
3.2.5. Phase transfer of iron oxide and aluminum ferrite nanocrystals.....	46
3.2.5.1. Oleic acid coated iron oxide.....	46
3.2.5.2. PAAOA coated iron oxide.....	46
3.2.5.3. PMAO coated iron oxide	47
3.2.5.4. PEI coated iron oxide	47
3.2.5.5. Oleic acid coated aluminum ferrite	47
3.2.5.6. Polyacrylic acid octylamine (PAA-OA) coated aluminum ferrite	47
3.2.5.7. PMAO coated aluminum ferrite.....	48
3.3. Results and Discussion	48
3.3.1. Aluminum ferrite nanocrystal.....	49
3.3.2. Nickel ferrite and nickel aluminum iron oxide nanocrystals	55
3.3.3. Phase transfer of aluminum ferrite nanocrystals.....	60
3.4. Conclusion	61

Control over the diameter, length, and structure of carbon nanotube carpets using iron oxide and aluminum ferrite nanocrystals	62
4.1. Introduction.....	62
4.2. Experimental Methods.....	66
4.2.1. Chemicals.....	66
4.2.2. Instrumentation.....	66
4.2.2.1. Scanning electron microscope (SEM)	66
4.2.2.2. Transmission electron microscope (TEM).....	66
4.2.2.3. Raman spectroscopy	67
4.2.3. Synthesis of precursor catalysts: iron oxide, aluminum iron oxide nanocrystals	67
4.2.3.1. Iron oxide nanocrystals.....	67
4.2.3.2. Synthesis of aluminum iron oxide nanocrystals	67
4.2.4. Growth of carbon nanotube (CNT) carpets.....	68
4.2.5. Calculation of surface coverage of nanoparticles	69
4.2.6. Calculation of the diameter of zero-valent iron.....	69
4.3. Results and Discussion	70
4.3.1. Diameter dependence of CNT on the varied size of starting nanocrystals.	72
4.3.2. The number of wall control of carbon nanotubes	80
4.3.3. The surface coverage and reaction pressure effect on CNT carpet quality.	83
4.3.4. Overall height of CNT carpet catalyzed by both aluminum ferrite and iron oxide nanocrystals.	86
4.3.5. CNT carpet growth by rapid saturation and slow growth process.....	89
4.4. Conclusion	94
Closed-edged graphene nanoribbons from large diameter collapsed nanotubes	96
5.1. Introduction.....	96
5.2. Experimental methods	100
5.2.1. Chemicals.....	100
5.2.2. Nanocrystal synthesis	100
5.2.3. Carbon nanotube growth condition	101
5.3. Results and discussion.....	102
5.3.1. Growth of a large diameter carbon nanotube carpet using preformed aluminum iron oxide nanocrystals.	102

5.3.2. Fitting the size distribution of SWCNT and DWCNT	112
5.4. Conclusion	120
High Temperature Decomposition of Cerium Precursors to Form Cerium oxide nanocrystals.....	122
6.1. Introduction.....	122
6.2. Experimental Methods.....	126
6.2.1. Chemicals.....	126
6.2.2. Instrumentation.....	126
6.2.2.1. X-ray diffraction (XRD), X-ray photoelectron spectroscopy (XPS), and small angle X-ray scattering (SAXS)	126
6.2.2.2. Dynamic light scattering (DLS) analysis.....	127
6.2.2.3. Transmission Electron Microscope (TEM)	127
6.2.2.4. Inductively coupled plasma atomic emission spectroscopy (ICP-AES) ...	128
6.2.3. Synthesis of Cerium oxide nanocrystal: precursor effect.....	128
6.2.3.1. Cerium oxide nanocrystal from Ce(acac) ₃	128
6.2.3.2. Cerium oxide nanocrystal from Ce-oleylamine	129
6.2.3.3. Cerium oxide nanocrystal from Ce(NO ₃) ₃ ·6H ₂ O.....	129
6.2.3.4. Cerium oxide nanocrystal from Ce(OH) ₄	130
6.2.4. Synthesis of Cerium oxide nanocrystal: concentration of monomer effect .	130
6.2.5. Synthesis of Cerium oxide nanocrystal: water as an additive	130
6.2.6. Synthesis of Cerium oxide nanocrystal: octadecylamine addition.....	131
6.2.7. Star, flower-shaped cerium oxide nanocrystal.....	131
6.2.8. Purification of nanocrystalline ceria	131
6.2.9. Preparation of water-soluble cerium oxide nanocrystal.....	132
6.2.9.1. Synthesis of poly(acrylic acid)-octylamine (PAAOA) amphiphilic copolymer.	132
6.2.9.2. PAAOA coated cerium oxide nanocrystal	132
6.2.9.3. Oleic acid coated cerium oxide nanocrystal	133
6.2.10. Nanoparticle concentration calculation	133
6.2.11. Cell viability test using water soluble nanoceria	134
6.3. Results and Discussion	135
6.3.1. Diameter control of cerium oxide nanocrystal.....	136
6.3.2. Star- and flower-shaped cerium oxide nanocrystals.....	141

6.3.3. The content of Cerium (III) in nanocrystals	142
6.3.4. Transferring the ceria nanocrystals into water	144
6.3.5. Antioxidant and toxicological evaluation of water soluble nanocrystalline ceria	148
6.4. Conclusion	152
Redox cycling behavior of cerium oxide nanocrystals and its dependence on nanocrystal diameter and surface coating.....	154
7.1. Introduction.....	154
7.2. Experimental methods	158
7.2.1. Chemicals.....	158
7.2.2. Instrumentation.....	159
7.2.2.1. UV-Vis spectroscopy	159
7.2.2.2. Transmission Electron Microscopy (TEM).....	159
7.2.2.3. X-ray photoelectron spectroscope (XPS)	159
7.2.2.4. Dynamic light scattering (DLS)	160
7.2.2.5. Inductively coupled plasma atomic emission spectroscopy (ICP)	160
7.2.2.6. GC-MS spectroscopy	160
7.2.2.7. Luminol test of water-soluble cerium oxide nanocrystals.....	161
7.2.2.8. Oxygen-radical absorbance capacity (ORAC) assay	162
7.2.2.9. Measurement of intracellular reactive oxygen species (ROS) generation	162
7.2.3. Synthesis of nanoceria.....	163
7.2.4. Phase transfer of nanoceria.....	164
7.2.4.1. Oleic acid coated nanoceria	164
7.2.4.2. Polyacrylic acid octylamine (PAA-OA) coated nanoceria:.....	165
7.2.4.3. PMAO coated nanoceria	165
7.2.4.4. PEI coated nanoceria.....	165
7.2.5. Nanoparticle concentration calculation	166
7.2.6. The calculation of the concentration of cerium oxide nanocrystals using the molecular weight of a cerium oxide nanocrystal.	166
7.2.7. The calculation of Ce(III) ions on the surface of one nanocrystal ¹⁴⁴	167
7.2.8. Cell viability test using water soluble cerium oxide nanocrystals.....	169
7.2.8.1. Cell Culture	169
7.2.8.2. MTS cell viability assay.....	169

7.3. Results and Discussion	170
7.3.1. Physico-chemical properties and mechanism for ceria reactions with hydrogen peroxides	170
7.3.2. Benchmarking of anti-oxidant capacity and trends with size and surface coating	184
7.3.3. Recycling behavior of nanoscale ceria and its dependence on surface coating	193
7.4. Conclusion	197
Conclusion	199
References	201

List of Figures

Figure 1.1 Crystal growth diagram.	3
Figure 1.2 TEM images of iron oxide nanocrystals.	6
Figure 1.3 TEM images of iron oxide nanocrystals.	7
Figure 1.4 Cubic fluorite structure of cerium oxide	9
Figure 1.5 Cerium oxide nanocrystals from reverse micelle	10
Figure 1.6 Cerium oxide nanomaterials from non-hydrolytic route (organic method)	12
Figure 1.7 Carbon nanotube growth process.	13
Figure 1.8 SWNT forest grown with water assisted CVD	14
Figure 1.9 Antioxidant property of cerium oxide	16
Figure 1.10 The expected redox cycling mechanisms	17
Figure 1.11 antioxidant properties of ceria	18
Figure 1.12 Schematic of effects which are occurring on the catalyst during carbon nanotube growth	19
Figure 1.13 Carbon nanotube carpet growth using both iron oxide and aluminum ferrite nanocrystals.	20
Figure 1.14 Cerium oxide nanocrystals that can protect against Ischemic stroke.	21
Figure 2.1 Iron oleate in an amber bottle	25
Figure 2.2 An experimental set up for nanocrystal synthesis	30
Figure 2.3 Iron oxide nanocrystals grow larger as the ratio of oleic acid to iron precursor increased	31
Figure 2.4 Longer reaction time grows monodisperse nanocrystals.	31

Figure 2.5 Iron oxide nanocrystals formed by oleyl alcohol addition.....	32
Figure 2.6 Decrease in diameter of iron oxide nanocrystals by adding oleyl alcohol.....	33
Figure 2.7 Iron oxide nanocrystals from 5 to 40 nm.	34
Figure 2.8 Growth of iron oxide nanocrystals depending on monomer concentration.	35
Figure 2.9 Time dependent growth of iron oxide nanocrystals.	36
Figure 2.10 TEM and GIF images of aluminum ferrite (from A to C) and manganese zinc ferrite nanocrystals (from D to F). All scale bars are 50 nm.....	37
Figure 2.11 TEM images of NiAlFeO, MnAlFeO, and Mn_{0.5}Zn_{0.5}AlFeO₄ nanocrystals. The average diameter of the nanocrystals are 3.5 ± 0.4, 5.5 ± 0.5, 7.2 ± 0.7 nm, respectively.....	38
Figure 2.12 Control over the diameter and composition of Mn_xFe_{3-x}O₄ nanocrystals.....	39
Figure 2.13 Diameter and composition control of Mn_xZn_{x-1}Fe₂O₄ nanocrystals.	39
Figure 3.1 Three different diameters of aluminum ferrite nanocrystals.	49
Figure 3.2 The diameter histograms of aluminum ferrite nanocrystals.....	50
Figure 3.3 GIF analysis of 11.2 nm aluminum ferrite nanocrystals.	52
Figure 3.4 XPS data of aluminum iron oxide nanocrystal.....	53
Figure 3.5 XRD data of aluminum iron oxide nanocrystals.....	53
Figure 3.6 High resolution TEM image of aluminum iron oxide nanocrystal... 	54
Figure 3.7 A variation of aluminum content in a nanocrystal.....	55
Figure 3.8 XRD of nickel ferrite nanocrystals.	57
Figure 3.9 XPS analysis of nickel ferrite nanocrystal.....	58

Figure 3.10 The effect of the ratio of nickel and iron precursors on the particle diameter, morphology and the composition.....	58
Figure 3.11 XRD of NiAlFeO₄ nanocrystal (black).	59
Figure 3.12 Water soluble aluminum ferrite nanocrystals.....	61
Figure 4.1 TEM images of aluminum ferrite (A to C) and iron oxide nanoparticles (D to I) in different sizes.	71
Figure 4.2 The histograms of the size distribution of aluminum ferrite (A to C) and iron oxide (D to I) nanoparticles.....	72
Figure 4.3 Carbon nanotube (CNT) growth process.	73
Figure 4.4 TEM images of CNTs grown by various sized aluminum ferrite and iron oxides.....	74
Figure 4.5 The histograms of the diameter distributions of CNTs grown by of aluminum ferrite (A to C) and iron oxide (D to I) nanoparticles.	75
Figure 4.6 Diameter dependence of CNT on the varied size of the reduced Fe precursor catalysts.....	76
Figure 4.7 TEM images of CNTs grown from two sizes of iron oxide nanocrystals.....	77
Figure 4.8 CNT carpet height varied from wide range of iron oxide catalyst (from 4 to 38 nm).....	78
Figure 4.9 Full width half maximum (FWHM) of the diameter distribution of CNTs (blue) and nanoparticles (red line).....	79
Figure 4.10 The statistics of the number of walls of CNTs grown by both aluminum ferrite and iron oxide.....	81
Figure 4.11 The number of wall control of CNTs.	82
Figure 4.12 Raman spectra of CNTs from AlFe₂O₄ and Fe₃O₄ nanocrystals indicating purity.....	84
Figure 4.13 Effect of reaction gas pressures (1.4 torr (A and C), and 25 torr (B and D)) and surface coverage of 4.0 nm aluminum iron oxide nanocatalysts on	

the substrate (from 7.22×10^{13} (A and B) to 9.03×10^{12} (C and D) nanoparticles/cm ²).	87
Figure 4.14 Comparison of CNT carpet height grown by both aluminum iron oxide and iron oxide nanocrystals on alumina wafer.	88
Figure 4.15 CNT carpet height at various surface coverage of 4 nm diameter of aluminum iron oxide nanocrystals depending on different CNT carpet growth condition.	91
Figure 4.16 SEM images of CNT carpets grown from different growth conditions.	92
Figure 4.17 The correlation of CNT carpet height and G to D ratio.	93
Figure 5.1 Synthesis of a large-diameter CNT carpet from mono-dispersed AlFe ₂ O ₄ preformed nanoparticles.	102
Figure 5.2 Characterization of aluminum iron oxide nanocrystals.	103
Figure 5.3 Quality of carbon nanotube grown by the precursor catalysts measured by Raman.	105
Figure 5.4 TEM images of the collapsed and uncollapsed CNTs.	107
Figure 5.5 AFM height measurements of the collapsed CNTs.	108
Figure 5.6 HRTEM images of the collapsed nanotubes.	109
Figure 5.7 Height measurement of carbon nanotube using AFM.	111
Figure 5.8 The fitting curves for the size distribution of the collapsed and uncollapsed nanotubes.	113
Figure 5.9 Linear relationship between the width of collapsed form and diameter of cylindrical form of the free standing SWCNTs.	114
Figure 5.10 Calculations for different miscounts.	115
Figure 5.11 Fraction of uncollapsed and collapsed SWCNT (a) and DWCNT (c) versus diameters in the sum (b, d).	117
Figure 5.12 Energy calculations for collapsed and uncollapsed tubes.	118

Figure 5.13 Calculated energy for uncollapsed and collapsed SWCNT on a single-layer graphene substrate.....	119
Figure 5.14 Size distributions of the catalyst particles, sum of the SWCNTs and sum of the DWCNTs.	120
Figure 6.1 Near spherical nanocrystalline cerium oxide.	136
Figure 6.2 Cerium oxide nanocrystals from cerium-oleylamine precursor... 	137
Figure 6.3 TEM micrographs of cerium oxide nanocrystal synthesized using 2 different cerium precursors: cerium oleylamine, and cerium hydroxide.....	138
Figure 6.4 The x-ray diffractograms of cerium oxide nanocrystals with various sizes and shapes.	138
Figure 6.5 Evolution of nanocrystalline ceria from spherical to star-shaped.	142
Figure 6.6 XPS data of cerium oxide nanocrystal with various size and shape.	143
Figure 6.7 Transfer yields of cerium oxide nanocrystal from hexane into water.....	145
Figure 6.8 Water soluble cerium oxide nanocrystals.....	146
Figure 6.9 Comparisons of the effective dimensions of cerium oxide nanocrystals stabilized in water using three different methods: TEM, SAXS, and DLS.	147
Figure 6.10 Effect of nanoceria on the viability of Human Dermal Fibroblast (HDF) cells.	149
Figure 6.11 Cell viability study of PAAOA (polyacrylicacid octylamine) and PAA (polyacrylicacid).	150
Figure 6.12 H₂O₂ quenching depends on the size of the cerium oxide nanocrystals.....	151
Figure 7.1 The calculation of the number of unit cells on the surface of 3.8 nm cerium oxide nanocrystal.....	167
Figure 7.2 TEM micrographs (A to C) of water soluble nanoceria.....	171

Figure 7.3 Phase transfer efficiency of water soluble nanoceria coated with 4 different phase transfer agents.....	172
Figure 7.4 Hydrodynamic size of nanoceria.	173
Figure 7.5 H₂O₂ quenching of water-soluble nanocrystalline cerium oxides.	174
Figure 7.6 Redox cycling of cerium oxide through Fenton-type reaction.....	175
Figure 7.7 XPS data of 3.8 nm CeO₂ before and after H₂O₂ injection.....	176
Figure 7.8 PH dependent antioxidant capacity of oleic acid coated cerium oxide suspension.....	178
Figure 7.9 The calibration curve of O₂ in GC-MS analysis.....	179
Figure 7.10 The H₂O₂ calibration curve for the luminol test.....	180
Figure 7.11 Decomposed H₂O₂ calculation using the red shift UV-Vis band and GC-MS data.....	181
Figure 7.12 Quantitative analysis of H₂O₂ quenching of cerium oxide nanocrystals.....	182
Figure 7.13 Quantitative analysis of H₂O₂ quenching of cerium oxide nanocrystals.....	183
Figure 7.14 The different extents of H₂O₂ quenching capacity depending on various diameters and surface stabilizers on nanoceria.....	185
Figure 7.15 The magnitude of the red shift UV-Vis band of oleic acid and PMAO coated ceria nanocrystal suspension after H₂O₂ injection.	186
Figure 7.16 Oxygen-radical absorbance capacity (ORAC) assay of oleic acid coated – (red), PMAO coated – (blue) nanoceria and Trolox (black).	188
Figure 7.17 Antioxidant capacity of cerium oxide nanocrystals.....	189
Figure 7.18 Cell viability of Human Dermal Fibroblast (HDF) cell line in the presence of 3.8 and 8.2 nm coated cerium oxide nanocrystals coated with oleic acid.	191
Figure 7.19 Intracellular ROS measurement.....	193

Figure 7.20 Antioxidant property of water-soluble nanoceria coated with bilayer surface structures.....	194
Figure 7.21 Loss of colloidal stability of PEI coated 3.8 nm nanoceria after H₂O₂ injection.	195
Figure 7.22 Antioxidant capacity of ceria nanocrystal suspension (2.78 μM of nanocrystal concentration: 1 μmol of cerium (III) concentration) depending on different amount of H₂O₂ injections for 18 cycles.	197

List of Tables

Table 5-1. Summary of values of equivalent energy points for SWCNT and DWCNT in the literature and the methodologies employed.	98
Table 5-2 Detailed information in the height measurements of the collapsed structures (CE₂GNR, CE₄GNR and CE₆GNR) shown in Figure 5.7 provided by SIMAGIS software package.....	112
Table 7-1 XPS analysis of individual peaks.....	177

Chapter 1

Nanocrystalline metal oxides: syntheses and applications

1.1. Introduction

Nanotechnology is the study and application using materials with the size under 100 nm. These materials, nanocrystals, create extinct chemical and physical properties and make various biological and industrial applications available. For example, colloidal iron oxide can be useful as a contrast agent, drug delivery, and cancer diagnosis.¹ In addition, one of the popular rear earth metal oxides, cerium oxide, has the potential to be used as an automobile exhaust gas catalyst.²

Recently, the popularity of nanocrystals enables researchers to apply those materials to unexplored areas, reporting mass production of carbon nanotubes using iron oxide nanocrystals and the advantage of cerium oxide as a potential antioxidant. Monodisperse nanocrystals in large scale should be prepared with controllable size and shape to

understand the role of nanomaterials in these types of applications. In addition, surface modification, and toxicological evaluation for biological applications are still challenging points.

In this review, I provide a brief overview of monodisperse metal oxide (iron oxide and cerium oxide) nanocrystal synthesis and the applications using preformed metal oxide nanocrystals (carbon nanotube (CNT) growth using iron oxide nanocrystals as precursor catalysts and a biological application using cerium oxide nanocrystal as an antioxidant).

1.2. Nanocrystal growth mechanism

Metal oxide nanocrystals formed by non-hydrolytic route (organic method) have high crystalline, uniform size, and narrow diameter distribution. Monodisperse metal oxide nanocrystals are formed by decomposition of metal precursors in the presence of surface stabilizers (surfactants) and a high boiling point solvent.^{2c, 3} After the reaction, nanocrystals covered by surfactants are colloiddally stable in various non-polar organic solvents, such as toluene, methylene chloride, and hexane.^{3a}

Formation mechanism of metal oxide nanocrystals undergoes nucleation and growth process. In LaMer model, starting reactants form monomers prior to nucleation process.⁴ As reaction goes on at elevating temperatures, concentration of monomers reaches supersaturation level and nucleation process starts forming nuclei by consuming monomers. The decrease in monomer concentration (under the critical level) leads to growth process; already formed nuclei start growing larger until the monomer

concentration is reduced to its equilibrium level.^{4b} At this stage, size focusing occurs by stopping the reaction quickly before Ostwald ripening of nanocrystals begins.⁵ Monomer depletion gives rise to ripening of the nanocrystals. In this period, larger particles keep growing larger, and smaller particles get smaller.⁶ Therefore, fast nucleation and quick termination of the nanocrystal synthesis before monomer depletion level is a key for monodisperse nanocrystal synthesis.

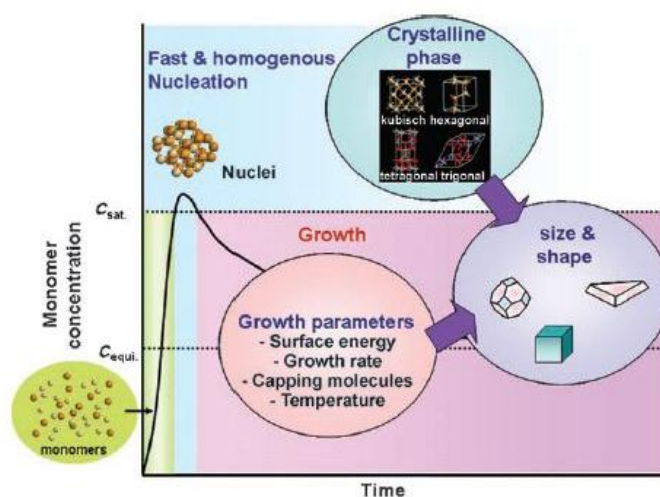


Figure 1.1 Crystal growth diagram.

When the monomer concentration reaches a supersaturation, nucleation occurs and monomer is consumed to grow nuclei, which results in the decrease of monomer concentration. During these nucleation and growth stages, the control of growth parameters and crystalline phase is critical in determining the final size and shape of nanocrystals. C_{sat} = saturation concentration, $C_{equiv.}$ = equilibrium concentration.⁷

1.3. Monodisperse nanocrystal synthesis

1.3.1. Iron oxide

Iron oxide is a chemical compound made of iron and oxygen. There are largely three different types of iron oxide depending on the oxidation states of iron ions in the crystal structure such as, iron (II) oxide (FeO, wüstite), iron (II, III) oxide (Fe₃O₄, magnetite), and iron (III) oxide (Fe₂O₃, hematite or maghemite).⁸ When the size of iron oxide decreased from bulk to nano regime, chemo physical properties and magnetic properties of iron oxide are changed.⁹ For example, ferromagnetic bulk magnetite turns to superparamagnetic magnetite nanocrystals.^{9b, c} Nano scale iron oxide enables us to use these nanomaterials for biomedical applications including drug delivery,¹⁰ MRI contrast agents,¹¹ and tumor hyperthermia¹² due to their magnetic properties and biocompatibility with low toxicity. Nanocrystalline iron oxide is synthesized by various methods such as co-precipitation,¹³ microemulsion,¹⁴ and thermal decomposition.^{2c, 3j} Among them, thermal decomposition method forms monodisperse iron oxide nanocrystals by decomposition of metal precursors via non-hydrolytic route. The resulting nanocrystals are colloidally stable by capping the surface of nanomaterials with surface stabilizers (polymer or surfactant) to prevent particle-particle aggregation.^{3a, 15}

1.3.1.1. Synthesis of iron oxide nanocrystals

To synthesize monodisperse iron oxide nanocrystals, the starting iron precursor should be decomposed fully in nucleation and growth process. Therefore the reaction temperature in the nanocrystal synthesis is settled by the decomposition temperature of an

iron precursor. Rockenberger *et al* first reported a non-hydrolytic route using an organometallic compound as a precursor for nanocrystal synthesis in 1999.¹⁶ They reported that iron oxide nanocrystals (γ -Fe₂O₃, d = 6.3 nm) were synthesized by decomposition of FeCup₃ (iron *N*-nitrosophenylhydroxylamine) at over 200 °C.¹⁶ This motivated the application of other metal organic precursors to synthesize monodisperse iron oxide nanocrystals. For example, iron pentacarbonyl (at 300 °C), iron acetylacetonate (at 265 °C), iron oleate (at 320 °C), and iron chelated complexes (at 220 °C) were used as iron precursors for monodisperse iron oxide nanocrystal (γ -Fe₂O₃ or Fe₃O₄) synthesis.^{2c, 3d, 3g, 17} Recently, this group demonstrated the synthesis of monodisperse iron oxide nanocrystal using the mixture of iron oxy-hydrate with oleic acid at 320 °C.^{3j}

The diameter of the nanocrystals was crucially manipulated via several systematic conditions, such as the ratios of surfactant to iron precursor, cosurfactant, seed mediated growth, growth temperature, and heating rate. Hyeon *et al* developed the systematic control over the diameter of iron oxide nanocrystals ranging from 4 to 22 nm in diameter; the higher ratio of a surfactant to an iron precursor forms larger diameter of the nanocrystals at 300 °C.^{3d, 18} Use of a higher reaction temperature than 300 °C also affected the increase in diameter of the nanocrystals in trioctylamine as a solvent at 360 °C.^{2c} On the other hand, the low temperature decomposition of iron precursor at 250 °C with fast heating rate (10 °C/min) in the presence of cosurfactant (both oleic acid and oleyl alcohol) yielded the smallest nanocrystals having 1.5 nm in diameter. Fast nucleation of iron precursor at low temperature by adding cosurfactant led to smaller iron oxide nanocrystals.

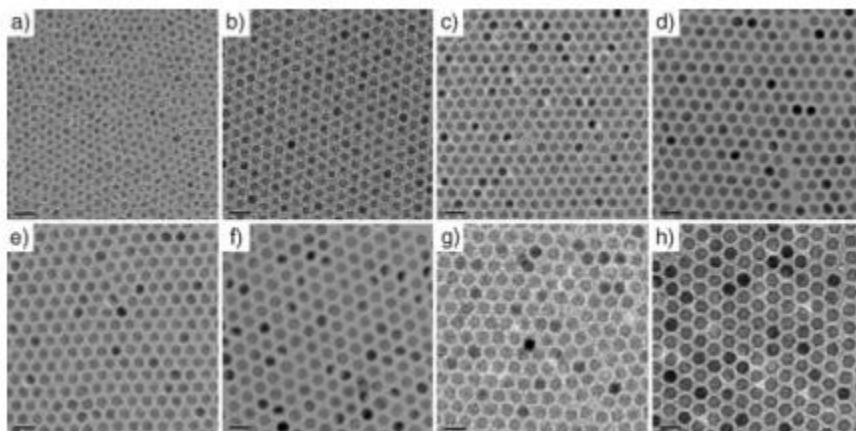


Figure 1.2 TEM images of iron oxide nanocrystals.

Iron oxide (γ - Fe_2O_3) nanocrystals were synthesized by decomposition of iron oleate. (a-h) 6,7,8,9,10,11,12, and 13 nm iron oxide nanocrystals.¹⁸

In the classical LaMer mechanism, the number of tiny particle (nuclei) are formed via fast nucleation at high temperature and grow bigger nanocrystals by consuming monomers.^{4a} In this standard model, using preformed nanocrystals as seeds can replace nucleation and growing larger nanocrystals. Sun *et al* demonstrated seed mediated growth method (Sun's method); with 4 nm iron oxide nanocrystals as seeds, larger nanocrystals of up to 20 nm in diameter were synthesized.^{3g} This method was further modified by controlling the period of heating at 220 °C (for 30 min or 1 h) and 300 °C (for 30 min or 1h) to yield the nanocrystals up to 100 nm truncated octahedral nanoparticles.¹⁹ Heating rate is another parameter to control the diameter of iron oxide nanocrystals. Guardia P et al reported that slow heating rate (0.8 °C/min) grew the largest nanocrystals of 180 nm; iron oxide cube ranging from 45 to 180 nm in edge length was grown by the mixture of decanoic acid and dibenzyl ether at 200 °C for 1h.^{1a}

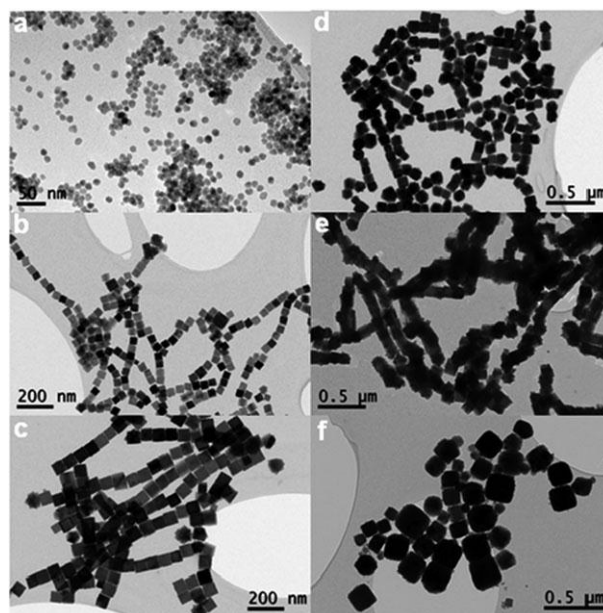


Figure 1.3 TEM images of iron oxide nanocrystals. (a) 13 nm, (b) 45 nm, (c) 67 nm, and (d) 180 nm edge length iron oxide cubes, respectively.^{1a}

While the diameter of iron oxide nanocrystals was controlled (from 4 to 180 nm) from various experimental conditions via iron precursor decomposition method. In addition, the morphology of iron oxide nanocrystals also transformed with size from spherical to cube, truncated octahedral, or rod with broad diameter distribution. Different morphology of iron oxide may have an effect on both magnetic properties (such as paramagnetic and superparamagnetic) and crystal structure of the crystal (Fe, FeO, FeOOH, Fe₂O₃, and Fe₃O₄).^{1a, 2c, 3g, 18-20} To better understand size and phase (crystal structure) dependent magnetic properties of iron oxide nanocrystals, libraries of wide range of monodisperse iron oxide nanocrystals (without phase transformation) are still necessary.

1.3.2. Cerium oxide

Cerium oxide (ceria, CeO_2) is a rare earth metal oxide that has two different states, Ce (III) and Ce (IV), in a cubic fluorite structure. This mixed valence state is preceded by defects on the surface of cerium oxide particles where oxygen ions are stored, released and transported. The mixed oxidation state is catalytically important because of its redox reaction.^{2a, 21} It is important to maximize surface area by synthesizing particles in the nanoscale regime to maximize its catalytic properties. It was reported that nanocrystalline cerium oxide (nanoceria) has more oxygen vacancies on the surface and hence, an increase in catalytic activity with high surface area.²² This is related to the amount of Ce^{3+} on the surface of nanoceria because the oxygen atom is released from its lattice position leaving behind two electrons that localize on two cerium atoms, reducing Ce^{4+} to Ce^{3+} .²³ Qiu *et al.* reported that nanoscale cerium oxide has higher oxygen vacancies than microscale cerium oxide.²⁴

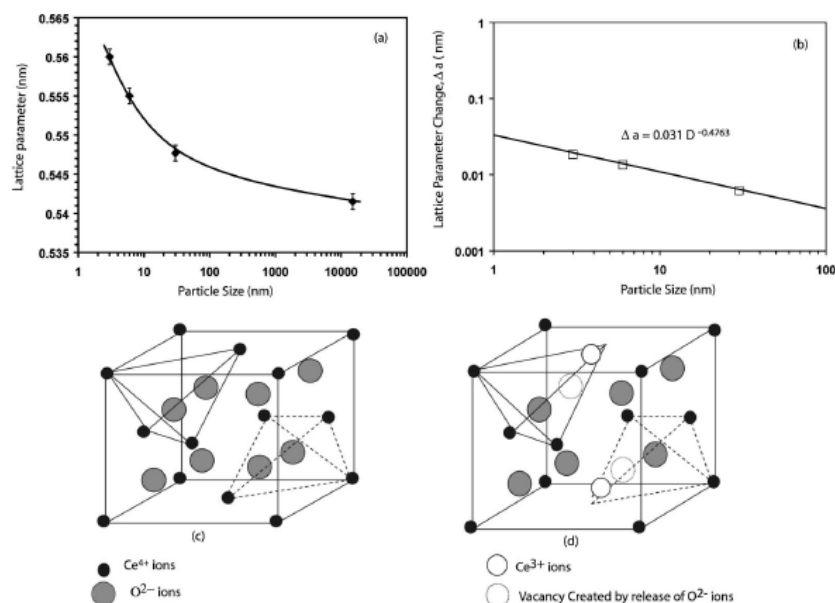


Figure 1.4 Cubic fluorite structure of cerium oxide.

(a) Semilog plot of the lattice parameter as a function of the particle size. (b) Log-log plot of the change in the lattice parameter vs particle size. (c) Cartoon diagram of bulk ceria crystal structure showing intact CaF₂ structure. (d) Distorted crystal structure of nanoceria due to oxygen vacancy creation and replacement of Ce⁴⁺ ions by Ce³⁺ ions.²⁵

1.3.2.1. Synthesis of cerium oxide nanocrystals

Nanocrystalline cerium oxide can be produced by aqueous methods, such as hydrothermal, inverse coprecipitation, microemulsion, microwave, and sonochemical method. Generally, cerium salts, such as cerium nitrate, cerium chloride, and ammonium cerium nitrate, were dissolved in an aqueous solvent and the diameter, and shape were controlled by temperature, pressure, and pH. Zhou *et al.* reported that 10-15 nm ceria nanocrystals were prepared using cerium nitrate (Ce(NO₃)₃·6H₂O) and ammonium hydroxide in water at high temperature (about 1350 °C) through hydrothermal method.²⁶ Also, the morphology of the nanocrystals (wire, tube, and

spherical shaped cerium oxide) could be controlled by temperature and pressure.²⁷ Microwave and sonochemical method resulted in 2 nm cerium oxide nanocrystals.²⁸ Although the aqueous method produced highly crystalline nanocrystals with high yields, the resulting materials are easily undergoing aggregation with poor diameter distribution. However, organic solvent or surfactant assisted aqueous methods yield homogeneous cerium oxide nanocrystals with narrow diameter distribution. Yang *et al.* added a stabilizing agent (oleic acid and t-butylamine in toluene) to a hydrothermal condition and obtained 4-100 nm cube shape ceria.²⁹ In addition, a water-in-oil microemulsion method formed monodisperse cerium oxide nanocrystals ranging from 2.6 to 4.1 nm in diameter.³⁰

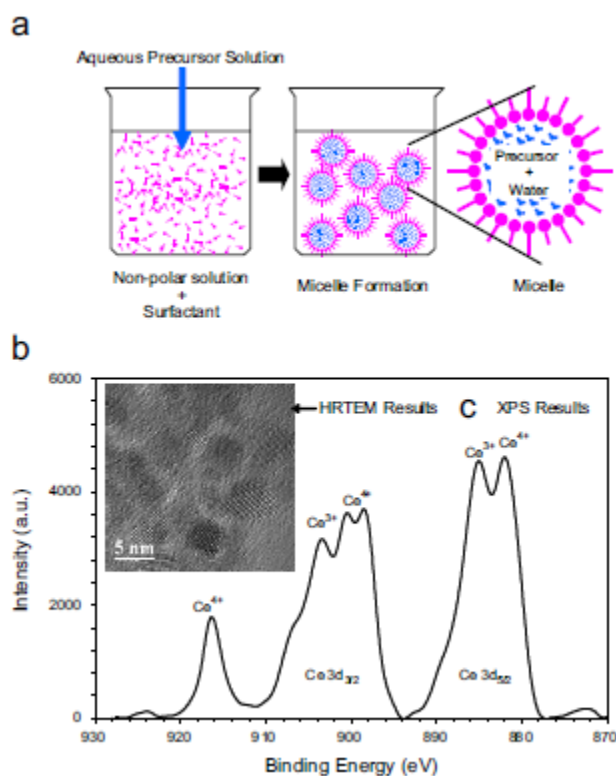


Figure 1.5 Cerium oxide nanocrystals from reverse micelle.

(a) a scheme of microemulsion technique. (b and c) nanocrystalline cerium oxide formed by reverse micelle process and XPS analysis.³¹

A non-aqueous route (an organic method) for cerium oxide is an extraordinary method having advantages of single step, morphology control, high crystallinity, and surface chemistry with good reproducibility. To synthesize high crystalline monodisperse cerium oxide nanocrystals, high boiling temperature solvent is necessary to decompose cerium precursor completely. High temperature solvents (such as Decalin (180 °C), 1-tetradecene (250 °C), octyl ether (290 °C), and 1-octadecene (320°C)) enabled cerium precursors (cerium oleate) to be decomposed completely resulting in 5-20 nm ceria nanocrystals.³² While the reaction temperature is related to the nanocrystal formation, the diameter and shape of cerium oxide nanocrystals were more closely influenced by the ratios between cerium precursor and surfactant, cosurfactant, and time. Control over the diameter (2-5 nm) and shape (spherical, tadpole, and wire) of cerium oxide nanocrystals were reported by Yu et al.; the ratio of cerium precursor to surfactants (oleic acid and oleylamine), reaction temperature, and time changed the shape and diameter of the nanocrystals.³³ Nanocrystal growth rate control also changed the shape from spherical to 3D structure; Wang et al. reported flower-shape (at 120 °C for 8 min) and cube-shaped nanoceria (at 240 °C for 24h) using $\text{Ce}(\text{NO}_3)_3 \cdot 6\text{H}_2\text{O}$ in octadecylamine.³⁴ Use of cosurfactant or additive also transformed the shape of cerium oxide nanocrystals. Ahniyaz et al reported about 10 to 25 nm dumbbell and rod-shaped ceria using cerium oleate and octadecylamine.³⁵ Recently, this group reported diameter and shape controlled cerium oxide nanocrystals; the mixed surfactant of oleic acid and oleylamine forms star and cube shaped cerium oxide, and the additive (water and octadecylamine) increased the diameter up to 10 nm.

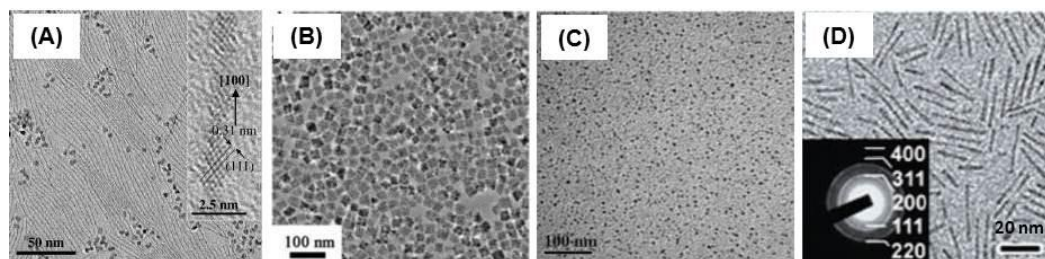


Figure 1.6 Cerium oxide nanomaterials from non-hydrolytic route (organic method). Various shaped cerium oxide nanocrystals synthesized by organic method. (a) tadpole³³ (b) cube³⁴ (c) spherical^{32a} (d) rod shape.³⁵

1.4. Applications of nanocrystals

1.4.1. Iron oxide for carbon nanotube growth

Diameter control for carbon nanotubes (CNTs) is essential for most applications because their structural and physical properties are critically affected by chirality and diameter.³⁶ It is possible to manipulate CNT diameter by changing the dimensions of metal catalysts deposited on substrates via either electron beam or sputtering methods for CNTs formed via catalysts and chemical vapor deposition.³⁷ Recently, the diameter of CNTs was shown to directly scale with the size of the deposited metallic catalyst.³⁸ However, when catalysts are deposited in gas phase methodologies, it is not possible to probe the upper limit of this relationship as the metal begins to form discontinuous films as opposed to discrete islands. Such catalysts also exhibit wide size distributions prompting some speculation that more uniform catalyst materials could improve the diameter distribution of CNTs.

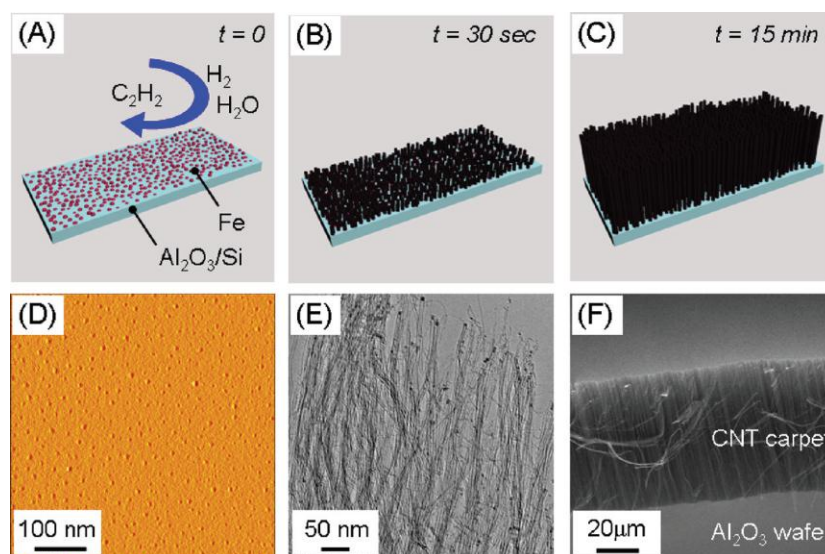


Figure 1.7 Carbon nanotube growth process.

Nanocrystals on alumina wafer were used to catalyze carbon nanotube carpet growth flowing C_2H_2 , H_2 , and H_2O (A,D). After nucleation of carbon on the nanocrystals, carbon nanotubes started growing (B,E). A 15 min reaction rendered vertically aligned thick carbon nanotube carpet (C,F).³⁹

The use of preformed nanocrystals as catalysts for CNT formation offers many advantages for carbon nanotube manufacturing. These materials could be printed or coated onto substrates prior to chemical vapor deposition (CVD), and for the reasons outlined above offer the potential for forming CNT with very different diameters and uniformity than those grown from gas-phase deposited catalysts.^{2c} Hafner *et al* was first to use pre-synthesized nanoparticles for CNT synthesis and obtained single- and double-walled CNTs from Fe-Mo nanoparticles.⁴⁰ Later, near monodisperse Fe-Mo (3 to 14 nm) and Ni (3 to 7 nm) nanoparticles were shown to catalyze CNT formation and this work highlighted that the conditions for favorable growth were quite limited.⁴¹ Pre-formed iron nanoparticles (3 to 13 nm) were also used to catalyze CNT growth and some tunability was achieved by varying temperature and gas flow rates.⁴² However, in these examples

the preformed catalysts were too broad in their size distribution to fully explore the relationship between catalyst dimensions and the resultant CNT dimensions and structures.

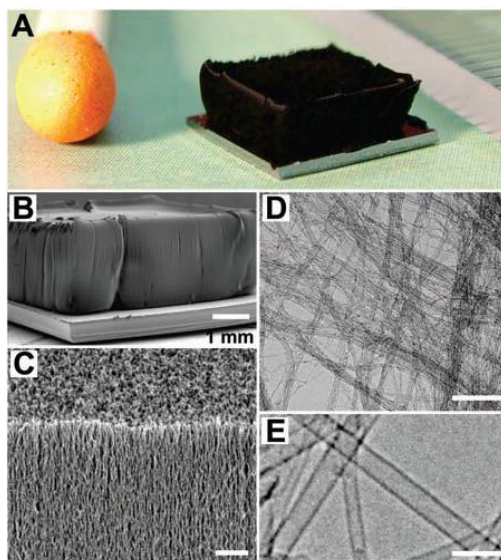


Figure 1.8 SWNT forest grown with water assisted CVD.

(A) picture of a 2.5 nm tall SWNT forest on a 7 mm by 7 mm silicon wafer. A matchstick on the left and ruler with millimeter markings on the right is for size reference. (B) SEM image of SWNT forest. (C) SEM image of the SWNT forest ledge. Scale bar, 1 μm. (D) Low resolution TEM image of the nanotubes. Scale bar, 100 nm. (E) High resolution TEM image of the SWNTs. Scale bar, 5 nm.⁴³

An important format for CNT applications is the carpet morphology, termed vertically aligned carbon nanotube (VA-CNT) carpets. These samples are of great interest because the densely packed structures are ideal for gas or fluid flow membranes, super-capacitor electrodes, and any other technology that benefits from aligned CNTs with high surface area.⁴⁴ The original report of CNT carpet formation reported a 50 micron high carpet of aligned CNTs formed using iron nanoparticles catalysts formed via electron beam deposition.⁴⁵ Since then, improvements in the quantity, length and quality

of these carpets has been linked to the specific details of the catalyst, including its composition, size and morphology.⁴⁶ Nishino *et al* reported that monodisperse 3.2 nm diameter Fe-Mo nanoparticles prepared from an organic method were used to grow CNT carpets for the first time and 2.8 nm diameter single walled-CNTs (SWNT) were prepared with high purity over 99.99 %.⁴⁷ After this, various ranged prepared nanoparticles were utilized to grow CNT carpets. However, the resulting CNTs were predominantly multi-walled CNTs (MWNT) with poor diameter control when using iron oxide nanoparticles from 4.5 to 16 nm.⁴⁸ More recently, this group has demonstrated that organically modified iron oxide nanocrystals could serve as catalysts for CNT growth in spite of their surface coating and oxidized state.^{46d} Presumably after treatment in reducing conditions and high temperatures, the organic moieties are volatilized and the iron oxide reduced to the active iron form required for CNT catalysis.⁴⁹

1.4.2. Cerium oxide as an antioxidant

Cerium oxide (CeO_2 , ceria) is one of the lanthanide metal oxides, having good reversible catalytic properties induced by the redox cycle between two oxidation states of cerium, cerium (III) and cerium (IV).^{50,51} This feasibility allows ceria to have oxygen non-stoichiometry composition, CeO_{2-x} ; oxygen vacancy exists on the defect site of ceria generated by oxygen atom release, leaving behind electrons, and reducing cerium (IV) to cerium (III) on the surface of cerium oxide.^{23,52} Deshpande *et al.* reported that nano-size cerium oxides led to more number of oxygen vacancy formation than bulk size of the comparable materials, resulting in CeO_{2-x} .²⁵ The oxygen buffer property of ceria makes it ideal for the industrial applications such as, water-gas shift catalyst, UV absorber, oxygen

ion conductor, and solid oxide fuel cells.^{53,2a, b, 22b, 54} Recently, the redox cycling of the oxygen non-stoichiometry cerium oxide nanocrystal was applied to the biological system as an antioxidant.⁵⁵

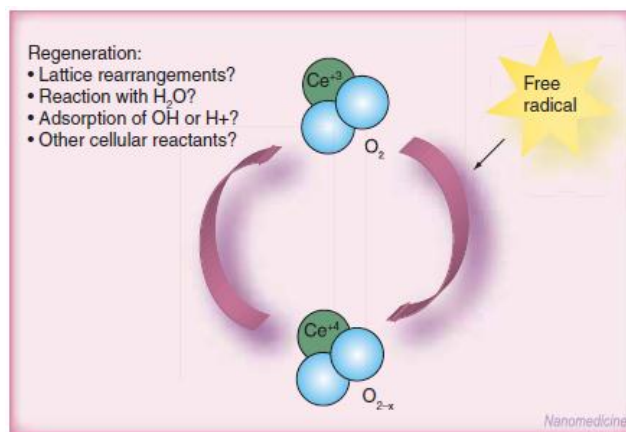


Figure 1.9 Antioxidant property of cerium oxide.

During free radical scavenging, cerium changes between the +3 to the +4 valence state, accompanied by an alteration in the defect structure of the oxide lattice.⁵⁶

Although there are numerous experimental findings showing potential radical scavenger properties of cerium oxide, the mechanistic study of the redox cycling of nanoceria in the presence of hydrogen peroxide has not been explored deeply. Several researches reported that cerium (III) may react with the same molar H_2O_2 in the reversible catalytic reaction mechanism.⁵⁷ On the other hand, Heckert *et al.* proposed the redox cycling of nanoceria in the presence of H_2O_2 using the Fenton/Harbor Weiss reaction;⁵⁸ in this process, doubled molar H_2O_2 decomposed into H_2O and O_2 in the redox cycling of cerium oxide.^{31, 55, 58-59} Recently, Xue *et al.* showed that the reaction between cerium oxide and hydrogen peroxide may go through a Fenton-like reaction based on the photometric measurement using methyl violet; the color of methyl violet persisted in the

presence of cerium oxide by scavenging the hydroxyl radical ($\bullet\text{OH}$), the intermediate in the mechanism of Fenton reaction generated by H_2O_2 .⁶⁰

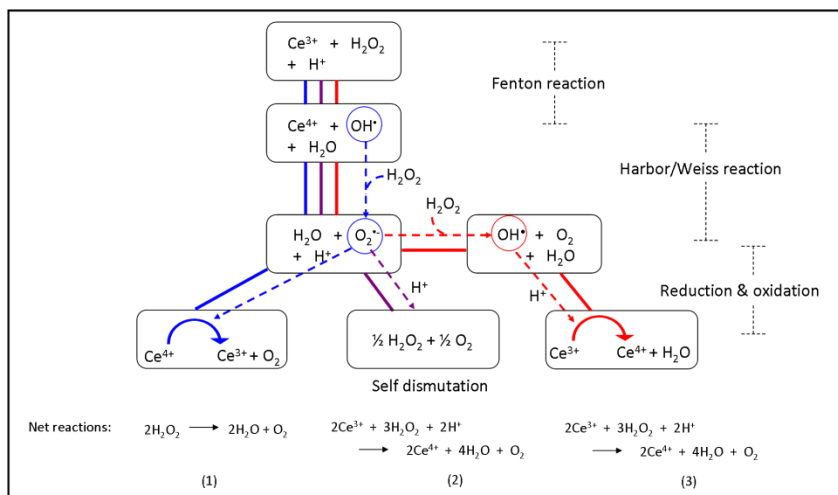


Figure 1.10 The expected redox cycling mechanisms.

Cerium oxide reacts with H_2O_2 with three different ways. cerium (III) is oxidized by reacting with H_2O_2 (Fenton reaction), generating hydroxyl radical (OH^\bullet), and superoxide anion (O_2^\bullet) under Harbor/Weiss reaction. The oxidized cerium (IV) is reduced by O_2^\bullet (cerium (III) recovery). However, cerium (III) recovery process does not occur quickly (especially induced by excess H_2O_2 addition), O_2^\bullet may go under self dismutation process (2) or keep reacting with more H_2O_2 by Harbor/Weiss reaction (3). The reaction of cerium oxide with H_2O_2 may undergo all three mechanism processes.

Several studies reported the antioxidant properties of cerium oxide against reactive oxygen species (ROS) driven diseases such as cancer, Alzheimer's diseases, cardiac dysfunction, radiation induced cell death, and aging.⁶¹ Das *et al.* reported that nanoceria protected adult rat spinal cord neurons against oxidative stress.³¹ Perez *et al.* showed antioxidant property of nanoceria for the improved cancer therapeutics.^{57b} More recently, Kim *et al.* first showed that cerium oxide nanocrystals reduced ischemic brain damage induced by reactive oxygen species in living animals (Male Sprague-Dawley rats).⁶² In these studies, hydrogen peroxide mediated redox cycling of nanoceria produced by co-precipitation or microemulsion method was demonstrated using colorimetric assay,

monitoring the reversible color change of nanoceria solution. More recently, this group has reported that monodisperse nanocrystalline ceria with the diameters from 3 to 10 nm synthesized by high temperature metal precursor decomposition in organic media was phase-transferred to water, then the redox cycling of nanoceria has been demonstrated despite its double layered surface coating (polyacrylic acid-octyl amine and oleylamine).^{32b}

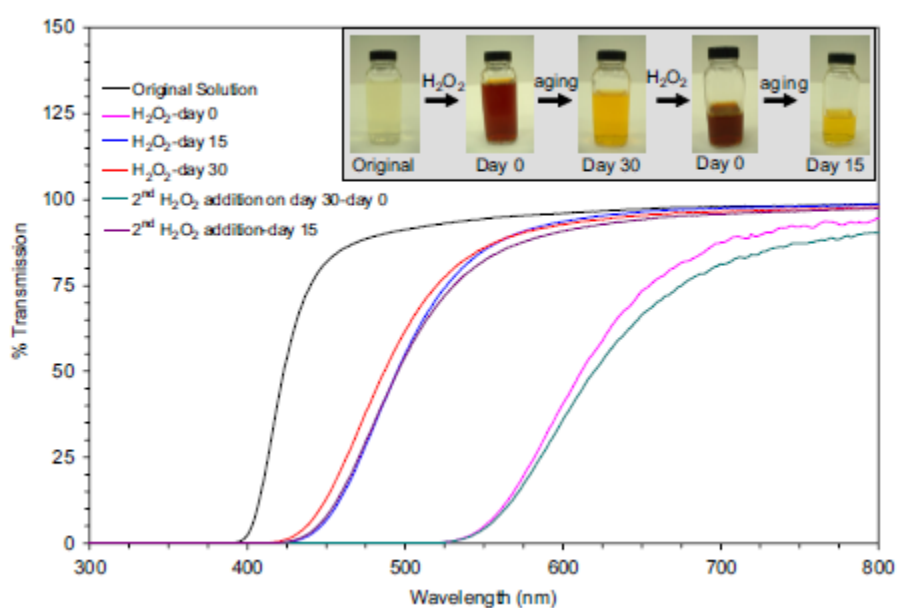


Figure 1.11 antioxidant properties of ceria.

UV- Vis measurement of cerium oxide nanocrystals treated with hydrogen peroxide at different time intervals.³¹

1.5. Summary and outlook

Monodisperse iron oxide and cerium oxide nanocrystals were synthesized from non-aqueous route (high temperature metal precursor decomposition). Morphology and dimension of nanocrystals were controlled by reaction temperature, time, the ratio of

surfactant to metal precursor, and cosurfactant. The resulting nanocrystals can be phase-transferred for further applications by changing the functional group on the outer shell of the nanocrystal structure.^{3a, 32b, 63}

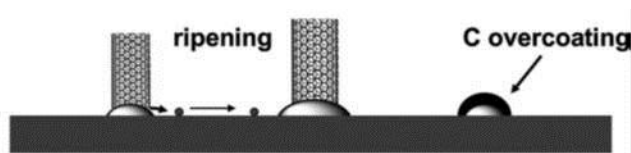


Figure 1.12 Schematic of effects which are occurring on the catalyst during carbon nanotube growth. Carbon over-coating and Ostwald ripening (catalyst poisoning) are labeled as a potential termination mechanism.⁶⁴

Diameter controlled carbon nanotube were achieved by preformed iron oxide nanocrystals as precursor catalysts. We should understand the interface chemistry between nanocatalyst and the substrate (such as Al_2O_3 , SiO_2 , and TiO_2) to prepare high quality carbon nanotubes.⁶⁵ Catalyst poisoning at high temperature in the growth system may lead to multi walled carbon nanotube or CNT with defects.⁶⁴ Ferrite nanocrystal can be used as a key catalyst for high quality carbon nanotube growth to avoid nanocrystal migration on the substrate. Transition metal doped iron oxide may prevent catalyst poisoning by strong interaction between nanocrystal and the substrate.

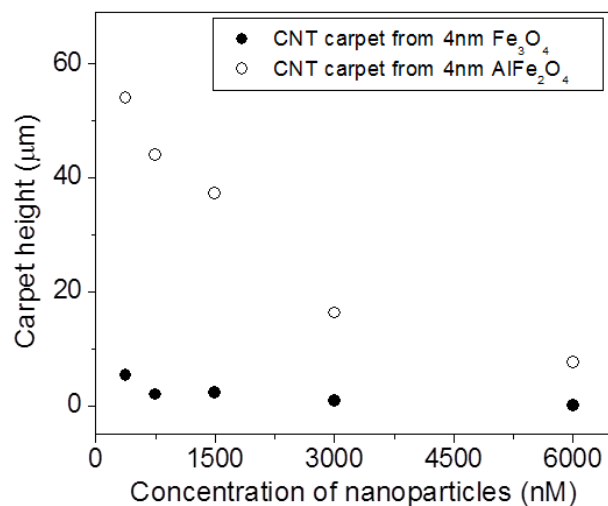


Figure 1.13 Carbon nanotube carpet growth using both iron oxide and aluminum ferrite nanocrystals.

Aluminum ferrite nanocrystal grew carbon nanotube faster than pure iron oxide nanocrystals.³⁹

Cerium oxide nanocrystal is a potential antioxidant material having numerous interesting reactive oxygen species scavenger properties in biological media.⁶⁶ The diameter and surface coating dependent antioxidant properties of cerium oxide were measured with various analytical characterizations.⁶⁷ However, in order to better understand the mechanism of redox cycling of ceria in the presence of reactive oxygen species, a quantitative analysis that examines the reaction ratio between hydrogen peroxides and cerium (III) on the surface of nanoceria is required. Furthermore, the in vivo research based on mechanistic and in vitro results will give an answer about a use of cerium oxide nanocrystals as an antioxidant to reduce oxidative stress in therapeutic research.

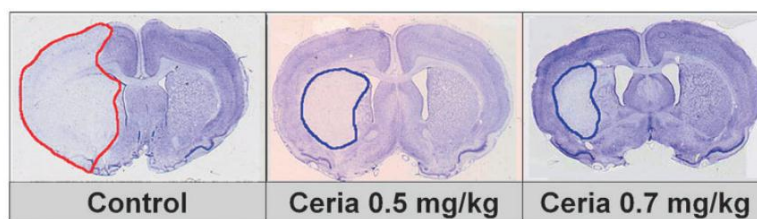


Figure 1.14 Cerium oxide nanocrystals that can protect against Ischemic stroke. Untreated (control) and ceria nanocrystal treated (0.5 and 0.7 mg/kg) ischemic brain slices clearly showing that 0.5 and 0.7 mg/kg ceria nanoparticles can significantly reduce infarct volumes.⁶²

Chapter 2

Synthesis of magnetic metal oxide nanocrystals through non-hydrolytic route

2.1. Introduction

Magnetic metal oxides are the mixed metal oxides having magnetic properties, such as magnetite and various ferrites ($M_xFe_2O_4$, M=divalent transition metal cations, such as Ni, Mn, Co, and Zn).⁶⁸ It has a cubic inverse spinel structure consisting of iron (III) in tetrahedral holes and both M (II) and iron (III) in octahedral holes. These types of magnetic metal oxides are widely used for magnetic recording, environmental remediation, magnetic resonance imaging, bioseparations and drug targeting.^{1b-e, 2c, 3j, 69} Furthermore, large scale uses of iron oxides in industry range from ore refinement to ferrofluids based oscillation damping and position sensing.^{20, 69b, 70}

Nanocrystalline iron oxides and ferrites have the potential to be used more effectively than bulk materials in the aforementioned industrial and biological applications because of their high surface areas, uniform size with narrow distribution, and size dependent physico-chemical properties.^{4c} A synthetic route that prepares monodisperse magnetic iron oxide nanocrystals with high crystallinity is of crucial importance. There have been a lot of interests in monodisperse magnetic iron oxide nanocrystal synthesis with controllable diameter and composition during the last two decades.⁷¹

One route for the development of uniform nanocrystals is high temperature metal precursor decomposition method (non-hydrolytic route). Rockenberger *et al* first demonstrated iron oxide nanocrystal synthesis under non-hydrolytic route.¹⁶ Hyeon *et al* achieved the control over the diameter of iron oxide nanocrystals with narrow diameter distribution using an iron oleate salt as an iron precursor.^{3d} Sun *et al* produced various ferrite nanocrystals by the decomposition of metal acetylacetonate precursor at high temperature (at 265 °C).²⁰ Recently, this group reported that iron carboxylate precursor formed by the mixture of iron oxy-hydrate and the excess oleic acid (with the ratio of 1:4) at elevated temperature is pyrolysed to produce highly monodisperse iron oxide nanocrystals especially at 320 °C.^{3a, 3j, 63b}

Previous researches taught us that metal precursor decomposition at high temperature led to monodisperse magnetic iron oxide nanocrystals with high quality. In addition, there are many other experimental parameters to be considered to produce material libraries with a wide range of diameters and elemental composition. In this chapter, I have demonstrated and optimized the conditions to control over the diameter and composition of monodisperse iron oxide and various ferrite nanocrystals. Iron oxide nanocrystals

ranging from 3 to 40 nm were synthesized by controlling iron monomer concentration, the ratio of iron precursor to surfactant, and the additional co-surfactant. Various ferrite nanocrystals with varied composition ratio were also prepared by changing the concentration of metal precursors. Various examples for nanocrystal synthesis will provide better understanding of nanocrystal formation and design of the nanocrystal with tunable features.

2.2. Experimental methods

2.2.1. Chemicals.

Iron oxide, hydrated (Goethite, $\text{FeO}(\text{OH})$, catalyst grade, 30-50 mesh), aluminum hydroxide ($\text{Al}(\text{OH})_3$, reagent grade), nickel acetate tetrahydrate ($\text{Ni}(\text{OCOCH}_3)_2 \cdot 4\text{H}_2\text{O}$, 98 %), manganese chloride tetrahydrate ($\text{MnCl}_2 \cdot 4\text{H}_2\text{O}$, 99 %), zinc acetate ($\text{Zn}(\text{OCOCH}_3)_2 \cdot 4\text{H}_2\text{O}$, 99.99 %), oleic acid (OA, technical grade, 90%), oleyl alcohol (technical grade, 85%), 1-octadecene (ODE, technical grade, 90%) were purchased from Sigma-Aldrich; aluminum oleate was purchased by Fisher Scientific. All nanoparticles were synthesized under nitrogen (N_2 , 99.999%).

2.2.2. Synthesis of iron oxide nanocrystals

2.2.2.1. Iron oleate synthesis

Iron oleate as an iron precursor was prepared by iron oxide, hydrate (FeOOH , 20 mmol, 1.8 g), oleic acid (OA, 80 mmol, 22.4 g) and 1-octadecene (60 g) at 240 °C for 4h.

Iron oleate was also synthesized by the reaction of iron chloride (20 mmol, 3.24g) with sodium oleate (60 mmol, 18.3 g) in the mixture of ethanol (40 g), water (20g), and hexane (60 g) at 60 °C for 6 h. The resulting black colloid was washed using ethanol, acetone, and hexane. For details, 10 ml of black colloid was collected in 50 ml centrifuge tube and 20 ml of ethanol and 20 ml of acetone was mixed together. Then, the tube containing a black precipitate was centrifuged at 6,000 rpm for 15 min. The purification process was repeated in triplicate. The resulting black colloid (iron oleate) was finally stored in hexane in an amber color bottle. (Figure 2.1)

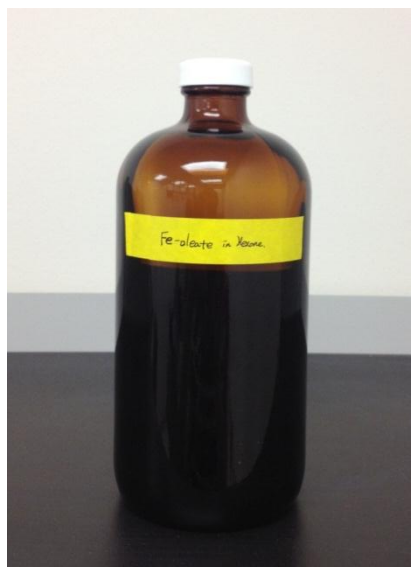


Figure 2.1 Iron oleate in an amber bottle.

2.2.2.2. Nanocrystals from iron oleate

Iron oxide nanoparticles ranging from 5 to 14 nm were prepared by using iron oleate (from 0.015 to 0.15 mmol), oleic acid (from 0.3 to 5 mmol) in 5 g of ODE at 320 °C for desired reaction time (from 1 to 3 h) under ultrapure N₂ condition.

2.2.2.3. Nanocrystals from the mixture of iron oleate and oleyl alcohol

Iron oxide nanocrystals (from 3 to 7 nm) were synthesized by the mixture of iron oleate (1.67 mmol), oleic acid (from 1 to 3 mmol), and oleyl alcohol (from 1 to 3 mmol) in 15 g of ODE at 280 °C for 1h.

2.2.2.4. Nanocrystals from high monomer concentration

The mole ratio between iron oxy-hydroxide (FeOOH) and oleic acid (OA) was fixed to 1/4. The high molar concentration of FeOOH (from 1 to 50 mmol) and OA (from 4 to 200 mmol) was mixed in 40 mmol (10 g) of ODE at room temperature. FeOOH was not soluble in the presence of OA in ODE at room temperature but dissolved at 240 °C where iron carboxylate precursor prepared. Iron oxide nanocrystals grew at 315 °C for desired time (from 1 to 12 h).

2.2.3. Synthesis of Ferrite nanocrystals

2.2.3.1. Nickel, manganese, and zinc oleate synthesis

Nickel oleate was prepared by the reaction of nickel acetate (10 mmol, 1.76 g) and oleic acid (20 mmol, 5.64 g) in 10 g of ODE at 90 °C for 2h.⁷² Manganese oleate was

synthesized by the reaction of manganese chloride (10 mmol, 1.25 g) with oleic acid (20 mmol, 5.64 g) in 10 g of ODE were heated at 180 °C for 2 h.⁷³ Zinc oleate was prepared by the mixture of zinc acetate (10 mmol, 1.83 g), oleic acid (20 mmol, 5.64 g) in 10 g of ODE at 210 °C for 2 h.⁷⁴ The purification of metal oleate was treated by the same method used for iron oleate precursor purification using ethanol, acetone, and hexane.

2.2.3.2. Manganese iron oxide ($\text{Mn}_x\text{Fe}_{3-x}\text{O}_4$)

The mixture of iron oleate (0.03 mmol) and manganese oleate (from 0.0003 to 0.03 mmol) were used with 2 mmol of oleic acid in 5 g of 1-octadecene (ODE) at 320 °C for 2h.

2.2.3.3. Nickel iron oxide ($\text{Ni}_x\text{Fe}_{3-x}\text{O}_4$)

The mixture of iron oleate (0.03 mmol) and nickel oleate (from 0.0015 to 0.03 mmol) were used with oleic acid (from 2 to 8 mmol) in 5 g of 1-octadecene (ODE) at 320 °C for 1 to 6 h.

2.2.3.4. Zinc iron oxide ($\text{Zn}_x\text{Fe}_{3-x}\text{O}_4$)

The mixture of iron oleate (0.03 mmol) and zinc oleate (from 0.0003 to 0.03 mmol) were used with 2 mmol of oleic acid in 5 g of 1-octadecene (ODE) at 320 °C for 2 h.

2.2.3.5. Aluminum iron oxide ($\text{Al}_x\text{Fe}_{3-x}\text{O}_4$)

The mixture of iron oleate (0.05 mmol) and aluminum oleate (0.02 mmol) were used with 2 mmol oleic acid in 5 g of 1-octadecene (ODE) at 320 °C for 2 h. Instead of iron

oleate, iron oxy-hydrate (FeOOH) can be also used as an iron source. For example, 0.7 mmol FeO(OH) and 0.3 mmol Al(OH)₃ with 3 mmol oleic acid in 5 g ODE at 320 °C for 1 h grew about 10 nm aluminum ferrite nanocrystals. To control the diameter and aluminum contents of the nanocrystals, the molar concentration of iron and aluminum oleates, additional molar oleic acid, and reaction time were varied. More details were mentioned in Chapter 3.

2.2.3.6. Nickel aluminum iron oxide (NiAlFeO₄)

The mixture of iron oxy-hydroxide (0.7 mmol), nickel oleate (0.4 mmol), and aluminum oleate or aluminum hydroxide (0.6 mmol) were used with 2 mmol of oleic acid in 5 g of 1-octadecene (ODE) at 320 °C for 2 h.

2.2.3.7. Manganese zinc iron oxide (Mn_xZn_{x-1}Fe₂O₄)

The mixture of iron oleate (0.03 mmol), manganese oleate (from 0.009 to 0.015 mmol), and zinc oleate (from 0.015 to 0.03 mmol) were used with 2 mmol of oleic acid in 5 g of 1-octadecene (ODE) at 320 °C for 2 h.

2.2.3.8. Manganese aluminum iron oxide (MnAlFeO₄)

The mixture of iron oleate (0.03 mmol), manganese oleate (0.03 mmol), and aluminum oleate (0.03 mmol) were used with 2 mmol of oleic acid in 5 g of 1-octadecene (ODE) at 320 °C for 2 h.

2.2.3.9. Manganese zinc aluminum iron oxide ($Mn_{x-1}Zn_xAlFeO_4$)

The mixture of iron oleate (0.03 mmol), manganese oleate (0.015 mmol), zinc oleate (0.015 mmol), and aluminum oleate (0.03 mmol) were used with 2 mmol of oleic acid in 5 g of 1-octadecene (ODE) at 320 °C for 2 h.

The resulting ferrite nanocrystals were purified using methanol, acetone, and hexane. More specifically, 1g of the resulting colloidal nanocrystals was mixed with 10 ml of hexane, 20 ml of methanol, and 20 ml of acetone and centrifuged at 4500 rpm for 30 min. This process was repeated three times. The cleaned colloidal nanocrystals were redispersed in hexane.

2.3. Results and discussion

2.3.1. Diameter control of iron oxide nanocrystals

Monodisperse iron oxide nanocrystals were synthesized by the decomposition of iron oleate as an iron precursor in the presence of fatty acid (oleic acid) in ODE. As shown in Figure 2.2, all starting precursors were mixed at room temperature in a three neck round bottom flask. This reaction solution undergo pre-heating step to evaporate hexane (at 60 °C for 1 h) and to remove moisture (at 120 °C for 2 h). Iron oleate complex starts decomposing and dissociating one of three oleate ligands at 200-240°C.^{2c} The other two ligands dissociate at around 300 °C. Nucleation completely ends resulting in growth stage between 300-320 °C only when all the ligands dissociate from the iron oleate complex.^{2c}

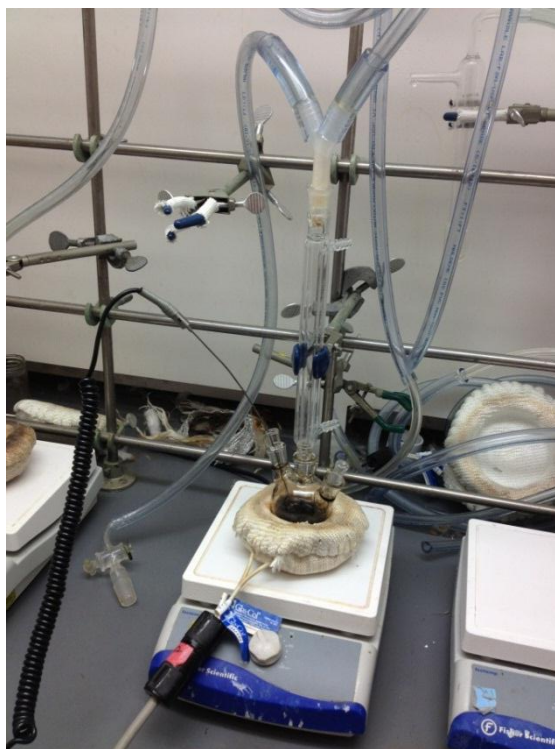


Figure 2.2 An experimental set up for nanocrystal synthesis.

Reaction temperature, reaction time, and the ratio between iron precursor and surfactants are important parameters to control over the diameter of monodisperse iron oxide nanocrystals. Monodisperse iron oxide nanocrystals were grown only after 320 °C; below the temperature of 320 °C led to broad distribution of the nanocrystals resulted from Ostwald ripening. Increasing oleic acid concentration grew the nanocrystals larger as shown in Figure 2.3; the nanocrystals ranged from 5 to 14 nm as oleic acid concentration increased from 0.5 to 4 mmol. Short reaction time (1 h) rendered polydisperse iron oxide nanocrystals (7.0 ± 1.5 nm) but monodisperse iron oxide nanocrystals were synthesized after longer reaction time (longer than 2 h) (Figure 2.4).

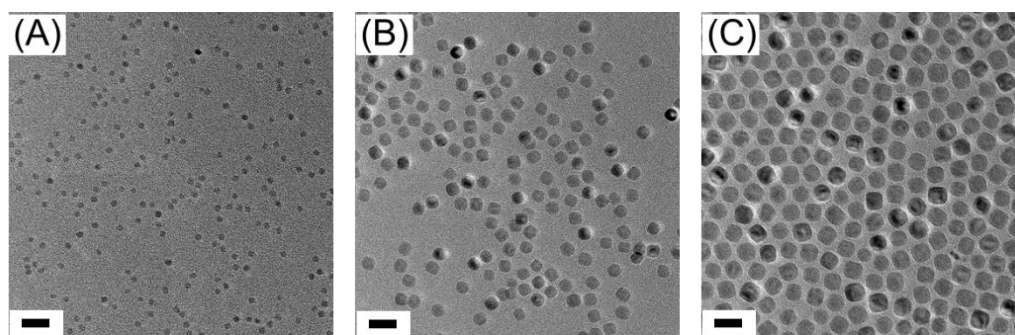


Figure 2.3 Iron oxide nanocrystals grow larger as the ratio of oleic acid to iron precursor increased. Iron oxides were prepared using 1.67 mmol of iron oleate with oleic acid (0.5, 2, and 4 mmol from (A) to (C), respectively) at 320 °C for 2h. Diameters of iron oxides are 5.3 ± 0.5 , 10.7 ± 0.8 , and 14.0 ± 1.2 nm from (A) to (C), respectively. All scale bars are 20 nm.

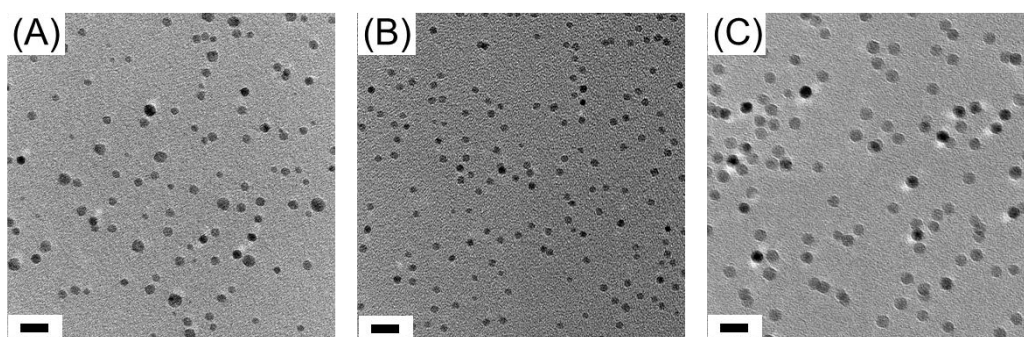


Figure 2.4 Longer reaction time grows monodisperse nanocrystals. The diameter distribution is narrow when nanocrystals were grown for long reaction time. Nanocrystals were synthesized by 1, 2, and 3 hour reaction from (A) to (C), respectively. Each reaction was treated using 1.67 mmol of iron oleate with 0.5 mmol of oleic acid at 320 °C. Diameters of iron oxides from (A) to (C) are 7.0 ± 1.5 , 5.6 ± 0.5 , and 9.9 ± 0.9 nm, respectively. All scale bars are 20 nm.

The smallest iron oxide nanocrystals were obtained by using cosurfactant, such as oleyl alcohol at low reaction temperature (280 °C). TEM images in Figure 2.5 show that monodisperse iron oxide nanocrystals having 8 nm turns to small diameter of the nanocrystals (3 nm) as higher ratio of oleyl alcohol to oleic acid was applied. We

monitored the diameters of iron oxide nanocrystals as the ratio of oleyl alcohol to oleic acid increases in Figure 2.6. We expect that the slow nucleation and growth of iron oxide nanocrystals induced by low reaction temperature at 280 °C in the presence of cosurfactant (oleyl alcohol) may prevent the further growth of nanocrystals.

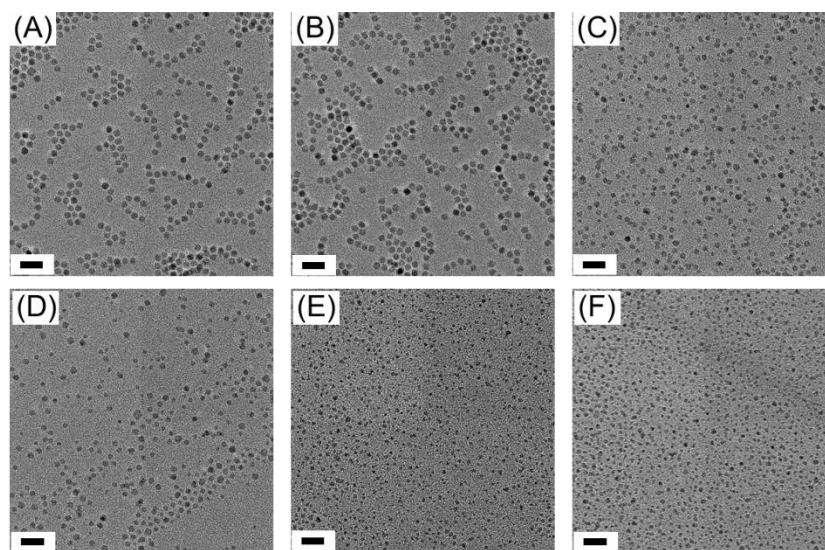


Figure 2.5 Iron oxide nanocrystals formed by oleyl alcohol addition.

Diameters of nanocrystals decreased from increasing concentration of oleyl alcohol addition. Oleic acid : oleyl alcohol is 3:0, 3:1, 3:3, 2:3, 1:3, and 0:3 from (A) to (F), respectively. Size of iron oxide nanocrystals from (A) to (F) is 6.6 ± 0.4 , 6.6 ± 0.5 , 5.8 ± 1.3 , 6.5 ± 1.0 , 3.1 ± 0.5 , and 4.0 ± 0.7 nm, respectively. All scale bars are 20 nm.

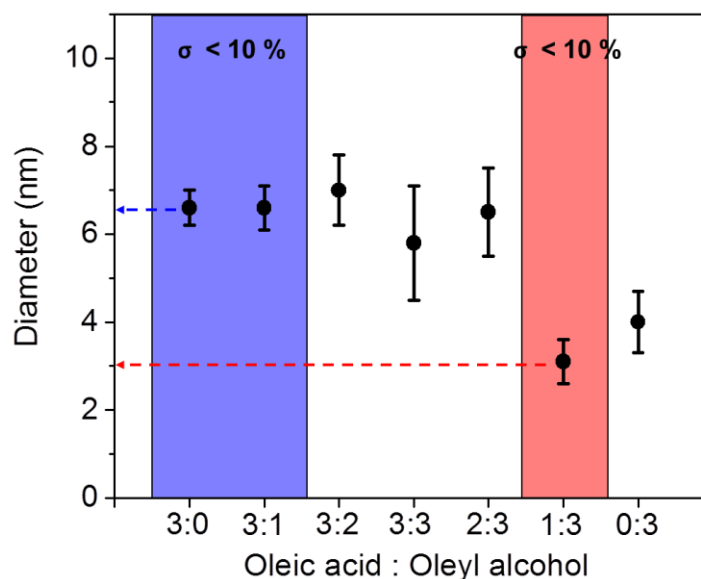


Figure 2.6 Decrease in diameter of iron oxide nanocrystals by adding oleyl alcohol. Iron oxides were formed by 1.67 mmol of iron oleate at 280 °C for 1h. When the ratio of oleic acid/oleylalcohol was 3:0, 3:1, and 1:3, monodisperse nanocrystals ($\sigma < 10\%$) were synthesized.

In the nanocrystal growth process, 1.6 mmol of iron oleate in 10 g of ODE may be too low concentration to keep growing iron oxide nanocrystals after the nucleation stage; after forming large number of nuclei, iron oxides do not grow larger because of the scarcity of monomer in the growth stage of the nanocrystals. However, if the monomer concentration is still high enough to keep growing the nanocrystals in the growth stage, the resulting nanocrystals can increase larger and larger. Towards this end, we accomplished the high monomer concentration in iron oxide nanocrystal synthesis by increasing iron precursor concentration in the fixed amount of ODE (10 g) (in this case, FeOOH was used as an iron precursor with oleic acid and the ratio of FeOOH to oleic acid was fixed to 1:4).

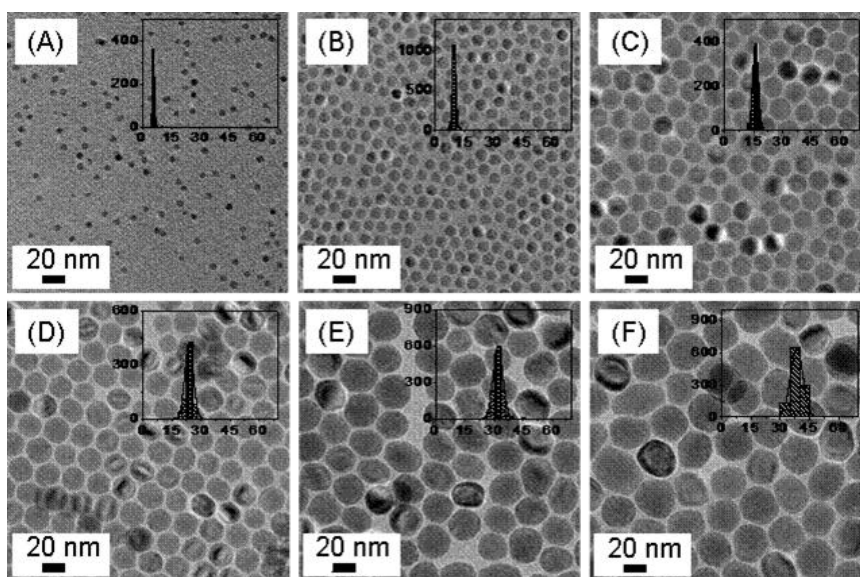


Figure 2.7 Iron oxide nanocrystals from 5 to 40 nm.

Diameters of nanocrystals are 5.7 ± 0.5 , 10.2 ± 0.7 , 16.0 ± 1.4 , 23.9 ± 2.2 , 32.1 ± 2.5 , 38.4 ± 3.3 nm from (A) to (F), respectively. All nanocrystals are dispersible in hexane.

The concentrated iron monomer in the reaction condition increased the diameters of iron oxide nanocrystals up to 40 nm. TEM images in Figure 2.7 show monodisperse iron oxide nanocrystals ranging from 5 to 40 nm. The nanocrystals grew larger as the concentration of iron precursor (FeOOH) increased from 10 to 50 mmol (Figure 2.8). The significant increase in diameter of the nanocrystals occurred from the condition using low amount of ODE (10g) but the growth rate was found to be slow from the reaction in large amount of ODE (60 g).

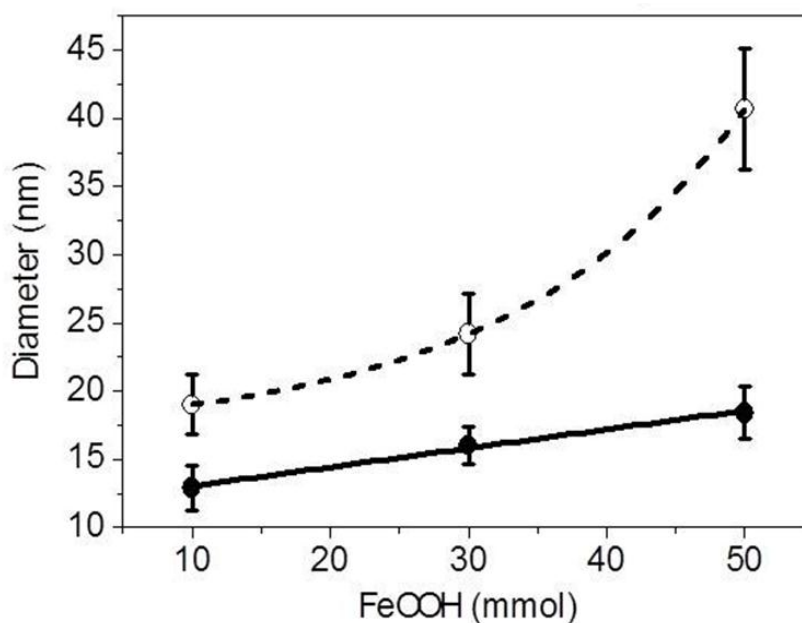


Figure 2.8 Growth of iron oxide nanocrystals depending on monomer concentration. Nanocrystals were grown in 10 g of ODE (dot line) and 60 g of ODE (bold line) at 320 °C for 12 h. In each reactions, the ratio of FeOOH to oleic acid was 1:4.

Nanocrystal diameter broadening induced by the formation of bigger nanocrystals at the expense of the dissolution of smaller nanocrystals does not occur although monomer concentration gets depleted at 320°C with time.^{4b, c, 6a, 6d, 76, 3i} After performing long time nanocrystal synthesis for 12 h, we did not find any evidence about ripening of nanocrystals. As shown in Figure 2.9, the resulting iron oxide nanocrystals grown for 1 to 12 h have narrow diameter distribution ($\sigma < 10\%$). In addition, the diameter did not change much as a function of reaction times. For example, 33 nm in diameter increased to 38 nm of iron oxides from 1 to 12 h in 10 g of ODE; iron oxide in 60 g of ODE increased the diameter from 17 nm to 19 nm from 1 to 12 h.

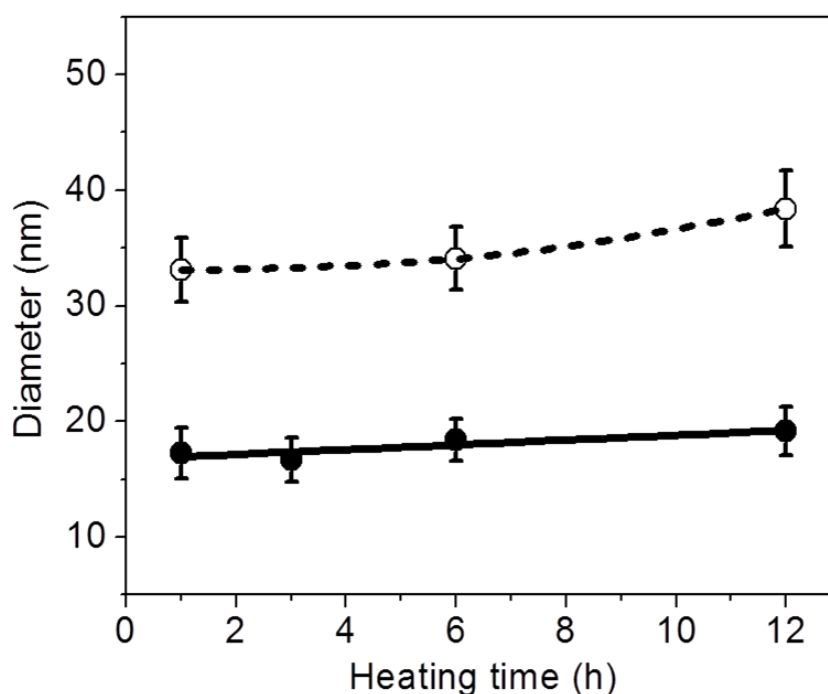


Figure 2.9 Time dependent growth of iron oxide nanocrystals.

Nanocrystals were grown in 10 g of ODE (dot line) and 60 g of ODE (bold line) at 320 °C from 1 to 12 h. The ratio between FeOOH and oleic acid is 50:200 mmol. Reaction time has a minimum effect on the growth of nanocrystals.

2.3.2. Diameter control of ferrite nanocrystals

Ferrite nanocrystal has the structure replacing some Fe (II) or Fe (III) ions with other di- or tri-valent transition metal ions, such as Co, Mn, Fe, Mg, Zn, Ni, Cr and Al, in the octahedral or tetrahedral sites of the spinel lattice of magnetite ($\text{Fe}^{\text{II}}\text{Fe}_2^{\text{III}}\text{O}_4$).^{20,77} The replacement of iron ions in iron oxide nanocrystals with other transition metal ions results in the formation of binary, ternary, and quaternary metal oxide nanocrystals. Two, three, or four different metal oleates were decomposed at high temperature (at 320 °C) at the same time and formed binary, ternary, or quaternary

mixed metal oxide structures. For example, aluminum iron oxide (aluminum ferrite) nanocrystals were obtained using the mixture of iron and aluminum oleate precursors and manganese zinc iron oxide (Manganese zinc ferrite) nanocrystals were prepared by the mixture of iron, manganese, and zinc oleate (Figure 2.10).

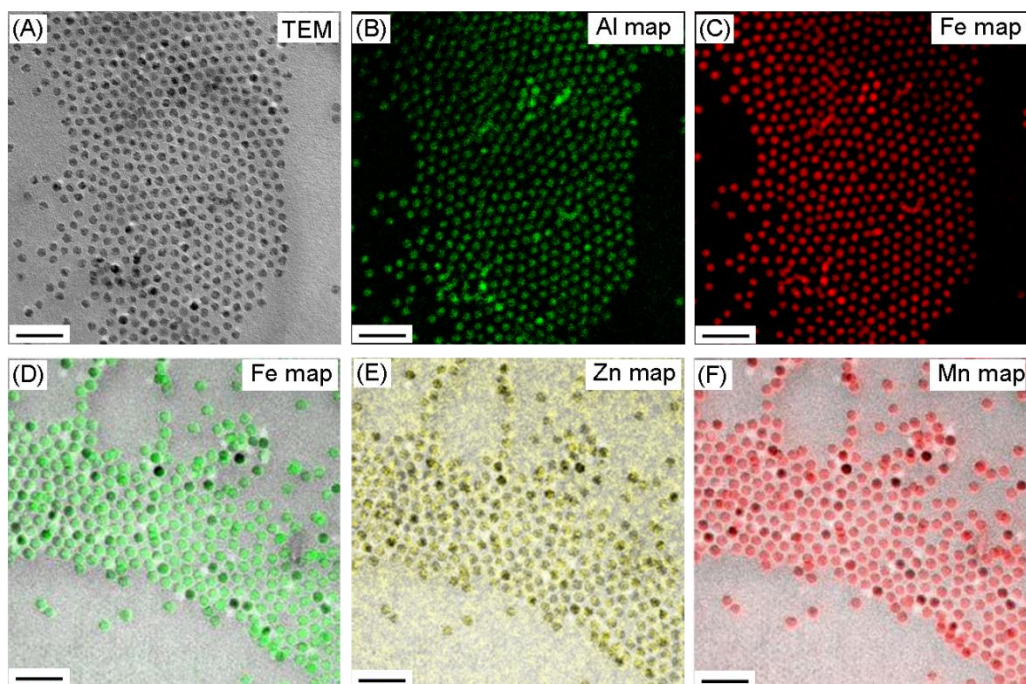


Figure 2.10 TEM and GIF images of aluminum ferrite (from A to C) and manganese zinc ferrite nanocrystals (from D to F). All scale bars are 50 nm.

This method enabled us to have the libraries of various ferrite nanocrystals including manganese ferrites, nickel aluminum ferrites, manganese aluminum ferrite, manganese zinc ferrites, and manganese zinc aluminum ferrite nanocrystals (Figure 2.10, and Figure 2.11). In addition, elemental mapping in GIF analysis (Figure 2.10) proves that the resulting spherical nanocrystals are alloy structure containing two or three transition metal cations.

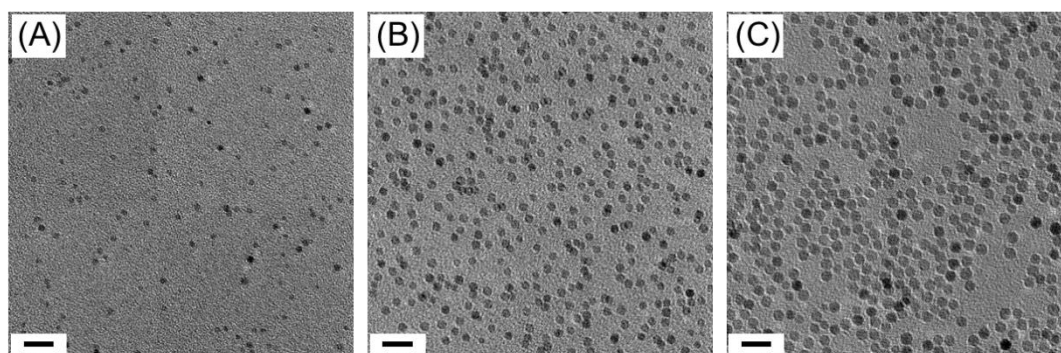


Figure 2.11 TEM images of NiAlFeO, MnAlFeO, and $\text{Mn}_{0.5}\text{Zn}_{0.5}\text{AlFeO}_4$ nanocrystals. The average diameter of the nanocrystals are 3.5 ± 0.4 , 5.5 ± 0.5 , 7.2 ± 0.7 nm, respectively.

Controlling metal oleate precursors concentrations changes the composition ratio of metals in ferrite nanocrystals. Figure 2.12 shows that the composition of manganese and iron in manganese ferrite nanocrystals is varied by changing the molar ratio of starting precursors, manganese and iron oleate precursors. The higher content of manganese in the manganese ferrite nanocrystal sample was found from the higher ratio of manganese oleate to iron oleate. Using different concentration ratio of three different metal precursors also changes the composition of ternary metal oxide nanocrystals. For example, various molar ratio of manganese, zinc and iron oleates led to different content of each element in $\text{Mn}_x\text{Zn}_{x-1}\text{Fe}_2\text{O}_4$ ($0 < x < 1$) (Figure 2.13).

Although varied ratios of metal oleates changes the diameter of ferrite nanocrystals, more complete control over the diameter of monodisperse ferrite nanocrystals is necessary with various elemental and structural analysis. The diameter control of mixed metal oxides (ferrites) may be affected by reaction times, surfactant ratios, and cosurfactant as we have seen from numerous results of iron oxide nanocrystal synthesis. This will be the subject of future work.

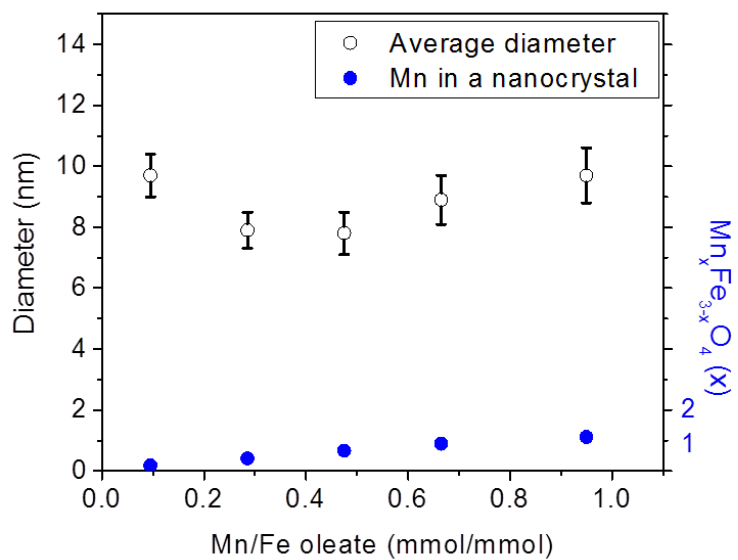


Figure 2.12 Control over the diameter and composition of $Mn_xFe_{3-x}O_4$ nanocrystals.

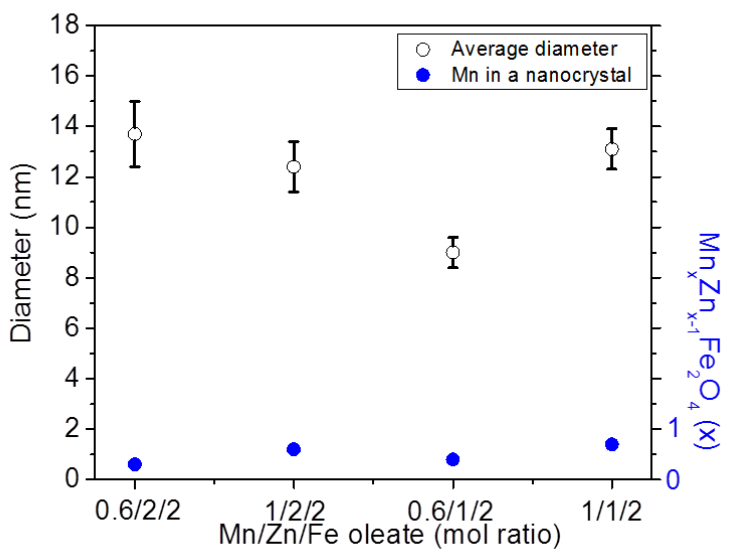


Figure 2.13 Diameter and composition control of $Mn_xZn_{x-1}Fe_2O_4$ nanocrystals.

2.4. Conclusion

I demonstrate monodisperse iron oxide nanocrystal synthesis under high temperature decomposition of iron oleate precursor method. The diameter of iron oxide nanocrystals ranged from 3 to 40 nm by controlling the ratios of iron precursor to surfactant, iron monomer concentration, and cosurfactant. Mixed metal oxide nanocrystals were also prepared by the mixture of various metal oleate precursors. The composition of binary, ternary, quaternary metal oxide nanocrystals were highly related to the ratio of the starting precursor materials. This will have the potential to be used for the magnetic property measurement study depending on the diameter and composition of monodisperse magnetic nanocrystals.

Chapter 3

Synthesis of monodisperse aluminum ferrite nanocrystals

3.1. Introduction

Ferrite is a cubic spinel structured material consisting of face closed packed oxygen with transition metal ions (Mn, Fe, Co, Ni, and Zn) having oxidation states of +2 and +3 in either tetrahedral or octahedral site in a crystal. Various ferrite nanocrystals are promising materials in the field of biomedical sensing, imaging, and data storage.^{70, 78} Most of ferrite forms $M^{2+}Fe_2^{3+}O_4^{2-}$ composition by the replacement of Fe^{2+} with M^{2+} (M = Mn, Co, Ni and Zn) in iron oxide nanocrystal. This type of ferrite nanocrystals were widely prepared using ionic metal precursors such as, metal chloride or nitrate hydrated via reverse micelles, hydrothermal, and coprecipitation methods because of their simplicity and cost efficiency.^{77d, 79} Recently, high temperature metal-organic precursor decomposition method improved the uniformity

of manganese, cobalt or nickel ferrite with wide range of diameter nanocrystal.^{20, 77g, 77i, 80} Compared to divalent ferrite, trivalent ferrite, such as aluminum substituted iron oxide (aluminum ferrite), is not much explored with its magnetic measurement study.

Aluminum ferrite is an iron oxide containing certain amount of Al^{3+} by the substitution of Fe^{3+} in either tetrahedral or octahedral sites in iron oxide crystal structure.⁸¹ Potential applications of aluminum ferrite are diverse; Namai *et al* showed possible use of this type of material for an electromagnetic wave absorber in wireless electronic devices, and recently this group utilized AlFe_2O_4 nanocrystals as precursor catalysts to synthesize various carbon structures such as, single walled carbon nanotubes and graphene nanoribbons.^{39, 81a, 82} Aluminum ferrite was also synthesized by various aqueous routes and controlled the diameter of nanocrystals or the amount of aluminum contents in a nanocrystal.^{80c, 81a, b, 83} However, monodisperse wider range of diameter aluminum ferrite has never been synthesized by high temperature metal precursor decomposition method. In addition, controllable aluminum doping in an iron oxide nanocrystal will suggest better understanding of crystal structure of aluminum ferrite.

In this research, for the first time, uniform nanocrystalline aluminum ferrite was synthesized by decomposition of aluminum and iron precursors at high temperature in the presence of oleic acid. This type of ferrite material grew the diameter by changing nanocrystal growth time and the mol ratio of metal precursor to oleic acid. Aluminum ferrite had a varied composition; the concentration ratio of aluminum to iron in a nanocrystal was greater as the amount of the applied aluminum precursor increased. The addition of various phase transfer agents such as, polymaleic

anhydride-alt-1-octadecene (PMAO), polyacrylic acid-octylamine (PAA-OA), and oleic acid formed the bilayer structure on the surface of ferrite nanocrystals resulting in water soluble materials without losing homogeneity.

3.2. Experimental Methods

3.2.1. Chemicals

Iron oxide, hydrated (Goethite, $\text{FeO}(\text{OH})$, catalyst grade, 30-50 mesh), aluminum hydroxide ($\text{Al}(\text{OH})_3$, reagent grade), oleic acid (OA, technical grade, 90%), 1-octadecene (ODE, technical grade, 90%), poly (maleic anhydride-alt-1-octadecene) (PMAO, $M_n = 30000 - 50000$), poly (acrylic acid) (PAA, $MW = 1800$), polyethyleneimine (PEI, $M_w = 25,000$), and octylamine (99%) were purchased from Sigma-Aldrich; dimethylformamide (DMF, 99.9 %) were purchased from Fisher scientific; aluminum oleate was purchased by Fisher Scientific; 1-ethyl-3-[3-dimethylaminopropyl]carbodiimide hydrochloride (EDC) was purchased from Thermo Scientific. All nanoparticles were synthesized under nitrogen (N_2 , 99.999%).

3.2.2. Instrumentation

3.2.2.1. Transmission electron microscope (TEM)

The particle sizes were measured through transmission electron microscope (TEM) TEM specimens were prepared using ultra thin carbon type-A 400 mesh copper grids (Ted Pella Inc.). The TEM micrographs were taken by a JEOL 2100 field emission

gun TEM operating at 200 kV with a single tilt holder. The size and size distribution data were obtained by counting >1000 nanocrystalline particles using Image-Pro Plus 5.0.⁸⁴

3.2.2.2. X-ray diffraction (XRD), and X-ray photoelectron spectroscopy (XPS)

X-ray powder diffraction (XRD) patterns were obtained using a Rigaku D/Max Ultima II. 2θ range was from 10 to 80 degree with a Cu $K\alpha$ radiation (1.54 Å) and the X-ray was generated at 40 kV and 40 mA. XPS data were collected using a PHI Quantera XPS and X-ray spot size was 200.0 μm with pass energy of 26.00 eV at 45.0°.

3.2.2.3. Inductively coupled plasma atomic emission spectroscopy (ICP-AES)

The particle concentrations were measured by a Perkin Elmer inductively coupled plasma atomic emission spectroscopy (ICP-AES) instrument equipped with autosampler.

3.2.3. Synthesis of nanocrystalline iron oxide (magnetite)

3.2.3.1. Iron oxide nanocrystals prepared by Goethite (FeOOH)

FeOOH was utilized as an iron precursor in the presence of oleic acid (OA). FeOOH was not soluble in the presence of OA in ODE at room temperature but dissolved at 240 °C where iron carboxylate precursor prepared. The nucleation started after 280 °C and nanocrystal was grown at 320 °C for desire reaction times (from 1 to 12 hrs). Diameter of nanocrystal was controlled by different molar ratio between FeOOH and OA. For details, the ratio between FeOOH and OA was fixed to 1/4. The high molar concentration of

FeOOH (from 1 to 50 mmol) and OA (from 4 to 200 mmol) was mixed in 40 mmol (~10 g) of ODE at room temperature. Iron oxide nanoparticles grew at 320 °C for desired time.

3.2.3.2. Iron oxide nanocrystals prepared by iron oleate

Iron oxide nanocrystals below 10 nm were achieved by using iron carboxylate (iron oleate) as an iron precursor. Iron carboxylate precursor was prepared by iron oxide, hydrate (FeOOH, 1 mmol, 0.09 g), oleic acid (OA, 4 mmol, 1.12 g) and 1-octadecene (ODE, 15mmol, ~4g) at 240 °C for 1h. The resulting black precipitate was purified using acetone, methanol, and hexane. For the details, 5ml of the resulting precipitate was washed using 25ml of acetone and 25 ml of methanol. The purification was treated at least 3 times. The well cleaned precipitate was dissolved in 15 ml of hexane. The purified precursor was separated from un-reacted salts and other impurities by centrifugation at 4500 rpm for 30 min. This process is available for the large scale preparation. The resulting iron carboxylate was soluble in other non-polar solvents, hexane, chloroform, and toluene. The concentration of iron carboxylate precursor was measured by ICP and the resulting [Fe] was 3mg/mL. Iron oxide nanoparticles were prepared by using various amount of iron carboxylate (from 0.015 to 0.15 mmol), oleic acid (from 0.3 to 5 mmol), and reaction time (from 1 to 3 hrs.) under ultra pure N₂ condition.

3.2.4. Synthesis of nanocrystalline aluminum ferrite

The method for aluminum ferrite nanocrystals were modified the conventional wet chemical method by decomposition of metal precursor in the presence of a surfactant at high temperature this group reported previously.^{3j, 63b} For details, 4.0 nm aluminum

ferrite was prepared using the mixture of 0.045 mmol iron oleate, 0.019 mmol aluminum oleate, and 2 mmol OA in 5 g ODE at 320 °C for 2 h. 11.2 nm aluminum ferrite was synthesized by 0.7 mmol FeO(OH), 0.3 mmol Al(OH)₃ with 3 mmol OA in 5 g ODE at 320 °C for 1 h. For 16.7 nm aluminum ferrite, 0.7 mmol FeO(OH), 0.3 mmol Al(OH)₃ with 4 mmol OA in 5 g ODE at 320 °C for 1 h.

The resulting ferrite nanocrystals were purified using methanol, acetone, and hexane. More specifically, 1g of the resulting colloidal nanocrystals was mixed with 10 ml of hexane, 20 ml of methanol, and 20 ml of acetone and centrifuged at 4500 rpm for 30 min. This process was repeated three times. The cleaned colloidal nanocrystals were redispersed in hexane.

3.2.5. Phase transfer of iron oxide and aluminum ferrite nanocrystals

The as-synthesized nanocrystal was transferred to aqueous solution by encapsulation methods using probe sonication.^{3a, 63b, 85}

3.2.5.1. Oleic acid coated iron oxide

The procedure for the preparation of oleic acid bilayer iron oxide nano crystals are followed by the method mentioned by Prakash et al.^{3a}

3.2.5.2. PAAOA coated iron oxide

The synthesis of PAA-OA amphiphilic polymer was adapted from previous reports.⁸⁶ 18 mmol of PAA-OA were added to 0.5 ml of iron oxide in ethyl ether solution ([Fe] = 1.0 mg/ml) with 10 ml of ultra pure water. Aqueous and organic phases were mixed by

application of a probe-sonicator (UP 50H, DR.HIELSCHER) for 5 min at 60 % amplitude and full cycle. The resulting solution was further stirred for 1 day to evaporate the ether and to obtain a clear yellow brown solution. The transfer yield of the final solution was 54.0 %.

3.2.5.3. PMAO coated iron oxide

2.0 μmol PMAO was added to 1ml of nanocrystal in chloroform solution ($[\text{Fe}] = 2.0 \text{ mg/ml}$) with 10 ml of ultra pure water. The solution was probe-sonicated in the same condition, mentioned above. The transfer efficiency was 90.7 %.

3.2.5.4. PEI coated iron oxide

0.2 μmol PEI was added to 0.5 ml of nanocrystal in chloroform solution ($[\text{Fe}] = 2.0 \text{ mg/ml}$) with 10 ml of ultra-pure water. The solution was probe-sonicated in the same condition, mentioned above. The transfer efficiency was 70.5 %.

3.2.5.5. Oleic acid coated aluminum ferrite

3.2 μmol of oleic acid was stirred with 0.5 ml of nanocrystal in ethyl ether solution ($[\text{Fe}] = 1.6 \text{ mg/ml}$) and 10 ml of ultra-pure water. The solution was probe-sonicated in the same condition, mentioned above. The transfer yield of the final solution was 62.3 %.

3.2.5.6. Polyacrylic acid octylamine (PAA-OA) coated aluminum ferrite

The synthesis of PAA-OA amphiphilic polymer was adapted from previous reports.⁸⁶ 2.7 μmol of PAA-OA were added to 0.5 ml of aluminum ferrite in ethyl ether solution

([Fe] = 1.6 mg/ml) with 10 ml of ultra-pure water. The mixed solution was sonicated using the probe sonicator at the same experimental set up, mentioned above. The transfer efficiency was 73.5 %.

3.2.5.7. PMAO coated aluminum ferrite

13.6 μmol PMAO was added to 1ml of nanocrystal in chloroform solution ([Fe] = 0.3 mg/ml) with 10 ml of ultrapure water. The solution was probe-sonicated in the same condition, mentioned above. The transfer efficiency was 90.1 %.

Purification of as-prepared water-soluble nanoceria was carried out using ultracentrifugation (Sorvall Discovery 100 SE Ultracentrifuge) at 41000 rpm for 4 hrs, followed by syringe filtration (pore size of 0.45 μm , WHATMAN-NYL). All the resulting phase transfer nanoceria pellets were re-dispersed and stable in Mili-Q water.

3.3. Results and Discussion

Aluminum ferrite was synthesized by incorporation of Al^{3+} into the spinel lattice structure of iron oxide under high temperature decomposition of aluminum and iron precursors. This procedure is similar to the synthetic method of various divalent ions, such as, Mg, Cr, Mn, Fe, Co, Ni, and Zn ferrite nanoparticles by non-aqueous high temperature process.^{20, 77a-i} In the synthetic process for aluminum ferrite, we used the mixed metal precursors of iron/aluminum oleate or $\text{FeOOH}/\text{Al}(\text{OH})_3$ in the presence of oleic acid. The starting chemicals, FeOOH and $\text{Al}(\text{OH})_3$, could prepare iron and aluminum oleate by the assistance of oleic acid at elevating temperature (240~260 $^\circ\text{C}$) and decompose at 320 $^\circ\text{C}$ resulting in aluminum ferrite nanocrystals with controllable

molar ratio between Fe and Al.^{3j, 63b, 75, 87}

3.3.1. Aluminum ferrite nanocrystal

Specific experimental conditions (ex, different metal precursors, reaction times, varied molar ratio between metal precursors and a surfactant) enabled to prepare various diameter monodisperse nanocrystalline aluminum ferrites as shown in Figure 3.1 and Figure 3.2.^{3j} Specifically, extremely small amount of metal precursors (iron oleate, 0.045 mmol; aluminum oleate, 0.019 mmol) in the presence of a little oleic acid (2 mmol) led to the smallest ferrite nanocrystals with 4.0 nm diameters. Whereas, higher molar metal precursors (FeOOH, 0.7 mmol; Al(OH)₃, 0.3 mmol) with 3 mmol of oleic acid increased the diameter to 11.2 nm and higher molar oleic acid (4 mmol) grew larger diameter to 16.7 nm aluminum ferrite. Longer reaction time with higher molar oleic acid led to larger diameter aluminum ferrite (22.2 nm ± 2.1 nm from 5 mmol oleic acid injection and 2h reaction time) but the size broadness (20.5 ± 3.0 nm) occurred after 3 h heating of nanocrystal growth because of Ostwald ripening.

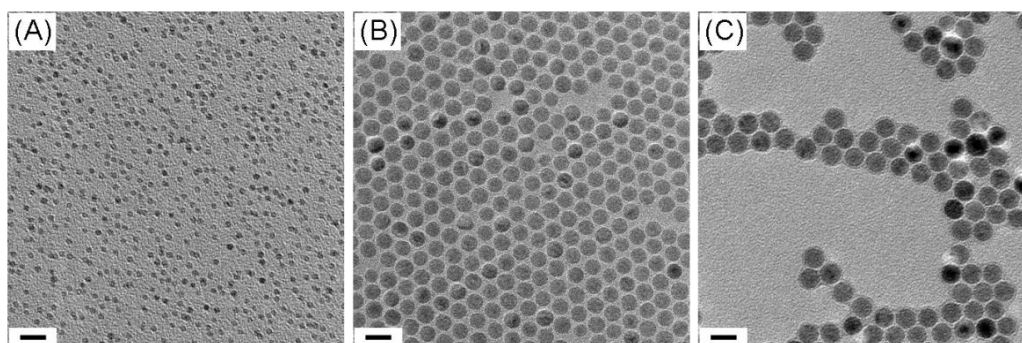


Figure 3.1 Three different diameters of aluminum ferrite nanocrystals.

(A) 4.0 ± 0.4 , (B) 11.2 ± 0.7 , and (C) 16.7 ± 1.4 nm. The histograms from A to C were shown in supplemental figure 1. The stoichiometric ratio of Al, Fe and O in 4.0, 11.2, and 16.7 nm nanocrystals were AlFe₂O₄ based on the ICP results; ICP data showed the ratio of [Al] to [Fe] was 0.26 / 0.73, 0.33

/ 0.66, and 0.36 / 0.63 from (A) to (C), respectively. In addition, EDS analysis of the smallest nanocrystal (4.0 nm) verified the molar ratio of Al to Fe in a nanocrystal was AlFe_2O_4 (weight percent of Al and Fe in EDS analysis was 20.1 and 79.9 %). All scale bars are 20 nm. For the statistics of average particle diameters, over 1000 particles were counted from multiple images using Image-Pro Plus 5.0.⁸⁴

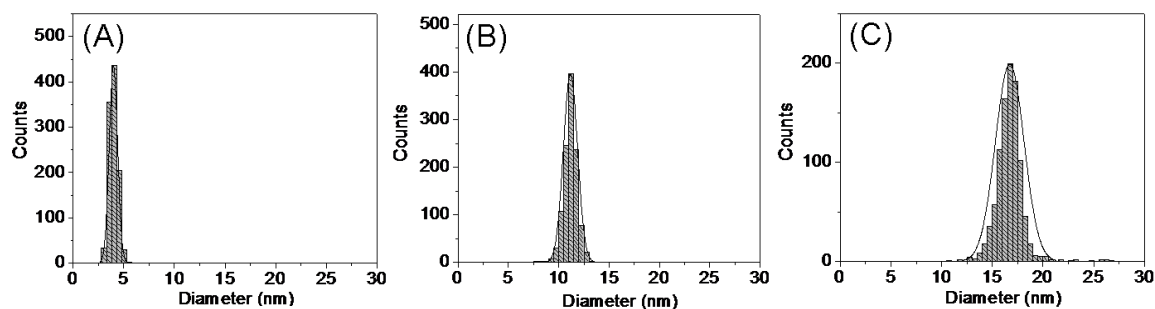


Figure 3.2 The diameter histograms of aluminum ferrite nanocrystals. The histograms from A to C were from TEM images in Figure 3.1.

The mixed metal precursor injection (iron and aluminum precursors) synthesized the alloyed aluminum ferrite structure and the replacement of iron with aluminum did not transform the crystal structure of iron oxide. GIF analysis clearly gave the evidence that the synthesized particle contained both aluminum and iron in every single sphere as shown in Figure 3.3; The mapping position of two different metals, aluminum and iron, is identical in the same spherical nanocrystal. X-ray photoelectron spectroscopy (XPS) data in Figure 3.4 also verified the existence of Fe, Al in the nanocrystals. In the crystal aluminum ferrite, aluminum may be incorporated in octahedral sites in Fe_3O_4 crystalline because Al^{3+} has strong preference for the octahedral sites.^{81c, 83a, 88} XRD data in Figure 3.5 showed that the synthesized nanocrystal had very similar diffraction patterns as Fe_3O_4 and Al_2FeO_4 with slightly

shifted diffraction angles. This shift depending on the increasing contents of Al in magnetite nanocrystal was explained by Wolska et al.^{81b, 83b} The possible individual peaks of various phased aluminum, alumina, aluminum hydroxide, or amorphous aluminum oxide were not found in the XRD analysis. High resolution-transmission electron microscopy (HR-TEM) image of aluminum ferrite also showed that aluminum ions successfully replaced iron ions in iron oxide nanocrystal structures preserving lattice distance of (110) and (311) plane of 0.204 and 0.249 nm which are close to 0.203 and 0.252 nm of spacing between the lattice fringes of iron oxide (Figure 3.6).

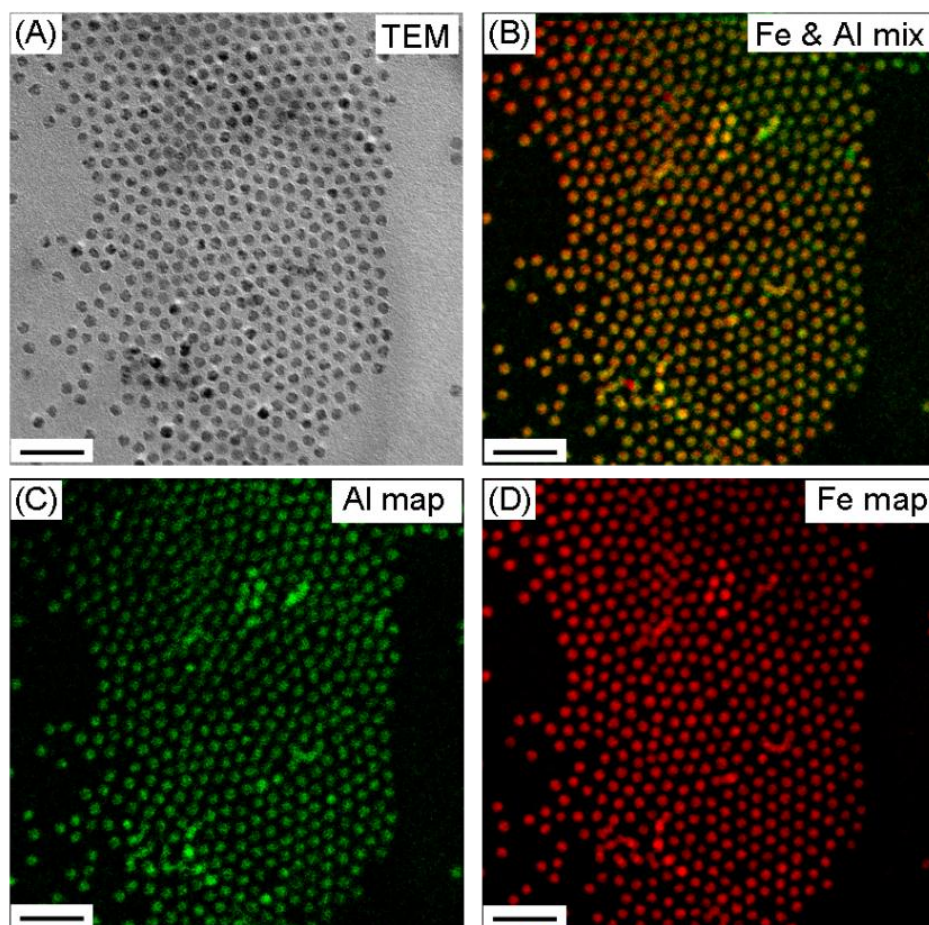


Figure 3.3 GIF analysis of 11.2 nm aluminum ferrite nanocrystals.

(A) TEM image of aluminum ferrite nanocrystals. (B) GIF mapping of iron and aluminum. (C) GIF mapping of aluminum (green) (D) GIF mapping of Fe (red). All scale bars are 50 nm.

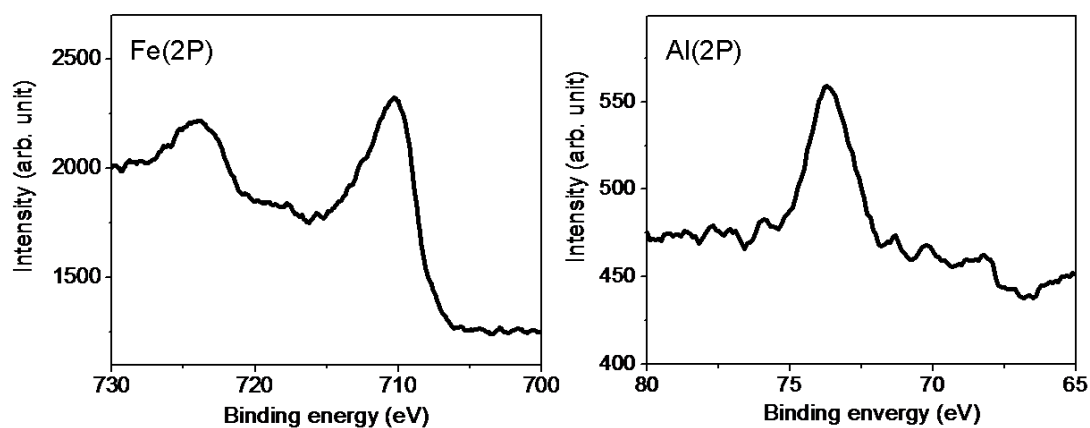


Figure 3.4 XPS data of aluminum iron oxide nanocrystal. The Fe2P and Al2P regions were analyzed to determine the existence of Fe and Al.

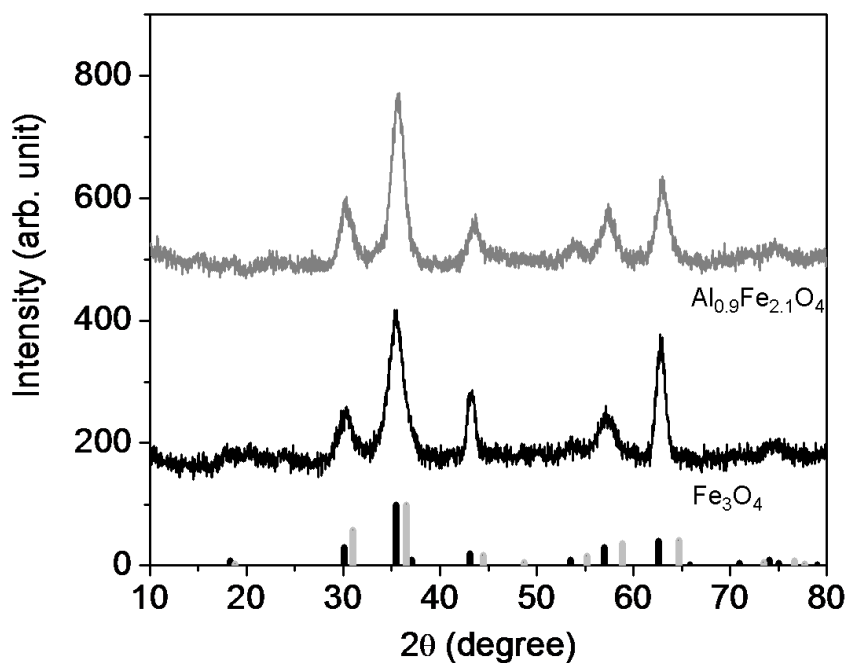


Figure 3.5 XRD data of aluminum iron oxide nanocrystals. Nanocrystalline magnetite and aluminum ferrite are compared. The reference vertical lines at the bottom chart represent Fe_3O_4 (JCPDS Card # 19-0629 (black)) and AlFe_2O_4 (JCPDS Card # 34-0192 (light gray)).

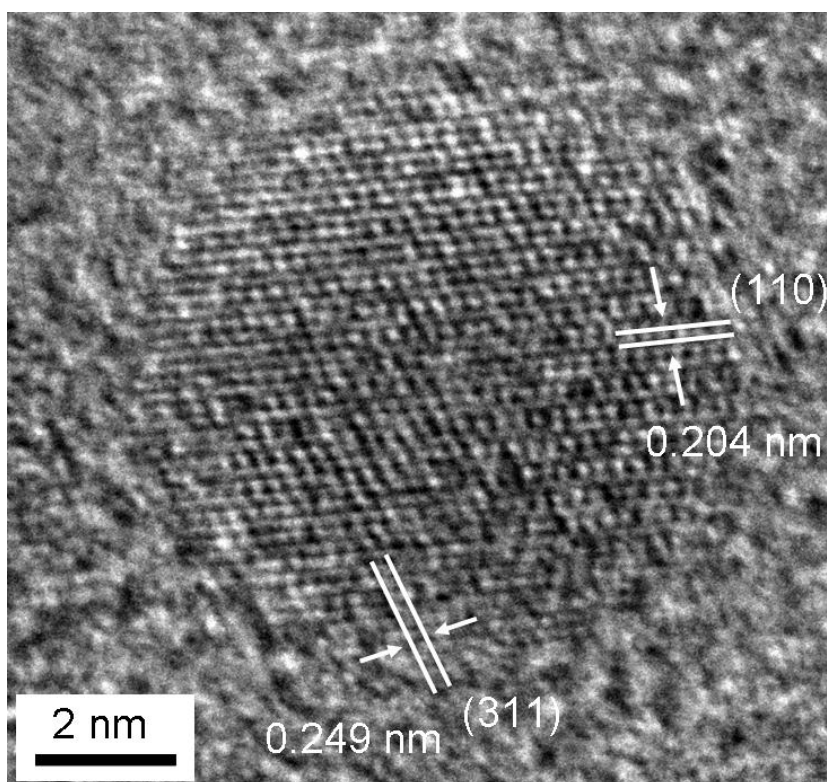


Figure 3.6 High resolution TEM image of aluminum iron oxide nanocrystal. The crystal fringe distances of 0.204 and 0.249 nm indicate (110) and (311) planes, respectively.

The use of the increasing molar aluminum precursor compared to iron precursor rendered the high contents of aluminum in a nanocrystal; aluminum content was from 18 to 50 % as Al/Fe precursor increased from 0.15 to 1.0, respectively. Trivalent ions, such as Al^{3+} , can replace at most 66 % of iron ions in magnetite crystal structure since there are 33 % of Fe^{2+} in octahedral site and 66 % of Fe^{3+} in octahedral and tetrahedral sites. We expect that Al^{3+} may not only replace Fe^{3+} in octahedral site but also substitute Fe^{3+} in tetrahedral site based on the composition result of $\text{Al}_{1.5}\text{Fe}_{1.5}\text{O}_4$ by 50 % replacement of iron with aluminum as shown in Figure 3.7.^{81a, b} However, too much injection of aluminum precursor ruined monodispersity of nanocrystal;

when the ratio of aluminum to iron oleate was over 1.0, the diameter distribution was wider over $\sigma > 20\%$. The different mol ratio between two different metal precursors, scarcity of oleic acid, and separated nucleation might result in broad nanocrystal distribution.

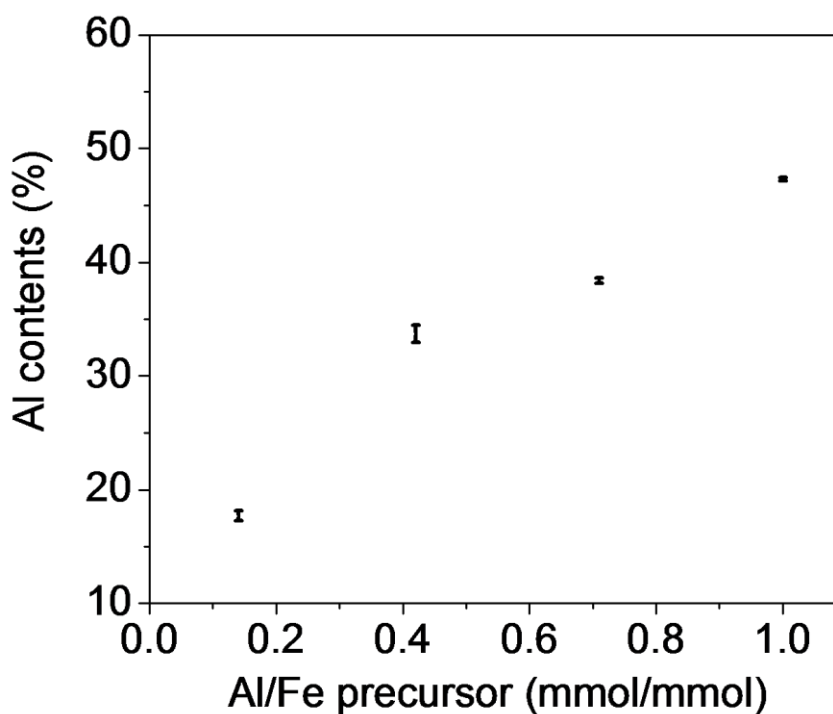


Figure 3.7 A variation of aluminum content in a nanocrystal. The higher mol ratio of aluminum oleate to iron oleate rendered the increasing aluminum content in an aluminum ferrite particle.

3.3.2. Nickel ferrite and nickel aluminum iron oxide nanocrystals

This type of nanoparticle synthetic process using metal oleate precursor is also applicable to synthesize wide range of diameter divalent ferrite nanocrystal with controllable composition. For example, nickel ferrite synthesis was demonstrated using the mixture of nickel and iron oleate under the same experimental condition

used for aluminum ferrite synthesis. The mol ratio of nickel to iron oleate under 0.4 produced nickel ferrite but the higher molar ratio of those two precursors led to nickel oxide and nickel ferrite mixture as shown in Figure 3.8, Figure 3.9, and Figure 3.10. In addition, the starting materials' ratio obviously controlled the composition; molar ratio between nickel and iron oleate of 0.4 synthesized monodisperse 6 nm NiFe_2O_4 . Since the highest content of nickel in nickel ferrite is 33 %, the excess of nickel precursor injection formed by-product such as nickel oxide as verified from XRD (Figure 3.8). This caused the average size broadness (Figure 3.10). The increasing amount of surfactant, longer reaction time, and the use of the other type of metal precursor mixture, FeOOH with NiOH , had an effect on the preparation of larger diameter particles (9.0 ± 0.7 nm). Furthermore, three different metal precursor mixture (aluminum, nickel, and iron oleates) with the 1:1:1 molar ratio prepared 4 nm NiAlFeO_4 nanocrystals ($D = 3.8 \pm 0.4$ nm) in the presence of 2 mmol oleic acid. (Figure 3.11). More complete study about divalent ferrite and ternary ferrite nanocrystals will be the future subject.

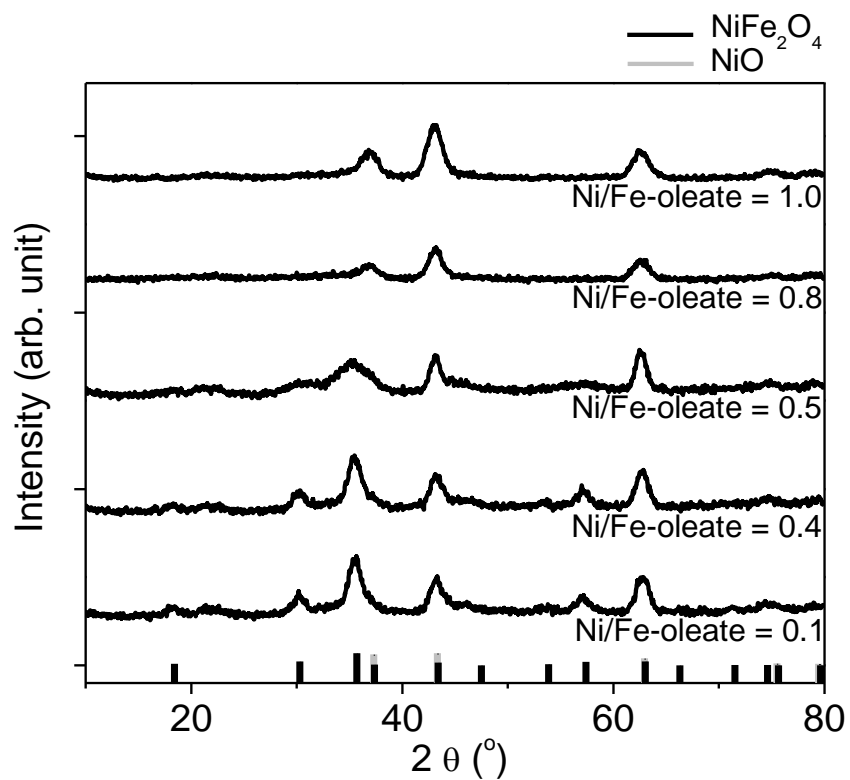


Figure 3.8 XRD of nickel ferrite nanocrystals.

The lower mol ratio of nickel oleate to iron oleate led more closely to the formation of NiFe₂O₄. In contrast, the higher ratio of nickel oleate compared to iron oleate (over 0.5) prepared NiO rich species. The reference vertical lines at the bottom of the chart were NiFe₂O₄ (JCPDS Card # 44-1485 (black)), and NiO (JCPDS Card # 04-0835 (light gray)).

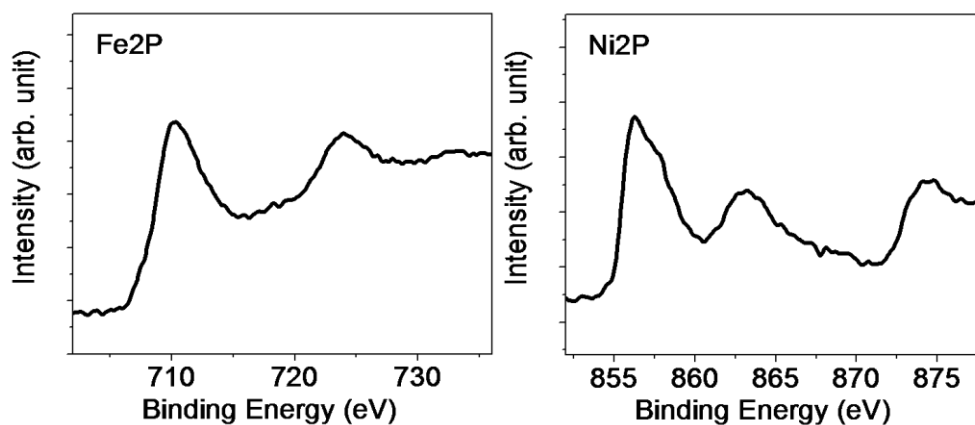


Figure 3.9 XPS analysis of nickel ferrite nanocrystal. The Fe2P and Ni2P regions were analyzed to determine the existence of Fe and Al.

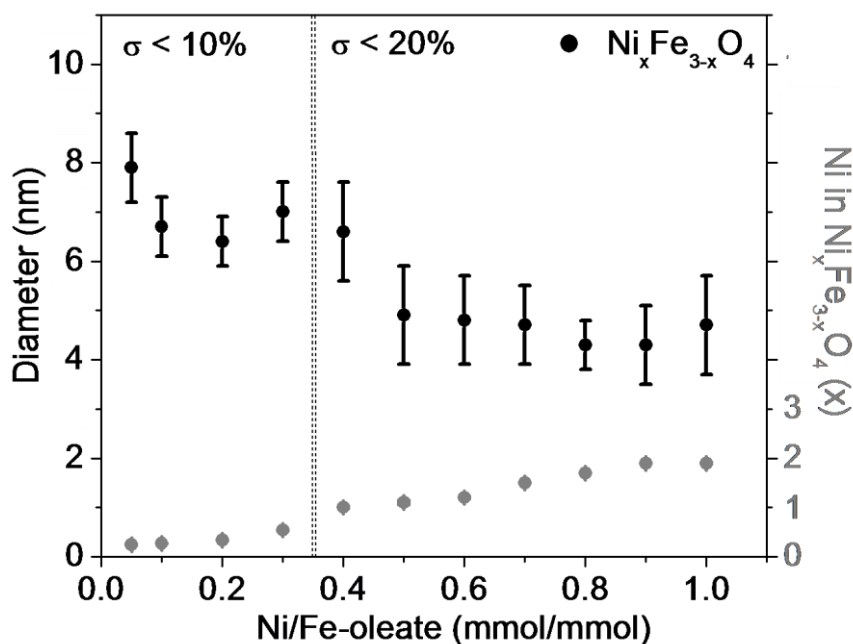


Figure 3.10 The effect of the ratio of nickel and iron precursors on the particle diameter, morphology and the composition.

The lower mol ratio between nickel and iron oleate from 0.05 to 0.3 synthesized highly monodisperse nickel ferrite ($\sigma < 10\%$). The nickel content increased gradually as the applied nickel precursor increased. However, obviously polydisperse nickel ferrite was formed after the ratio of Ni/Fe-oleate was over 0.4. NiFe₂O₄ was formed from 0.3 mol ration of Ni/Fe-oleate with 2 mmol of oleic acid at 320 °C for 2 h.

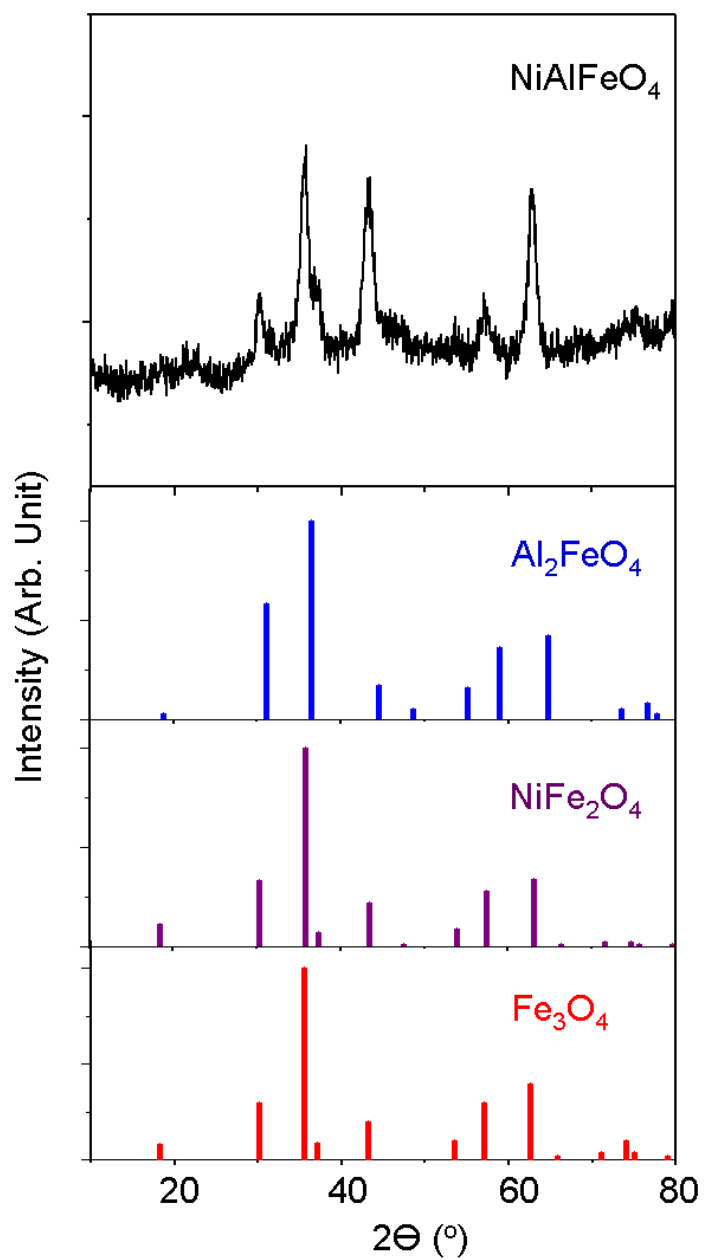


Figure 3.11 XRD of NiAlFeO₄ nanocrystal (black).

The reference vertical lines represent Fe₃O₄, (JCPDS Card # 19-0629), NiFe₂O₄ (JCPDS Card # 44-1485), and AlFe₂O₄ (JCPDS Card # 34-0192). This diffraction pattern is also well matching to the reported data by Mozaffari and Raghavender *et al.*^{88a, 89}

3.3.3. Phase transfer of aluminum ferrite nanocrystals

For the further biological application, the engineered nanocrystals need to be soluble in water. Toward this end, the simple injection of various amphiphilic polymers (ex, Polymaleic anhydride-alt-1-octadecene (PMAO), $M_n = 50000$; Polyacrylic acid-octylamine (PAA-OA) $M_n = 2783$; and oleic acid) transferred the phase of colloidal nanocrystal from non-aqueous to aqueous.^{63b,85-86, 90,3a} Both high and small molecular weight polymer successfully led to phase-transfer and did not affected on the nanocrystal morphology and diameters without forming nanoparticle aggregates as shown in Figure 3.12. In addition, particular amount of polymer injection made water-soluble aluminum ferrite nanocrystal solution with high transfer yield up to 90 % by the assistance of probe sonication (see supplemental discussion). However, too much amount of polymer injection resulted in lower efficiency of transfer yield with cloudy solution. This could be due to the formation of micelles by excess polymer after critical micelle concentration level (CMC).⁹¹

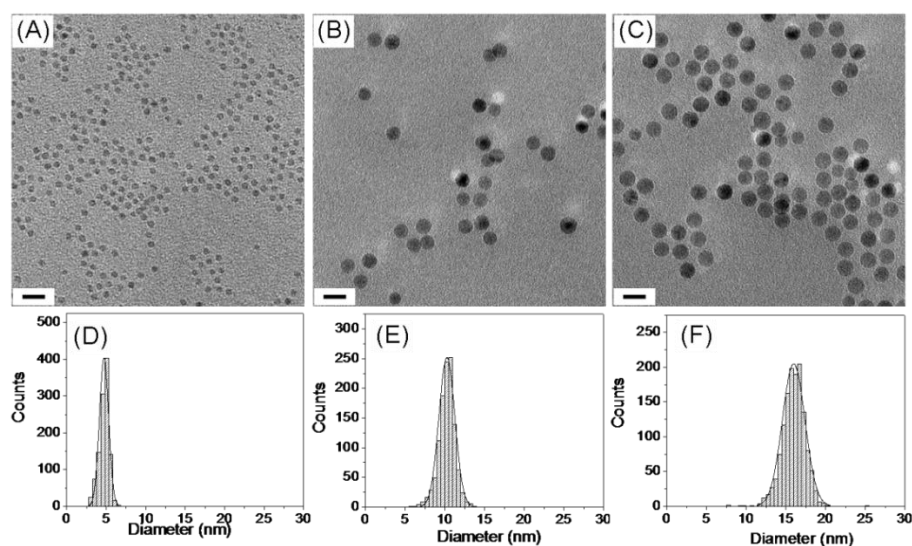


Figure 3.12 Water soluble aluminum ferrite nanocrystals.

TEM images (from a to c) and diameter histograms (from d to f) of PAA-OA coated aluminum ferrite nanocrystals. All water soluble nanocrystals were from three samples shown in Figure 1. Average diameter of nanocrystals from (a) to (c) was 4.7 ± 0.5 , 10.3 ± 1.0 , and 15.4 ± 1.4 nm, respectively. Phase transferred nanocrystals did not lose the morphology and diameter distribution. All scale bars are 20 nm.

3.4. Conclusion

In summary, high crystalline aluminum ferrite nanocrystals were formed by conventional wet chemical method by decomposition of iron and aluminum precursors in the presence of oleic acid at high temperature ($320\text{ }^{\circ}\text{C}$). The higher mol ratio of oleic acid to metal precursors and longer reaction time obviously increased the diameter of nanoparticles. Aluminum content in a ferrite nanocrystal was greater as the applied amount of aluminum precursor increased. The addition of various phase transfer agents such as, PMAO, PAA-OA, and oleic acid formed the bilayer structure on the surface of ferrite nanocrystals resulting in water soluble materials without losing homogeneity.

Chapter 4

Control over the diameter, length, and structure of carbon nanotube carpets using iron oxide and aluminum ferrite nanocrystals

4.1. Introduction

Carbon nanotubes can be applied in diverse technologies, ranging from medical imaging to transparent and conductive coatings; in nearly every instance, the material performance depends on the uniformity and tunability of nanotube diameter as well as wall number (e.g. single-walled versus multi-walled).^{36, 92} One strategy for controlling these essential material features is to manipulate the metal catalysts used in carbon

nanotube production. In the first examples, these catalysts were aerosols of reactive iron particles; a carbon feedstock such as ethylene when exposed to these metals decomposed above 800 °C yielding carbon that solubilized in the metals. Carbon nanotube growth, it was believed, initiated when carbon concentrations became high enough to start the formation of graphitic shells at the metal particle surface.⁹³ Kukovitsky *et al* showed that reduction in the size of the metal catalysts led to smaller diameter carbon nanotubes, and the findings suggested that the breadth of the particle dictated the tube diameter; later work illustrated how the composition of the catalyst, particularly with the introduction of molybdenum, could change the helicity and number of tube walls.⁹⁴

More recently iron catalysts formed in the gas phase have been supported on substrates such as alumina, and carbon nanotube growth occurs from the surface forming thick and dense films.^{95,96} These vertically aligned carbon nanotube carpets (VA-CNT) are particularly ideal for applications including separation membranes, super-capacitors, and field-emitters.⁴⁴ Yamada *et al* demonstrated that when catalysts deposited through gas phase processes were smaller, it was possible to make very small diameter (e.g. 2 nm) carbon nanotubes.^{38a} Whether the diameter of the catalyst defined tube diameter over all catalyst sizes remains an open question for catalysts deposited via the gas phase. While this process yields catalysts with diameters well under 3 nm, the materials can ripen on the surface at high metal coverages. This increases the catalyst size distributions and precludes the formation of catalysts larger than 3 nm. More systematic studies that examine fully how catalyst structure can dictate carbon nanotube structure require alternate approaches to catalyst formation.^{37b, 38b}

One strategy is to form iron oxide nanoparticles as catalyst precursors through chemical means, evaporate them onto substrates, and then reduce them to metals in the growth chambers prior to carbon nanotube growth.^{49, 42, 65e} During the last process, the organic coatings present on the particles are volatilized and the catalyst shrinks in size and converts to zero-valent iron particles.^{46d, 49} Hafner *et al* was the first to demonstrate the feasibility of this approach by applying broadly distributed Fe-Mo nanoparticles to the growth of double-walled carbon nanotubes.⁴⁰ Nishino *et al* reported that 3.2 nm diameter colloidal Fe-Mo nanocrystals could be used to grow high quality single-walled CNT carpets.⁴⁷ Iron oxide nanocrystals from 4.5 to 16 nm in diameter also were applied to the growth of primarily multi-walled nanotube films.⁴⁸ More recently, our group has demonstrated that organically modified iron oxide nanocrystals could serve as catalysts for CNT growth in spite of their surface coating and oxidized state.^{46d, 49} This prior work leaves open the question of whether larger catalysts would grow increasingly larger carbon nanotubes; moreover, the observations from several studies indicate that generally it is difficult to produce single-walled material using colloidal catalysts.^{40-41, 42, 46d, 48-49, 82b}

Also unexplored for both the chemically and gas-phase prepared catalysts is whether catalyst dopants can be used to gain further control over carbon nanotube structure and growth. Existing research has underlined that the importance of the growth substrate to CNT growth; alumina, for example, outperforms TiO₂, SiO₂, and ZrO₂ in forming uniform and dense CNT films presumably because the strong interactions between metallic iron and alumina limit ripening of the catalyst particles at high temperatures.⁶⁵ The addition of aluminum into a precursor catalyst such as iron oxide, forming aluminum ferrite, could mimic or even augment this effect resulting in less catalyst ripening and

narrower CNT diameter distributions. Additionally, by replacing some iron with aluminum the catalyst particles would contain less iron available for carbon nanotube growth. This could lead to the production of CNT with smaller diameters as compared to similar sized pure iron oxide catalysts.

Here we examine how both aluminum ferrite and iron oxide nanocrystals can be applied as catalysts for carbon nanotube growth (CNTs) in a water-assisted chemical vapor deposition process. These particles (d from 4 to 40 nm) were highly uniform in diameter ($\sigma < 10\%$); this feature allowed for a systematic examination of how catalyst composition and size affected carbon nanotube structure. The evaporation of nanocrystal solutions onto alumina yielded sub-monolayer coverage of particles; at temperatures above 750 °C, exposure of these substrates to both acetylene and water resulted in the production of carbon nanotubes. The outer diameter of the carbon nanotubes (CNTs) increased as the particle diameter increased; additionally, larger catalyst particles yielded CNTs with increasing numbers of walls. However, the smallest aluminum ferrite catalysts coupled with limited acetylene delivery resulted in films with over 60% single-walled carbon nanotube content. While many features of the CNT growth were similar between the aluminum ferrite and the iron oxide nanocrystals, two differences were apparent. First, CNT growth rates were 10 times faster for the ferrites than for pure iron oxides, and as a result thicker films could be formed by starting with aluminum ferrites. Also, the quality of the CNTs, as measured by Raman spectroscopy, was substantially improved when aluminum ferrite was used as a catalyst.

4.2. Experimental Methods

4.2.1. Chemicals

Iron oxide, hydrated [FeO(OH), catalyst grade, 30-50 mesh], aluminum hydroxide (Al(OH)₃, reagent grade), oleic acid (technical grade, 90%), and 1-octadecene (ODE, technical grade, 90%) were purchased from Sigma-Aldrich. All nanocrystals were synthesized under nitrogen. For the CNT carpet growth, ultra high purity ethyne (C₂H₂, acetylene) and molecular hydrogen (H₂) gases were purchased from Matheson Tri-Gas.

4.2.2. Instrumentation

4.2.2.1. Scanning electron microscope (SEM)

SEM samples were placed on 45° SEM mounts and SEM images were taken by FEI Quanta 400 field emission SEM at 10.0 kV. The height of CNT carpet was measured by Image-Pro Plus 5.0 (Media Cybernetics, Inc., Silver Spring, MD).

4.2.2.2. Transmission electron microscope (TEM)

TEM specimens for iron oxide were made by dropping the solution on ultra-thin carbon type-A 400 mesh copper grids (Ted Pella Inc.) and let them dry naturally. CNTs grown on the substrate were gently transferred onto Lacey formvar/carbon, 300 mesh copper grids (Ted Pella Inc.) to make the CNT specimens. The TEM micrographs were taken on a JEOL 2100 field emission gun TEM operated at 200 kV with a single tilt holder. The size and size distribution data were obtained by counting >1000 nanocrystalline particles using Image-Pro Plus 5.0.

4.2.2.3. Raman spectroscopy

The Raman spectra were collected with a Raman spectrometer (Renishaw, Gloucestershire, U.K.). CNT carpet samples were placed on a glass slide and a 785 nm laser was introduced on the top of the CNT carpets.

4.2.3. Synthesis of precursor catalysts: iron oxide, aluminum iron oxide nanocrystals

4.2.3.1. Iron oxide nanocrystals

Monodisperse iron oxide nanocrystals with a wide size range from 4 to 40 nm were synthesized based on the literature.^{3j} The purified iron oxide nanocrystals were purified using methanol and precipitated by adding acetone. The cleaned colloidal nanocrystals were redispersed in hexane.

4.2.3.2. Synthesis of aluminum iron oxide nanocrystals

4 nm aluminum iron oxide was obtained by using 0.045 mmol iron oleate, 0.019 mmol aluminum oleate, and 2 mmol oleic acid in 5 g ODE at 320 °C for 2 h. 10 nm aluminum iron oxide was prepared by 0.7 mmol FeO(OH), 0.3 mmol Al(OH)₃ with 3 mmol oleic acid in 5 g ODE at 320 °C for 1 h. For 15 nm aluminum iron oxide, 10 nm nanocrystal preparation conditions were used except for using 4 mmol oleic acid.

The iron oxide and aluminum iron oxide nanocrystals were purified using methanol and precipitated by adding acetone. The cleaned colloidal nanocrystals were redispersed in hexane. Their particle sizes were measured through transmission electron microscope

(TEM), and their particle concentrations were measured by a Perkin Elmer Inductively coupled plasma atomic emission spectroscopy (ICP-AES) instrument equipped with autosampler.

4.2.4. Growth of carbon nanotube (CNT) carpets

Colloidal nanocrystals in hexane (20 μ l) were deposited on an alumina coated substrate (10 x 10 mm, $\text{Al}_2\text{O}_3/\text{SiO}_2$, 100 nm thick Al_2O_3 deposited through atomic layer deposition (ALD) on SiO_2 wafer, Sundew Technologies LLC). The colloidal nanocrystal solution on the substrate was naturally dried at room temperature and then heated at 400 $^\circ\text{C}$ for 3 h to burn away oleic acid, the surface ligand on the nanocrystals.

CNT carpets were grown by a water-assisted hot filament chemical vapor deposition (HF-CVD) following a previously reported procedure.⁶⁴ The condition of gas flow for carpet growth chamber was 210 standard cubic centimeters (sccm) of H_2 , 2 sccm of C_2H_2 . The flow of water molecules were generated by bubbling 200 sccm of H_2 through the NANOpureTM water (Thermo Scientific) at room temperature. The total pressure under the gas flow condition was 1.4 torr. A higher pressure (25 torr) was used to initiate CNT growth on the surface of the nanocrystals. With the gas pressure 25 torr, the nanocrystal deposited $\text{Al}_2\text{O}_3/\text{Si}$ wafer was placed in the loading chamber and moved into the growth chamber. The reactor pressure was reduced to 1.4 torr after 30 second in the hot zone. The iron oxide nanocrystals deposited on the wafer were reduced to iron particles using atomic hydrogen (H) generated through H_2 dissociation on a hot filament (0.25 mm tungsten; the current, voltage and power were 7.5 A, 6.0 V, and 45 W, respectively). The

hot filament was left on for 30 sec, and then turned off. CNTs were grown for 15 min at 750 °C.

4.2.5. Calculation of surface coverage of nanoparticles

To obtain nanoparticle concentrations, ICP analysis of total iron concentration in solution are used after the digestion with nitric acid. In the calculation, we assumed a particle volume of $\frac{4}{3} r^3$ where r is the average radius of the nanocrystal as determined by TEM measurements, counting over 1,000 particles; then we took the density of Fe_3O_4 (5.1 g/ml) and AlFe_2O_4 (4.6 g/ml) and could calculate the particle weight. As an example, the volume of a 4.0 nm diameter particle of AlFe_2O_4 is 3.35×10^{-20} ml, which provides a total mass per particle of 1.5×10^{-19} g. Using this data, and Avogadro's number, we find that 40 ppm of iron in a solution results in a nanoparticle concentration of 4.5×10^{17} nanoparticles/L (755 nM). Since 20 μl of nanoparticle solution was dropped on the substrate (1 cm x 1 cm, alumina coated Si wafer), surface coverage of nanoparticles are 9.0×10^{12} nanoparticles/cm².

4.2.6. Calculation of the diameter of zero-valent iron.

The diameter of the reduced nanocrystal was calculated by using the average diameter of AlFe_2O_4 nanocrystal observed by TEM and density of Fe_3O_4 , AlFe_2O_4 . For the details, the mass of 4.0 nm AlFe_2O_4 nanoparticle is 1.54×10^{-19} g. Since the mass fraction of Fe in AlFe_2O_4 is about 0.57 (molecular weight of Al, Fe, and O is 26.98, 58.93, and 15.99 g/mol, respectively.), mass of Fe is 8.79×10^{-20} g. The calculated mass of Fe is converted

to volume using density of Fe (7.8 g/ml) and finally, we find that the diameter of Fe is 2.78 nm. This number is 30 % reduced size from 4.0 nm AlFe_2O_4 nanocrystal.

4.3. Results and Discussion

Monodisperse nanocrystals prepared via colloidal chemical methods were used here as precursors for the small iron particles necessary for CNT growth. As shown in Figure 4.1 and Figure 4.2, these materials can be produced with diameters ranging from 4 to 40 nanometers, and also with size distributions generally under 10 % on the diameter.^{3j} For this effort we expanded upon the conventional iron oxide synthesis to incorporate aluminum, yielding similar sized and highly uniform aluminum ferrite nanocrystals under the appropriate conditions. Specifically, for the work described we used three sizes of aluminum ferrite (4.0 ± 0.4 ; 9.5 ± 0.7 ; 14.1 ± 1.1 nm) and six sizes of iron oxide (4.3 ± 0.5 ; 10.2 ± 0.7 ; 16.0 ± 1.4 ; 23.9 ± 2.2 ; 32.1 ± 2.5 ; 38.4 ± 3.3 nm). All particles were stabilized by oleic acid coatings which rendered them well dispersed and non-aggregating in hexane.

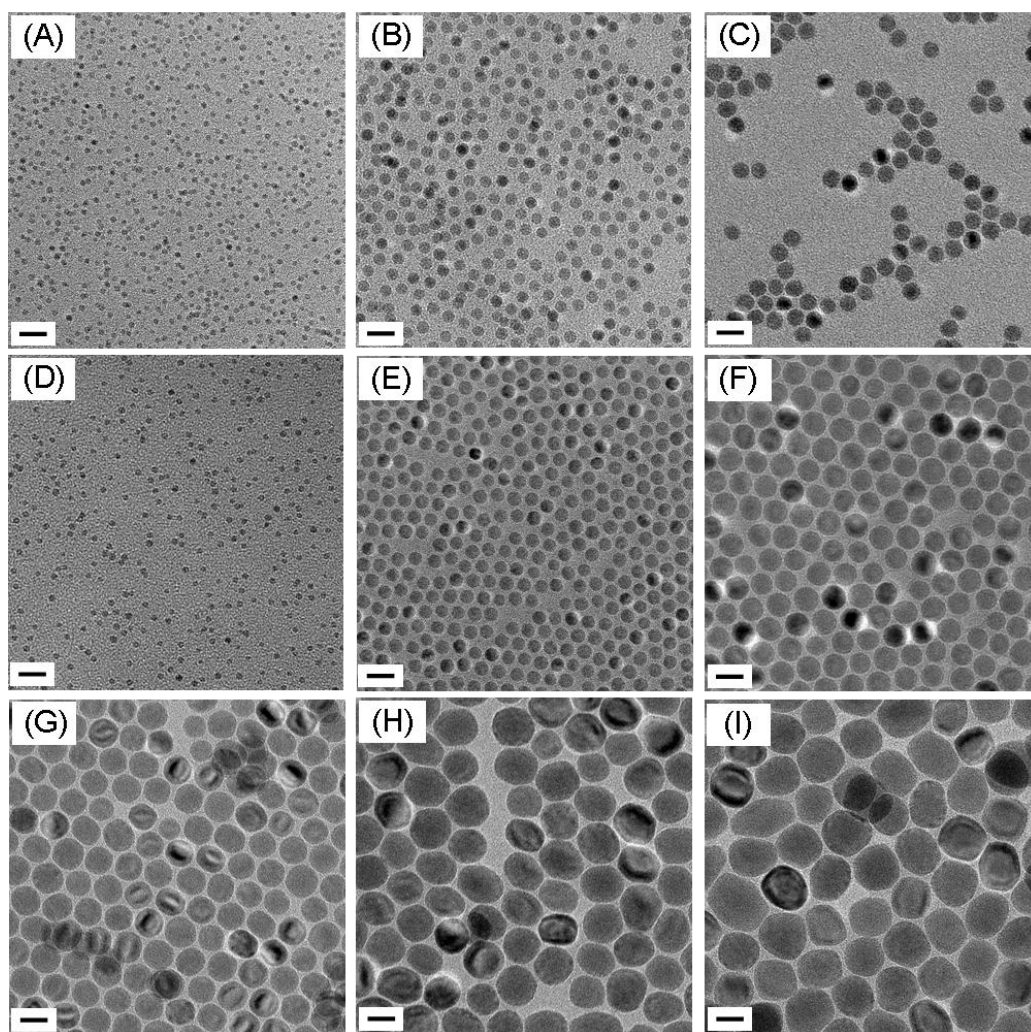


Figure 4.1 TEM images of aluminum ferrite (A to C) and iron oxide nanoparticles (D to I) in different sizes.

The sizes are 4.0 ± 0.4 , 9.5 ± 0.7 , 14.1 ± 1.1 nm (A to C), 4.3 ± 0.5 , 10.2 ± 0.7 , 16.0 ± 1.4 , 23.9 ± 2.2 , 32.1 ± 2.5 , and 38.4 ± 3.3 nm (D to I), respectively. All scale bars are 20 nm.

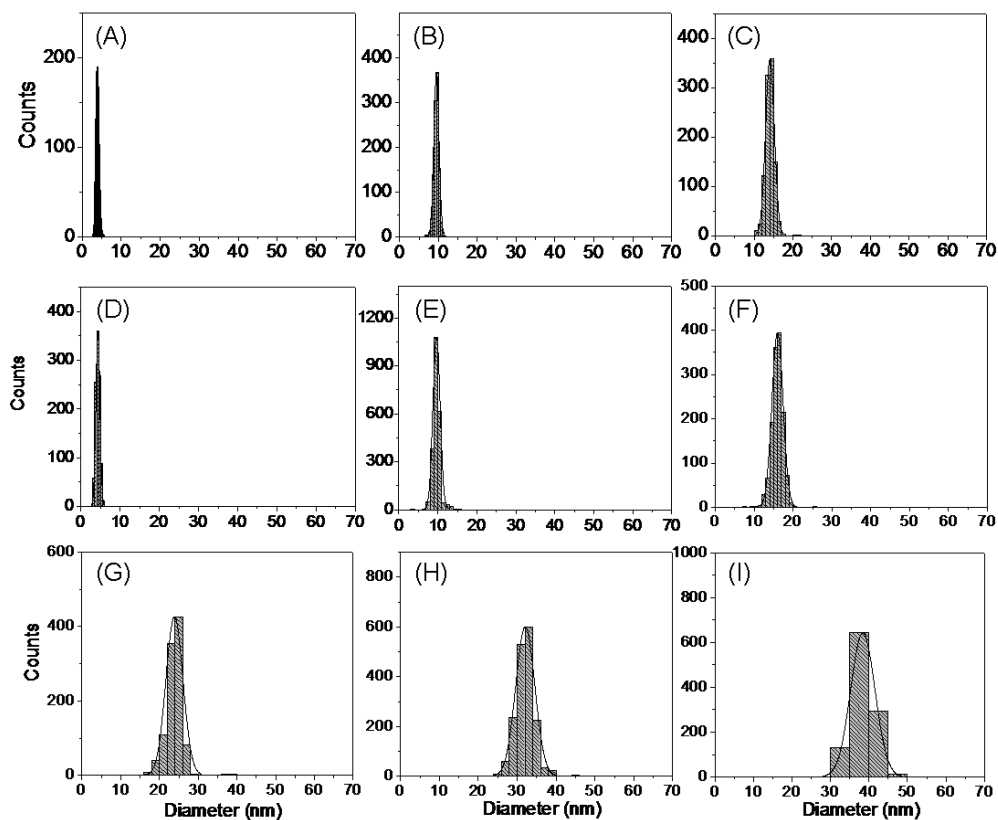


Figure 4.2 The histograms of the size distribution of aluminum ferrite (A to C) and iron oxide (D to I) nanoparticles.

The x and y axes are the size of the nanoparticles (nm) and their counts, respectively.

4.3.1. Diameter dependence of CNT on the varied size of starting nanocrystals.

All diameters and compositions of catalyst precursors formed carbon nanotubes using a water-assisted chemical vapor deposition process. The hexane solvent was evaporated away from nanocrystal suspensions applied to alumina substrates resulting in a sub-monolayer of particles; exposure of these substrates to both acetylene and water at 750 °C

resulted in the production of carbon nanotubes (Figure 4.3). Both the size and composition of the catalysts had a significant effect on the diameter, wall number and carpet height as will be discussed. Additionally, for the largest size (e.g. 38 nm diameters) of precursor catalyst the CNT carpet height was significantly reduced.

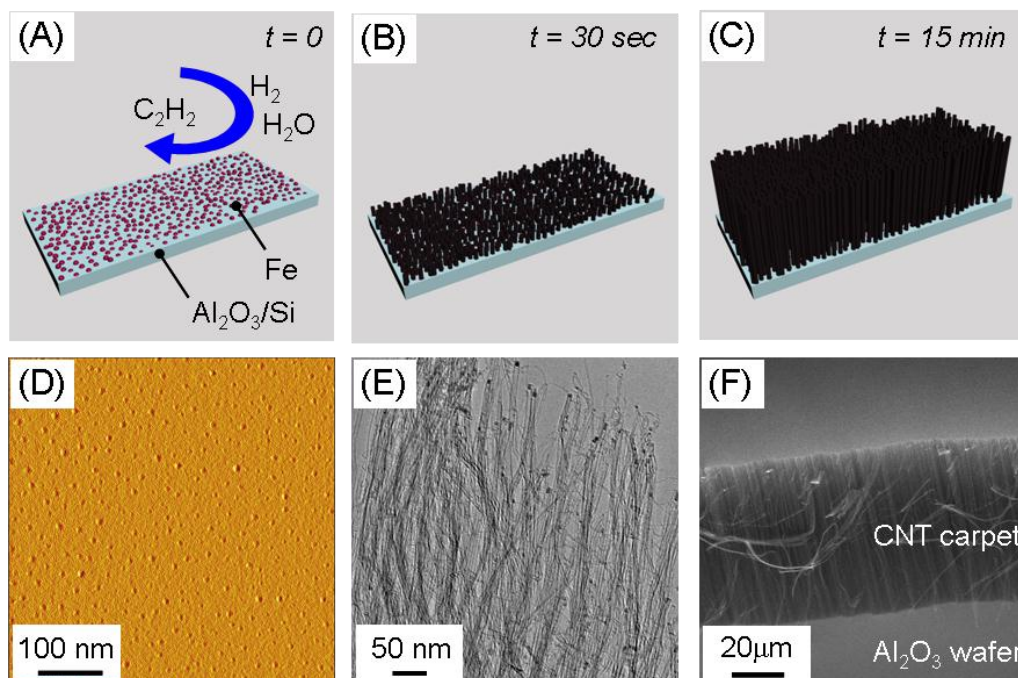


Figure 4.3 Carbon nanotube (CNT) growth process.

Nanoparticles on alumina wafer were used to catalyze CNT carpet growth flowing C_2H_2 , H_2 , and H_2O (A and D). After nucleation of carbon on the nanoparticles, CNTs started growing (B and E). A 15 min reaction rendered vertically aligned thick CNT carpet (C and F).

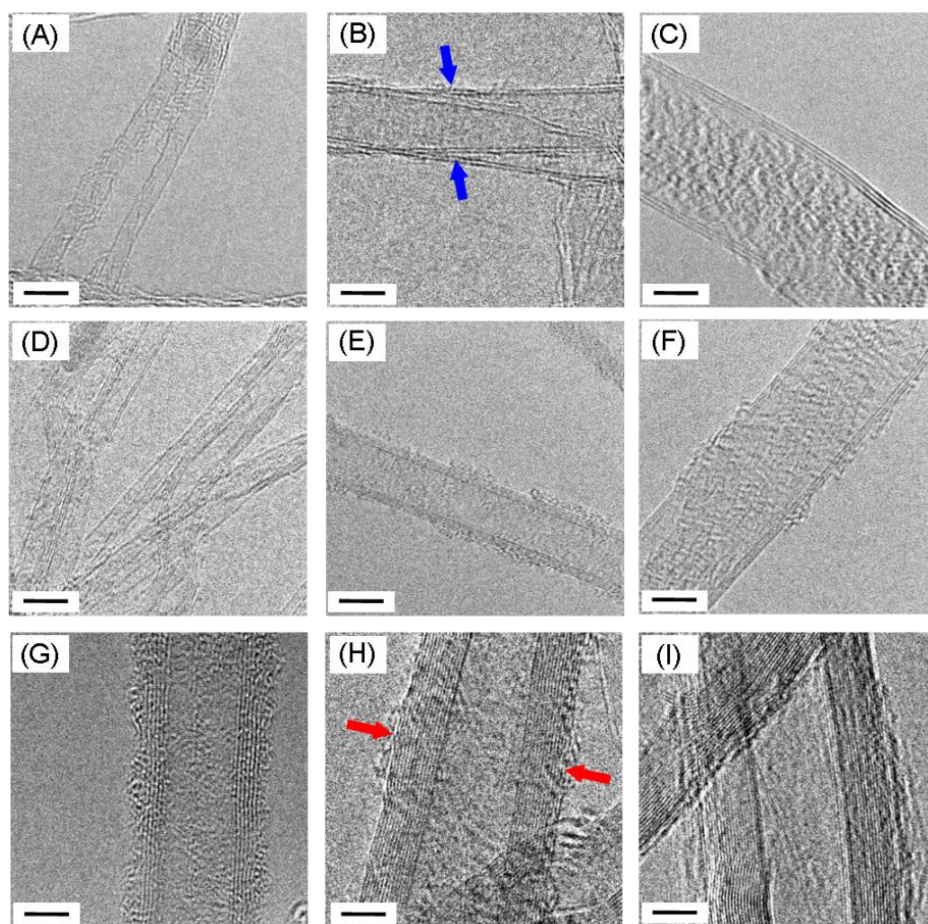


Figure 4.4 TEM images of CNTs grown by various sized aluminum ferrite and iron oxides. The mean diameter of CNTs are 3.3 ± 0.9 , 6.6 ± 1.2 , 9.8 ± 2.0 nm grown by AlFe_2O_4 from 4 to 14 nm (A to C). Iron oxide from 4.3 to 38.4 nm grew CNTs having outer diameter of 4.1 ± 1.0 , 8.8 ± 3.4 , 12.1 ± 2.5 , 14.0 ± 4.5 , 16.5 ± 5.0 , 17.9 ± 6.1 nm (D to I). All scale bars are 5 nm. For the size distribution analysis, the mean diameter with standard deviation of the CNTs was measured by counting about 300 CNTs. The blue arrows in panel B show a clear double-walled structure while the red arrows in panel H highlight a multi-walled carbon structure.

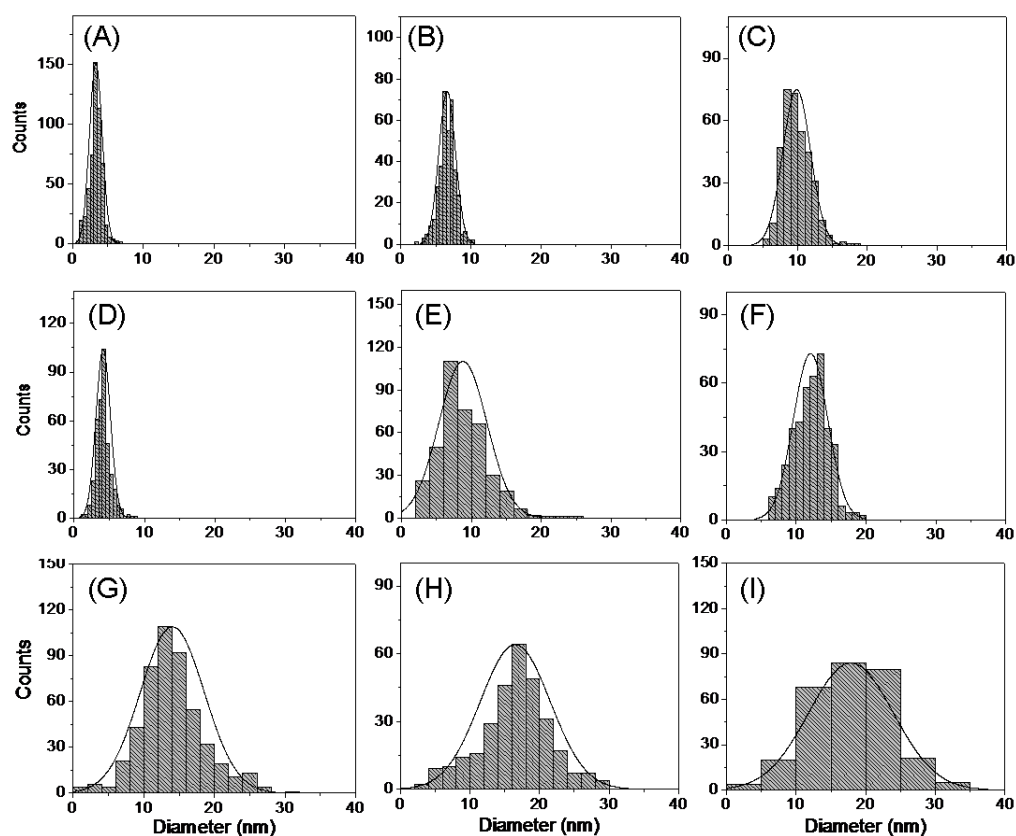


Figure 4.5 The histograms of the diameter distributions of CNTs grown by of aluminum ferrite (A to C) and iron oxide (D to I) nanoparticles.

The x and y axes are the diameter of CNTs (nm) and their counts, respectively.

Within these dense carpets are many individual CNT, and transmission electron microscopy (TEM) was applied to quantify their outer diameters (Figure 4.4, and Figure 4.5). For all cases, the larger catalyst particles yielded CNTs with larger diameters. Figure 3 shows representative TEM images of CNTs prepared by each of the nine different catalysts. Generally, over three hundred carbon nanotubes were measured to arrive at the average outer diameter; assuming a normal distribution, this is appropriate sampling to specify with good confidence (95%) the average diameter.⁸⁴ Qualitatively, it is apparent in the images that the diameter of CNT increases as the diameter of the

catalyst increased. For example, a 4.0 nm diameter aluminum ferrite nanocrystal produced mainly single- and double-walled CNT with 3.3 nm outer diameter; in contrast a larger iron oxide particle ($d = 16.0$ nm) produced more multi-walled materials with diameters of 12.1 nm. Figure 4.6 illustrates this trend over the complete range of samples and compares the CNT diameters to the estimated diameter of the resulting reduced catalyst. Note that we assume that the precursor catalysts are fully reduced to the zero-valent metal under the CNT growth conditions; this leads to a 30% reduction in their original oxidized diameters (See the Experimental Section). Below 16 nanometers, the correlation between the calculated catalyst diameter and the CNT diameter is nearly one for both iron oxide and the aluminum ferrites. Little catalyst ripening occurs for these growth conditions. Also, in agreement with past work is the observation that the tube diameter is fixed by the particle diameter; this suggests that the growing carbon tube forms on opposite sides of the metal catalyst.^{96b, 97}

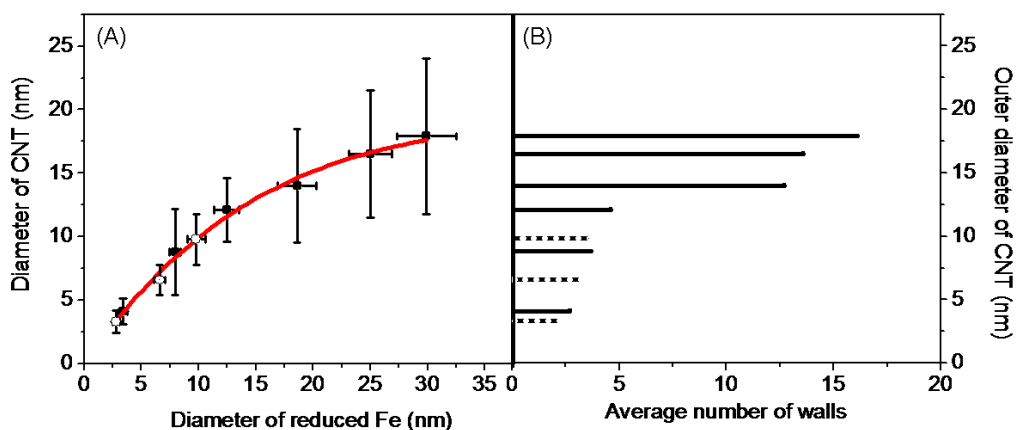


Figure 4.6 Diameter dependence of CNT on the varied size of the reduced Fe precursor catalysts. The bar chart shows the average number of walls of CNT grown by aluminum ferrite (empty circle and dot line) and iron oxide (bold circle and bold line). The reduced Fe nanocatalyst size was calculated by using the density of AlFe_2O_4 (4.6 g/ml), Fe_3O_4 (5.1 g/ml) and Fe (7.8 g/ml).

For the three largest catalysts the relationship between the nanoparticle diameter and CNT diameter is much less pronounced (Figure 4.4, Figure 4.5, and Figure 4.6). The trends observed for smaller precursor catalysts are distinctly different from that seen in the largest samples; the difference in CNT diameters when grown from 23 and 38 nm iron oxide nanocrystals is only 4 nm. Also for these larger sizes the growth rates of the tubes are substantially reduced, and we see more evidence of iron wicking into the tube ends (Figure 4.7, and Figure 4.8).

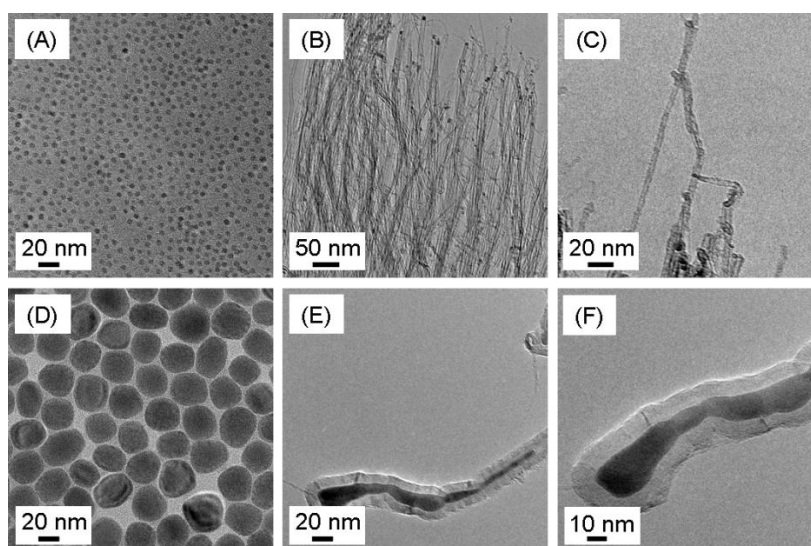


Figure 4.7 TEM images of CNTs grown from two sizes of iron oxide nanocrystals. (A to C) 4.3 nm iron oxide and the resulting CNTs. (D to F) 38.4 nm iron oxide nanoparticles and the CNTs.

Several researchers have suggested that iron must be fully molten to allow for the rapid diffusion and migration of graphitic materials to opposite sides of catalysts.^{96b, 97} We speculate that the larger nanocrystals are not completely molten at the 750 °C used for CNT growth. Bulk iron has a melting point of 1535 °C. Smaller nanocrystals are known to have a reduced melting point due to their high surface energies; however, this

effect is minimal ($< 10\%$) for iron nanocrystals with diameters larger than 15 nanometers.⁹⁸ We note also that for CNT grown from the larger catalysts, the breadth of the CNT diameter distribution is notably broader than that found for CNT grown from smaller materials (Figure 4.9). This is consistent with the observation that when catalyst diameters are large enough, the CNT diameter is no longer defined by the particle's diameter. Multiple nucleation sites on the larger particles, and the more random location of the growing tube walls, contributes to the less uniform materials.⁹⁹

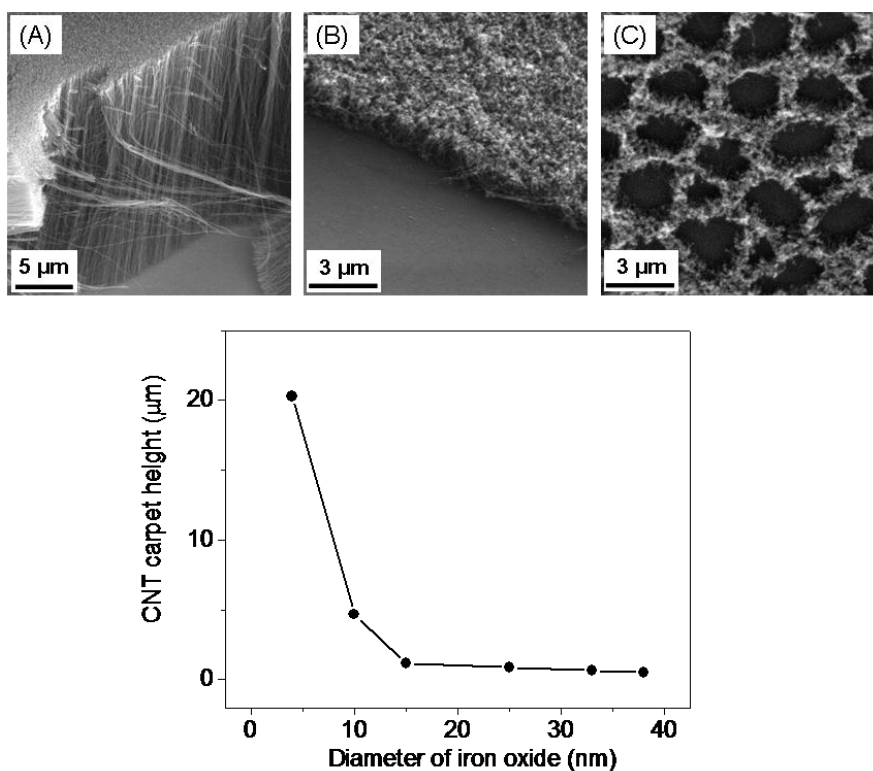


Figure 4.8 CNT carpet height varied from wide range of iron oxide catalyst (from 4 to 38 nm). (A) The tallest carpet was obtained from 4.3 nm iron oxide nanocrystals (20.3 μm , surface coverage of 9.03×10^{12} nanoparticles/ cm^2). However, the carpet grew slowly as the applied nanocrystal diameter increased: (B) 16.0 nm iron oxide (surface coverage = 7.22×10^{11} nanoparticles/ cm^2) yield to 1.2 μm and (C) 38.4 nm iron oxide (surface coverage = 9.63×10^{10} nanoparticles/ cm^2) grew 0.5 μm CNT carpets. The bottom graph shows the catalyst diameter dependent carpet height graph. CNT carpets were all grown at 750 $^\circ\text{C}$ for 15 min at 1.4 torr.

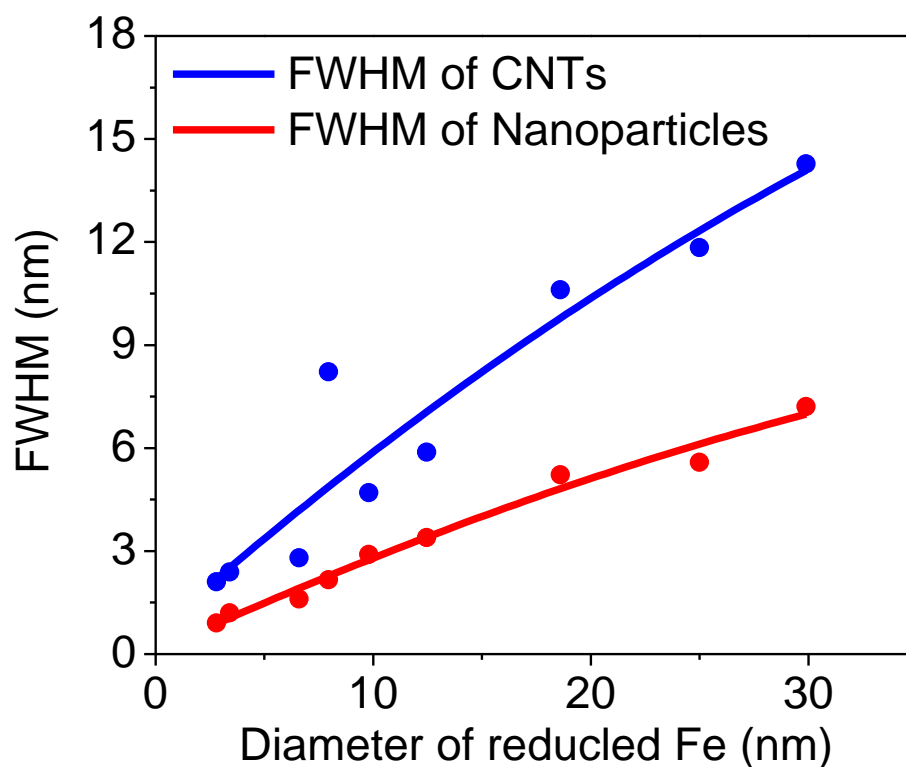


Figure 4.9 Full width half maximum (FWHM) of the diameter distribution of CNTs (blue) and nanoparticles (red line).

A close examination of CNT produced via aluminum ferrite precursors as compared to the iron oxide system reveals some improvement in the diameter dispersion of the CNT. Figure 4 shows that the most uniform CNT were produced with the aluminum ferrite nanocrystals; the iron oxide nanocrystals of similar sizes had slightly larger outer diameter distributions. Colloidal nanocrystals start wetting at CNT growth temperatures and are adhered on the wafer having crystal-to-liquid state, and initiating carbon nucleation and growth process.¹⁰⁰ In this process, aluminum in the nanocrystal may inhibit ripening of particles as it migrates to the alumina surface at high temperatures; the aluminum may diffuse out of the particle and interact with the free available oxygen. Al-

O has a far more favorable bond strength than Fe-O (210 kJ/mol higher) because of its smaller ionic radius (Al^{3+} : 53.5 pm, Fe^{3+} : 64.5 pm, O^{2-} : 126 pm).¹⁰¹ This high bonding energy increases the melting point and catalyst ripening could be highly prevented by this strong aluminum oxygen bonding between aluminum ferrite nanocrystals and the alumina wafer in the nanocatalyst wetting.

4.3.2. The number of wall control of carbon nanotubes

The catalyst diameter and composition also controls the amount and number of single, double, triple and multi-walled CNT; as anticipated, single-walled nanotubes (SWNTs) are most prevalent when smaller nanocrystals are used. The very smallest nanoparticles (e.g. $d = 4$ nm) formed single-, double-, and triple-walled carbon nanotubes, and the percentage of multi-walled tubes increased smoothly as the diameter of the catalyst increased (Figure 4.6). This parallels observations from thin films and catalyst islands deposited via gas phase methods; SWNTs were grown only by a thin 2 nm iron layer while more double-walled and multi-walled nanotubes were observed when iron layers were nearly 3 nm in thickness.^{38a, b} Using a process similar to the one applied here, Nishino *et al* showed that with 3.2 nm Fe/Mo high fractions of SWNT were also observed.⁴⁷ Here we find a significant fraction of SWNT even for precursor catalysts as large as 4 nanometers, and that for catalysts much larger than this wall numbers increase substantially.

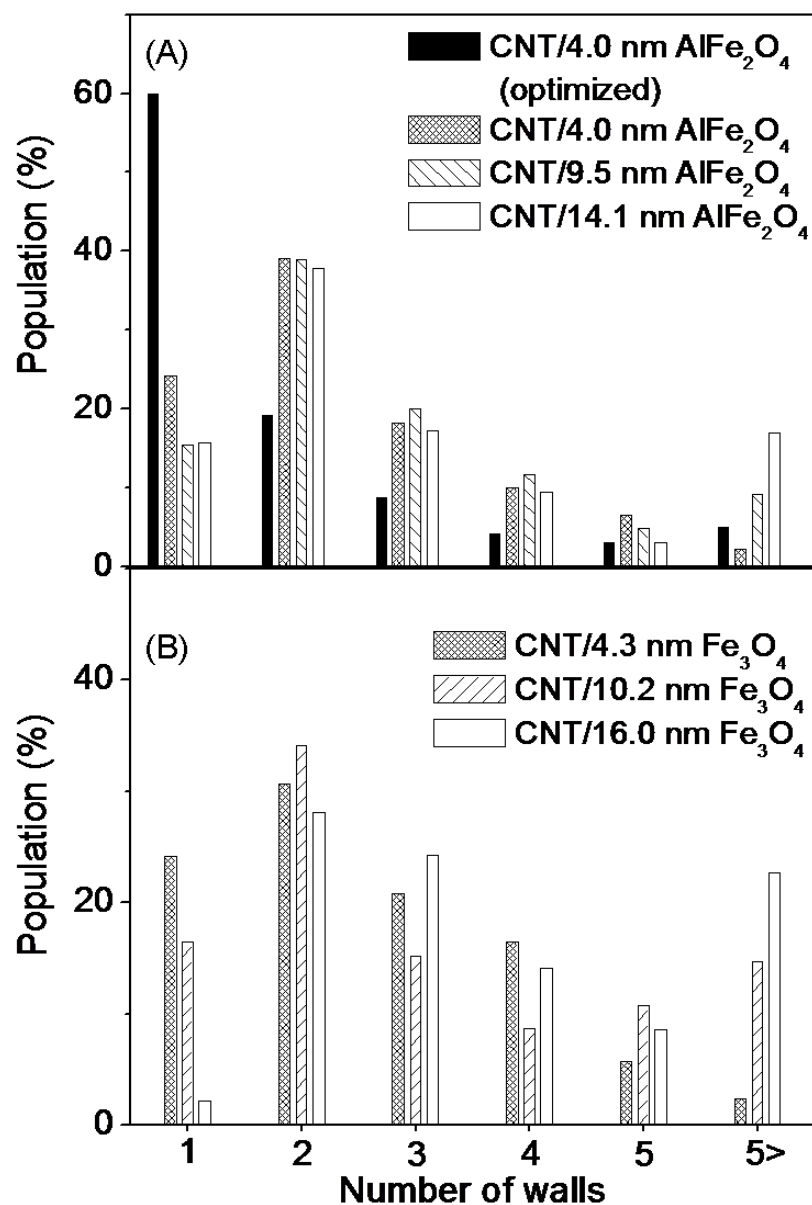


Figure 4.10 The statistics of the number of walls of CNTs grown by both aluminum ferrite and iron oxide.

To analyze the number of walls, about 300 CNTs were counted on high magnification (over 300 k) in a high resolution TEM. All CNTs were grown by drop dried nanoparticles on ALD alumina wafer at 2.0 sccm C₂H₂ flow rate. The highest percentage of single-walled nanotube (about 60 %) was achieved by optimizing the conditions to: 4.0 nm AlFe₂O₄ on sputtered alumina wafer at 0.5 sccm of C₂H₂. Bigger iron oxide over 25 nm prepared multi-walled tubes having more than 5 walls; the average number of walls of CNTs grown by 23.9, 32.1, and 38.4 nm iron oxide was 12.7, 13.6 and 16.1, respectively.

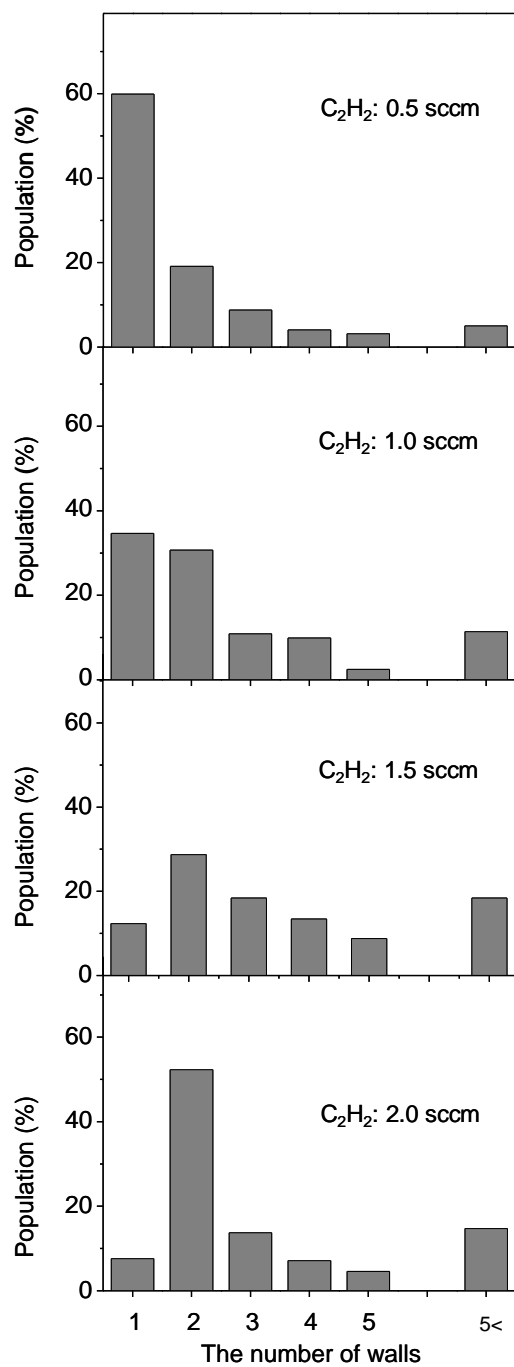


Figure 4.11 The number of wall control of CNTs.

The study of the wall number control was performed on an alumina wafer (Al_2O_3/Si , 10 nm thick Al_2O_3 deposited by electron beam method). The surface coverage of 4.0 nm aluminum ferrite nanocrystals was 9.03×10^{12} nanocrystals/cm² (750 nM). The slower flow rate of C_2H_2 leads to higher populations of single-walled CNT.

To further increase the amount of single-walled nanotubes, it was necessary to slow the rate of introduction of the carbon source (C_2H_2) and use exclusively aluminum ferrite materials. Over 60% of the carpet material was single-walled nanotube when aluminum ferrite particles were used with a slow acetylene flow rate (0.5 sccm) (Figure 4.10, and Figure 4.11). In contrast, 55% of the carpet material was double-walled for the same catalyst at reactant flow rates (2.0 sccm). Zhang *et al* found that slow introduction of carbon feedstock not only reduces the incidence of increased wall number, but also reduces the amount of amorphous carbon.¹⁰² By introducing C_2H_2 at a slower rate, there are fewer collisions of C_2H_2 with the side walls of growing CNTs. A potential disadvantage of relying on slower reaction rates to form more single-walled nanotubes is the reduction in the carpet heights. Here, the carpet height decreased from 9 to 3 μm as the acetylene flow rate was decreased from 2.0 to 0.5 sccm, respectively.

4.3.3. The surface coverage and reaction pressure effect on CNT carpet quality.

CNT quality is also an important feature of these materials; amorphous carbon and disordered carbon in the tubes can limit desirable electronic and mechanical properties. We found that films grown from smaller catalysts led to notably higher quality materials for all conditions. The quality of the CNTs grown from both aluminum ferrite and iron oxide nanocrystals were characterized by Raman spectroscopy.^{100a, 103} The D ($\sim 1340\text{ cm}^{-1}$) band results from defects on nanotubes such as, hetero-atoms, vacancies, heptagon-pentagon pairs, impurities (amorphous carbon), and forming wall-wall interactions; the G ($\sim 1590\text{ cm}^{-1}$) band indicates the presence of well-ordered sp^2 carbons. Thus the G to D

ratio is a common standard for characterizing carbon nanotube quality.^{64, 104} Figure 4.12 illustrates the significant increase in the G band over the D band in films produced from smaller and smaller catalysts.^{103, 105} Certainly part of this data reflects the increase in the wall numbers seen in carpets produced from larger particles (Figure 4.4, Figure 4.5, and Figure 4.6). However, it may also be that in larger particles carbon super-saturation may not result in the formation of graphitic caps because the materials are not fully molten; this would result in amorphous carbon deposition.^{38b, 48, 97b, 100b, 106}

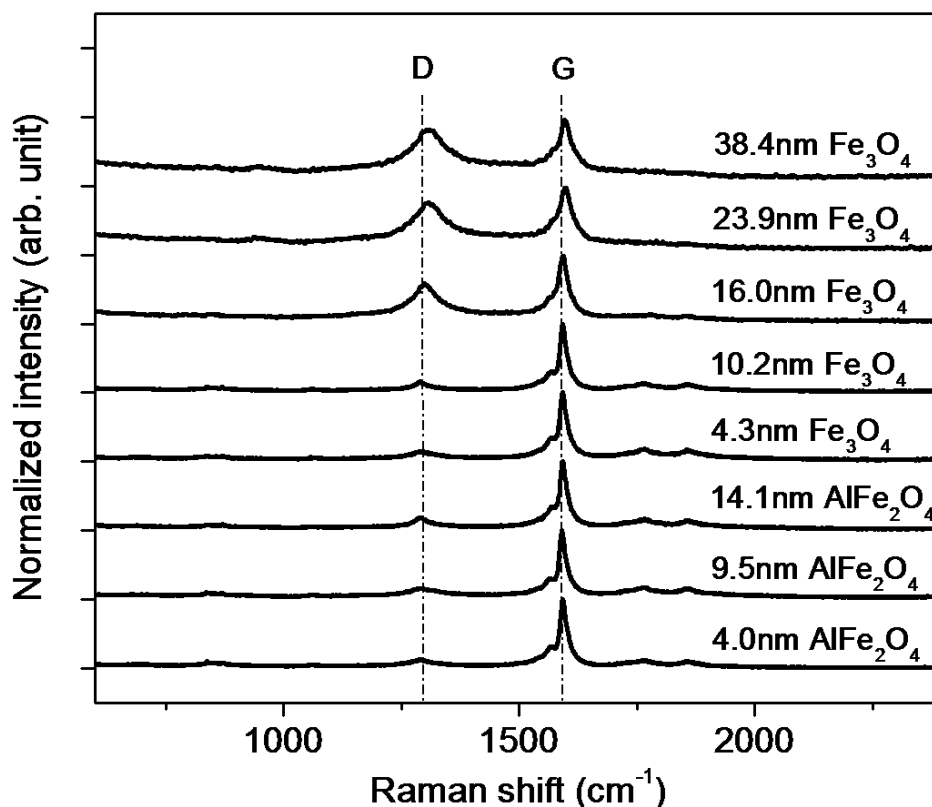


Figure 4.12 Raman spectra of CNTs from AlFe_2O_4 and Fe_3O_4 nanocrystals indicating purity. The induced laser polarization was parallel to the alignment of the CNT carpet samples. The G (1590 cm^{-1}) to D (1340 cm^{-1}) ratio of CNT from 4.0, 9.5, 14.1 nm AlFe_2O_4 nanoparticles is 11.4, 8.8, 7.1, respectively. I_G/I_D of CNT from 4.3 to 38.4 nm Fe_3O_4 is 9.8, 8.0, 2.0, 1.2, and 1.1, respectively. All CNT samples are carpet grown at 1.4 torr for 15 min.

An unexpected finding was that the inclusion of the dopant aluminum in the iron catalysts greatly improved the quality of the carbon nanotubes. Figure 4.12 shows that for all three sizes, the aluminum ferrite nanocrystals formed CNT with very high quality ($G/D = 11.4$) as compared to the best CNT formed from pure iron oxide crystals ($G/D = 9.8$). Additionally, the tube quality was less sensitive to the aluminum ferrite catalyst diameter than CNT grown from pure iron oxide. For these doped nanocrystals, 30% of the iron is substituted with aluminum; after the particles are fully reduced, this would result in substantially smaller catalyst diameters than those catalysts formed from pure iron oxide. Smaller catalysts lead to less multiple nucleation and more efficient nucleation of the graphitic shells necessary for high quality CNT growth.^{97b, 106} We cannot rule out other processes by which the aluminum may actively promote CNT growth, and these are the subject of ongoing study.

The quality of the CNT films was also a sensitive function of both the surface coverage of nanocrystals and the reaction pressures; generally, monolayer coverages with no aggregation were the best conditions for growth. The highest G to D ratio was measured from the CNT carpets grown when the surface of wafer was covered by a monolayer of aluminum ferrite (750 nM, 9.03×10^{12} nanocrystals/cm²). In addition, CNT carpets had higher G to D ratios at 1.4 torr ($I_G/I_D = 11.4$) than those grown at 25 torr ($I_G/I_D = 1.3$). Pint *et al* reported controllable CNT quality depending on reaction pressure.⁶⁴ It was noted that while growing CNT carpets, certain amounts of C₂H₂ might be consumed in the formation of amorphous carbon or increasing the number of walls rather than letting a few walls of CNTs grow vertically.^{103b, 105} The increase in the number of walls could be related to the diffusivity and solubility of the carbon in the

activated catalyst as well as its shape.^{98a, 107} Basically, fast diffusion and a high solubility of carbon can increase the number of walls rather than grow longer CNTs. Thus, we observed at higher pressures poorer quality CNTs were prepared as evidenced by the reduced G/D ratio ($I_G/I_D = 1.3$).

4.3.4. Overall height of CNT carpet catalyzed by both aluminum ferrite and iron oxide nanocrystals.

Finally, we examined what conditions would promote the formation of thick CNT films. Generally, surface coverages of precursor catalysts near a monolayer and higher reaction pressure promoted carpet growth. Figure 4.13 shows CNT carpet height dependence on the surface coverage of 4.0 nm aluminum ferrite nanocrystals on alumina wafer. At 1.4 torr for 15 min, CNT carpet's height increased from 1.8 to 22.1 μm when the nanocrystal concentration decreased from 6000 nM (7.22×10^{13} nanocrystals/ cm^2) to 750 nM (9.03×10^{12} nanocrystals/ cm^2). CNT carpet was the thickest when the nanocatalyst layer on the wafer closed to a monolayer (750 nM, 9.03×10^{12} nanocrystals/ cm^2) and this catalyst coverage yield 280.3 μm at 25 torr. A fast supply of large quantity of carbon source at high pressure with perfect coverage of catalyst can build up carbon structure fast and result in thicker nanotube carpets.

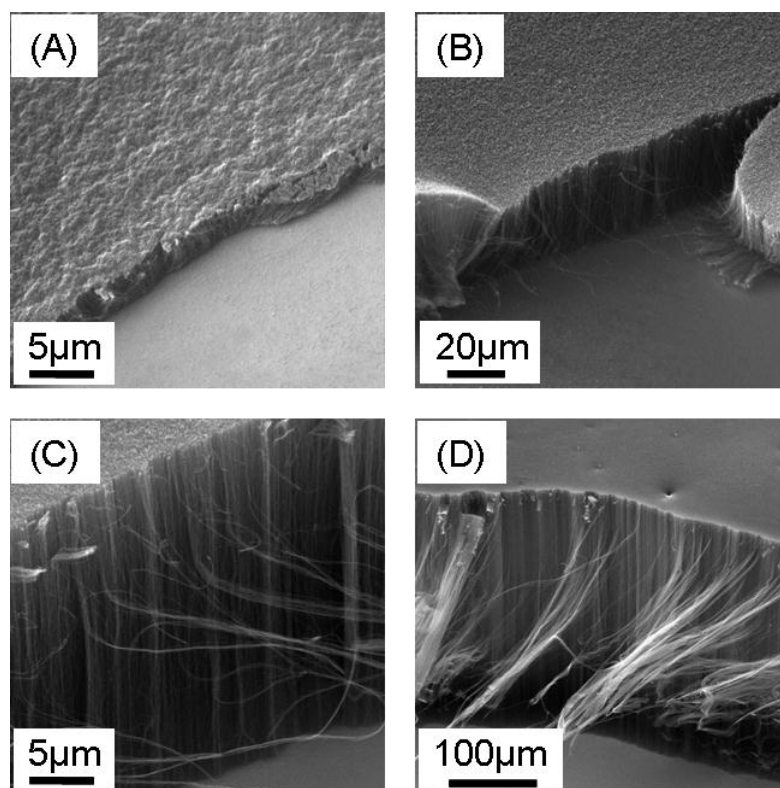


Figure 4.13 Effect of reaction gas pressures (1.4 torr (A and C), and 25 torr (B and D)) and surface coverage of 4.0 nm aluminum iron oxide nanocatalysts on the substrate (from 7.22×10^{13} (A and B) to 9.03×10^{12} (C and D) nanoparticles/cm²).

SEM images show that the highest CNT carpet was obtained from high pressure (25 torr) and low nanoparticle concentration (750 nM, 9.03×10^{12} nanoparticles/cm²). The lower surface coverage below 9.03×10^{12} nanoparticles/cm² grew shorter CNT carpet height (see Supplemental Figure 8 and 9).

Even thicker films resulted when we used smaller catalysts and the inclusion of an aluminum dopant lead to the thickest films. Figure 4.14 shows the height of carpets formed with varying catalyst types; for the same conditions, heights were more than ten-fold higher for the aluminum ferrite catalysts. CNT carpet heights were from 0.1 to 5.3 μm as the concentration of iron oxide nanocrystals decreased from 6000 nM (7.22×10^{13} nanocrystals/cm²) to 750 nM (9.03×10^{12} nanocrystals/cm²). However, CNTs from

aluminum ferrite nanocrystals were grown from 7.6 to 54 μm at the same surface coverage of nanocrystals.

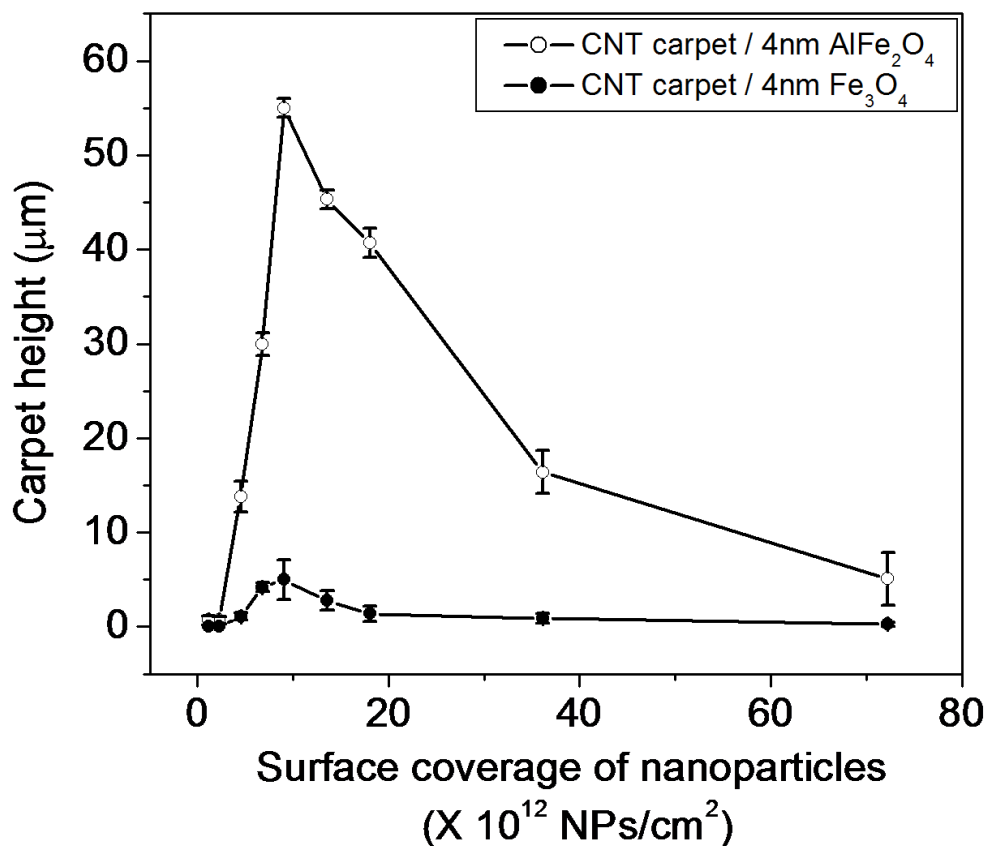


Figure 4.14 Comparison of CNT carpet height grown by both aluminum iron oxide and iron oxide nanocrystals on alumina wafer.

CNT carpets were grown by slow growth at 1.4 torr for 15 min after 30 s rapid super-saturation at 25 torr (see supplemental discussion and figure 8, 9, and 10). The average CNT carpet height with error bar was obtained from the center and the edge parts of each sample.

We speculate that the strong interaction between aluminum containing nanocrystals and the substrate may prevent the removal of catalysts by penetration into the substrate (forming an alloy with the support substrate) and after all, increase the life time of catalysts.^{100b, 108} Also, aluminum ferrite nanocrystal has less active iron than equivalent

iron oxide material; this also results in a smaller active catalyst and faster carpet growth. There is also strong size dependence apparent in these data: larger particles produce more slowly growing carpets. However, the ferrite data cannot be completely explained based on the size of the reduced iron catalyst that forms. A more complete analysis of the wide range of ferrite application to CNT carpet growth is the subject of a future publication.

4.3.5. CNT carpet growth by rapid saturation and slow growth process

CNT carpet growth is highly affected by the reaction pressure and the concentration of nanocatalyst on the substrate. It was found that high pressures (25 torr) allowed more reaction gas molecules to react with nanocatalysts, resulting in rapid growth of CNTs. Alternatively, low pressures (1.4 torr) grow short carpets because not as many carbon sources collide with the nanocatalyst, and CNTs slowly grow vertically.⁹⁵ However, the growth of taller, high quality CNT carpet is always challenging because taller carpets often result in poor quality (disorganized carbon structure or carbon impurities induced by high intensity D band in Raman spectra) grown by high pressure.

We postulate that controlling the super-saturation of carbon on the nanocatalyst may have an effect on the CNT carpet growth system. Basically, cylindrical graphene sheets will start growing vertically as soon as carbon precipitation on the nanocatalyst is super-saturated.⁹⁶ Rapid super-saturation of carbon can be achieved by supplying a large quantity of the carbon source at a high pressure. In addition, high quality CNTs will be obtained by the organization of cylindrical graphene sheets at a low pressure. In this research, various reaction processes were attempted in order to determine the optimal conditions for fast saturation and slow growth. The nanocatalyst deposited substrate was

kept initially at high pressure (25 torr) for rapid super-saturation for 10, 30, and 60 s and then the CNT carpet started growing at 1.4 torr for 15 min.

Figure 4.15 and Figure 4.16 show the carpet height change depending on the 4.0 nm AlFe_2O_4 nanoparticles' surface coverage and various super-saturation times from 0 s to 60 s. It was found that the longer rapid super-saturation time led to the taller CNT carpets. In the observation of CNT carpet growth and its quality depending on different super-saturation time, the high quality CNT carpets with high G ($\sim 1590 \text{ cm}^{-1}$) to D ($\sim 1340 \text{ cm}^{-1}$) ratios (I_G/I_D) were prepared by 10 and 30 s super-saturation followed by slow growth. However, 10 s super-saturation led to very short carpets ($\sim 2 \mu\text{m}$) and its growth rate was similar to that obtained without rapid super-saturation growth. However, 30 s super-saturation grew densely packed carpets with high I_G/I_D with fast CNT carpet growth. It seems that 10 s super-saturation is not enough to reach super-saturation of carbon on the surface of reduced nanocatalysts. On the other hand, 30 s at 25 torr in the reduction process led to fast super-saturation of carbon on the reduced nanocatalyst and hence, CNTs grew dramatically taller. Therefore, 30 s rapid super-saturation was the optimal condition for growing good quality, taller CNT carpet.

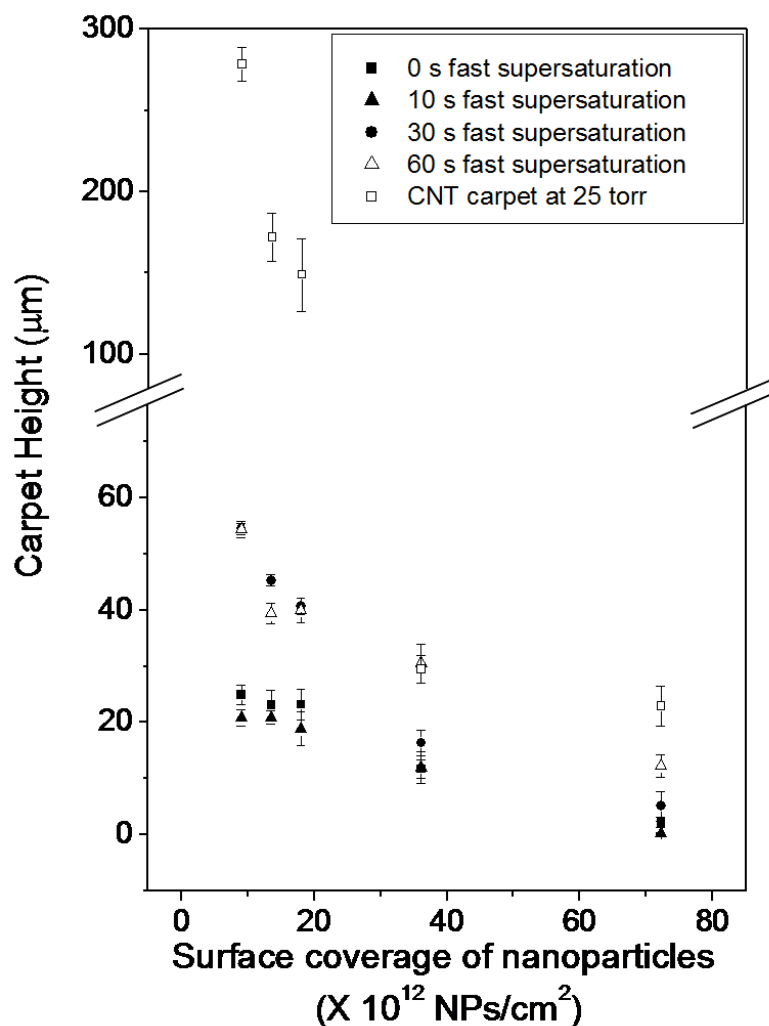


Figure 4.15 CNT carpet height at various surface coverage of 4 nm diameter of aluminum iron oxide nanocrystals depending on different CNT carpet growth condition.

For the fast supersaturation of carbon on AlFe_2O_4 nanoparticles, nucleation of carbon was treated at 25 torr for 0 (■), 10 s (▲), 30 s (●), and 60 s (Δ). After rapid super-saturation of carbon, CNT carpets were grown at 1.4 torr for 15 min. The highest carpet was obtained at 25 torr for 15 min (□). CNT carpets grown at 1.4 torr without initial rapid super-saturation at 25 torr increased carpet height from 2.2 to 24.9 μm as nanoparticle concentration decreased. Applying 10 s fast super-saturation at 25 torr gave similar growth rate as the one from 1.4 torr. However, super-saturation at 25 torr for 30 s led to taller carpet heights from 5.1 to 54.6 μm as the AlFe_2O_4 nanoparticle concentration decreased. Rapid super-saturation times longer than 30 s grew similar heights of CNT carpets until 60 s. If the carpet was prepared only at 25 torr for 15 min, the carpet growth height was dramatically increased from 22.9 to 278.3 μm as the nanocrystal concentration decreased.

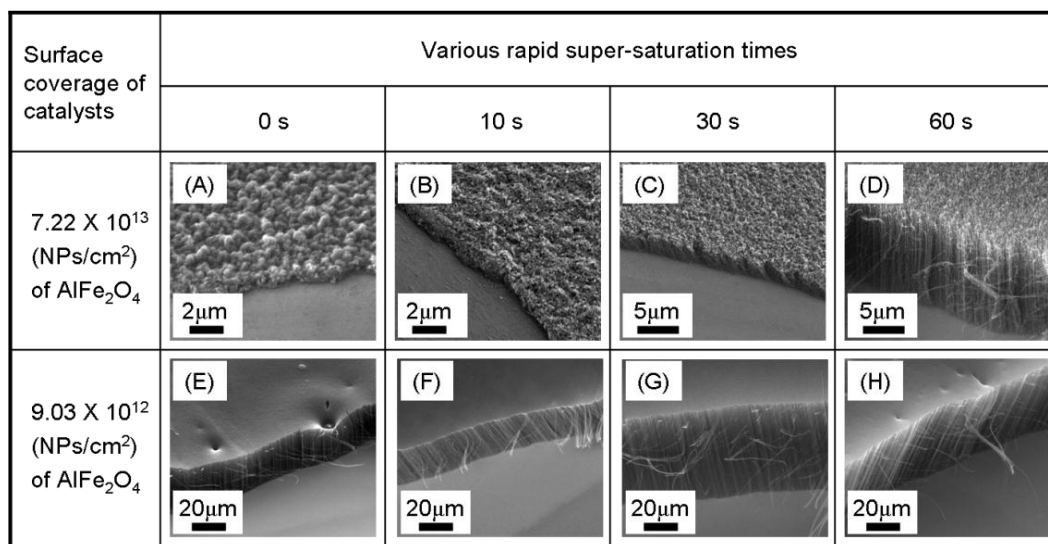


Figure 4.16 SEM images of CNT carpets grown from different growth conditions.

4 nm AlFe₂O₄ nanoparticles' surface coverages were 7.22×10^{13} nanoparticles/cm² from A to D and 9.03×10^{12} nanoparticles/cm² from E to H. All CNT carpets were grown by slow growth at 1.4 torr for 15 min after 0 s, 10 s, 30 s, and 60 s rapid super-saturation at 25 torr.

The inside of the CNT carpets grown by rapid super-saturation followed by slow growth showed higher quality carpets with better I_G/I_D compared to the top of the carpets as shown in Figure 4.17. This is caused by the slow growth with well-ordered sp^2 structure at low pressure (1.4 torr) just after 30 s fast super-saturation at high pressure (25 torr). On the other hand, the top of the CNT carpets had low quality as CNT carpet height increased because the top of the CNTs was grown at high pressure (25 torr) induced by rapid super-saturation process. The taller CNT carpets grown by small number of nanocatalysts led to the high I_G/I_D (the highest value was 14.2 with 54 μm , 9.03×10^{12} nanoparticles/cm²) of the inside of CNTs. However, in the case of short carpets at higher nanoparticle concentrations, the bottom of the CNTs had lower quality ($I_G/I_D = 4$) in contrast to the top ($I_G/I_D = 6$) because the higher number of nanocatalysts was utilized.

When the bottom of the CNTs was analyzed by Raman spectroscopy, the inside of carpets as well as the carbon residues on the surface of nanocatalysts could be detected and influenced with a poor I_G/I_D .

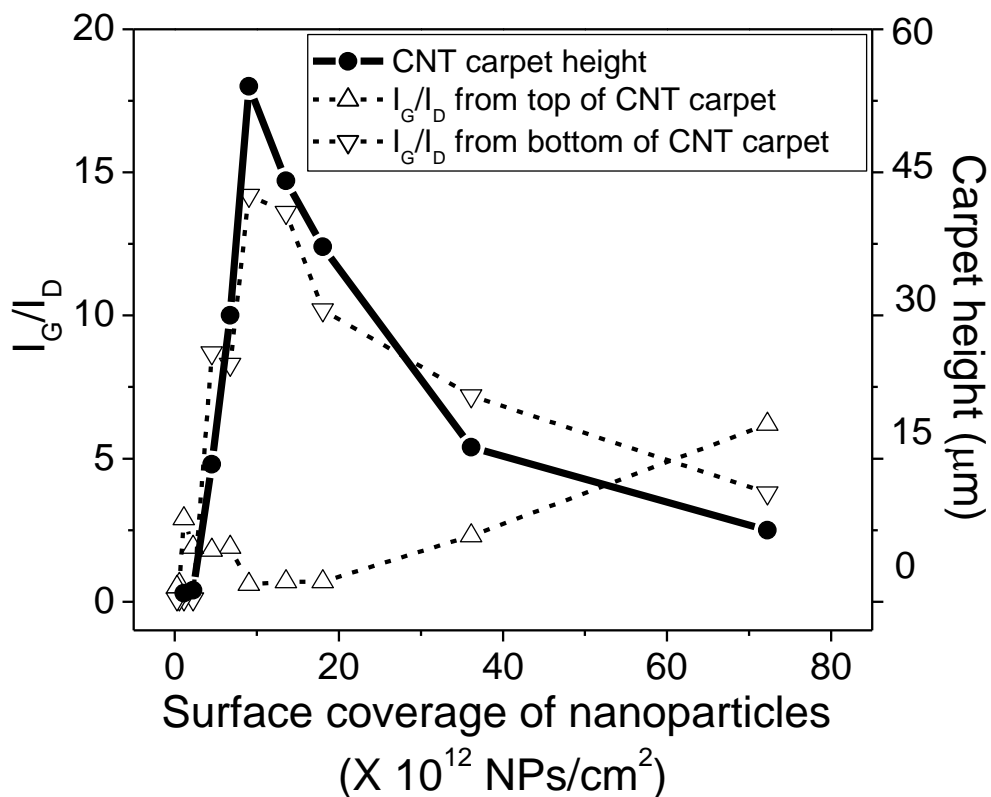


Figure 4.17 The correlation of CNT carpet height and G to D ratio.

All CNT carpets were grown at 1.4 torr for 15 min after 30 s rapid super-saturation. 4.0 nm AlFe_2O_4 nanoparticles were used for catalyst precursors. The higher carpet height had better quality at the bottom of the CNTs.

The carpet grew higher up to 58 μm with better I_G/I_D (14.2) as AlFe_2O_4 concentration was closed to a monolayer (9.03×10^{12} nanoparticles/cm²). The carpets became shorter and less populated with lower I_G/I_D when the nanoparticle concentrations approached to 0 nM. This lower I_G/I_D on the inside of CNTs could be due to the defect on the side wall of

CNT. In the case of short carpets grown by lower concentrations of nanoparticles ($< 9.03 \times 10^{12}$ nanoparticles/cm²), the carpet growth may be finished quickly before the entire growth time (15 min) caused by ripening or poisoning of the small number of nanoparticles on the wafer. Even though the growth of the carpet is terminated, the reaction gases, such as C₂H₂, H₂, and the water molecules are still supplied and hence, these molecules would react on the side wall of the already grown CNTs. This influence would effect on the top as well as at the bottom of the carpet, resulting in lower I_G/I_D on the inside of the carpet, when the carpet is shorter.

4.4. Conclusion

In summary, uniform iron oxide and aluminum ferrite nanocrystals formed in a conventional wet chemical method could be applied as precursor catalysts for the growth of carbon nanotubes (CNT). The application of colloidal nanocrystals offered the opportunity to tune the resulting CNT structure through both the reaction conditions, as well as the composition, size and coverage of the precursor catalysts. For example, as the nanocatalysts increased in dimensions they produced increasingly larger CNT. Also, the numbers of walls in the final CNT product were a sensitive function of the starting catalyst size: under the appropriate reaction conditions, the smallest catalysts could yield materials with over 60% single-walled carbon nanotubes. More typically, samples were mixtures of double, triple and larger multiple tubes. Finally, the incorporation of aluminum into the catalyst resulted in both higher quality as well as thicker carpets.

These data illustrate that catalyst surface coverage, dimension, and composition can be used to tailor the structural features, as well as the quality, of CNT carpets.

Chapter 5

Closed-edged graphene nanoribbons from large diameter collapsed nanotubes

5.1. Introduction

Carbon nanotubes (CNTs) with different diameters and helicity have distinct chemical and physical properties. Diameter-selective and diameter-controlled growth of CNTs has been developed for specific applications, such as field-effect transistors, field-emission displays and hydrogen storage.^{36d, 109} Synthesis of large diameter CNTs, especially single-walled carbon nanotubes (SWCNTs) within a range of 1.4~5.6 nm has been realized with laser vaporization, arc discharge, and chemical vapor deposition (CVD) method.^{42, 110}

When the diameter increases, cylindrical SWCNTs become energetically unstable. A number of theoretical studies have demonstrated that there exists a tube diameter (D_{eqe}) where the energy of the collapsed tube is the same as that of the round geometry.¹¹¹ Near the D_{eqe} energy, there exists a diameter region where both geometries can co-exist at high temperatures. This has been referred to as a metastable region for the CNT structure. The cross section configuration of the fully collapsed structure is composed of two highly strained circular edges bridged by a flat middle section. We refer to this geometry as a closed edged graphene nanoribbon (CE_xGNR) configuration which is stabilized by Van der Waals interaction between two opposing walls. Theoretical studies have found D_{eqe} to be an increasing function of the number of walls.^{111a, b} Table 5-1 summarizes a number of reported values of D_{eqe} from the literatures and the methodologies employed to deduce them. In those studies, $D_{\text{metastable}}$ ranges were given for SWCNT and double-walled carbon nanotubes (DWCNT), $D_{\text{metastable}}$ ranges and D_{eqe} for triple-walled carbon nanotubes (TWCNT) have also been calculated.^{111e, 111g-j}

In addition to the diameter, SWCNT collapse is also correlated to external factors, such as temperature, pressure, Van der Waals force induced by a substrate or neighboring tubes in bundles, toxic addition in the reaction system, mechanical strain and electron bombardment.^{111a, 111c, 111e, 111g, 112} Modeling of the transition between a cylindrical and collapsed configuration in different environments has been studied extensively.^{112a, 113} Furthermore, unusual edge states and promising electronic, mechanical and electromechanical behavior of collapsed SWCNTs has been documented and predicted.¹¹³⁻¹¹⁴ Nanotube collapsing allows for the band gap modification by its

transverse self-collapse, avoiding the employment of structural perturbations which disturb the sp^2 bonding framework or the position of the tube ends.^{114c}

Table 5-1. Summary of values of equivalent energy points for SWCNT and DWCNT in the literature and the methodologies employed.

Reference	D_{eqe} for SWCNT (nm)	D_{eqe} for DWCNT (nm)	Methodology
111a	3.6 ~ 8.6	3.8 ~ 10.4	Experimental and continuum model analysis (bending modulus used $k = 1.4$ eV; $\epsilon_{vdW} = 25 \sim 100$ meV/atom; crossover shapes were calculated from geometrical assumptions)
111d	5.9 ~ 6.0	-	Molecular dynamics simulation using MPSim (force field, derived through QM calculations; bending modulus $k = 912 \sim 963$ GPa depending on chirality)
111f	2	-	Molecular dynamics simulation (REBO potential to represent covalent bonds; adaptive Lennard-Jones potential to represent van der Waals interaction)
111c	2.2	-	Extrapolation from molecular dynamics simulations of collapsing of hexagonally close-packed bundles of SWNT using DL_POLY code

			(macromolecular force field DREIDING parameterized for carbon)
¹¹¹ⁱ	4.1	5.0	Atomic-scale finite-element method simulation and order-N atomistic simulation method based on Brenner potential for carbon ($\epsilon_{vdW} = 2.39$ meV/atom)
^{111h}	1.9	-	Continuum model analysis and molecular simulation using Discover molecular dynamics program through Materials Studio 3.0 (polymer consistent force field used)
^{111j}	6.2	8.0	Atomistic simulations (second-generation Tersoff-Brenner potential and Lennard-Jones potential; $\epsilon_{vdW} = 2.39$ meV/atom)
Present work	2.6	4.0	Molecular dynamics simulation using LAMMPS (AIREBO potential with no torsion term; $\epsilon_{vdW} = 53.6$ meV/pair)

Although, the formation of a collapsed structure is largely independent of tube chirality, the structure of collapsed SWCNTs can be flat, warped or twisted due to lattice registry dependent Van der Waals interaction between the two opposing walls.^{111c, 111e, 111j, 115} The morphology of collapsed nanotubes has been demonstrated by TEM, STM and AFM measurements.^{111b, 114b, 116} In previous efforts in synthesizing large diameter CNTs, Zettl group, Kiang *et al.* and Ajayan group have observed the collapsed and twisted structures of multi-walled carbon nanotubes (MWCNTs), SWCNTs and

DWCNTs, respectively.^{38c, 111b, 117} Recently, Alvarez *et al.* observed collapsed DWCNTs with a ribbon-like structure.¹¹⁸ However, very few observations were obtained in TEM images and the collapsed phenomenon of few-walled CNTs was not discussed in detail. In this study, synthesis of large-diameter few-walled CNTs was accomplished using nearly mono-disperse aluminum ferrite nanoparticles. TEM characterization was used to distinguish between uncollapsed and collapsed carbon nanotubes based on whether tubes exhibited kinks as expected for collapsed tubes but not for uncollapsed tubes. Formulas for conversion of the widths of collapsed tubes to their respective round configurations were theoretically determined and permitted a direct comparison of diameter distributions for both collapsed and uncollapsed tubes.

5.2. Experimental methods

5.2.1. Chemicals.

Iron oxide, hydrated (FeO(OH); catalyst grade, 30-50 mesh), oleic acid (technical grade, 90%), 1-octadecene (ODE, technical grade, 90%) were purchased from Sigma-Aldrich. Iron oleate ([Fe] = 3 mg/mL) was synthesized using the method mentioned in the previous research, and aluminum oleate was purchased by Fisher Scientific.^{3j}

5.2.2. Nanocrystal synthesis

All iron oxide nanoparticles were synthesized under nitrogen. Aluminum iron oxide was obtained by modifying the standard method for mono-dispersed iron oxide nanocrystals; iron and aluminum oleate were decomposed in the presence of oleic acid at

320 °C for 2 h.^{3j} For the purification of as-synthesized nanocrystals, 5 mL of resulting colloid was washed and precipitated using 25 mL methanol and 25 mL acetone by centrifugation at 4500 rpm for 30 min. The resulting black colloid was redispersed in 15 mL hexane.

5.2.3. Carbon nanotube growth condition

The substrate was prepared using a SiO₂ wafer, on which the Al₂O₃ layer was formed by sputtering aluminum or spin-coating water dispersed alumoxane solution. An aluminum layer with a uniform thickness of 10 nm was prepared in a sputter coater. Synthesis of water-soluble Al₂O₃ particles and fabrication of an Al₂O₃/SiO₂ layer from solution were achieved by a previously reported technique.^{46d} A preformed AlFe₂O₄ nanoparticle solution was diluted into different concentrations, followed by drop drying onto Al₂O₃/SiO₂ substrates. Prior to growth, in order to remove the oleic acid coating and expose the preformed metal oxide nanoparticles, the samples were calcined at 200 °C for 2 h in oxygen with a flow rate of 200 sccm. The growth of carbon nanotubes was carried out in a hot filament chemical vapor deposition (CVD) apparatus at 750 °C, which has been described elsewhere.^{64, 118} H₂ (210 sccm), C₂H₂ (2 sccm) were supplied during the reduction and growth stages as reducing agent and carbon source gas, respectively. H₂O was supplied by bubbling H₂ throughout degassed water at 200 sccm to assist carpet super-growth. The catalyst particles were reduced at 25 Torr in a 30 s reduction process, during which a tungsten filament was activated by ramping to a current of 9~10 A. The high temperature of the filament (typically ~2500 °C) enables dissociation of H₂ to form atomic hydrogen, which rapidly reduced the preformed nanoparticles to catalytically

active metal particles. The pressure was then reduced to approximately 4 Torr and the hot filament was switched off. Nanotube growth was then continued for an additional 10 min.

5.3. Results and discussion

5.3.1. Growth of a large diameter carbon nanotube carpet using preformed aluminum iron oxide nanocrystals.

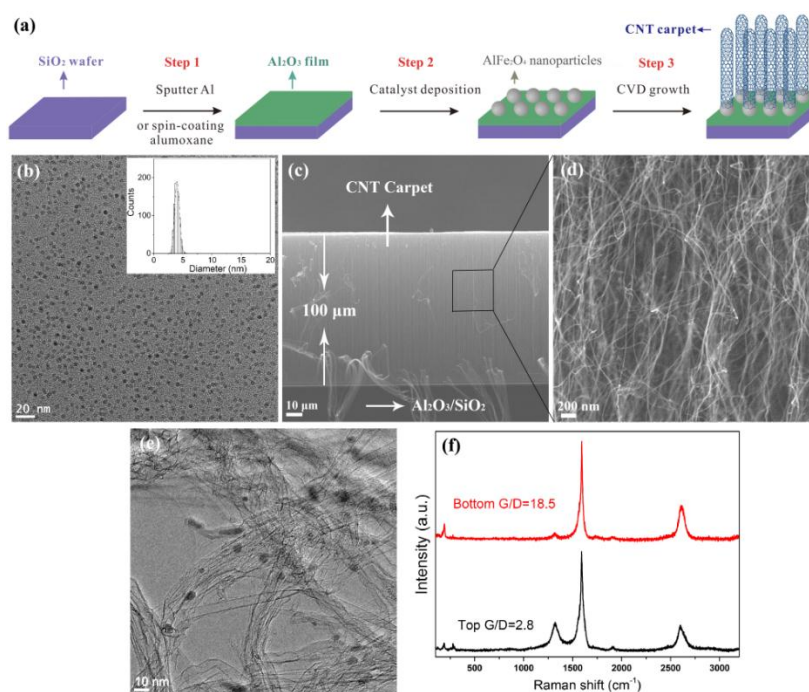


Figure 5.1 Synthesis of a large-diameter CNT carpet from mono-dispersed AlFe_2O_4 preformed nanoparticles.

(a) Schematic description of the preparation process of the collapsed CNTs. (Step 1) Sputtering aluminum or spin coating water-soluble alumina particles on SiO_2 surface to fabricate $\text{Al}_2\text{O}_3/\text{SiO}_2$ substrate. (Step 2) Drop drying preformed AlFe_2O_4 nanoparticle solution on the substrate surface and calcining at 200°C to form metal oxide catalyst layer. (Step 3) Growing the CNT carpets by water-assisted CVD method. **(b)** TEM image of uniformly dispersed preformed nanoparticles with oleic acid coating. The inset histogram shows the diameter distribution of the preformed nanoparticle, with an average size of 4.0 ± 0.4 nm. **(c)** SEM image of the CNT carpet with a height of ~ 100 μm grown on $\text{Al}_2\text{O}_3/\text{SiO}_2$ substrate in 10 min growth. **(d)** Close-up SEM image of the CNTs arrays at higher magnification, corresponding to the indicated region in (c). **(e)** TEM image of the large-diameter CNT.

(f) Raman spectra of the top and bottom region of the CNT carpet, showing G/D ratios of 2.8 and 18.5, respectively.

The synthetic process involving deposition of catalyst particles on a substrate and growth of collapsed CNTs is illustrated in Figure 5.1. A TEM image in Figure 5.1 displays of 4.0 nm preformed AlFe_2O_4 nanoparticles. These nanoparticles have a narrow size distribution, with an average diameter of 4.0 ± 0.4 nm. The size homogeneity of the preformed nanoparticles and their chemical composition were also demonstrated with lower magnification TEM image, AFM image and X-ray diffraction (XRD) pattern in Figure 5.2.

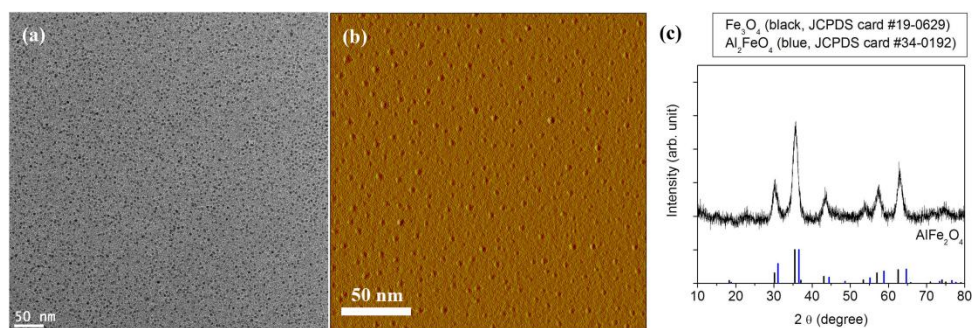


Figure 5.2 Characterization of aluminum iron oxide nanocrystals.

(a) Low-magnification TEM image of nearly mono-dispersed preformed AlFe_2O_4 nanoparticles with an average diameter of 4.0 ± 0.4 nm. (b) AFM image of AlFe_2O_4 nanoparticles on SiO_2 surface. (c) X-ray diffraction (XRD) pattern of aluminum ferrite nanocrystals. Diffraction peak positions of nanocrystalline magnetite Fe_3O_4 (black) and Al_2FeO_4 (blue) are vertically aligned at the bottom in the graph for comparison to the aluminum ferrite synthesized in our experiment. The diffraction peak positions of the AlFe_2O_4 nanocrystal are between those of the nanocrystalline magnetite Fe_3O_4 (black) and Al_2FeO_4 (blue).

The nearly mono-dispersed nanoparticles have been employed in synthesis of large diameter CNTs in previous studies.^{42, 118} It has been shown that by using these well-defined preformed nanoparticles one is able to achieve diameter-controlled synthesis of

CNTs. An additional advantage is that particle size can be controlled over a large size range. This cannot be achieved by catalyst evaporation onto a substrate to form catalyst islands. The dense and vertical growth of nanotube carpet on the $\text{Al}_2\text{O}_3/\text{SiO}_2$ substrate was achieved in a CVD process from AlFe_2O_4 nanoparticles with various concentrations (from 22 nM to 375 nM, as shown in Figure 5.3). As can be seen in the SEM image (Figure 5.1), a carpet height of $\sim 100 \mu\text{m}$ was obtained in 10 min growth from the nanoparticles with an optimized concentration (25 nM), indicating a high growth rate of $\sim 10 \mu\text{m}/\text{min}$. A portion indicated by a square frame in Figure 5.1 is shown in a higher magnification SEM image. A large amount of kinking and bending is evident. The TEM picture (Figure 5.1) shows that the sample is predominantly SWCNTs, with typically bent and twisted structures, indicating large numbers of collapsed SWCNTs. Catalyst particles encapsulated at the nanotube ends are also visible.

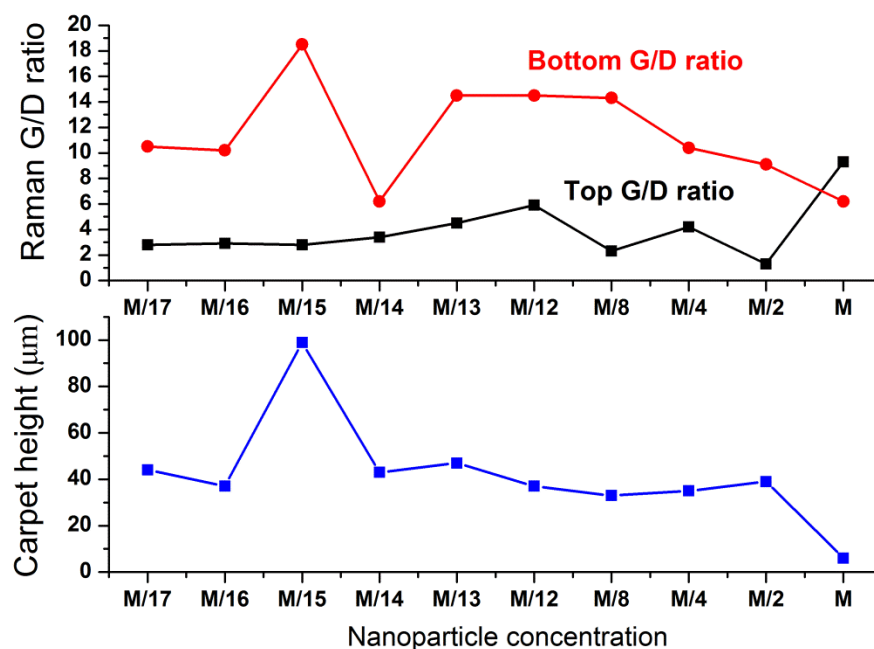


Figure 5.3 Quality of carbon nanotube grown by the precursor catalysts measured by Raman. The bottom G/D ratio (red and round dots), top G/D ratio (black and square dots) and height (blue and square dots) of nanotube carpet grown from preformed AlFe_2O_4 nanoparticles versus the nanoparticle concentration (M is the original concentration of AlFe_2O_4 nanoparticles 375 nM). The nanotube can be grown from AlFe_2O_4 nanoparticles with a wide concentration range from 22 nM to 375 nM. Carpet with the highest bottom G/D ratio of 18.5 and the highest carpet height of 100 μm was obtained from the optimized particle concentration 25 nM.

Raman spectra of the nanotube sample were taken from both the top and bottom region of the nanotube carpet using a wavelength of 633 nm for excitation. Radial breathing modes (RBMs) are clearly observed in the range of $100\sim 300\text{ cm}^{-1}$. Moreover, the subsidiary peak shown in the low frequency range of the G band and the lack of subsidiary peak on its high wave number side indicates that the nanotubes in the sample are mainly single-walled, in agreement with the TEM observation (Figure 5.1).^{116b} The carpet bottom shows a G/D ratio of ~ 18.5 , much higher than that in the top region (~ 2.8). It is found that the base-growth mechanism dominates in our conditions since residues of catalyst particles

in high density can still be seen anchored to the substrate after removing the nanotubes.¹¹⁹ Catalytic processes that cause amorphous carbon formation during the initial stage of nanotube growth are likely responsible for the lower G/D ratio commonly found at the top of a carpet. The bottom G/D ratio is a better indicator of nanotube quality and we take the ratio of 16-18 to be indicators of largely defect free SWCNTs. Thus we expect their mechanical behavior to be quite similar to that for the calculated mechanical behavior of structurally perfect nanotubes.

Figure 5.4 shows the TEM images of collapsed and uncollapsed nanotubes including SWCNT, DWCNT and TWCNT. Kinked, folded, and twisted structures which are typical features of collapsed nanotubes are clearly observed (as indicated by the arrows in Figure 5.4).^{111e} These structures are used as an identifier of closed edged graphene nano-ribbons. A collapsed and twisted MWCNT ribbon is also observed in TEM analysis. The widths of the flattened ribbons in this image formed by SWCNT, DWCNT, TWCNT and MWCNT are found to be 4.6 nm, 8.0 nm, 7.8 nm and 8.2 nm, respectively. Previous studies have suggested that collapse does not necessarily occur throughout the entire tube and is most likely caused by mechanical activation rather than thermal activation.^{111j, 120} It has also been suggested that kinked deformations formed locally in some regions on the nanotube might serve as an initiator for an entire flattening of a tube through a zipper effect.^{111b} Others have attributed collapsed structures to high pressure during the reaction.¹²¹ Collapsed nanotubes with twisted structures have also been observed with multi-walled CNTs (MWCNTs) in other studies.^{111b, 121a} Lattice registration between opposing walls is thought to be responsible for the twisted phenomenon: the interaction between the two paralleled graphene walls (innermost walls in the DWCNTs, TWCNTs and MWCNTs) tends to achieve the lowest energy AB stacking via the translations along radial and

axial directions. Thus, achievement of more favorable interlayer registry acts as driving force for twisting or warping of collapsed nanotubes.

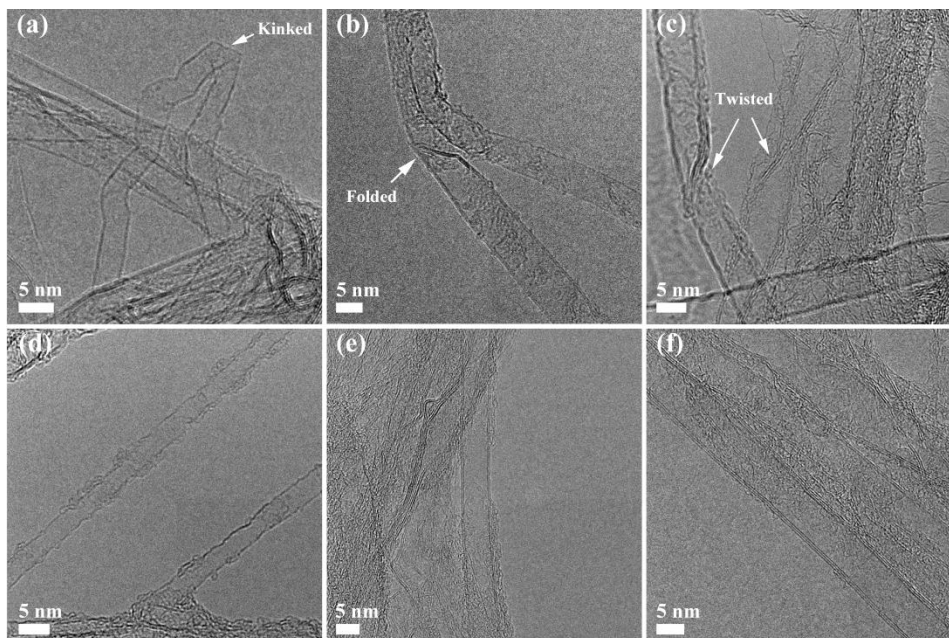


Figure 5.4 TEM images of the collapsed and uncollapsed CNTs.

(a), (b) and (c) TEM images for collapsed SWCNT, DWCNT and TWCNT, respectively. (d), (e) and (f) TEM images for uncollapsed SWCNT, DWCNT and TWCNT, respectively. Kinked, folded and twisted deformation parts are shown in collapsed nanotubes, indicating they are collapsed to corresponding bi-layer, four-layer, six-layer and multi-layer closed edge graphene nano-ribbons. The uncollapsed nanotubes are identified by their straight geometry, with typically smaller diameters than that of collapsed nanotubes.

As shown in Figure 5.5(b), the presence of the twisted collapsed nanotubes is usually observed to be freestanding, which suggests the translations between the innermost two walls achieves a favorable lattice stacking which prevents the twisted ribbon from untwisting.¹¹⁵ In order to better understand the difference of the structural characteristics between the collapsed and uncollapsed nanotubes in the TEM images, TEM pictures of the uncollapsed SWCNT, DWCNT and TWCNT are also provided in Figure 5.5 (d-f) for comparison with the collapsed ones. We have assumed that the uncollapsed nanotubes are observed as straight structures

without kinks and bends. The diameters of the uncollapsed SWCNT, DWCNT and TWCNT are observed to be 3.6 nm, 6.3 nm and 7.1 nm, respectively, smaller than the observed widths of the collapsed nanotubes as expected. These structural and morphological features of the collapsed and uncollapsed nanotubes are utilized to distinguish these two counterparts during collection of their counts and performing the statistics detailed in the following discussion. More TEM pictures showing the collapsed nanotube features are provided in Figure 5.6.

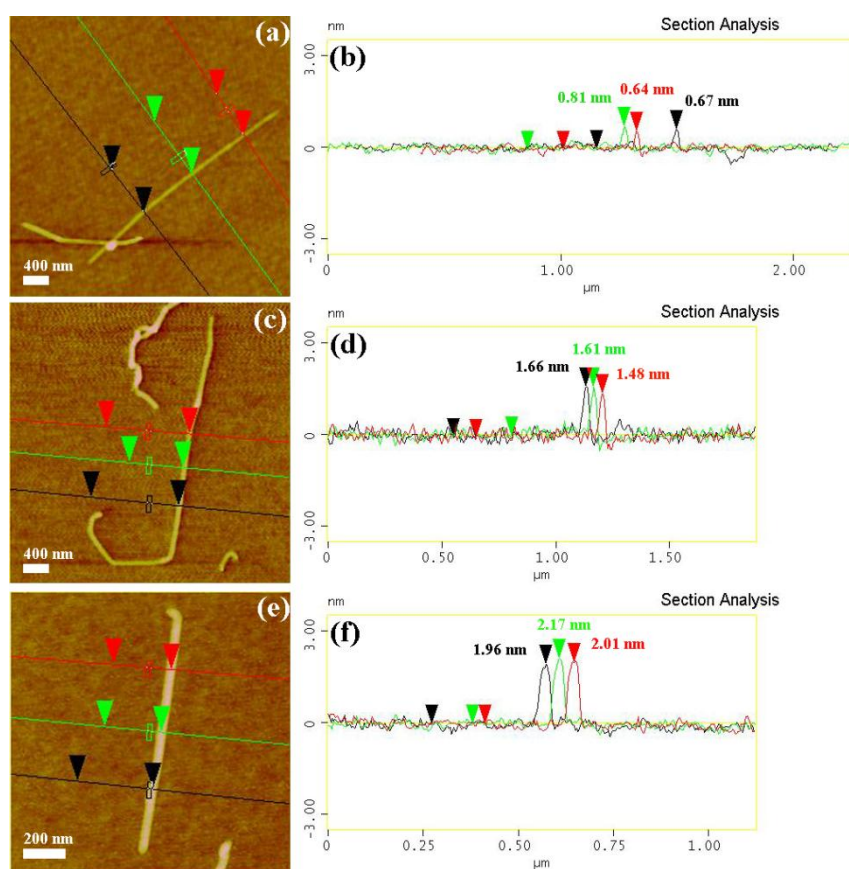


Figure 5.5 AFM height measurements of the collapsed CNTs.

(a), (c) and (e) AFM images of collapsed SWCNT, DWCNT and TWCNT. Ribbon-like structures are shown in AFM images. (b), (d) and (f) The height profiles of the corresponding collapsed SWCNT, DWCNT and TWCNT. Height measurements were taken along the corresponding colored lines indicated in the AFM images.

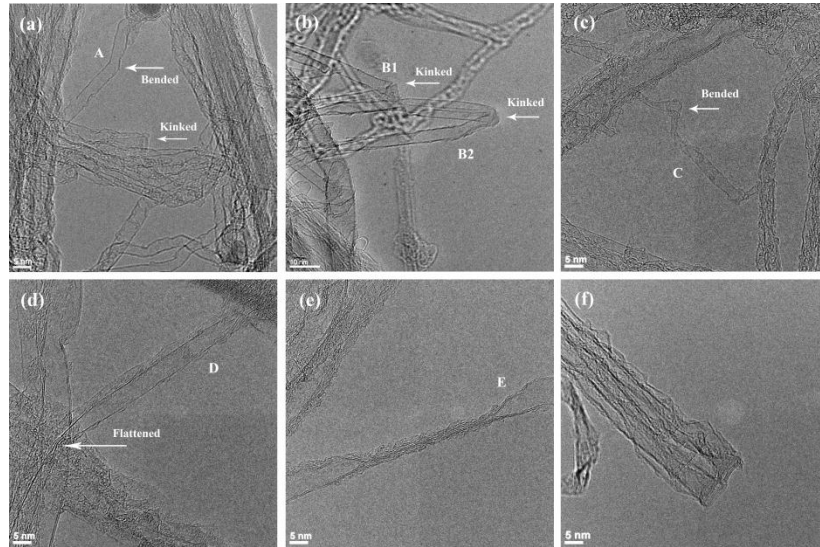


Figure 5.6 HRTEM images of the collapsed nanotubes.

(a), (b), (c), (d) Collapsed SWCNTs with bended, kinked and flattened features in their structures, as noted by the arrows. The widths of CE₂GNRs as noted by A, B1, B2, C and D in images are measured to be 3.5 nm, 4.1 nm, 4.1 nm, 3.2 nm and 5 nm, respectively. After conversion into cylindrical diameters using equation provided in Fig. 5b, their original diameters are 2.4 nm, 3.4 nm, 3.4 nm, 2.1 nm and 3.3 nm, respectively, which are around D_{eq}^{exp} for CE₂GNR 2.64 nm. (e) A center-flattened collapsed DWCNT with cantilevered shape. More than four layers can be observed in the center-flattened region. The extra lattice planes might be attributed to the appearance of the bulbs on only one side of the tube image. The width of CE₄GNR as noted by E in image is measured to be 7.2 nm. Likewise, its original after conversion is 4.9 nm, larger than D_{eq}^{exp} for CE₄GNR 4.02 nm. (f) Cross-sections of two collapsed TWCNTs with 'dog-bone' geometries.

Tapping-mode AFM was used to study the collapsed structure of carbon nanotubes. A suspension of nanotubes was prepared by bath sonication in dichloroethane solution. Subsequently, a drop of the suspension was spin-coated onto the surface of a cleaned silicon wafer and dried at room temperature. The sample was analyzed by AFM (Digital Instruments, Nanoscope III Veeco Metrology Group, Santa Barbara, CA) using a TETRA 15/Au tip (K•TEK Nanotechnology LLC, Digital Instruments). The number of walls of a collapsed nanotube is defined from the height measurement information. It is known that the height of single graphene layer is around 0.34 nm, which is also the interlayer distance of graphite. Thus we infer that the

heights of the fully collapsed SWCNT (bi-layer graphene), DWCNT (four-layer graphene), TWCNT (six-layer graphene) and four-walled nanotube (eight-layer graphene) are around 0.7 nm, 1.4 nm, 2.0 nm and 2.7 nm, respectively, which we use for the following estimation of the number of walls for collapsed nanotubes. Our approximation is consistent with the definition for number of layers reported by Yu *et al.*¹²² Shown in Figure 5.5 (a-c) are AFM height images of a collapsed SWCNT, DWCNT and TWCNT, respectively. Their corresponding height profiles are presented in Figs. 3b, d and f. Images are shown in same height scale on each nanotube. The heights were measured along the correspondingly lines marked at three different set points along the nanotube length. The length of collapsed nanotubes in these images are typically 1~2.5 μm , much shorter than the CNT carpet height, probably due to cutting off during the sonication process. As shown in Figure 5.5 (b), the heights in three different regions are 0.6 nm, 0.8 nm and 0.7 nm, respectively, corresponding to two closely stacked graphene layers. Height averaging along the length of the nanotube with a SIMAGIS software package (Carbon Nanotube Length, Height, Curvature, and Aspect Ratio Analysis. Ver. 2. Nanotechnology. Smart Imaging Technologies, Houston, Texas) provides an average height of 0.7 nm. (More detailed information on measuring average height of nanotube by SIMAGIS can be founded in Figure 5.7 and Table 5-2) This strongly indicates that the SWCNT has fully collapsed into a closed edged bi-layer graphene nano-ribbon. A collapsed DWCNT with a length of $\sim 3 \mu\text{m}$ is shown in Figure 5.5 (c), and the deformed parts that change the orientations of the nanotube are visible. The AFM section analysis shows the height of the nanotube is in the range of 1.4 to 1.7 nm, and a SIMAGIS average measurement gives an average height of ~ 1.3 nm, consistent with the height of a flattened DWCNT. When measuring a collapsed TWCNT, the AFM section analysis and a SIMAGIS measurement give an average height of 2.1 nm, which is consistent with the height of

a fully collapsed TWCNT. The contrast variation shown in each AFM height image (Figure 5.5 (a, c and e)) is also consistent, indicating the additional carbon layers in the collapsed DWCNTs and TWCNTs.

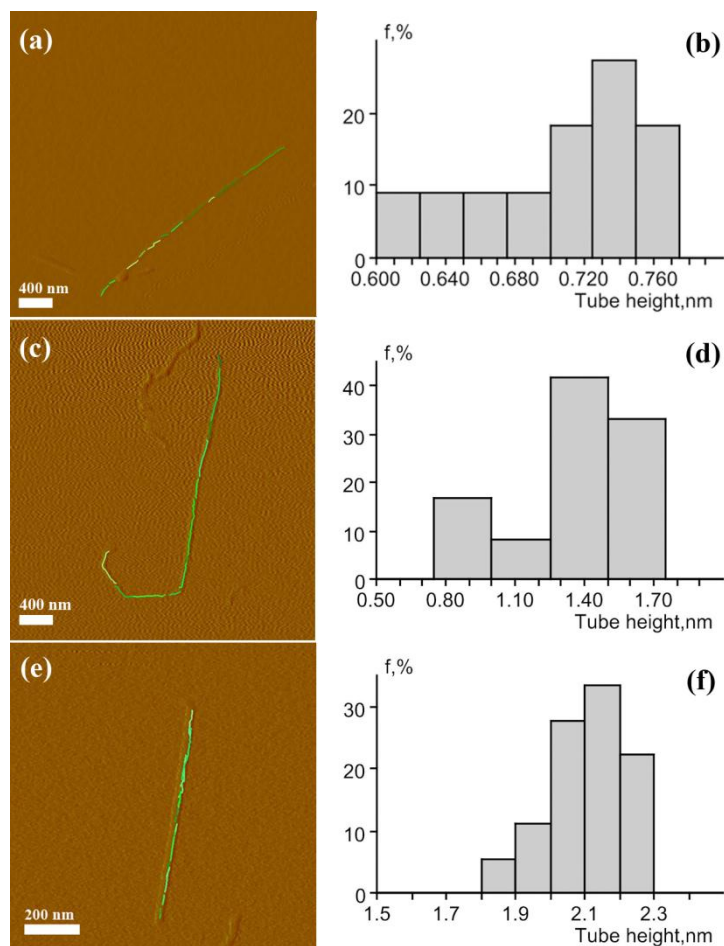


Figure 5.7 Height measurement of carbon nanotube using AFM.

Nanotube height averaging along the length measured by a SIMAGIS software package (Carbon Nanotube Length, Height, Curvature, and Aspect Ratio Analysis. Ver. 2. Nanotechnology. Smart Imaging Technologies, Houston, Texas). After importing the original AFM image, SIMAGIS is able to divide the entire nanotube length into a number of short tube sections on CE₂GNR (a), CE₄GNR (c) and CE₆GNR (e). The derived statistics of the average height distribution of sections for corresponding CE₂GNR (b), CE₄GNR (d) and CE₆GNR (f) measured by SIMAGIS software.

Table 5-2 Detailed information in the height measurements of the collapsed structures (CE₂GNR, CE₄GNR and CE₆GNR) shown in Figure 5.7 provided by SIMAGIS software package

Analyzed tube	Number of divided tubes	Minimum height (nm)	Maximum height (nm)	Average height (nm)	Standard deviation
CE ₂ GNR	11	0.61	0.77	0.71	0.05
CE ₄ GNR	12	0.79	1.69	1.33	0.29
CE ₆ GNR	18	1.81	2.28	2.10	0.12

5.3.2. Fitting the size distribution of SWCNT and DWCNT

According to the structural identifiers for distinguishing the two different structures, we collected the total counts of collapsed and uncollapsed SWCNTs and DWCNTs from hundreds of HRTEM images. Coexistence of collapsed and uncollapsed structures can usually be found in one image. Sum counts of 641 SWCNTs have been collected, in which the collapsed and uncollapsed SWCNTs account for 44% and 56%, respectively. Likewise, 650 DWCNTs have been counted, in which the collapsed and uncollapsed DWCNTs account for 53% and 47%, respectively. The fitting curves for the size distribution of the uncollapsed nanotubes (diameters of SWCNTs or DWCNTs) and the collapsed nanotubes (measured width of CE₂GNR or CE₄GNR) are plotted in Figure 5.8.

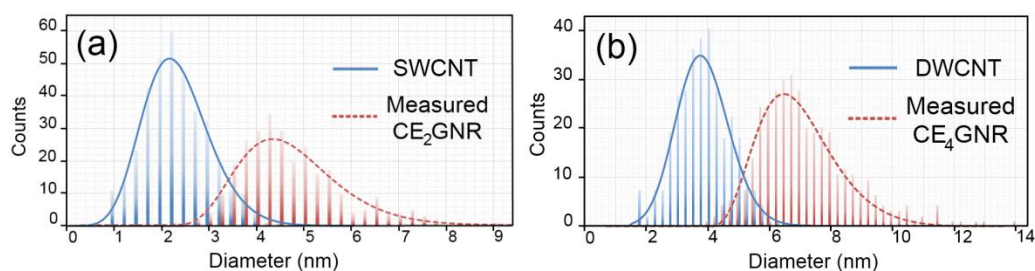


Figure 5.8 The fitting curves for the size distribution of the collapsed and uncollapsed nanotubes. **(a)** Size distribution of uncollapsed SWCNTs (diameters) and collapsed SWCNTs (CE₂GNR). **(b)** Size distribution of uncollapsed DWCNTs (diameters) and collapsed DWCNTs (CE₄GNR). Column bars showing the counts versus diameters of each structure are fitted by the corresponding colored curves (blue and solid line for the uncollapsed structures, red and dash line for the collapsed structures).

In order to convert the widths of the collapsed SWCNTs and DWCNTs to the diameters of its uncollapsed state, we generated collapsed and uncollapsed SWCNTs with different diameters and optimized the geometry using molecular dynamics simulations implemented in LAMMPS (shown in Figure 5.9 (a)). The Van der Waals interaction energy reaches a maximum when the distance of two opposing walls get close to 0.34 nm (as shown in the inset in Figure 5.9 (a)), which is the interlayer spacing of adjacent sheets in a graphite crystal. The height of the highly strained bulbs on the two edges is found to be a constant around 0.49 nm independent of the initial nanotube diameter (Figure 5.9 (a)), which is comparable to the diameter of C60 (0.7 nm).¹²³ Therefore, the width of the fully collapsed structure is linearly dependent on the width of the flattened region which is set by its diameter as a cylinder. Using optimized geometries we found linear relationship between the width of collapsed form and diameter of cylindrical form of the free standing SWCNTs (Figure 5.9 (b)). The same procedure was performed for SWCNT

and DWCNT on a substrate (as a model of a substrate we used a graphene plane for simplicity).

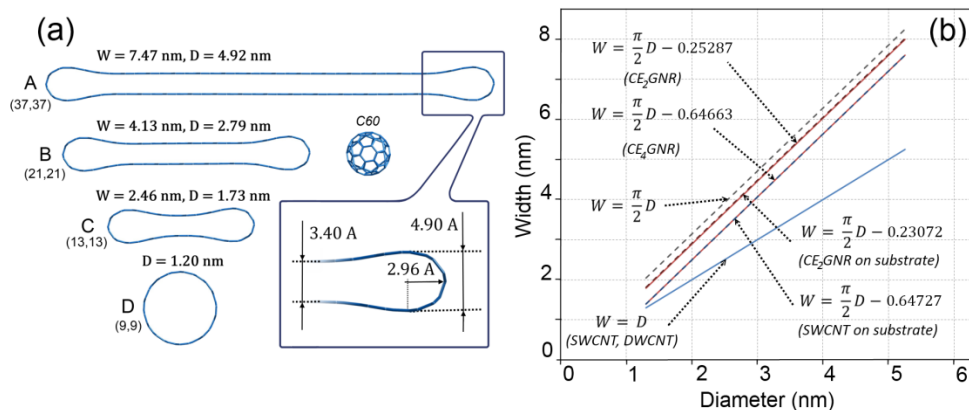


Figure 5.9 Linear relationship between the width of collapsed form and diameter of cylindrical form of the free standing SWCNTs.

(a) Uncollapsed and collapsed SWCNTs with different diameters in free space generated by LAMMPS molecular dynamics simulation. The geometry of a collapsed SWCNT consists of two highly strained bulbs on the two edges and a collapsed region where the two opposing walls are flattened and stabilized due to the Van der Waals interaction, leaving the interlayer distance as 3.4 Å. The heights of the two edged bulbs are found to be a constant around 4.9 Å independent of initial diameter of the nanotube. The height of the bulb is comparable in size to C60 molecular. (b) The linear relationships between measured width (W) and original cylindrical diameter (D) for uncollapsed and collapsed structures in free space ((SWCNT, DWCNT), (CE_2GNR) and (CE_4GNR)) and on a substrate ((SWCNT on substrate) and (CE_2GNR on substrate)) are shown by the straight lines and their corresponding equations. For simple comparison, a conversion equation of $W = \pi D/2$ is given if the formation of highly strained bulbs is not taken into account.

Using those equations, the measured widths of collapsed SWCNTs and DWCNTs in Figure 5.1 were converted into the diameters in their uncollapsed state. Figure 5.11 shows the resulting distribution of diameters of collapsed and uncollapsed SWCNTs and DWCNTs and their sum. The cross-section point of the fitting curves of uncollapsed and collapsed structures is taken to represent the equivalent energy point (referred to as D_{eqe}^{exp}), at which there is no energy difference between the collapsed and uncollapsed nanotube. Below D_{eqe}^{exp} , the cylindrical tube is the energetically favorable geometry, whereas the

collapsed structure becomes energetically more stable when the diameter is above $D_{\text{eqe}}^{\text{exp}}$ because the Van der Waals force between two walls will exceed bond bending stiffness. The $D_{\text{eqe}}^{\text{exp}}$ values for SWCNT and DWCNT are found to be 2.6 nm and 4.0 nm, respectively, from our experimental fitting. This determination of equal energies for the two structures assumes that they are in thermodynamic equilibrium with each other. It is also likely that the equilibrium temperature is close to the growth temperature, 750°C, with the respective structure populations frozen by the rapid cooling of the sample. It is possible that the measured equivalent energy point is affected by the experimental miscounting of uncollapsed nanotubes since a collapsed tube can appear straight in TEM images. A sensitivity check of the energy equivalence point to miscounting was carried out by assuming that miscount of nanotubes may have occurred for nanotubes greater than 1.5 nm with the miscount increasing linearly by diameter up to 50% at a diameter of 6 nm. For this degree of miscounting the energy equivalence point was found to decrease by only 0.1 nm. Calculations for different miscounts are shown in Figure 5.10.

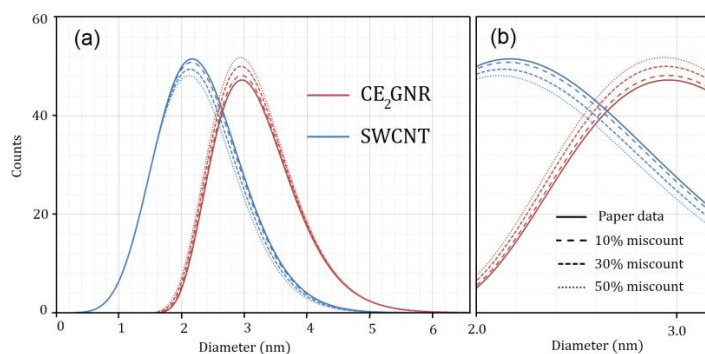


Figure 5.10 Calculations for different miscounts.

(a) Variation of $D_{\text{eqe}}^{\text{exp}}$ for CE₂GNR with the increase of the percentage of the miscount for uncollapsed and collapsed SWCNTs, which might be caused by the misidentification from the TEM

images. (b) Closed-up image of the cross-section region in (a) clearly shows $D_{\text{eqe}}^{\text{exp}}$ doesn't change much from the value indicated in the manuscript which is shown by the cross-section point of the solid lines.

The structures corresponding to the diameters shown by A, B, C and D in Figure 5.11 (a) can be found in Figure 5.9 (a). Larger critical diameter for DWCNT than that for SWCNT can be interpreted from an energy point of view. Upon collapsing, the graphitic layers will increase their bending energy by forming the two-edged highly strained bulbs at the expense of the attractive Van der Waals energy obtained by the innermost walls. The increase of the deformation energy from forming bulbs happens to each graphitic layer, whereas only the innermost walls gain the attractive energy. Therefore, the compensation to the increase of the deformation energy requires the increase of the D_{eqe} with increasing the number of walls.^{111b, 111i} The fractions of the uncollapsed and collapsed SWCNTs and DWCNTs versus their diameters are shown on the top in Figure 5.11 (a) and (c), from which we can tell the population changing of the uncollapsed and collapsed structures below and above the $D_{\text{eqe}}^{\text{exp}}$. Moreover, given a certain diameter, the fraction of each structure as part of the sum is shown.

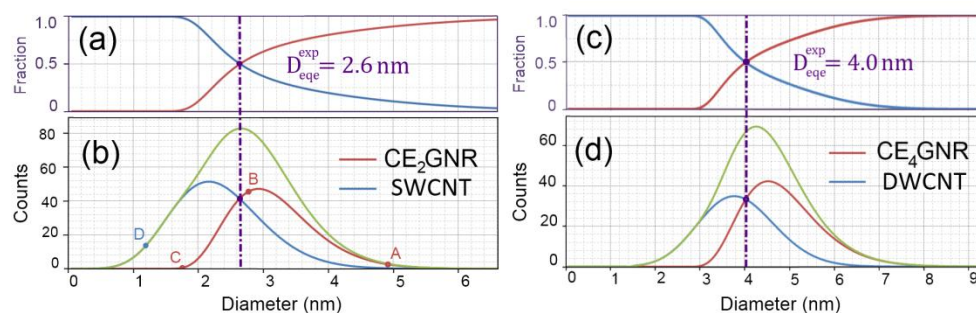


Figure 5.11 Fraction of uncollapsed and collapsed SWCNT (a) and DWCNT (c) versus diameters in the sum (b, d).

The resulting diameter distributions of uncollapsed (SWCNT and DWNT shown by blue fitting curves) and collapsed structures (CE₂GNR and CE₄GNR shown by red fitting curves) and their sum (shown by green fitting curves) after conversion of measured widths of the collapsed structures into the cylindrical diameters using the equations for CE₂GNR and CE₄GNR shown in Figure 5.9 (b). Cross-section point of the fitting curves for uncollapsed and collapsed structure corresponds to the critical diameter (D_{eqe}^{exp}) ('exp' represents that the diameter is obtained from experimental data, 'eqe' represents the equivalent energy point), above which the collapsed form of SWCNT or DWCNT is energetically favorable. From the fitting of our experimental data, the D_{eqe}^{exp} s for SWCNT and DWCNT are found to be 2.6 nm and 4.0 nm, respectively.

Using molecular dynamics with AIREBO potential (torsion term excluded to gain reasonable bending modulus of $k=1.4$ eV) we performed energy calculations for collapsed and uncollapsed tubes of different diameters, as shown in Figure 5.12. The energy of Van der Waals interaction can be adjusted (in our simulations it was represented by depth of minima of Lennard-Jones potential) in order to match D_{eqe}^{cal} with D_{eqe}^{exp} . It was found that value of $\epsilon_{vdw} = 54$ meV/pair is the best to achieve this goal. For DWCNT we used the same parameters as for SWCNT and obtained good agreement with experimental data. The calculated energy changing of uncollapsed and collapsed structure around the equivalent energy point is consistent with other studies.^{111d, 111f, 111j}

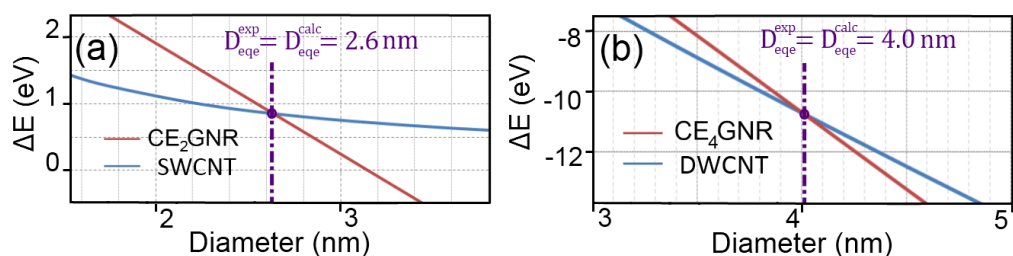


Figure 5.12 Energy calculations for collapsed and uncollapsed tubes.

Calculated energy for uncollapsed and collapsed SWCNT (a) and DWCNT (b) with different diameters in free space by performing LAMMPS molecular dynamics with AIREBO potential (no torsion term). The energies of uncollapsed SWCNT and DWCNT are shown by blue curves, and the energies of collapsed SWCNT and DWCNT are shown by red curves. By using van der Waals interaction energy $\epsilon=53.6$ meV/pair, the calculated diameter $D_{\text{eqe}}^{\text{cal}}$ ('cal' represents the diameter that is obtained from calculation, 'eqe' represents the equivalent energy point) corresponds very well to the $D_{\text{eqe}}^{\text{exp}}$ for both SWCNT and DWCNT.

Energy calculations are also performed for the SWCNT on a single-layer graphene substrate. The $D_{\text{eqe}}^{\text{cal}}$ for it was found to be 1.9 nm, smaller than that of SWCNT in free space, which suggests that the substrate enhances the stability of the collapsed structure, consistent with the results reported by Yu *et al.*¹²² As shown in the upper geometry in Figure 5.12, the Van der Waals interaction between the cylindrical SWCNT and substrate can distort its circular shape and induce a radial deformation. On the other hand, the rigid circular shape still tends to be maintained to the maximum extent at smaller tube diameters. The interplay between the surface Van der Waals interaction and the rigid bond bending stiffness results in a partial collapsed and elliptical geometry.^{111c} The heights of the edged bulbs of the fully flattened SWCNT on a substrate are found to be 0.75 nm from the substrate surface, which is about twice of the height of a single-layer graphene on substrate.

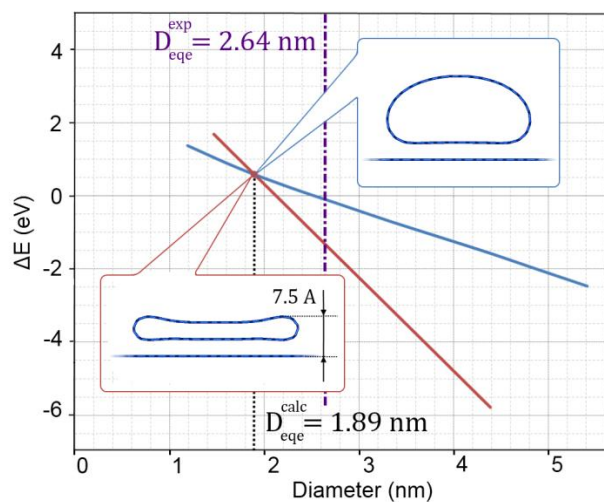


Figure 5.13 Calculated energy for uncollapsed and collapsed SWCNT on a single-layer graphene substrate.

$D_{\text{eqe}}^{\text{cal}}$ of SWCNT on a substrate is around 1.89 nm, smaller than the $D_{\text{eqe}}^{\text{exp}}$ of SWCNT in free space. Energies of uncollapsed and collapsed SWCNT on a substrate versus diameters are shown by blue and red lines, respectively. Correspondingly, their uncollapsed and collapsed geometries are also shown next to the energy curve.

Figure 5.14 shows the diameter distributions of SWCNT, DWCNT and catalyst particles. The particles playing the catalytic role in growing nanotubes are iron particles reduced from the metal oxide state. Their size distribution is calculated for the iron only size from the metal oxide particle size distribution and percent of iron in the oxide and the density of Fe (7.8 g/ml) and AlFe_2O_4 (4.6 g/ml). Compared to the initial monodisperse nanoparticles, the broadened size distribution of the SWCNTs and DWCNTs is a strong indication that Ostwald ripening, where some particles grow larger and some smaller, takes place during the pre-heating, reduction and growth process. Also clearly, the growth of double-walled nanotubes is strongly favored at larger diameters.

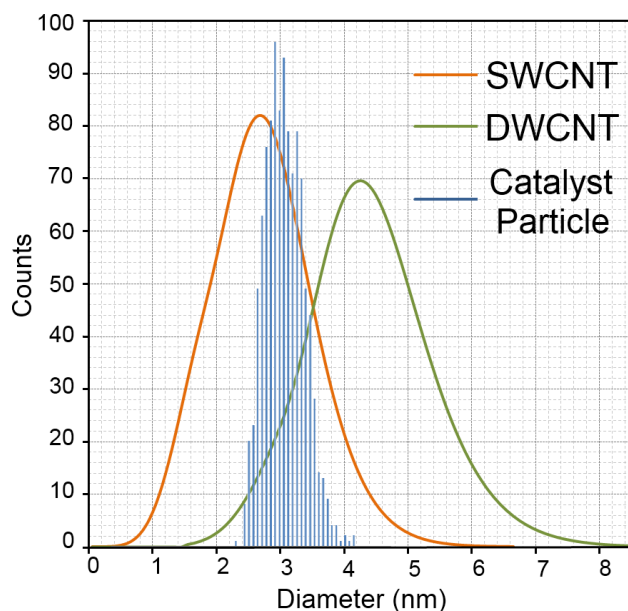


Figure 5.14 Size distributions of the catalyst particles, sum of the SWCNTs and sum of the DWCNTs. Size distribution of iron only catalyst particles (Fe) is obtained from that of the metal oxide particles (AlFe_2O_4).

5.4. Conclusion

In summary, large diameter few-walled carbon nanotubes (CNTs) have been produced using nearly mono-dispersed preformed aluminum ferrite nanoparticles with an average diameter of 4.0 ± 0.4 nm. CNTs with sufficiently large diameter are observed to collapse into closed edged graphene nano-ribbons (CE_xGNR), including collapsed SWCNT, DWCNT and TWCNT). TEM characterization of CE_xGNR , collapsed versus uncollapsed used the presence of kinked, folded or twisted deformations as an indicator that a carbon nanotube has collapsed into a ribbon-like structure, while uncollapsed are identified by a lack of such structures and are typically observed to be straight. Using the structural identifiers, diameters and measured widths of abundant collapsed and

uncollapsed SWCNT and DWCNT have been collected from TEM images. By experimentally fitting the size distribution and computationally calculating the energy of the uncollapsed and collapsed SWCNT and DWCNT, a zero energy difference between the two forms for SWCNT and DWCNT is found at 2.6 nm and 4.0 nm, respectively, with the assumption equilibrium between the two states. Theory also indicates that the D_{eqe} is even smaller for tubes sitting on a surface, i.e. 1.9 nm for a SWCNT sitting on a graphene surface. The assignment of equal energy for the two structures at a diameter where the populations of both are equal makes the assumption that the two structures are in thermodynamic equilibrium at a temperature that is likely to be near the growth temperature of 750°C since the sample is rapidly cooled to room temperature from the growth temperature. This also assumes that the population change of the uncollapsed and collapsed SWCNT and DWCNT around the equal energy diameter provides a measure of the fraction of each structure for specific diameters at the growth temperature.

Of significant interest is that collapsed nanotubes provide a route to well-defined two, four etc. layered graphene nano-ribbons with a well-defined edge. It is of great interest and a considerable challenge to further experimentally characterize the CE_xGNTs electrically and optically and determine whether the original chirality of an uncollapsed tube influences the properties of the collapsed graphene nano-ribbon. Because the edges are highly strained it is also likely that one can selectively functionalize the edges to further effect interesting electrical and optical changes.

Chapter 6

High Temperature Decomposition of Cerium Precursors to Form Cerium oxide nanocrystals

6.1. Introduction

Cerium oxide (ceria, CeO_2) is a rare earth metal oxide with a cubic fluorite structure that contains ceria in two different oxidation states, Cerium (III) and Cerium (IV). This mixed valency is thought to arise from surface defects which can store, release and transport oxygen and oxygen vacancies, a set of properties that has led ceria to be referred to as an “oxygen buffer”.^{2a, 21, 124} Nanocrystalline ceria finds application in commerce as an ultraviolet absorber, oxygen ion conductor, solar cell, and anode for solid oxide fuel cells.^{22a, 54} Recently, the oxygen buffering capability of ceria has been shown to protect biological systems from oxidative stress and radiation damage.^{31, 56, 61a,}

^{61g, 66-67, 125} The Cerium (III) presumably available at nanoparticle surfaces reacts with reactive oxygen species in water; over time, and in some cases quite slowly, the Cerium (IV) reverts back to its original state in a manner suggestive of a catalytic process.^{31, 61a, 66, 125a-d}

Both the surface passivation chemistry and Cerium (III) content of nanocrystals can greatly influence their anti-oxidation properties.^{31, 67, 125c} Studies of these structure-function relationships have to date relied on nanoparticles of ceria formed in aqueous solutions via either coprecipitation, microemulsion or hydrothermal routes.^{31, 55-56, 61a, 61g, 66-67, 125} Tarnuzzer *et al* prepared cerium oxide nanoparticles from 2 to 5nm and showed they could protect against radiation induced cell damage.^{61a} Chen *et al* used similarly prepared cerium oxide nanoparticles to prevent retinal degeneration caused by reactive oxygen intermediates.^{125d} Later, various surface agents (e.g. Dextran, polyacrylic acid (PAA), polyethylene glycol (PEG)) were used to sterically stabilize cerium oxide nanoparticles in the most relevant biological media.^{66-67, 125e} Changes in the antioxidant properties of the materials were noted as the surface chemistry was altered; coatings on particles can in principle interfere with the electron transfer between surface Cerium (III) and solution oxidants. Few studies have comprehensively examined the role of nanoparticle size on antioxidant properties. However, comparisons between two different sizes of ceria suggest smaller materials are more reactive, presumably because they contain more Cerium (III).⁵⁵

Systematic studies of the role of nanocrystal size, shape, and surface chemistry in the antioxidant properties of ceria require the development of uniform materials with broadly tunable features. One route to forming such libraries is through the thermal

decomposition of ceria precursors in organic solvents. At temperature in excess of 200 °C, these precursors decompose to form ceria particles that are non-aggregated, uniform ($\sigma < 10\%$) and highly crystalline.^{17, 126} The molar ratio of cerium starting material to surfactant has a moderate influence on nanoparticle size as well as shape.³³ Gu *et al* synthesized 5 to 20 nm diameter ceria nanocrystals from cerium oleate and oleic acid in various solvents at high temperature.^{32a} With the addition of oleylamine, Wang *et al* showed that the same could yield flower-shaped and cube-shaped cerium oxide nanocrystals.³⁴ Ahniyaz *et al* reported larger dumbbell and rod-shaped ceria using cerium oleate and octadecylamine.³⁵ To produce material libraries for antioxidant studies, however, requires new reaction conditions optimized in particular for spherical, and larger ($d > 8$ nm) crystallites.

One outstanding question is whether nanocrystalline ceria formed in the processes described above can be applied as an antioxidant in water. One issue is whether these materials contain sufficient Cerium (III) to react with species such as peroxides; while the precursors can contain both Cerium (III) and Cerium (IV), the oxidation states of ceria in the particles synthesized by high temperature metal precursor decomposition in organic media has never been reported. Also, because the crystallites nucleate and grow in organic solutions they must be phase transferred into water for biological applications; such a phase transfer is in principle not difficult as many similar metal oxide nanocrystals have been shown to generate stable, aqueous suspensions after treatment with the appropriate surface agent.^{3a, 63} However, after such a transfer process the inorganic ceria interface will be covered with an organic coating and a layer of tightly bound surfactant (e.g. oleylamine). This organic interface could preclude electron transfer between

oxidants in solution and the cerium (III) at the nanoparticle surface, rendering the materials effectively inert. Indeed, such an explanation is generally offered to explain the reduced cytotoxicity of nanocrystalline ceria.^{66, 125c, 125i}

Here we report that nanocrystalline ceria produced from the thermal decomposition of cerium precursors can act as an antioxidant in aqueous suspensions. Materials were produced from several cerium precursors, and through the addition of co-surfactants and water it was possible to form crystallites from 3 to 10 nanometers in diameter. The Cerium (III) content of these nanocrystals synthesized by high temperature decomposition of cerium precursors in organic media was measured for the first time, and was comparable to those found for ceria formed directly in water. Like other metal oxides formed in similar routes, these nanocrystalline ceria materials could be efficiently transferred into water using phase transfer agents. These water suspensions remained clear and homogeneous even after Cerium (III) at the particle surface reacted with hydrogen peroxide. The extent of the Cerium (III) conversion to Cerium (IV) depended on the initial concentration of Cerium (III) in the nanocrystals. These data suggest that nanocrystalline ceria formed from the thermal decomposition of precursors in organic solutions may be suitable for biological applications. Additionally, the uniformity of the products offers materials that can be used to probe how nanocrystal structure may affect antioxidant and toxicological behavior.

6.2. Experimental Methods

6.2.1. Chemicals

Cerium(III) nitrate hexahydrate ($\text{Ce}(\text{NO}_3)_3 \cdot 6\text{H}_2\text{O}$ (99 %), cerium acetylacetonate hydrate ($\text{Ce}(\text{acac})_3$), cerium (IV) hydroxide ($\text{Ce}(\text{OH})_4$), oleic acid (technical grade, 90 %), oleylamine (technical grade, 70%), octadecylamine (technical grade, 90 %), 1,2-hexadecanediol (HDD, technical grade, 90 %), 1-octadecene (ODE, technical grade, 90 %), poly (acrylic acid) (PAA, $M_w = 1800$), and octylamine (99 %) were purchased from Sigma-Aldrich; Sodium bicarbonate and dimethylformamide (DMF) were purchased from Fischer Scientific; 1-ethyl-3-[3-dimethylaminopropyl]carbodiimide hydrochloride (EDC) was purchased from Thermo Scientific; H_2O_2 (30 % (w/w)) and HNO_3 were purchased from Fisher Scientific. All ceria nanocrystals were synthesized under ultrahigh purity nitrogen. The CellTiter 96(R) Aqueous One Solution Cell Proliferation Assay (MTS assay, Promega) was used as received.

6.2.2. Instrumentation

6.2.2.1. X-ray diffraction (XRD), X-ray photoelectron spectroscopy (XPS), and small angle X-ray scattering (SAXS)

X-ray powder diffraction (XRD) patterns were recorded using a Rigaku D/Max Ultima II with a zero-back ground sample holder. 2θ range was from 10 to 80 degree with a $\text{Cu K}\alpha$ radiation (1.54 \AA). The X-ray was generated at 40 kV and 40 mA. XPS data were collected using a PHI Quantera XPS with a monochromatic Aluminum 38.6 W

X-ray source and 200.0 μm X-ray spot size with a pass energy of 26.00 eV at 45.0°. Small angle X-ray scattering analysis was conducted by RIGAKU SMARTLAB. 0.8 mm diameter capillary tube was used for sampling, and data was collected at 2θ range from 0.15 to 4 degrees with Cu $K\alpha$ radiation.

6.2.2.2. Dynamic light scattering (DLS) analysis

The hydrodynamic diameters of cerium oxide nanocrystal with various sizes coated with PAAOA and OA was measured. Cerium oxide nanocrystals in pH 7 and 9 solutions were analyzed with Malvern Nano ZS system by Malvern Instruments (Malvern Zetasizer Nanoseries, Malvern, UK) operated at 25 °C. All average size was obtained over 3 times with minimum intensity of 200,000 cps.

6.2.2.3. Transmission Electron Microscope (TEM)

TEM specimens were made by evaporating one drop of cerium oxide nanocrystal solution onto ultrathin carbon type-A 400 mesh copper grids (Ted Pella Inc.). The TEM micrographs were taken by a JEOL 2100 field emission gun TEM operating at 200 kV with a single tilt holder. The size and size distribution data were obtained by counting >1000 nanocrystalline particles using Image-Pro Plus 5.0 (Media Cybernetics, Inc., Silver Spring, MD). With large sampling sizes, both average size and size distributions are only minimally affected by population size.⁸⁴

6.2.2.4. Inductively coupled plasma atomic emission spectroscopy (ICP-AES)

To measure the cerium concentration of water-soluble cerium oxide nanocrystal, ICP-AES was carried out using a Perkin Elmer ICP-AES instrument equipped with autosampler. ICP-AES samples were prepared by digestion of aqueous fractions using HNO₃ (99 %) and H₂O₂ (30 %) in a 5 ml of diluted cerium oxide nanocrystal sample. In all cases, cerium oxide nanocrystal ICP samples were 500 times diluted solution. The solution volume was decreased by heating (approximately 100 °C) to a fourth of its original volume. When the solution was dried to about 1/4 volume, 100µl nitric acid was added. The obtained sample was treated with further addition of 50 µl of nitric acid and 1 ml of H₂O₂ until effervescence was minimal, indicating full dissolution and ionization of the ceria. The resulting colorless solution was transferred into a 5 ml volumetric flask and then diluted to 5 ml using deionized water.

6.2.3. Synthesis of Cerium oxide nanocrystal: precursor effect

6.2.3.1. Cerium oxide nanocrystal from Ce(acac)₃

Ce(acac)₃ (0.437 g, 1.0 mmol), 1,2-hexadecanediol (1.292g, 5.0 mmol), and oleylamine (0.802g, 3.0 mmol) were mixed in 5.0 g of ODE at room temperature. The solution was stirred at 80 °C for 30 min and then heated to 315 °C for 2 h. Ceria nanocrystals were formed at 280 °C, and the narrowest distribution ($\sigma < 10\%$) was found at 315 °C.

6.2.3.2. Cerium oxide nanocrystal from Ce-oleylamine

Cerium oleate was prepared from a mixture of $\text{Ce}(\text{NO}_3)_3 \cdot 6\text{H}_2\text{O}$ (4.34 g, 10.0 mmol) and oleylamine (8.02 g, 30.0 mmol) in 20 g of ODE at 80 °C for 3h. The resulting yellow precipitate was washed using ethanol, acetone and dissolved in hexane. Cerium oxide nanocrystal was synthesized using cerium oleate precursor (5.0 ml, $[\text{Ce}] = 5.0 \text{ mg/ml}$) with varying amounts of oleylamine (from 0.5 to 4.0 mmol) in 5.0 g of ODE at 260 °C for 2 h.

6.2.3.3. Cerium oxide nanocrystal from $\text{Ce}(\text{NO}_3)_3 \cdot 6\text{H}_2\text{O}$

$\text{Ce}(\text{NO}_3)_3 \cdot 6\text{H}_2\text{O}$ was also used for near-spherical cerium oxide nanocrystal. $\text{Ce}(\text{NO}_3)_3 \cdot 6\text{H}_2\text{O}$ (0.434 g, 1.0 mmol) and oleylamine (0.802 g, 3.0 mmol) were added to 4.0 g of ODE at room temperature. The mixture was stirred at 80 °C for 30 min until a clear brownish yellow solution was formed. The resulting solution was then heated to 260 °C for 2 h. The size of cerium oxide nanocrystal increased modestly (e.g. 1 nm) as the temperature (from 230 to 300 °C) and the heating time (from 1 to 6 h) increased. A higher concentration of cerium-oleylamine monomer, as well as the addition of water and octadecylamine (from 1.5 to 15 mmol) provided the best control over the final crystallite sizes.

6.2.3.4. Cerium oxide nanocrystal from Ce(OH)₄

Ce(OH)₄ (0.16 g, 1 mmol) was mixed with oleylamine (0.802 g, 3.0 mmol) in 4.0 g of ODE at room temperature. The mixture started dissolving after 180 °C and changing color to pale purple at 260 °C. This colloidal solution was heated at 260 °C for 2 h. The synthesized nanocrystals were polydisperse.

6.2.4. Synthesis of Cerium oxide nanocrystal: concentration of monomer effect

The molar ratio between Ce(NO₃)₃·6H₂O and surfactants (oleylamine and/or octadecylamine) was fixed at 1:3. The high molar concentration of cerium nitrate hexahydrate (from 1.0 to 10.0 mmol) and oleylamine (from 3.0 to 30.0 mmol) was mixed in 10 g of ODE at 80 °C for 30 min, forming a brownish yellow mixture. After that, the temperature was increased to 260 °C for 2 h.

6.2.5. Synthesis of Cerium oxide nanocrystal: water as an additive

Ce(NO₃)₃·6H₂O (from 1.0 to 10 mmol), oleylamine (from 3 to 30 mmol) or oleylamine (from 1.5 to 15 mmol) with octadecylamine (from 1.5 to 15 mmol), 4.0 g of ODE and distilled water (from 4 to 40 mmol) were mixed at 80 °C for 30 min. The mixture was heated to 260 °C and then aged for 2 h. Highly monodispersed and large cerium oxide nanocrystal resulted with the addition of water.

6.2.6. Synthesis of Cerium oxide nanocrystal: octadecylamine addition

1.0 mmol of $\text{Ce}(\text{NO}_3)_3 \cdot 6\text{H}_2\text{O}$, 1.5 mmol of oleylamine and 1.5 mmol of octadecylamine were dissolved in 4.0 g of ODE at 80 °C for 30 min; after raising the temperature to 260 °C the reaction was allowed to sit for 2 h. For large cerium oxide nanocrystal, high concentration of cerium precursor (from 1 to 10 mmol) with oleylamine (from 1.5 to 15 mmol) and octadecylamine (from 1.5 to 15 mmol) were used.

6.2.7. Star, flower-shaped cerium oxide nanocrystal

$\text{Ce}(\text{NO}_3)_3 \cdot 6\text{H}_2\text{O}$ (0.434g, 1.0 mmol) and oleic acid (0.847 g, 3.0 mmol) and 4.0 g of ODE were stirred at room temperature. The mixture was heated to 80 °C resulting in a yellow solution which contains cerium-oleate complex. The solution was further heated to various temperature (from 230 °C to 300 °C) followed with the injection of oleylamine (0.802 g, 3.0 mmol), and aged at the same temperature for desired reaction time (from 30 min to 6 h). In case of using $\text{Ce}(\text{acac})_3$ as a precursor, $\text{Ce}(\text{acac})_3$ (0.437 g, 1.0 mmol), 1,2-hexadecanediol (1.292g, 5.0 mmol), oleylamine (0.802g, 3.0 mmol), and oleic acid (0.847 g, 3.0 mmol) were used at the same condition mentioned above.

6.2.8. Purification of nanocrystalline ceria

The nanocrystals (1g) were purified by addition of 25 ml of methanol and 25 ml of acetone; the solutions were centrifuged and redispersed at least 5 times to remove unreacted cerium salt, surfactants, and ODE. Highly purified nanocrystalline ceria was re-dispersed in hexane and centrifuged at 4500 rpm for 30 min. The purified brown-black

ceria nanocrystals could be readily dispersed in other non-polar solvents, such as chloroform, THF, and toluene.

6.2.9. Preparation of water-soluble cerium oxide nanocrystal

Water-soluble cerium oxide nanocrystal was produced by using two phase transfer agents: an amphiphilic copolymer (PAAOA) and a fatty acid (oleic acid). Ultrapure water (MILLIPORE, 18.2M Ω cm) was used for the phase transfer of cerium oxide nanocrystal.

6.2.9.1. Synthesis of poly(acrylic acid)-octylamine (PAAOA) amphiphilic copolymer.

0.6 g of poly (acrylic acid) ($M_w = 1,800$) was dissolved in DMF and reacted with the addition of 0.58 g of EDC and 0.5 ml octylamine. The reaction mixture was stirred overnight and then, the DMF was removed via rotary evaporation. The resulting oily product was precipitated in acidified water and rinsed with water. The copolymer was vacuum dried and then re-dispersed in chloroform and made up to the concentration of 15 mg/ml.

6.2.9.2. PAAOA coated cerium oxide nanocrystal

Various amounts of PAAOA (3 to 30 ml) were added to 1 ml of cerium oxide nanocrystal/hexane solution (typically, 13.7 and 7.5 mg/ml of near-spherical and star cerium oxide nanocrystal, respectively) and stirred at room temperature for 4 h. The hexane and chloroform was removed via rotary evaporation. The resulting dried PAAOA coated ceria nanocrystals were re-dispersed in 0.1M Na₂CO₃ (pH ~9) solution.

6.2.9.3. Oleic acid coated cerium oxide nanocrystal

The oleic acid coated cerium oxide nanocrystal was obtained by modifying the previously published method from Prakash *et al.*^{12c} Various amount of oleic acid (10-80 μ l) were stirred with 1 ml of cerium oxide nanocrystal/ethyl ether solution (typically, 5.4 and 2.0 mg/ml of near-spherical and star-shaped cerium oxide nanocrystal, respectively) and 10 ml of ultra pure water. Full dispersion of nanocrystals was insured by application of a probe sonicator (UP 50H, Dr.Hielscher) for 5 min at 50 % amplitude and full cycle. A clear yellow brown solution was obtained after purification process. Purification of as-prepared water-soluble cerium oxide nanocrystal was carried out using ultracentrifugation (Sorvall Discovery 100 SE Ultracentrifuge) at 40,000 rpm for 4 h, followed by syringe filtration (pore size of 0.45 μ m, WHATMAN-NYL). This purification process was repeated 3 times.

6.2.10. Nanoparticle concentration calculation

Nanoparticle concentrations are found from analytical measures of total cerium concentration in solutions digested with acids. To require an estimate of the weight of a single particle we assumed a particle volume of $\frac{4}{3}\pi r^3$ where r is the average radius of the nanocrystal as determined by TEM measurements of over 1,000 particles; then we took the density of CeO₂ in the nanoparticle to be equivalent to that of the bulk phase (e.g. 7.65 g/ml) and could calculate the particle weight. As an example, the volume of a 5 nm diameter particle of CeO₂ is 6.54×10^{-20} ml, which provides a total mass per particle of

5.0×10^{-19} g. Using this data, and Avogadro's number, we find for a solution 3000 ppm in Cerium a nanoparticle concentration of 12,221.96 nM.

6.2.11. Cell viability test using water soluble nanoceria

Cell Culture: Human dermal fibroblasts (HDF, Cambrex) were purchased from Cambrex and cultured in Dulbecco's Modified Eagle's Medium (DMEM, ATCC, Manassas, VA), supplemented with 2 mM L-glutamine, 1% penicillin, 1% streptomycin, and 10% fetal bovine serum (FBS). Cells were detached from culture with trypsin and re-suspended in media for passaging to wells. Cells were used at passages 3-6 for experiments.

To evaluate the toxicity using HDF cells in the presence of nanoceria of different coatings, sizes and shapes, the standardized colorimetric assay, MTS (CellTiter 96, Promega), was used to evaluate mitochondrial activity. HDF cells were grown to 70% confluency in 96-well culture plates and introduced to PAAOA-coated near-spherical (5.2 nm) and star-shaped (18.5 nm) nanoceria. Nine sets were treated with nine different nanoceria concentrations (1, 5, 10, 25, 50, 100, 150, 200, 250 $\mu\text{g/mL}$); one set was treated as a blank and consisted of the solvent with no nanocrystals and the last set was used as the untreated control. The treated cells were incubated for 24 and 48 h at 37 °C under 5% CO₂. Then, the supernatant containing the nanocrystals was removed from the wells and replaced with 100 μL of fresh DMEM that is phenol-red free (Gibco/Invitrogen); 20 μL MTS stock solution was added to each well. The MTS assay is reduced by enzymes in live cells, producing a purple formazon dye. After incubating at 37 °C for 1 h, the absorbance at 490 nm of the dye produced was measured using a plate reader

(SpectraMax M2, Molecular Devices). Each experiment was repeated four times to obtain the average value. The LD₅₀ value, which gives the lethal dose required for half of the cells to die, was determined by calculating the percent viability of the cells. At the 24 hr exposure, the LD₅₀ values for near-spherical nanoceria was 16.71 µg/ml; and for star-shaped nanoceria, 3.55 µg/ml. After 48 hr, star-shaped nanoceria was found to be more lethal (Figure S4). Thus, from this assay, larger and sharply-shaped nanocrystals seemed to be detrimental to the human cells rather than spherical smaller nanocrystals.

6.3. Results and Discussion

In this work, we optimized the thermal decomposition of cerium precursors in organic solutions to form a range of cerium oxide particle sizes, shapes, and Cerium (III) content. Such control enables the production of cerium oxide nanocrystal libraries with a wide range of structures. Towards this end, we followed a now standard approach to forming metal oxide nanocrystals that has been applied to iron oxides, manganese oxides, and more recently cerium oxide.^{3a, 17, 32a, 33-35, 63, 126-127} The reaction begins with the dissolution of a cerium precursor in a high boiling point and inert organic solvent, in this case 1-octadecene (ODE). Specifically for cerium oxide the inclusion of amine surfactants (e.g. oleylamine) ensures non-aggregating and uniform sized nanocrystals.^{33-35, 127} At temperatures above 200 °C the precursors decompose and yield nuclei for cerium oxide crystallites. These crystallites rapidly grow over several hours and consume the available soluble cerium. After cooling the reaction to room temperature, purified nanocrystals can be concentrated through repeated centrifugation and dispersion cycles.

6.3.1. Diameter control of cerium oxide nanocrystal

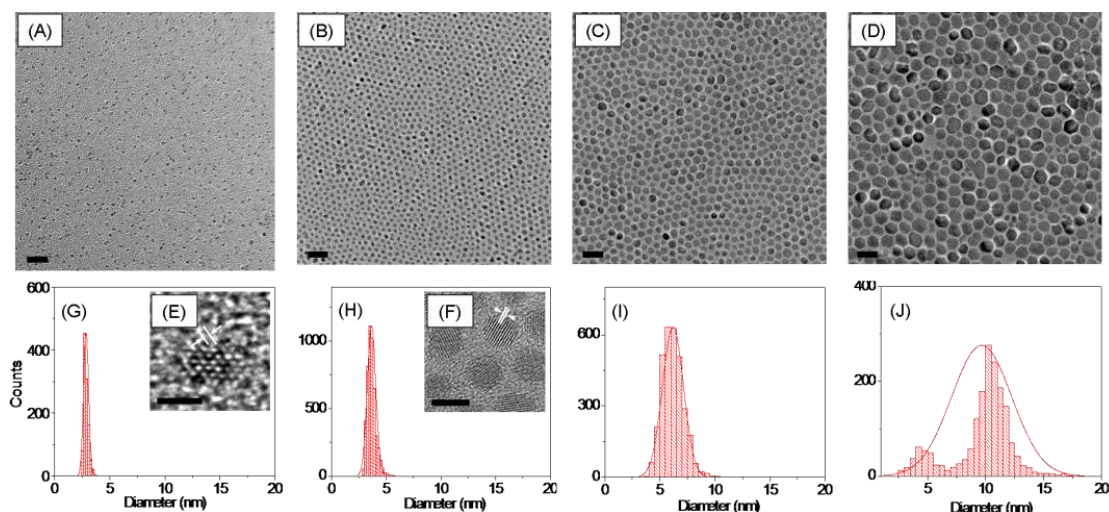


Figure 6.1 Near spherical nanocrystalline cerium oxide.

TEM micrographs (A to D) of cerium oxide nanocrystal and histograms of their corresponding size distributions (G to J) for particles counted in (A) to (D), respectively. All scale bars are 20 nm from (A) to (D). High resolution TEM micrographs (E and F) were from (A and F), and the scale bars are 2 and 5 nm, respectively. Nanocrystalline cerium oxide was synthesized from both $\text{Ce}(\text{acac})_3$ as well as $\text{Ce}(\text{NO}_3)_3 \cdot 6\text{H}_2\text{O}$. (A) 2.9 ± 0.2 nm of diameter cerium oxide nanoparticles formed by 1mmol of $\text{Ce}(\text{acac})_3$ with 5 mmol of 1,2 hexadecanediol and 3 mmol of oleylamine at 315 °C for 2h. (B) 3.6 ± 0.4 nm obtained from 1 mmol of $\text{Ce}(\text{NO}_3)_3 \cdot 6\text{H}_2\text{O}$ and 3 mmol of oleylamine, (C) 6.2 ± 1.0 nm prepared from 10mmol of $\text{Ce}(\text{NO}_3)_3 \cdot 6\text{H}_2\text{O}$ and 30 mmol of oleylamine, and (D) 9.7 ± 2.6 nm prepared from 10mmol of $\text{Ce}(\text{NO}_3)_3 \cdot 6\text{H}_2\text{O}$, 15 mmol of oleylamine, 15 mmol of octadecylamine, and 40 mmol of water at 260 °C for 2h. The inset shows high resolution TEM images of near-spherical cerium oxide nanocrystals (E and F); the (111) plane has a 0.31 nm lattice spacing. For all histograms, over 1000 particles were measured in multiple images and the data compiled using ImagePro.

Figure 6.1 shows example electron micrographs of materials produced from this reaction. The lattice fringes in the HR-TEM image were indexed to (111) plane of cubic fluorite structure of cerium oxide with a plane to plane distance of 0.31 nm, which compares well to the 0.32 nm spacing found in bulk ceria. Nanocrystal diameters between 3 to 7 nm could be generated from different kinds of precursors, including cerium (III) acetylacetonate hydrate ($\text{Ce}(\text{acac})_3$), cerium (III) oleylamine, cerium (III)

nitrate ($\text{Ce}(\text{NO}_3)_3 \cdot 6\text{H}_2\text{O}$) and cerium (IV) hydroxide ($\text{Ce}(\text{OH})_4$) (Figure 6.2). Most examples had narrow size distributions and well-dispersed isolated crystallites. The one exception was the aggregated materials formed with the hydroxide precursor. Water may be produced by this cerium source, and if bound to the nanoparticle surface it could alter the surface charge and promote particle aggregation.¹²⁸

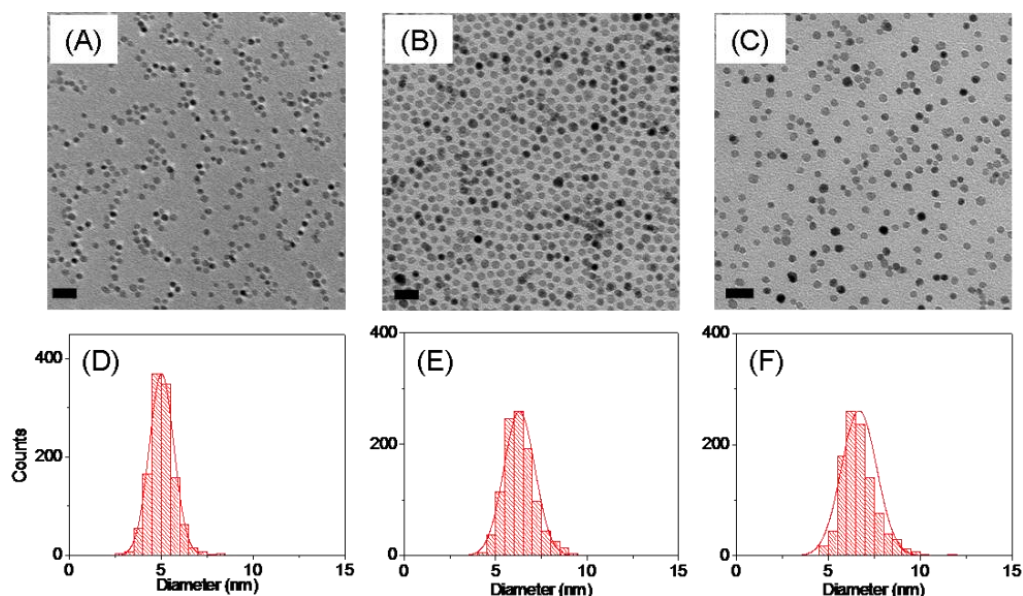


Figure 6.2 Cerium oxide nanocrystals from cerium-oleylamine precursor.

TEM images of cerium oxide nanocrystal prepared by cerium-oleylamine (5ml, $[\text{Ce}] = 5 \text{ mg/ml}$) decomposition in the presence of oleylamine (from 0.5 to 4 mmol) at 260 °C for 2h. (A to C) Cerium oxide nanoparticles synthesized by cerium-oleylamine decomposition with 0.5, 2, 4 mmol of oleylamine, respectively. (D to F) Size distribution of cerium oxide nanoparticles from A to C and the size is 5.0 ± 0.6 , 6.4 ± 0.8 , $6.7 \pm 1.0 \text{ nm}$, respectively. All scale bars are 20 nm.

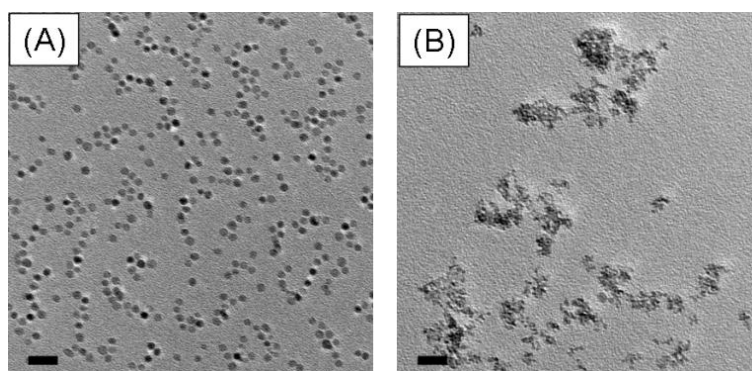


Figure 6.3 TEM micrographs of cerium oxide nanocrystal synthesized using 2 different cerium precursors: cerium oleylamine, and cerium hydroxide.

Scale bars are all 20 nm. (A) Near-spherical cerium oxide nanocrystal (5.0 ± 0.6 nm) synthesized from Ce-oleylamine, (B) Cerium oxide nanoparticles from $\text{Ce}(\text{OH})_4$.

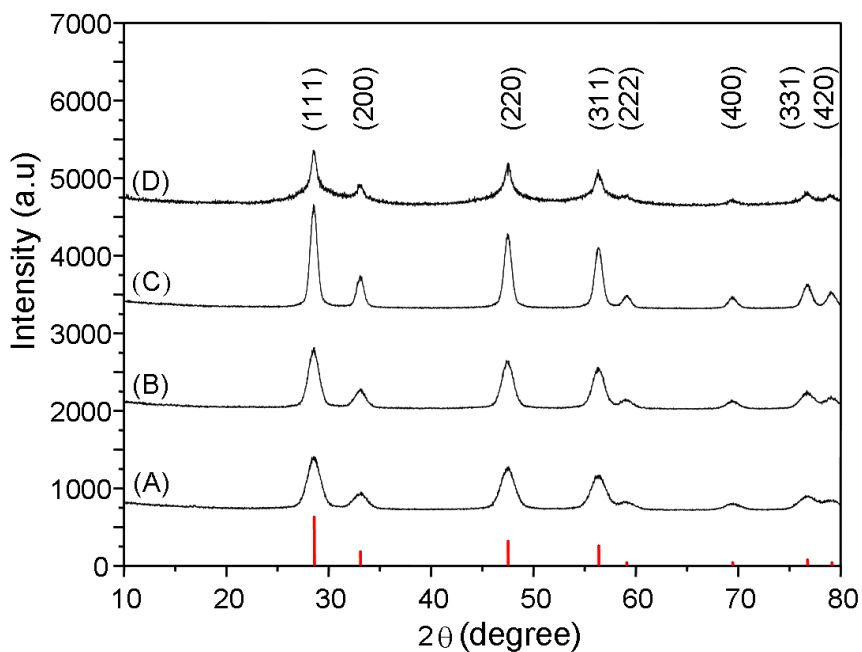


Figure 6.4 The x-ray diffractograms of cerium oxide nanocrystals with various sizes and shapes. The vertical lines on the bottom are from the JCPDS Card #34-0394. The cerium oxide nanocrystals have cubic fluorite structure. (A to C) Near-spherical cerium oxide nanocrystal with 3.6 ± 0.4 , 6.6 ± 1.0 , and 9.7 ± 2.6 nm, respectively. (D) Star-shaped cerium oxide nanocrystal with 18.5 ± 2.5 nm.

Figure 6.4 shows representative X-ray diffractograms of the solid nanocrystalline powders; all peaks match to the cubic fluorite structure (JCPDS Card #34-0394). The intensity of the XRD peaks increased and the widths sharpened as the size of the cerium oxide nanocrystal increased.

Even with significant time and temperature variations, the standard decomposition reactions described above yielded materials remarkably constant in size and form. Typically, $\text{Ce}(\text{NO}_3)_3 \cdot 6\text{H}_2\text{O}$ and oleylamine were combined in a molar ratio of 1:3 and introduced into ODE. At 150 °C nanocrystals could be observed in the mixture, with a diameter of 4.9 ± 0.9 nm. As the reaction temperature increased, the width of the size distribution narrowed up to 260 °C as shown in Figure 1B, F and H. However, when the reaction was heated above 260 °C a broader size distribution was obtained (4.4 ± 0.6 nm at 315 °C). At lower temperatures, there is poor exchange of material between nanoparticles. At higher temperature, Ostwald ripening is faster and leads to broadening of the distribution due to dissolution of smaller particles and formation of larger particles. For these reasons, the reaction time for the cerium precursors had to be carefully manipulated to ensure narrow size distributions. Ceria nanocrystals were formed with broad distribution (4.7 ± 1.1 nm) at 260 °C after only ten minutes; however, after two hours, the distribution became noticeably sharper with a σ of 10 %. Further heating lead to ripening of nanocrystals as Ostwald ripening became significant. A notable feature of these data, however, is that the average particle diameter remained constant even as the size distribution was changing substantially.

While time and temperature are powerful parameters for optimizing particle uniformity, the diameter of the ceria nanocrystals was best manipulated through the

inclusion of additives, in particular water and cosurfactants (Figure 1B to 1D). In agreement with past work, we found that an increase in oleylamine, from 1:3 to 1:6, resulted in larger and more elliptical nanocrystals.³³ The cerium precursor concentration also was a factor in size control and increasing this concentration a factor of ten could double the diameter of the nanocrystals. A surprising finding was that the addition of water had a significant effect on nanocrystal diameter (Figure 1D). Particle sizes generally increased with the addition of more water; however, if too much was added (in excess of 40 mmol typically) the resulting nanocrystals were aggregated and poorly uniform. Ould-Ely *et al* showed the manganese oxide nanocrystal size and shape could be manipulated in similar reactions through the addition of water which both enhances the solubility of the metal starting material as well as alters its propensity to form aggregates (e.g. micelles).¹²⁹ Such phenomena may also be important in the reactions studied here.

The combination of two amine terminated surfactants, oleylamine and octadecylamine, produced the largest diameters of cerium oxide. Larger ceria nanocrystals (6.0 ± 0.9 nm) were formed if each of these were used together, in constant molar ratios. By including water, nanocrystals of 9.7 ± 2.6 nm diameters could be formed. The addition of the cosurfactant increased the growth rate of the nanocrystals. For example, when the two amine surfactants were used particles grew from 3 to 10 nm in two hours as compared to a growth from 3 to 6 nm in the presence of oleylamine alone. The more rapid nanoparticle growth suggests that the cosurfactants as well as water promote the availability of cerium oleate for particle growth.

6.3.2. Star- and flower-shaped cerium oxide nanocrystals

The shape of the nanocrystals was most sensitive to surfactant additives with carboxyl functionalities, such as oleic acid (OA). When these were combined with the amine surfactants it was possible to form larger star-shaped cerium oxide nanocrystals. Further optimization of these conditions yielded flower-shaped materials. Like the star-shaped structures, these materials are much larger in dimensions ($d > 10$ nm) than the near-spherical structures (Figure 6.5). However, an examination of the micrographs shows that the shapes result from the aggregation of much smaller crystallites ($d < 3$ nm). The lattice planes seen in the near-spherical and star-shaped cerium oxide nanocrystals were separated by 0.29 nm, corresponding to the interplanar spacing of the (200) faces. X-ray diffraction of the star-shaped cerium oxide nanocrystals (Figure 6.4) shows broad and diffuse peaks with lower intensity, consistent with the appearance in the electron micrographs. The aggregation of smaller ceria nanocrystals into larger structures was observed first by Zhou *et al* after the decomposition of cerium (IV) ammonium nitrate in the presence of both fatty acids and amines.²⁵ These different surface analyzers could be selectively binding on the different facets, (111) and (100), on the nanocrystals. Between two facets, the high energy state of (100) turns to be stabilized by oleic acid because carboxyl group is prefer to bind on the (100) surface rather than (111) and hence, leading to the growth of nanostructure through (111) with star or flower shape.^{22b, 24, 130} The formation of these structures may be mediated by the shielding of repulsive surface charge induced by the binding of the amine and carboxylate surfactants; such phenomena have been observed with other metal oxide nanocrystals such as titania and zinc oxide.^{57b}

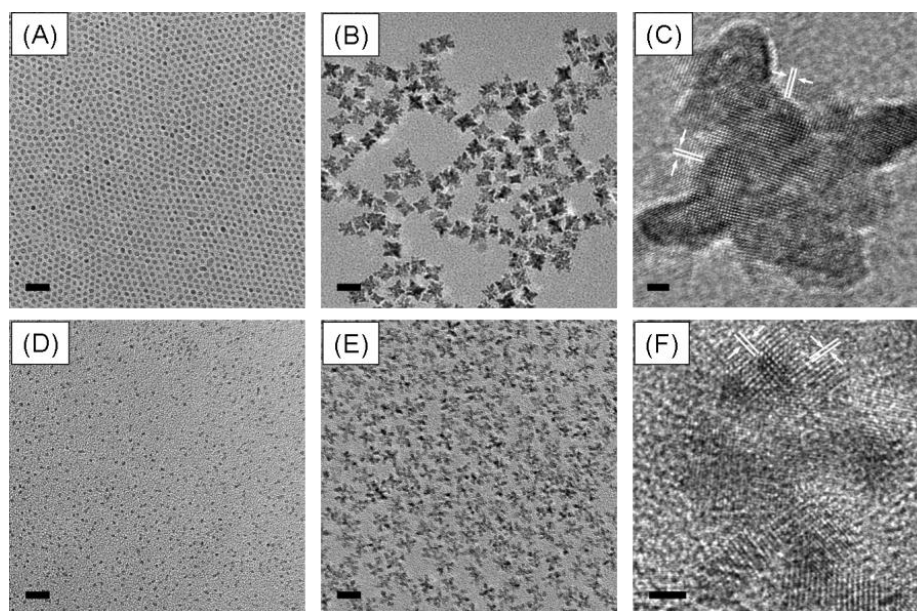


Figure 6.5 Evolution of nanocrystalline ceria from spherical to star-shaped.

All scale bars are 20 nm (A, B, D, and E) and 2 nm for high resolution TEM images (C and F). (A) Near-spherical cerium oxide nanocrystal (3.6 ± 0.4 nm) synthesized by 1 mmol of $\text{Ce}(\text{NO}_3)_3 \cdot 6\text{H}_2\text{O}$ with 3 mmol of oleylamine at 260 °C for 2h. (B) Star-shaped cerium oxide nanocrystal (18.5 ± 2.5 nm) synthesized by 1 mmol of $\text{Ce}(\text{NO}_3)_3 \cdot 6\text{H}_2\text{O}$ with 3mmol of both oleylamine and oleic acid. (D) Near-spherical cerium oxide nanocrystal (2.9 ± 0.2 nm) from 1 mmol of $\text{Ce}(\text{acac})_3$ with 3 mmol of oleylamine. (E) Flower-shaped cerium oxide nanocrystal (12.0 ± 1.4 nm) from 1mmol of $\text{Ce}(\text{acac})_3$ with 3mmol of both oleylamine and oleic acid. (C and F) High resolution TEM image of star-shaped (C) and flower-shaped (F) cerium oxide nanocrystal. Both show (200) plane with 0.29 nm lattice spacing. For all size histograms, over 1000 particles were measured in multiple images with the use of software package ImagePro.

6.3.3. The content of Cerium (III) in nanocrystals

In this reaction, both cerium (III) and cerium (IV) precursors are used. We examined whether these starting materials yielded nanocrystals with different concentrations of Cerium (III) and found that particle size, rather than precursor source, was the most important indicator of Cerium (III) content. X-ray photoelectron spectroscopy was used to quantify the Cerium (III) and Cerium (IV) on the surface of ceria nanocrystals. Photoelectron peaks from the Cerium 3d electrons were fit using the method described by

Deshpande *et al* resulting in a measure of the relative ratios of the reduced and oxidized cerium.¹³¹ Figure 6.6 shows an example of this data for five diameters of cerium oxide nanocrystals. In all samples there is a significant level of both Cerium (III) and Cerium (IV) indicating that both valence states are present.^{25, 87d, 132}

The Cerium (III) content of the smallest cerium oxide nanocrystals produced in this synthesis is comparable to that found for materials produced via different synthetic strategies. Specifically, the smallest diameter nanocrystals, about 3.5 nm, had a Cerium (III) content of ~45%. Perez *et al* reported that 53% of the surface ceria on particles produced by coprecipitation was Cerium (III); similarly, 48% of the cerium content in nanoparticles formed from ethylenediamine-mediated reactions was Cerium (III) while 44 % of the cerium in particles formed in microemulsions was reported to be Cerium (III).^{25, 130a, 133}

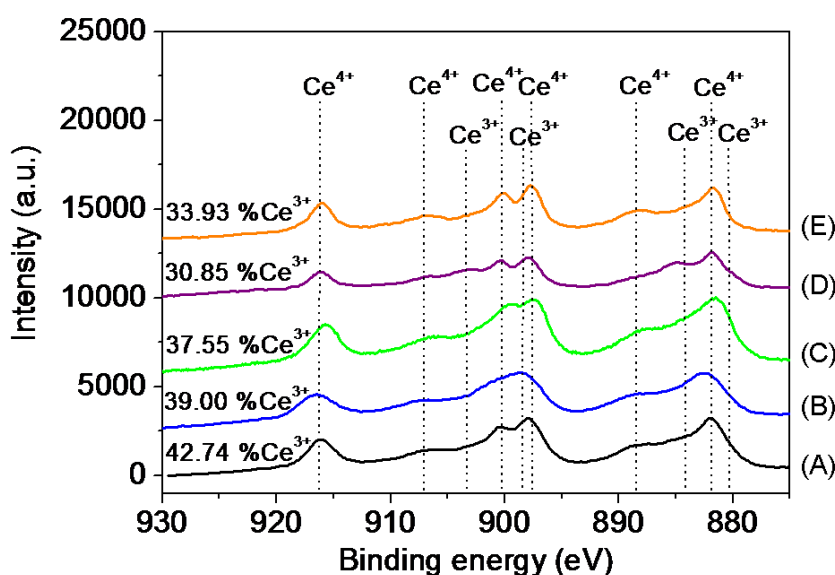


Figure 6.6 XPS data of cerium oxide nanocrystal with various size and shape. As size increases, the intensity of Ce³⁺ peaks does not change significantly from (A) to (E). (A to D) Near-spherical cerium oxide nanocrystal with 3.6 ± 0.4 , 6.2 ± 1.0 , 6.6 ± 1.0 and 9.7 ± 2.6 nm. (E) Star-shaped cerium oxide nanocrystal with 18.5 ± 2.5 nm.

The calculated atomic percentage of Cerium (III) in these materials decreased from 45 to 31 % as particle diameter increased from 3.5 to 10 nm. The dependence of Cerium (III) content on particle diameter has been observed before in materials formed in both aqueous and hydrothermal routes.^{130a, 134} One explanation is that the surface of very small nanocrystals is under enough strain to promote the loss of oxygen from the crystal structure. This can leave behind oxygen vacancies and convert Cerium (IV) to Cerium (III).⁹¹ Alternatively, the presence of Cerium (III) may reflect the starting precursors and their interactions with reaction additives. At these temperatures, the free surfactants are close to their thermal decomposition temperature and may release both CO and CO₂; these by-products could reduce the cerium precursors and influence the amount of Cerium (III) that is incorporated.¹³⁵

6.3.4. Transferring the ceria nanocrystals into water

Cerium oxide nanocrystals prepared at high temperature in organic solvents can only be applied in biological systems if they are effectively transferred into water.¹³⁶ Towards this end, polyacrylic acid-octyl amine (PAAOA) as well as oleic acid were applied here as phase transfer agents. As shown in the inset of Figure 6.7, the hydrophobic portion of these amphiphiles can interact with the hydrophobic surface of the cerium oxide nanocrystal. Figure 6.7 shows the transfer efficiency of two different shapes of cerium oxide nanocrystal increases with both the addition of the polymer, PAAOA, as well as the surfactant, oleic acid. If there is not enough of the phase transfer agent, then adequate coverage of the hydrophobic surfaces is not possible resulting in poor transfer yields. Alternatively, if too much phase transfer agent is added the yield can also decrease.

Under these conditions the surfactants are concentrated enough to form micelles, and this process competes effectively with bilayer formation.¹³⁷ Under the optimal conditions, however, both agents are efficient at particle transfer with yields approaching 80%.

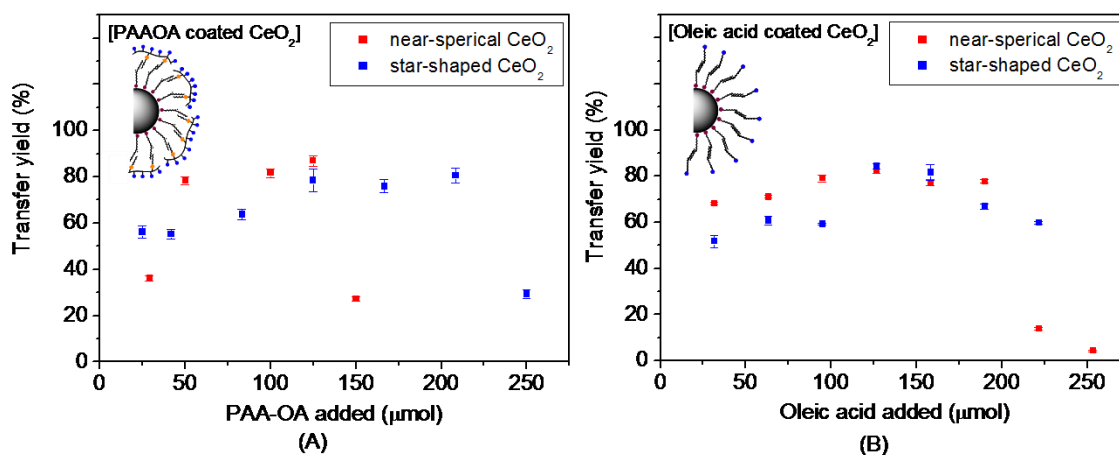


Figure 6.7 Transfer yields of cerium oxide nanocrystal from hexane into water.

The inset scheme is PAAOA (A), and oleic acid (B) coated cerium oxide nanocrystal. In each scheme, the blue, purple, and yellow dots stand for carboxyl group, amine group, and amide bond, respectively. (A) PAAOA coated cerium oxide nanocrystal. Various amounts of PAAOA (3 to 30 ml) were added to 1 ml of cerium oxide nanocrystal/hexane solution (typically, 13.7 and 7.5 mg/ml of near-spherical and star-shaped cerium oxide nanocrystal, respectively). (B) Oleic acid coated cerium oxide nanocrystal. Various amounts of oleic acid (10 to 80 μl) were stirred with 1 ml of cerium oxide nanocrystal/ethyl ether solution (typically, 5.4 and 2.0 mg/ml of near-spherical and star cerium oxide nanocrystal, respectively) and 10 ml of ultra pure water. The concentration of cerium oxide nanocrystal was analyzed via the measurement of atomic ceria using ICP-AES.

Both imaging and light scattering studies confirm that crystalline, non-aggregating materials are present in the aqueous suspensions of ceria nanocrystals. Electron micrographs (Figure 6.8) show that the materials retain their original size and shape after transfer into water; moreover, while it is not definitive evidence, the absence of significant particle aggregation in these dried films suggests the materials are not

aggregating after transfer into water. This is confirmed by both dynamic light scattering (DLS) and small-angle X-ray scattering (SAXS).

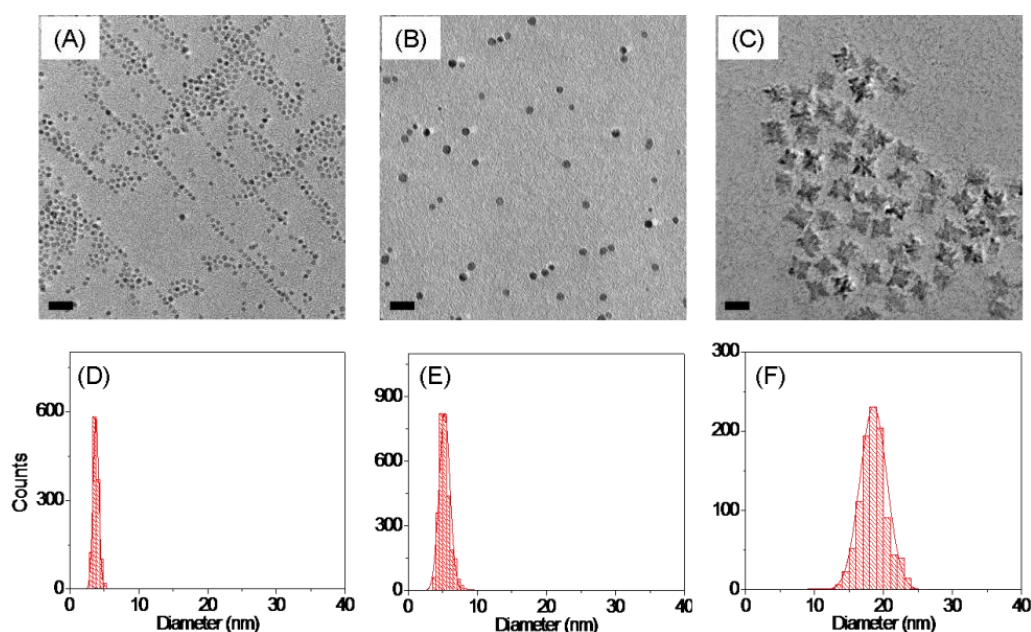


Figure 6.8 Water soluble cerium oxide nanocrystals.

TEM micrographs (A to C) of phase transferred water-soluble cerium oxide nanocrystal via PAAOA or oleic acid and diameter histograms (D to F) for particles counted in (A) to (C), respectively. (A) Near-spherical cerium oxide nanocrystal coated with oleic acid (3.8 ± 0.4). (B) Near-spherical cerium oxide nanocrystal coated with PAAOA (5.2 ± 0.8). (C) Star-shaped cerium oxide nanocrystal coated with PAAOA (18.5 ± 2.0 nm). All nanocrystals were successfully transferred from organic to water phase without size and shape change. All scale bars are 20 nm from (A) to (C). For all diameter histograms, over 1000 particles were measured in multiple images with the use of software package ImagePro.

Figure 6.9 compares the nanocrystal dimensions found from all three methods. The core size of PAAOA coated cerium oxide nanocrystal was 3.8 and 5.2 nm from microscopy; the core with shell thickness from SAXS was systematically larger as expected for both the polymer and oleic acid. In dynamic light scattering, the suspensions yielded particle distributions peaked near 6.5 and 10.5 nm respectively in good agreement

with SAXS. Additionally, these particle sizes were the same in two common buffer solutions illustrating the relative insensitivity of the solution stability to ionic strength and pH.

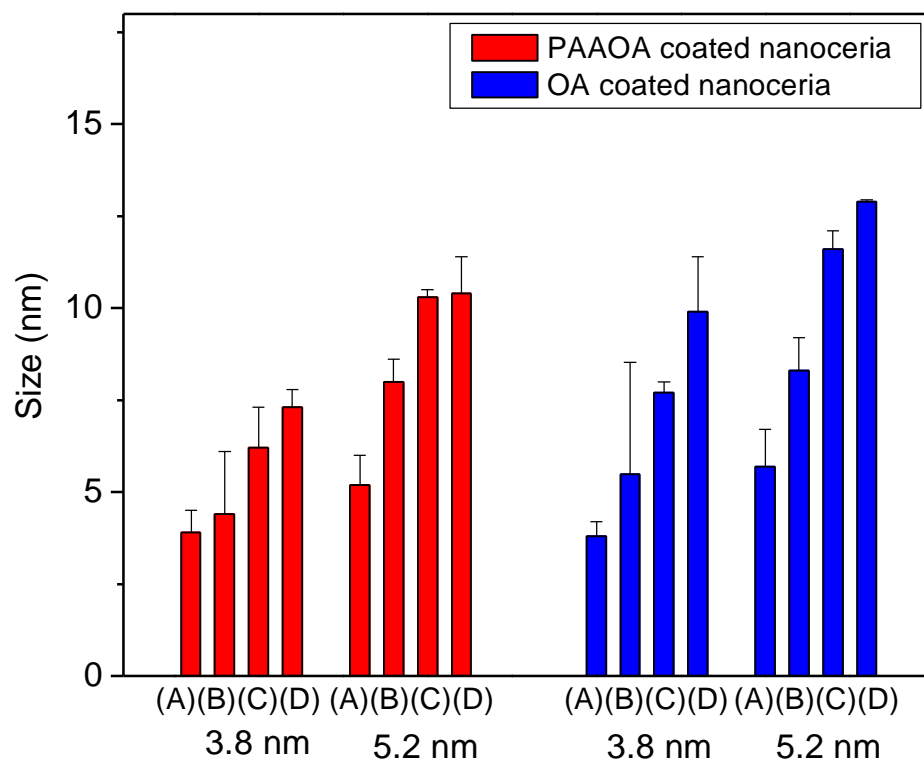


Figure 6.9 Comparisons of the effective dimensions of cerium oxide nanocrystals stabilized in water using three different methods: TEM, SAXS, and DLS.

Each tool is sensitive in different ways to the core and coating of the nanoparticle resulting in understandable differences between the reported crystallite sizes. In order to evaluate whether particle aggregation could occur at high pH we also evaluated pH 9 and found little difference in the observation of isolated, non-aggregated particles. The method key is as follows: (A) TEM, (B) SAXS, (C) DLS (pH7), and (D) DLS (pH9).

6.3.5. Antioxidant and toxicological evaluation of water soluble nanocrystalline ceria

To examine whether cerium oxide nanocrystals formed via these routes could be of interest in biological applications, the materials were screened using a simple acute cell viability assay. Such data cannot confirm that a substance is safe, but they are useful to identify potential hazards and benchmark a material against similar substances. This is a particularly important question for ceria as several researchers have reported that nanocrystalline cerium oxide can be toxic to cells *in vitro* because of oxidative stress.¹³⁵ We hypothesized that these biological effects would be minimized in our materials because their surfaces were stabilized; this renders the materials colloidally stable (e.g. non-aggregating) in the relevant buffers for cytotoxicity analysis and prevents cellular damage that may occur as nanoparticles sediment onto cells. Recently, several reports have highlighted that for more aggregated cerium oxide particles the surface coating can greatly reduce their toxicological effects.^{31, 55-56, 57b, 61a, 61g, 66-67, 125, 136}

Non-aggregated suspensions of 5.2 nm diameter near-spherical and 18.5 nm diameter star-shaped cerium oxide nanocrystals had little impact on cells *in vitro* up to ppm concentrations. To evaluate the material's acute toxicity, the suspensions of nanoparticles were added to the culture media of Human Dermal Fibroblast (HDF) cells (Figure 6.10, and Figure 6.11). The viability was examined after 24 and 48 hrs using a standard assay that measures mitochondrial function.^{137b} The smaller near-spherical materials killed 50% of the cells (LD₅₀) at a concentration of 17 µg/ml while the larger, star-shaped materials had a LD₅₀ of 4 µg/ml. Supplemental figure 5 contains the dose

dependence of the cellular viability for each condition. While both ceria samples had measurable *in vitro* cytotoxicity, LD₅₀ values in excess of 1 ppm at least for molecules are generally not considered indicative of a cytotoxic agent.⁶⁶ Because of the very large molecular weight of nanoparticles, when this weight measure is converted to a molarity the LD₅₀ values are on the order of 0.1 micromolar. We note that this general level of acute cytotoxicity is comparable to that reported for other nanocrystalline ceria formulations, which range from 1 nanomolar^{61a, 125a, b} to hundreds of micromolars.⁶⁶ Also, it is interesting to note that the star-shaped, larger, ceria had a greater impact on cells per particle as compared to the smaller nanocrystals. A more complete analysis of the *in vitro* cytotoxicity of these materials will be the subject of future work. Clearly, the design of highly biocompatible materials will be critical for any eventual application of nanocrystalline ceria as an antioxidant.

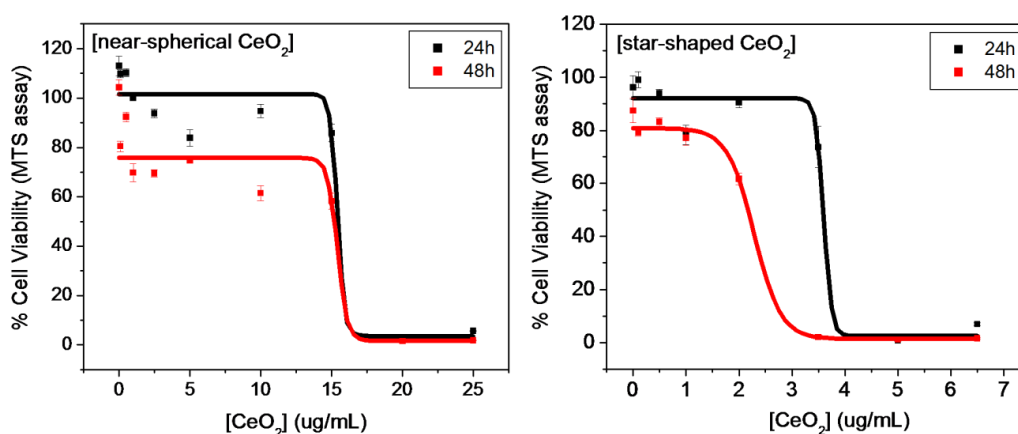


Figure 6.10 Effect of nanoceria on the viability of Human Dermal Fibroblast (HDF) cells.

After exposure to two different shaped ceria nanocrystals at different concentrations, data was analyzed for mitochondrial activity (MTS) after 24 and 48 h. (A) PAAOA coated near-spherical nanoceria of 5.2 ± 0.8 nm. (B) PAAOA coated star nanoceria of 18.5 ± 2.0 nm. HDF cells exhibited a decrease in viability and an LD₅₀ at (A) 16.71, 15.88 $\mu\text{g}/\text{ml}$ and (B) 3.55, 2.12 $\mu\text{g}/\text{ml}$ after 24 and 48 h, respectively. The surface coatings alone had no effect on cells up to 50 micromolar concentration (see Figure 6.11).

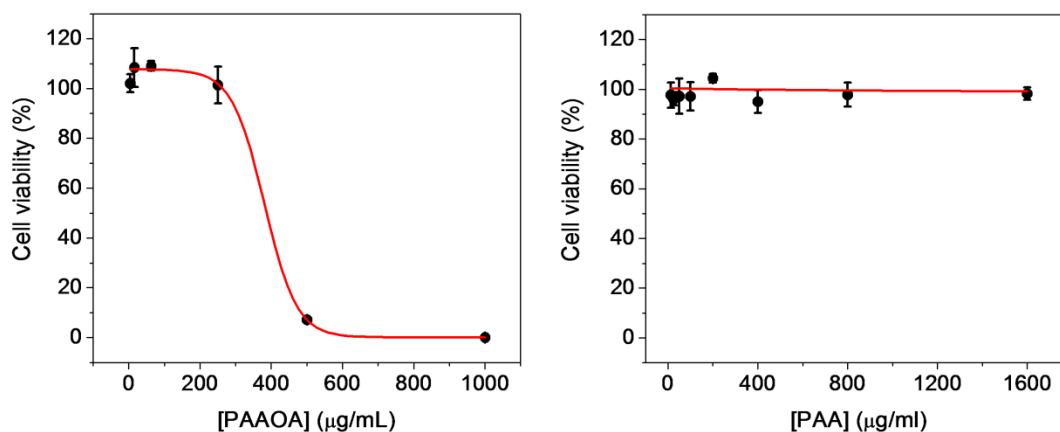


Figure 6.11 Cell viability study of PAAOA (polyacrylicacid octylamine) and PAA (polyacrylicacid). The value of LD₅₀ from PAAOA was 385.5 ppm (68.8 µM), which is an order of magnitude less toxic than that reported for our most biocompatible nanoparticles. PAA had no effect on cell viability up to 1600 ppm (888.9 µM).

Finally, we confirmed that the aqueous suspensions of nanocrystalline ceria could react with oxidants such as H₂O₂ in a manner similar to that found for ceria made directly in water. While the presence of an intervening organic surface coating did not preclude reactivity of other nanocrystalline ceria systems,^{31, 57b, 66-67, 125e} the tightly packed layer of oleylamine molecules that coat these particles could present a more significant barrier for electron transfer. To examine this possibility, we used the reaction of nanocrystalline ceria with hydrogen peroxide as a measure of the accessibility and reactivity of the Cerium (III). Both Das *et al* and Perez *et al* found that cerium oxide nanoparticles prepared by either a microemulsion or coprecipitation method reacted with H₂O₂ in water, converting Cerium (III) to Cerium (IV). Because the ultraviolet absorption of the particle shifts after the oxidation of Cerium (III), it is possible to assess the extent of the reaction colorimetrically.^{31, 57b} This prior work illustrated that at least for materials

formed in water, the capacity of a nanoparticle to reduce H_2O_2 scaled with the Cerium (III) content of the particles.

The ability for these nanocrystals to react with H_2O_2 was evaluated in comparable colorimetric analyses (Figure 6.12). For these studies, two very different particle sizes, 3 and 8 nm, were studied. First, polyacrylic acid octylamine (PAAOA) coated cerium oxide crystals ($5 \mu\text{M}$) were dispersed in 0.1M Na_2CO_3 ($\text{pH} \sim 9$) solutions. After injection of 1 mmol of H_2O_2 , the suspensions changed color from pale brown to deep yellow. This change in color is a signal that the Cerium (III) on the particle surface is reacting with the oxidant and forming Cerium (IV). Figure 6.12 shows the visual appearance of the solutions, as well as the corresponding change in transmittance.

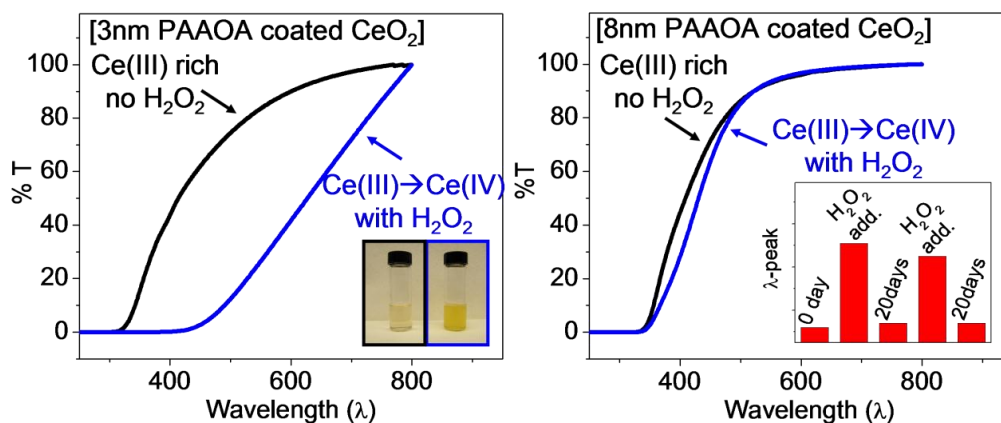


Figure 6.12 H_2O_2 quenching depends on the size of the cerium oxide nanocrystals.

The black UV-visible spectrum is the control sample, and the blue spectrum is the sample after injection of 1 mmol H_2O_2 . The inset digital images show the color change from transparent brown (black square) to deep yellow as the cerium oxide nanocrystal becomes more rich in Ce(IV) (blue square). The quenching ability of nanocrystalline cerium oxide was reversible as shown in the inset image of 8 nm PAAOA coated cerium oxide. The inset bar graph shows λ -peak shifting from 400 to 440 nm. Ce(III) of 3 nm PAAOA coated cerium oxide also recovered after about 40 days (see supplemental figure 4). The additional injection of H_2O_2 led to the transition from Ce(III) to Ce(IV) again.

These results indicate that these materials can act as effective antioxidants, even though they were originally formed in organic solutions. As is apparent in Figure 6.12, both sizes of ceria showed high reactivity to the hydrogen peroxide and neither solution showed any signs of aggregation. These observations suggest that the surface coatings remained intact even as solution phase peroxide reacted with the surface cerium. Additionally, the smaller cerium oxide nanocrystals had substantially more reactivity as compared with the larger materials. The primary difference between these two examples is their Cerium (III) content (Figure 6.6). As has been observed for other nanocrystalline ceria, the smaller materials were more reactive presumably because of their higher concentration of Cerium (III).

6.4. Conclusion

Cerium oxide nanocrystals with tunable sizes and various shapes were synthesized through the thermal decomposition of cerium precursors at high temperatures in octadecene. Uniform and tunable diameter materials could be produced by control over the cerium to surfactant molar ratio as well as the addition of co-surfactants and water. Smaller ceria nanocrystals had higher concentrations of Cerium (III) as compared to larger ones, an observation that may result from the expansion of the lattice in smaller sizes of nanocrystal. Amphiphilic polymers and oleic acid could be used to transfer the ceria from the octadecene into water with yields as high as 80%. *In vitro* toxicological studies of two different shapes of cerium oxide nanocrystals found no significant acute cytotoxicity. Finally, the Cerium (III) in the nanocrystals reacted with H₂O₂ in water

resulting in a substantial color change; smaller particles generally had more reactivity by virtue of their higher Cerium (III) content. These data illustrate that the antioxidant properties of nanocrystalline ceria are independent of the method of formation and can be measured even when particles are stabilized by phase transfer agents.

Chapter 7

Redox cycling behavior of cerium oxide nanocrystals and its dependence on nanocrystal diameter and surface coating

7.1. Introduction

Cerium oxide (CeO_2 , ceria) is a lanthanide metal oxide that by virtue of the redox potentials of cerium (III) and cerium (IV) can exhibit facile cycling between these two oxidation states.^{50,51} As a consequence, ceria can easily form non-stoichiometric compositions, CeO_{2-x} , as cerium (IV) is reduced to cerium (III) leaving behind oxygen vacancies in the lattice.^{23,52} In nanocrystals, these oxygen vacancies are thought to be clustered and stabilized at the particle surface which makes nanoscale ceria more effective at generating cerium (III) than the equivalent bulk material.^{25, 124a} In the redox cycling of cerium ions, cerium (IV) is metastable in water and under ambient conditions

will revert back to cerium (III). This behavior, termed “oxygen buffering”, make ceria ideal for applications such as water-gas shift catalysis, combustion catalysis, oxygen ion conductors, and solid oxide fuel cells.^{2a, 21, 53, 124, 2a, b, 22b, 54} More recently, the ability of cerium oxide nanocrystals to react with hydrogen peroxide in water has been demonstrated as a strategy for reducing unwanted reactive oxygen species (ROS) present in biological systems.⁵⁵

The reduction and oxidation reactions of nanocrystalline ceria are typically characterized via absorption spectroscopy. Aqueous suspensions of the particles are treated with reactive oxygen species, for example hydrogen peroxide, and the resulting Ce(IV) that forms has a distinctive yellow color that can be used to track semi-quantitatively the progress of these reactions.^{57b} When the concept was first demonstrated in ceria nanocrystals, researchers proposed that cerium (III) could react directly with H₂O₂ at the particle surface through an unspecified mechanism.⁵⁷ More recently Heckert *et al.* hypothesized that the reaction proceeds through an analog of the Fenton/Harbor-Weiss reaction;⁵⁸ in this process, H₂O₂ disproportionates into H₂O and O₂ at the cerium oxide surface.^{31, 55, 58-59} Xue *et al.* showed that the hydroxyl radical (•OH) is produced during the reactions, an observation consistent with a Fenton reaction generated by H₂O₂.⁶⁰

Whatever the molecular mechanism of the process, over the past few years there has been increasing interest in the therapeutic capacity of nanoscale cerium oxide for diseases such as cancer, Alzheimer's, cardiac dysfunction, radiation induced cell death, and aging.⁶¹ Das *et al.* reported that nanoceria protected adult rat spinal cord neurons against oxidative stress.³¹ Perez *et al.* showed how the antioxidation properties of nanocrystalline

ceria could improve cancer therapeutics; pH dependent antioxidant properties of nanocrystalline cerium oxide effectively provide cytoprotection from oxygen radicals to normal cells but not to cancer cells.^{57b} More recently, Kim *et al.* first showed that cerium oxide nanocrystals reduced ischemic brain damage induced by reactive oxygen species in living animals (Male Sprague-Dawley rats).⁶² While these *in vivo* examples are exciting, it is not clear whether they take full advantage of the ability for nanoscale ceria to cycle in its redox state: specifically after oxidation to Ce(IV), nanocrystals may return – slowly – to their original Ce(III) state. Once this has occurred they may react again to quench oxidative species, thereby resulting in extremely high antioxidant capacities due to this cycling behavior.^{31, 57b}

While these results are promising, the antioxidant capacity of nanoceria has not yet been benchmarked against radioprotectants and antioxidants already approved for clinical use.^{31, 56, 61a, 61g, 66-67, 125, 138} The conventional assay for such purposes, the oxygen-radical absorbance capacity or ORAC assay, uses a fluorescence-based indicator (β -phycoerythrin) in the presence of the target compound and a radical initiator (2,2'-azobis(2-amidinopropane)dihydrochloride (AAPH)).¹³⁹ The better the antioxidant capacity of the target compound, the more effective it is at reacting with the ROS generated by the initiator, thereby preserving the intensity of the fluorescence. Such assays are suitable for nanoscale materials; Lucente-Schultz *et al.* showed that the antioxidant property of pegylated single-walled carbon nanotubes was about 5 times higher than that of a known standard, Trolox.¹⁴⁰ Furthermore, the fluorescence assay for *in vitro* quantification to measure oxidative stress along with ROS generation can evaluate how much effectively the engineered cerium oxide nanocrystals can protect cells

against oxidative stress caused by additives such as hydrogen peroxide.^{57b} Cerium oxides scavenge the evolved ROS in cell culture media and inhibit the reaction between fluorescein dyes and ROS.¹⁴¹

While the *in vitro* and *in vivo* antioxidation properties of nanoscale ceria are promising, it is not clear how best to design the material for optimal performance. Crucial questions related to the size and surface dependence have been difficult to answer as all the nanocrystalline ceria studied to date have not used highly uniform nanocrystals with controlled size and surface chemistries.⁶⁷ Even more critical is the role of the particle coating in mediating the reaction between ROS and the nanocrystal surface. This interface must be thin enough to allow for facile surface reactions yet highly stable so as to resist any degradation due to side reactions with ROS. This latter point is particularly important as surface coating degradation can yield aggregated particles unsuitable for many biological applications.

In this research, we synthesized monodisperse libraries of cerium oxide nanocrystals using the high temperature decomposition of cerium precursors; the resulting uniform particles were phase transferred to water with high efficiency (>80%) using polyacrylic acid-octyl amine (PAAOA), oleic acid, polyethylene imine (PEI), and polymaleicanhydride-alt-1-octadecene (PMAO). After one exposure to hydrogen peroxide, smaller particles outperformed larger particles in terms of net amount of reactivity by virtue of their higher cerium (III) concentrations. The mechanism of the peroxide reaction was also evaluated using both GC-MS to monitor by-products and a Luminol test to quantify peroxide concentration: two moles of peroxide reacted with one mole of cerium (III) consistent with a Fenton-like reaction. The antioxidant capacity of

the oleic acid/ CeO₂ materials as measured by oxygen-radical absorbance capacity (ORAC) was 9 times higher than for a standard antioxidant like Trolox. These effects were also seen in in-vitro assays that measured the ability of the particles to protect against oxidative stress induced by peroxide exposures. Cerium oxide treated fibroblast reduced oxidative stress than untreated fibroblast. Finally, over repeated cycles, the oleic acid coated CeO₂ was the most effective material; for 18 cycles, one mole of cerium (III) could react with more than twenty moles of H₂O₂. Other nanoparticles with different surfaces would precipitate after several cycles presumably due to coating degradation.

7.2. Experimental methods

7.2.1. Chemicals

Cerium (III) nitrate hexahydrate (Ce(NO₃)₃·6H₂O (99 %), oleylamine (OM, technical grade, 70 %), 1,2 hexadecanediol (HDD, technical grade, 90 %), 1-octadecene (ODE, technical grade, 90 %), poly (acrylic acid) (PAA, Mw = 1800), octylamine (99 %), poly maleic anhydride-alt-1-octadecene (PMAO, Mw = 30,000-50,000), and polyethyleneimine (PEI, Mw = 25,000), tris(hydroxyl methyl)-aminomethane (99.9 %), luminol (97 %), potassium ferricyanide (K₃Fe(CN)₆, 99 %), Fluorescein sodium salt (FL), 2-2'-Azobis(2-amidinopropane)dihydrochloride (AAPH), and Racemic 6-hydroxy-2,5,7,8-tetramethylchromane-2-carboxylic acid (Trolox) were purchased from Sigma-Aldrich. Hydrogen peroxide (H₂O₂, 30 %), sodium hydroxide (NaOH, 1 N), sodium bicarbonate (NaHCO₃, 99.9 %) and dimethylformamide (DMF, 99.9 %) were purchased from Fisher scientific. 1-ethyl-3-[3-dimethylaminopropyl]carbodiimide hydrochloride

(EDC) was purchased from Thermo scientific. All ceria nanocrystals were synthesized under ultra-high purity nitrogen.

7.2.2. Instrumentation

7.2.2.1. UV-Vis spectroscopy

To measure antioxidant property of different diameter and surface coated nanoceria with H₂O₂, UV-Vis absorbance spectrums were obtained as a function of time using UV-Vis spectroscope (Cary 5000 UV-Vis-NIR spectrophotometer, Varian).

7.2.2.2. Transmission Electron Microscopy (TEM)

The TEM micrographs were taken by a JEOL 2100 field emission gun TEM operating at 200 kV with a single tilt holder using ultrathin carbon type-A 400 mesh copper grids (Ted Pella Inc.). The size and its distribution data were obtained by counting >1000 nanocrystalline particles using Image-Pro Plus 5.0 (Media Cybernetics, Inc., Silver Spring, MD).

7.2.2.3. X-ray photoelectron spectroscope (XPS)

XPS data was collected using a PHI Quantera XPS with a monochromatic Aluminum 38.6 W X-ray source and 200.0 μm X-ray spot size with a pass energy of 26.00 eV at 45.0°.

7.2.2.4. Dynamic light scattering (DLS)

The phase-transfer water-soluble nanocrystalline cerium oxide samples were characterized by dynamic light scattering (DLS) and zeta potential to measure the hydrodynamic size and surface charge, respectively. The hydrodynamic diameters and surface charge of different sized nanoceria covered with PAAOA, oleic acid, PMAO, and PEI were measured at 25 °C, using a Malvern Nano ZS system by Malvern Instruments (Malvern Zetasizer Nanoseries, Malvern, UK).

7.2.2.5. Inductively coupled plasma atomic emission spectroscopy (ICP)

The concentration of water transferred nanoceria was measured from ICP using a Perkin Elmer ICP-AES instrument equipped with an auto sampler. ICP samples were prepared by digestion of aqueous fractions using HNO₃ (99 %) and H₂O₂ (30 %) in a 5 ml of diluted nanoceria sample. The solution volume was decreased by heating to a fourth of its original volume. When the solution was dried to about 1/4 of the initial volume, 100 µl nitric acid was added. The obtained sample was treated by the further addition of 50 µl of nitric acid and 1 ml of H₂O₂ until effervescence stopped, indicating full dissolution of the ceria. The resulting colorless solution was transferred into a 5 ml volumetric flask and then diluted to 5 ml using DI-water.

7.2.2.6. GC-MS spectroscopy

Agilent Technologies 7890A GC system was used to measure the evolved oxygen amount during the decomposition of H₂O₂ in nanoceria solution. For the calibration of O₂ measurement, the vials (National Scientific Company (vial: C4020-210, septa: C4020-

36A)) were purged with nitrogen for 5 min and various amount of oxygen (0, 500, 1000, and 1500 μl) was injected into N_2 purged vials and 10 μl of the sample was injected into GC-MS using Pressure-Lok gas syringe (VICI Precision Analytical Syringe, Vacuum leak rate was less than 2.8×10^{-3} $\mu\text{l/hr.}$). These measurements were conducted in triplicates. Concentration (ppm) was calculated by considering the purged vials to be at 1atm, and then getting mass of the oxygen. The equation of oxygen calibration curve was $y=0.0007x$; y is relative abundance ratio of oxygen to nitrogen ($I_{\text{O}_2}/I_{\text{N}_2}$) and x is oxygen content (ppm).

To explore the abundance of evolved oxygen in nanoceria samples, the relative intensity ratios of oxygen to nitrogen were collected as a function of time after the injection of particular amount of H_2O_2 (1, 2, 5, and 10 μmol) in nanoceria solution (2.78 μM) in a 10 ml crimped vial.¹⁴²

7.2.2.7. Luminol test of water-soluble cerium oxide nanocrystals

H_2O_2 (6.45×10^{-4} M) from 0 to 50 μl was injected to an oleic acid coated 3.8 nm cerium oxide solution (0.011 μM). To measure the remaining concentration of H_2O_2 in the supernatant, the reaction solution was centrifuged at 43,000 rpm for 7 hrs. To measure chemiluminescence, 20 μl of the supernatant was mixed with 120 μl tris(hydroxyl methyl)-aminomethane buffer (pH \sim 10), 50 μl of 3% $\text{K}_3\text{Fe}(\text{CN})_6$, and 10 μl of luminol (1×10^{-2} M, pH \sim 10) in a 96-well plate(flat bottom, white polystyrene). The absorbance was measured at 485 nm by a spectrophotometer (SpectraMax M2, Molecular Devices, Sunnyvale, CA). This experiment was repeated in triplicate.

7.2.2.8. Oxygen-radical absorbance capacity (ORAC) assay

The assay was treated by the method mentioned by Lucente-Schultz et al.¹⁴⁰ Fluorescein sodium salt (FL, 0.2 μ M), 2-2'-Azobis(2-amidinopropane)dihydrochloride (AAPH, 0.15 M), and Racemic 6-hydroxy-2,5,7,8-tetramethylchromane-2-carboxylic acid (Trolox, from 1.5 to 10 μ M), and nanoceria (oleic acid coated- and PMAO coated- CeO_2 , from 1.5 to 10 μ M) were prepared in phosphate buffer saline (PBS) at pH 7.4 in a 96-well plate (flat bottom, black with clear bottom, polystyrene). The fluorescence intensity was measured at 530 nm by 485 nm excitation every minute for 6 h using a microplate reader (TECAN Infinite M200). The relative fluorescence intensity was measured by the assay (with antioxidant: 120 μ l FL + 20 μ l antioxidant + 60 μ l AAPH), Control 1 (without AAPH: 120 μ l FL + 20 μ l antioxidant + 60 μ l PBS), and Control 2 (without FL: 120 μ l PBS + 20 μ l antioxidant + 60 μ l PBS). The antioxidant capacity was calculated by measuring the area under curve (AUC) of the time dependent fluorescence intensity from the antioxidant (Trolox and nanoceria) and the blank (without the antioxidant) reported by Lúcio et al.¹⁴³ The assays were performed in triplicates.

$$\text{Antioxidant capacity (\%)} = \frac{\text{AUC}_{\text{Antioxidant}} - \text{AUC}_{\text{Blank}}}{\text{AUC}_{\text{Blank}}} \times 100$$

7.2.2.9. Measurement of intracellular reactive oxygen species (ROS) generation

Wild type Human Dermal Fibroblasts (GM00498) were obtained from Coriell Cell Repositories. Fibroblasts were grown at 37°C in 5% CO_2 in DMEM (Lonza), supplemented with 10% heat-inactivated fetal bovine serum and 1% glutamine Pen-Strep.

Medium was replaced every 3 or 4 days. Monolayers were passaged with TrypLE Express. We measured oxidative stress using Dihydrorhodamine 6G (DHR6G) and followed the method previously described by Qin et al.^{141a} Cells were cultured in medium containing cerium oxide nanocrystals for 24 hrs at 37 °C. The medium was replaced with fresh medium containing 2 mM hydrogen peroxide (H₂O₂) and samples were incubated for 2 h at 37 °C. Cells were washed with PBS and incubated with 5 μM DHR6G (Anaspec) in serum-free DMEM for 30 min at 37 °C. Cells were collected in PBS, centrifuged at 300 x g for 5 min, and washed with PBS. The fluorescence (FL) intensity was analyzed by flow cytometry (FACSCanto™II, BD Biosciences) using a 488-nm argon laser and 585/42 band pass filter. The relative fluorescence (FL_{relative}, %) was calculated by the equation mentioned below:

$$FL_{Relative} (\%) = \frac{FL_{Treated\ cells} - FL_{Untreated\ cells}}{FL_{Untreated\ cells}} \times 100$$

7.2.3. Synthesis of nanoceria

Three different diameter cerium oxide nanocrystals were synthesized by the decomposition of Ce(NO₃)₃·6H₂O in the presence of oleylamine at high temperature reported previously in this group.^{32b} 3.8 nm cerium oxide was synthesized by 1 mmol of Ce(NO₃)₃·6H₂O mixed with 3 mmol of oleylamine in 5 g ODE. 5.4 nm nanoceria was prepared by 5 mmol of Ce(NO₃)₃·6H₂O and 15 mmol of oleylamine in 5 g ODE. 8.2 nm nanoceria was obtained by adding water of 40 mmol in the cerium precursor and oleylamine mixture: the concentration of Ce(NO₃)₃·6H₂O and oleylamine were 10 and 40 mmol, respectively, in 5 g ODE. All chemicals were mixed at room temperature and

dissolved at 80 °C for 30 min. Nanocrystals were grown at 260 °C for 2 hrs under ultra-high pure nitrogen condition.

The as-prepared nanoceria was purified using ethanol, acetone and hexane at least 5 times to remove un-reacted cerium precursor, surfactants, and ODE. The resulting deep brown precipitate gave pure ceria nanocrystals which are re-dispersible in various nonpolar solvents such as, chloroform, hexane and toluene.

7.2.4. Phase transfer of nanoceria

The as-synthesized nanoceria was transferred to aqueous solution using ligand exchange^{63a} and encapsulation methods.^{3a, 63b, 85} The as-synthesized nanoceria was covered with oleylamine and stable in various non-polar solvents (e.g. chloroform, hexane, and toluene). When oleic acid was added to oleylamine covered nanoceria, the hydrophobic-hydrophobic interaction occurred and made nanoceria soluble in water because of the carboxyl groups on the outer surface of nanoceria. The addition of PAAOA and PMAO is similar to the oleic acid bilayer method, resulting in double layers. Both amphiphilic polymers have long hydrophobic chains (octylamine of PAAOA, and 1-octadecene of PMAO) forming a double layer with oleylamine on the surface of nanoceria. PEI has a large number of amine groups and hence, makes nanoceria soluble in water by ligand exchange method.

7.2.4.1. Oleic acid coated nanoceria

Particular amount of oleic acid (from 30 to 250 μmol) was stirred with 1 ml of nanoceria/ethyl ether solution (typically, 5.4 mg/ml) and 10 ml of ultra pure water.

Aqueous and organic phases were mixed by application of a probe-sonicator (UP 50H, DR.HIELSCHER) for 5 min at 60 % amplitude and full cycle. The resulting solution was further stirred for 1 day to evaporate the ether and to obtain a clear yellow brown solution.

7.2.4.2. Polyacrylic acid octylamine (PAA-OA) coated nanoceria:

The synthesis of PAA-OA amphiphilic polymer was adapted from previous reports.⁸⁶ Various concentrations of PAA-OA (from 0.5 to 50 μmol) were added to 1 ml of nanoceria/ethyl ether solution (typically, 2.5 mg/ml) with 10 ml of ultra pure water. The mixed solution was sonicated using the probe sonicator at the same experimental set up, mentioned above.

7.2.4.3. PMAO coated nanoceria

PMAO (0.01 - 2.5 μmol) was added to 1ml of nanoceria/chloroform solution (about 1 mg/ml) with 10 ml of ultra pure water. The solution was probe-sonicated in the same condition, mentioned above.

7.2.4.4. PEI coated nanoceria

PEI (0.1 - 16 μmol) was added to 1ml of nanoceria/chloroform solution (about 5.7 mg/ml) then probe-sonicated with the same condition, mentioned above.

Purification of as-prepared water-soluble nanoceria was carried out using ultracentrifugation (Sorvall Discovery 100 SE Ultracentrifuge) at 40,000 rpm for 4 hrs, followed by syringe filtration (pore size of 0.45 μm , WHATMAN-NYL). All the

resulting phase transfer nanoceria pellets were re-dispersed and stable in Mili-Q water, phosphate or sodium bicarbonate buffer solution (pH was from 5 to 10).

7.2.5. Nanoparticle concentration calculation

Nanoparticle concentrations are found from analytical measures of total cerium concentration in solutions digested with acids. To require an estimate of the weight of a single particle we assumed a particle volume of $\frac{4}{3}r^3$ where r is the average radius of the nanocrystal as determined by TEM measurements of over 1,000 particles; then we took the density of CeO_2 in the nanoparticle to be equivalent to that of the bulk phase (e.g. 7.65 g/ml) and could calculate the particle weight.^{32b} As an example, the volume of a 3.8 nm diameter particle of CeO_2 is 2.87×10^{-20} ml, which provides a total mass per particle of 2.2×10^{-19} g. Using this data, and Avogadro's number, we find for a solution 300 ppm in cerium a nanoparticle concentration of 2.78 μM .

7.2.6. The calculation of the concentration of cerium oxide nanocrystals using the molecular weight of a cerium oxide nanocrystal.

The concentration nanocrystalline cerium oxide was also calculated using the density of bulk cerium oxide and percentage of cerium (III) from XPS analysis. Briefly, to get the weight of one nanocrystal, the density of CeO_{2-x} was calculated based on the density of cerium oxide (CeO_2 : 7.6 g/ml; Ce_2O_3 : 6.2 g/ml), and 44 % of cerium (III) obtained by XPS analysis; the calculated density of CeO_{2-x} was about 7.0 g/ml. Then the molecular weight of a 3.8 nm cerium oxide nanocrystal was obtained using the volume of one 3.8 nm nanocrystal analytical and the Avogadro's number. For example, the volume of one

nanocrystal is $2.87 \times 10^{-20} \text{ cm}^3$, which provides the weight of a nanocrystal of $2.0 \times 10^{-19} \text{ g}$ and the weight of one mole of nanocrystal of 121218.13 g/mol. Since the cerium concentration measured by ICP is 300 mg/L, the total concentration of 3.8 nm cerium oxide nanocrystal suspension is $3.03 \text{ } \mu\text{M}$ ($0.0091 \text{ } \mu\text{mol}$). This is very close to the number of nanocrystal concentration described in the experimental section: $2.78 \text{ } \mu\text{M}$ of cerium oxide nanocrystal concentration.

7.2.7. The calculation of Ce(III) ions on the surface of one nanocrystal¹⁴⁴

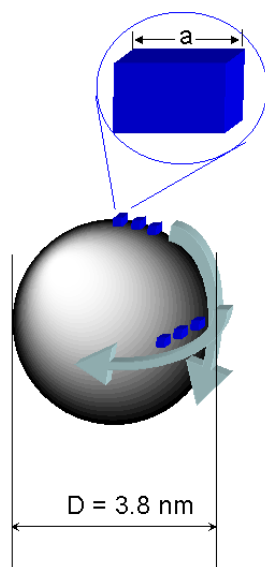


Figure 7.1 The calculation of the number of unit cells on the surface of 3.8 nm cerium oxide nanocrystal.

The number of Ce ions in one unit cell (Cubic fluorite) = 4 ions (8 at corners and 6 on the faces)

Let us consider that there is an outer shell of atoms surrounding the core of the nanoparticle. Thickness of this shell = $\frac{1}{2} \times 5.39 \times 10^{-10} = 2.69 \times 10^{-10}$ (m) (Thickness of the shell is assumed to be a half of the lattice constant.)

$$\text{Volume of the core} = \frac{4}{3} \times 3.14 \times (1.9 \times 10^{-9} - 2.69 \times 10^{-10})^3 = 1.82 \times 10^{-26} \text{ m}^3$$

$$\text{Volume of the cluster} = \frac{4}{3} \times 3.14 \times (1.9 \times 10^{-9})^3 = 2.87 \times 10^{-26} \text{ m}^3$$

$$\text{Volume of the shell} = 2.87 \times 10^{-26} - 1.82 \times 10^{-26} = 1.06 \times 10^{-26} \text{ m}^3$$

$$\text{Volume of single unit cell (a}^3\text{)} = (5.39 \times 10^{-10})^3 = 1.57 \times 10^{-28} \text{ m}^3$$

The number of unit cells on the shell of nanoparticle = Volume of the shell / Volume of single unit cell = $\frac{1.06 \times 10^{-26}}{1.57 \times 10^{-28}} = 67.4$ ea

Since each unit cell has 4 Ce ions, the number of Ce ions on the surface (shell) of nanoparticle = $4 \times 67.4 = 269.5$ ea

Base on the XPS study, Ce(III) is 44 % of Ce ions on the surface. Therefore, the number of Ce(III) is $269.5 \times 0.44 = 118.6 \approx 119$.

Concentration of cerium oxide nanoparticles = 2.78 μM

Volume of CeO₂ nanocrystal suspension = 3 ml

The number of Ce(III) in nanoceria solution =

N_A (particles/mol) $\times 8.34 \times 10^{-9}$ (mol) $\times 119$ (Ce(III)/particle) = $9.9246 \times 10^{-7} N_A$ of Ce(III)
(N_A is avogadro's number = 6.02×10^{23} particles/mol)

Therefore, about 0.99246 μmol of Ce(III) is in the nanoceria solution.

7.2.8. Cell viability test using water soluble cerium oxide nanocrystals

7.2.8.1. Cell Culture

Human dermal fibroblasts (HDF, Cambrex) were purchased from Cambrex and cultured in Dulbecco's Modified Eagle's Medium (DMEM, ATCC, Manassas, VA), supplemented with 2 mM L-glutamine, 1% penicillin, 1% streptomycin, and 10% fetal bovine serum (FBS). Cells were detached from culture with trypsin and re-suspended in media for passaging to wells. Cells were used at passages from 3 to 6 for experiments.

7.2.8.2. MTS cell viability assay

The standardized colorimetric assay, MTS (CellTiter 96, Promega), was used to evaluate mitochondrial activity. HDF cells were grown to 80 % confluency in 96-well culture plates and introduced to 3.8 nm oleic acid coated nanoceria (from 0 to 3.1 μM of nanocrystal concentrations). The treated cells were incubated for 24 at 37 °C under 5% CO_2 . Then, the supernatant containing the nanocrystals was removed from the wells and replaced with 100 μL of fresh DMEM that is phenol-red free (Gibco/Invitrogen); 20 μL MTS stock solution was added to each well. The MTS assay is reduced by enzymes in live cells, producing a purple formazon dye. After incubating at 37 °C for 1 h, the absorbance at 490 nm of the dye produced was measured using a plate reader (TECAN Infinite M200). Each experiment was repeated four times to obtain the average value.

7.3. Results and Discussion

7.3.1. Physico-chemical properties and mechanism for ceria reactions with hydrogen peroxides

Near-spherical ceria nanocrystals with diameters ranging from 4 to 8 nm were prepared by thermally decomposing cerium precursors in the presence of alkyl amines and water in 1-octadecene.^{32b} Figure 7.2 shows three different diameters of water-soluble nanocrystalline ceria produced from this reaction. The decomposition of cerium nitrate and oleylamine at 260 °C yielded the smallest nanocrystalline ceria. The addition of water promotes nanocrystal growth which in this study was used to produce the largest nanocrystals (8.2 ± 1.7 nm). These cerium oxide nanocrystals were phase transferred into aqueous solutions using amphiphilic surface agents such as fatty acids, co-polymers, and polyethyleneimine.^{3a, 32b, 63} The average diameters and morphology of the phase-transferred nanocrystals were identical to those observed for the as-prepared nanocrystals in organic solvents. Phase transfer yields exceeded 80 % under the appropriate conditions (Figure 7.3).

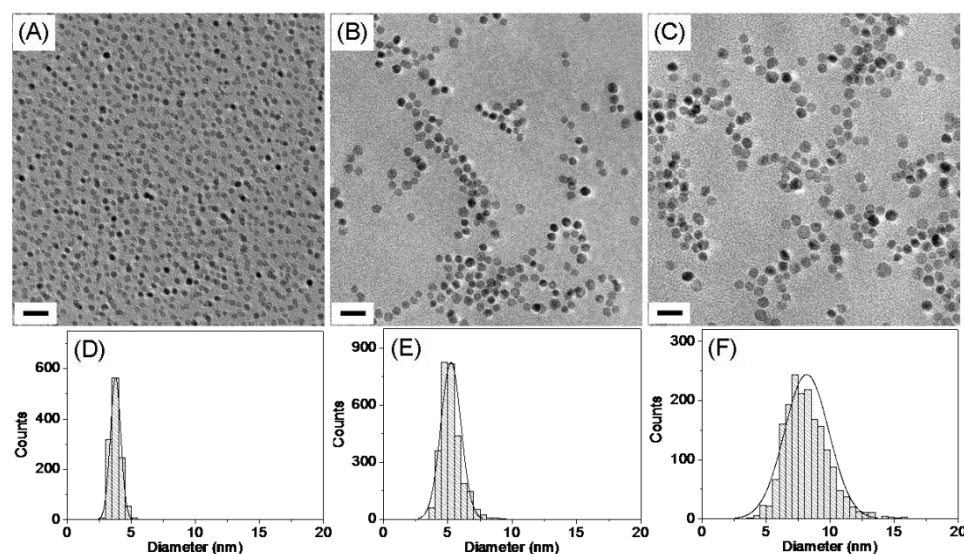


Figure 7.2 TEM micrographs (A to C) of water soluble nanoceria.

All scale bars are 20 nm from (A) to (C). (A) Oleic acid coated CeO_2 nanoparticles (3.8 ± 0.4 nm). (B) PEI coated CeO_2 nanoparticles (5.4 ± 1.0 nm). (C) PAA-OA coated CeO_2 nanoparticles (8.2 ± 1.7 nm). The size distribution histograms (D to F) are placed at the bottom of the corresponding images. To analyze the size, over 1000 particles were measured in multiple images using the software package ImagePro.

The hydrodynamic diameters of the nanocrystalline ceria in water reflected contributions from the inorganic core as well as the surface coating. The hydrodynamic diameters (D_H) of the four polymer coated cerium oxide nanocrystals are shown in Figure 7.4; these DLS measurements reveal that oleic acid and PAAOA applied to nanocrystal cores of 3.8 nm diameter produced materials with hydrodynamic diameters (D_H) of 5 nm. PEI and PMAO are larger molecular weight polymers and these coatings yielded particles with much larger D_H , 15 and 18 nm respectively. The inset images (A and B) in Figure 7.4 illustrate the compact structures of the former systems. The polymer coatings increased the hydrodynamic diameter irrespective of the core size of the nanocrystalline ceria. The zeta potential of oleic acid, PAAOA, and PMAO coated ceria nanocrystals

were -52.1, -41.4, and -34.2 mV, in contrast to amine functionalized polymer (PEI) coated ceria which was positively charged (0.2 mV).

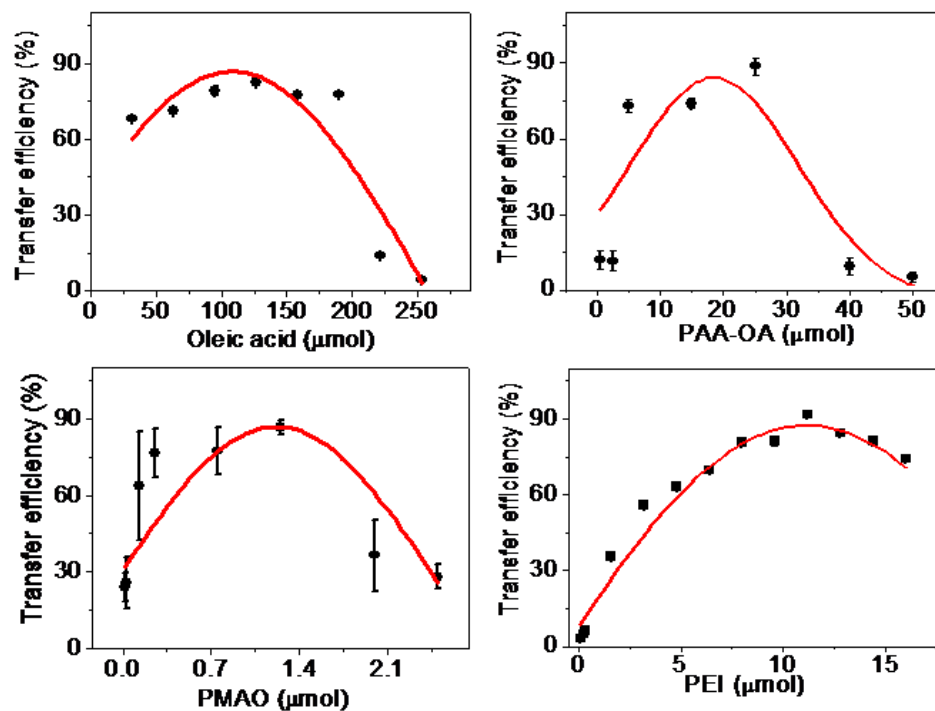


Figure 7.3 Phase transfer efficiency of water soluble nanoceria coated with 4 different phase transfer agents.

Lower concentration of phase transfer agents (oleic acid, PAAOA, PMAO and PEI) caused poor surface coverage that led to highly aggregated cerium oxide precipitates, which were not dispersible in water. Yet, higher concentration of phase transfer agents did not guarantee an increase in phase transfer efficiency because excess amount of surfactants formed micelles. These micelles lowered the solubility of water-soluble nanoceria.

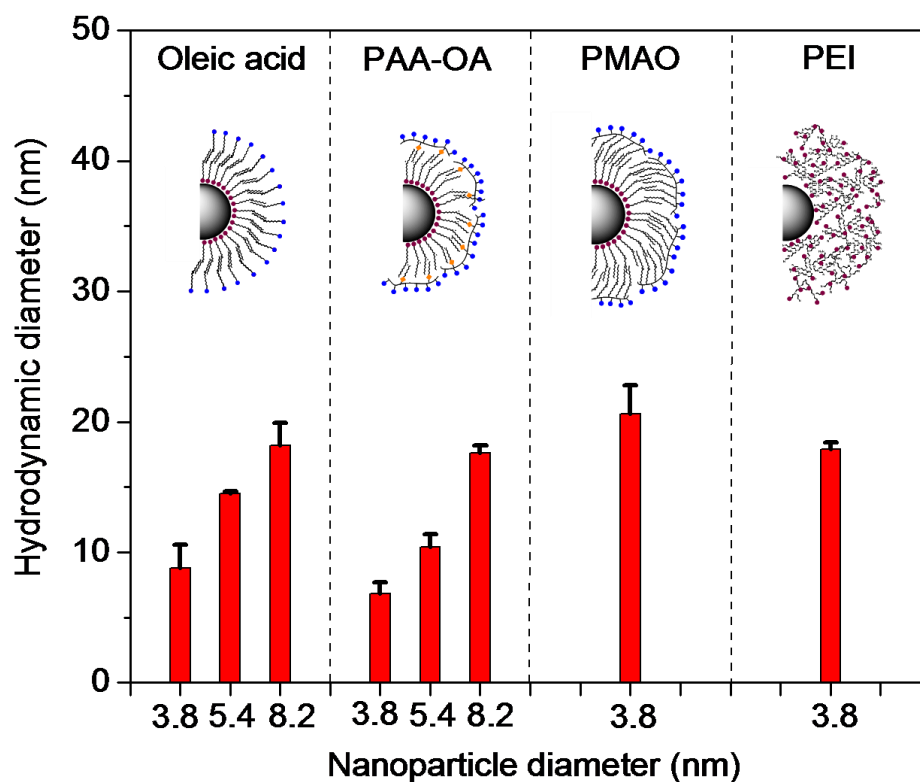


Figure 7.4 Hydrodynamic size of nanoceria.

The cartoon images show oleic acid, PAAOA, PMAO, and PEI coated nanoceria. In the structure, blue, yellow, and purple dots stand for carboxyl group, amide bond, and amine group, respectively. The average diameters of nanoceria covered with oleic acid, PAAOA, PMAO, and PEI were analyzed by dynamic light scattering (DLS). All samples were measured in triplicates.

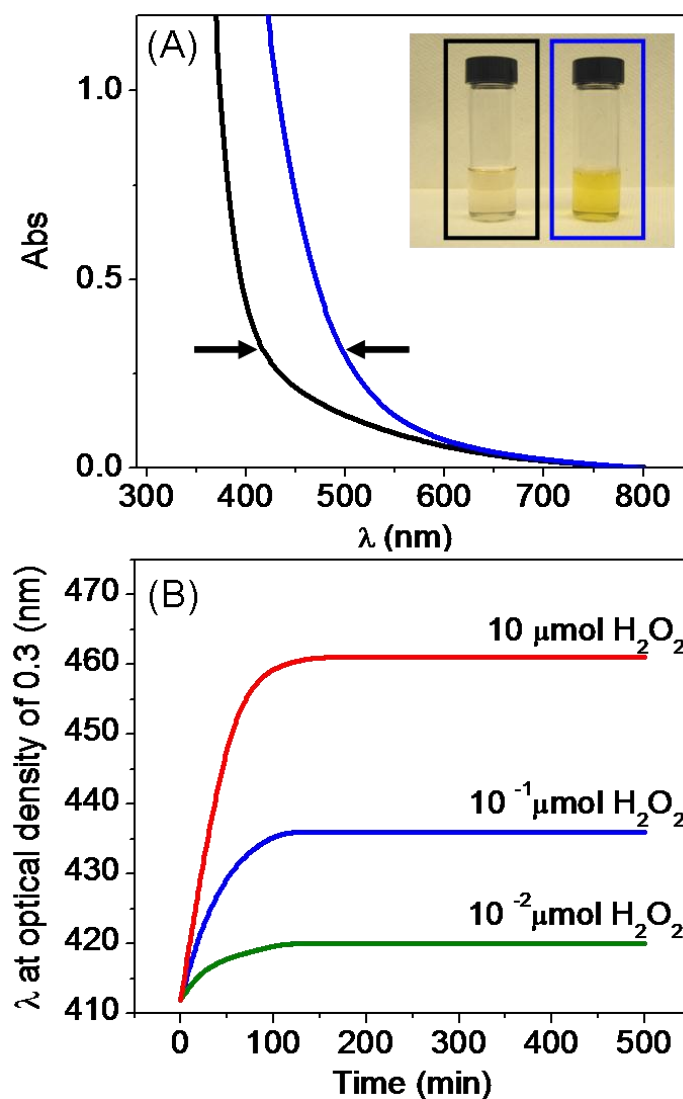


Figure 7.5 H₂O₂ quenching of water-soluble nanocrystalline cerium oxides.

(A) The inset UV-Vis band and the photo image demonstrate the red-shift from the control (black) to the as-reacted solution (blue) by the H₂O₂ injection. (B) The increasing extent of the red-shift of nanoceria suspension (2.78 μM) depending on the higher concentrations of H₂O₂ from 10⁻² to 10 μmol. 3.8 nm oleic acid coated nanoceria was used and the magnitude of the red-shifted wavelength of the UV-Vis band ($\Delta\lambda$) was measured between the control and the red-shifted band at optical density of 0.3.

Most studies of the antioxidant properties of nanoscale ceria have used colorimetric methods to examine the progress of a particle's reaction with H₂O₂; colorless pale yellow

cerium (III) gradually changes to the orange cerium (IV). Figure 7.5 shows how the absorption spectrum of a nanoceria suspension changes after H_2O_2 injection; the red-shift reflects the change of cerium (III) to cerium (IV).¹⁴⁵ The chemical reaction proposed to account for this color change is:^{66, 146}

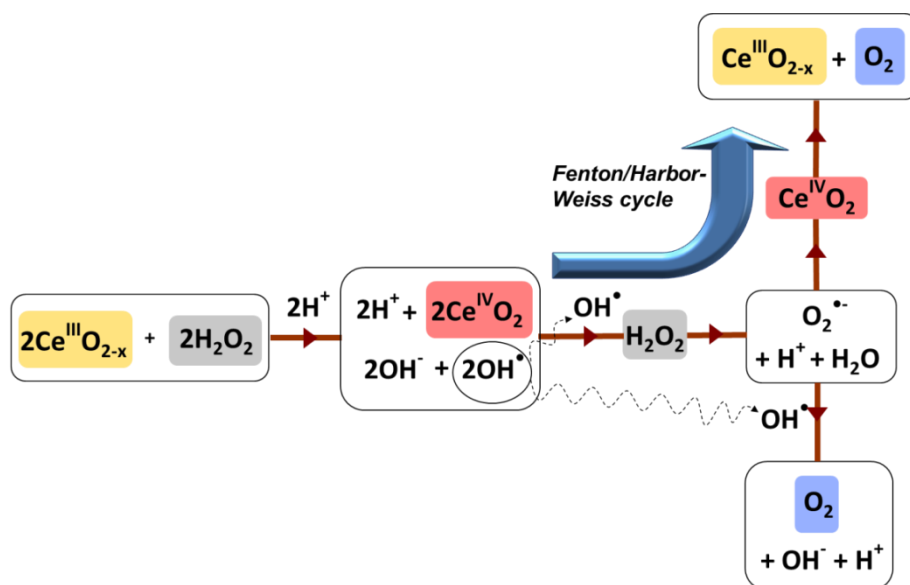


Figure 7.6 Redox cycling of cerium oxide through Fenton-type reaction.

Ce (III) reduce hydrogen peroxide and forms hydroxyl radicals and anions. These intermediate reactive oxygen species keep reacting with H_2O_2 and finally oxidized Ce (IV) is reduced to Ce (III) evolving oxygen (Fenton/Harbor-Weiss reaction; Ce(III): H_2O_2 : O_2 is 1:2:1.) However, if the reduction of Cerium ion does not occur and hydroxyl radical reacts with super oxide anion, Ce(IV) is not reduced and, the reaction ratio of cerium (III): H_2O_2 : O_2 is 2:3:1.5.

We verified that the shift in the absorption spectrum was consistent with changes in the cerium oxidation state using x-ray photoelectron spectroscopy (XPS). For example, after adding an excess of H_2O_2 to 3.8 nm cerium oxide, the cerium (III) concentration was reduced to 20 % from nearly 50 % prior to treatment (Figure 7.7). This finding illustrates that the active site on the surface of CeO_2 reacting with H_2O_2 is cerium (III)

and that the capacity of a ceria nanocrystal to react with H_2O_2 will be sensitive function of the starting cerium (III) concentration.^{130c}

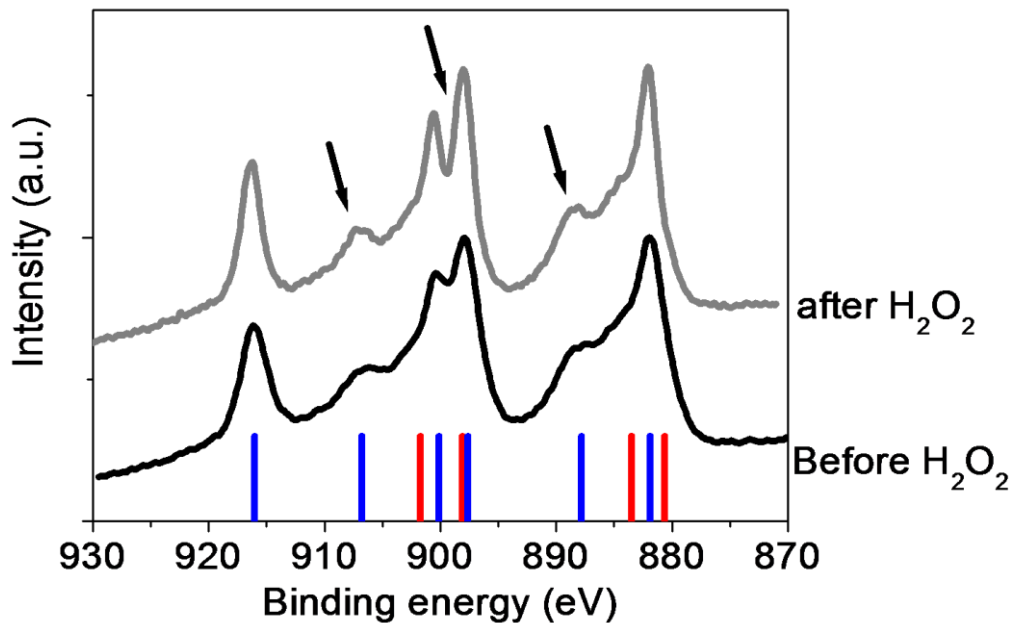


Figure 7.7 XPS data of 3.8 nm CeO₂ before and after H₂O₂ injection.

At the bottom of the chart, blue and red vertical lines stand for Ce(IV) and Ce(III), respectively. The arrow points reveal the clear difference between before and after H₂O₂ injection. Concentration of Cerium (III) and Cerium (IV) were calculated by the integration of the individual peaks from the fitted curve by MultiPak V7.0.1 (see Table 7-1).

Table 7-1 XPS analysis of individual peaks.

Cerium (III) concentration was calculated by $(V_1 + V_3 + V_6 + V_8)$.^{22b, 24-25, 32b, 130a, 130c} The ten individual peaks (from V_1 to V_{10}) were integrated in the cerium 3d region from 880 to 916 eV of the binding energy as shown in Figure 7.7.

	Size (nm)	V_1	V_2	V_3	V_4	V_5	V_6	V_7	V_8	V_9	V_{10}	%Ce(III)
Before H_2O_2 Injection	3.8	4.05 (880.64)	8.12 (881.93)	17.16 (883.54)	14.07 (887.84)	9.86 (897.66)	8.87 (898.39)	5.52 (900.18)	12.66 (901.77)	9.89 (906.62)	9.81 (916.01)	42.74
After H_2O_2 Injection	3.8	2.08 (881.04)	15.29 (882.42)	4.26 (884.32)	21.77 (887.31)	9.98 (897.58)	0.54 (898.14)	13.11 (899.77)	13.47 (902.23)	10.72 (906.80)	8.79 (916.56)	20.35

The underlying mechanism for the reaction between nanocrystalline ceria and hydrogen peroxide has been poorly defined for some time; while some investigators have proposed a direct reduction and oxidation process others suggest the reaction has more in common with a Fenton-type process of the type illustrated in reaction mechanism above; Karakoti *et al* hypothesized that the redox cycling of cerium ions occurs through Fenton type reaction producing hydroxyl anions and cerium peroxo complex.^{55, 57-58, 60, 66, 146} These two mechanisms can be distinguished by the very different reactant molar ratios expected: a 2:1 reactivity between H_2O_2 and cerium (III) is anticipated for a Fenton-type process as opposed to a 1:1 or 1:2 relationships for direct redox reactions. Also relevant is the fact that Fenton reactions usually proceed through hydroxyl radical intermediates, and thus are more pronounced at lower pH values.^{55, 58} (Figure 7.8)

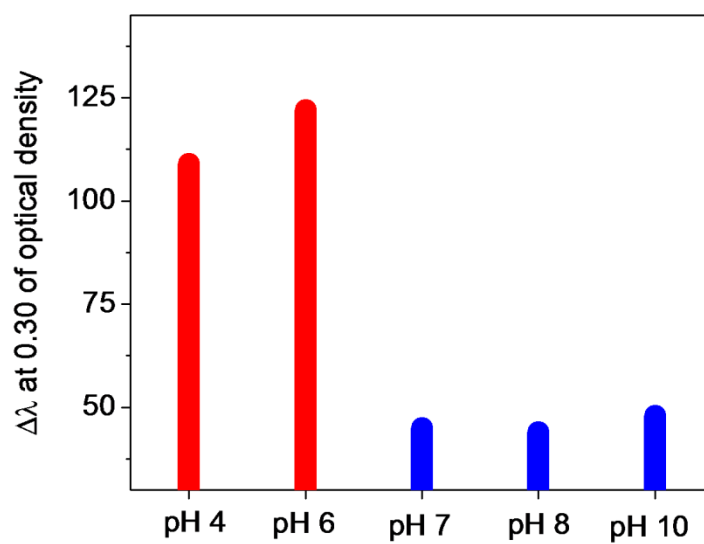


Figure 7.8 PH dependent antioxidant capacity of oleic acid coated cerium oxide suspension. Nanocrystalline ceria was more reactive with H_2O_2 in the less acidic condition than neutral and basic. However, oleic acid coated ceria nanocrystal ($\text{pH} < 6$) lost the colloidal stability resulting in the precipitates after 1 day.

To experimentally determine which mechanism may dominate for these particles, we measured the molar relationship between H_2O_2 and cerium (III) in this reaction. One analysis relied on GC-MS to quantify the O_2 evolved by the disproportionation of H_2O_2 as a function of time after the injection of peroxide in a nanoceria solution.¹⁴⁷ In addition, the remaining (un-reacted) H_2O_2 concentrations in nanoceria suspensions were measured by the luminol test.¹⁴⁸ To find the cerium (III) concentration we used the nanocrystal total cerium concentration as determined from ICP-AES, and the ratio between cerium (III) and cerium (IV) calculated from XPS (Figure 7.1).

These data, along with the pH dependence of the process, suggests that the antioxidant properties of nanocrystal ceria proceed through a Fenton type process. The amount of evolved oxygen after the decomposition of H_2O_2 by redox cycling of

nanoceria was found by measuring the relative abundance ratio of oxygen to nitrogen in a sealed vial (Figure 7.9).¹⁴²

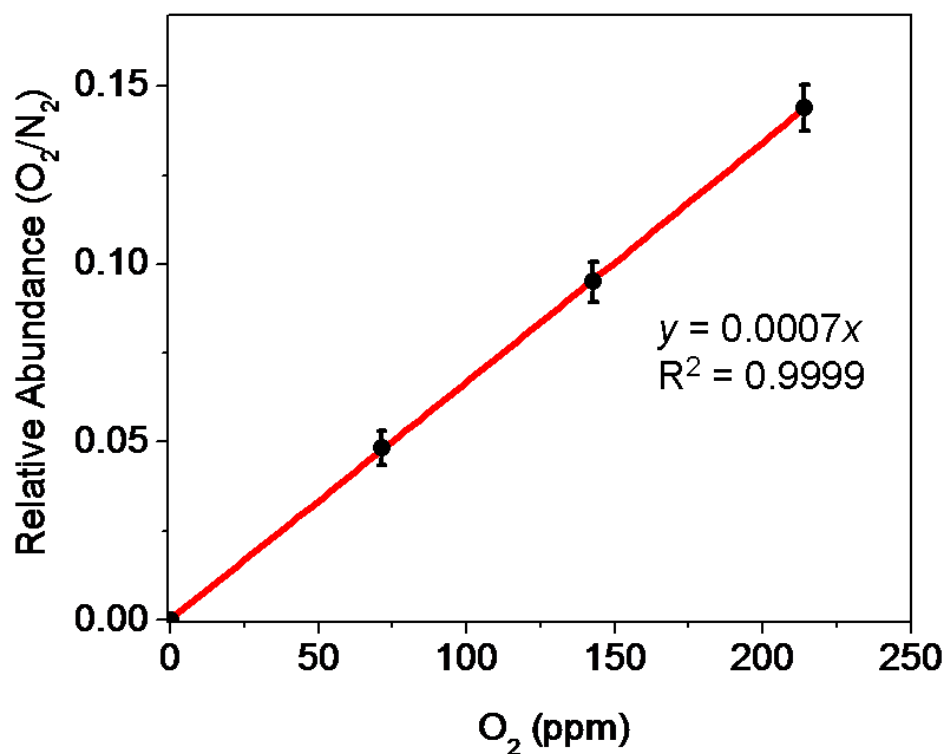


Figure 7.9 The calibration curve of O₂ in GC-MS analysis.

O₂ concentration was measured using relative abundance between O₂ and N₂. For details, 10 ml crimped vials were sealed tightly and purged with N₂ for 5 min. Then, 500, 1000, and 1500 μ l of O₂ were injected into N₂ purged vials and 10 μ l of the sample was injected into GC-MS using Pressure-Lok gas syringe (VICI Precision Analytical Syringe, Vacuum leak rate was less than 2.8×10^{-3} μ l/hr.). These measurements were repeated in triplicates. Concentration (ppm) was calculated by considering the purged vials to be at 1atm, and then getting mass of the oxygen.

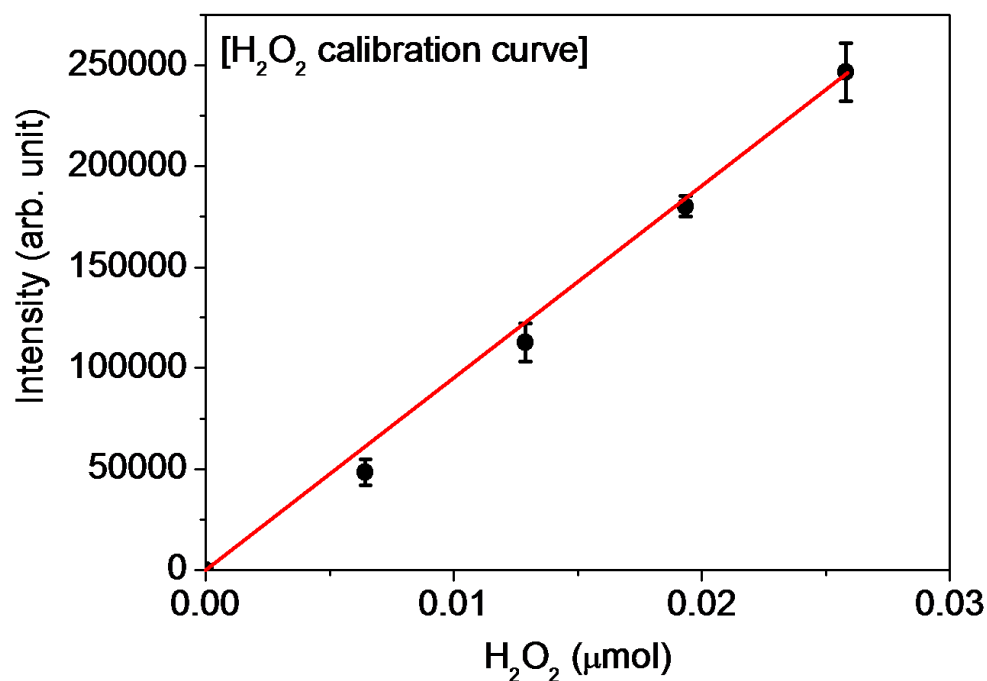


Figure 7.10 The H₂O₂ calibration curve for the luminol test.

The calibration curve was obtained by measuring the chemiluminescence of luminol as a function of the increasing concentration of the injected H₂O₂ (from 0 to 0.03 μmol). The equation of the curve was $y = 9.0 \times 10^6 x$ with 0.994 of R². (y = the intensity of luminescence, x = mol of H₂O₂)

The increasing O₂ evolution was monitored as a function of time. When the cerium (III) concentration was about 1 μmol (0.992 μmol), 1 and 2 μmol of H₂O₂ was fully decomposed by evolving about 0.5 and 1 μmol of O₂, respectively, whereas 5 and 10 μmol H₂O₂ addition left increasingly higher amount of unreacted H₂O₂. The same molar ratio was also found independently by measuring the amount of unreacted peroxide using a Luminol test (Figure 7.10).

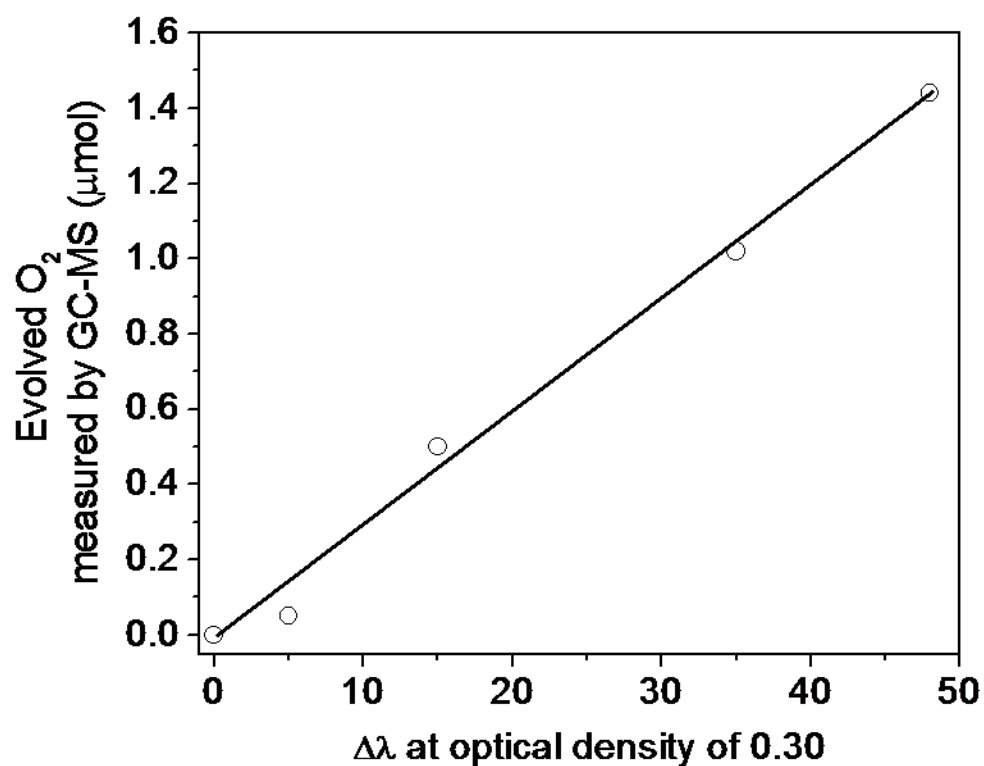


Figure 7.11 Decomposed H_2O_2 calculation using the red shift UV-Vis band and GC-MS data. Various molar concentrations of H_2O_2 (0, 0.1, 1, 5, 10 μmol) were injected into ceria nanocrystal suspensions (1 μmol of cerium (III) concentrations on the nanocrystals in the suspension). The decomposed H_2O_2 based on the measurement using GC-MS (Figure 7.12) was plotted as a function of the wavelength difference between the red shift UV-Vis band and the control at optical density of 0.30. The equation of the trend line was $y = 0.0298x$ (y is the evolved O_2 (μmol) and x is the $\Delta\lambda$ at optical density of 0.30) and $R^2 = 0.9915$. Using this equation and the disproportionation of H_2O_2 ($2H_2O_2 \rightarrow 2H_2O + O_2$), the total moles of the decomposed H_2O_2 were calculated in the multiple injections of H_2O_2 as shown in Figure 8. For example, oleic acid coated CeO_2 suspension under the multiple H_2O_2 injections showed 21.6 μmol of H_2O_2 decomposition for 18 cycles. (1 μmol of H_2O_2 was injected in every cycle.)

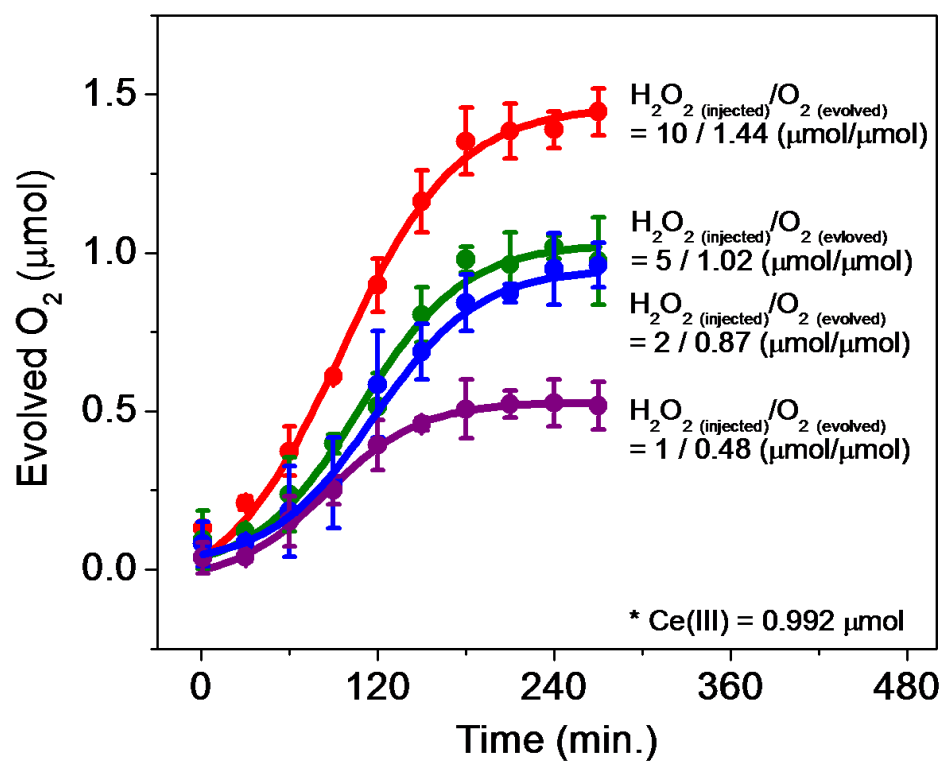


Figure 7.12 Quantitative analysis of H_2O_2 quenching of cerium oxide nanocrystals.

The evolved oxygen concentration increased when H_2O_2 was decomposed in 2.78 μM nanoceria suspension (pH = 7, cerium (III) = 0.992 μmol). The concentration of evolved oxygen was monitored and measured by GC-MS as a function of time. The ratio of H_2O_2 to cerium (III) was 2 to 1 (H_2O_2 decomposition reaction; $2H_2O_2 \rightarrow 2H_2O + O_2$). The measurements were repeated three times.

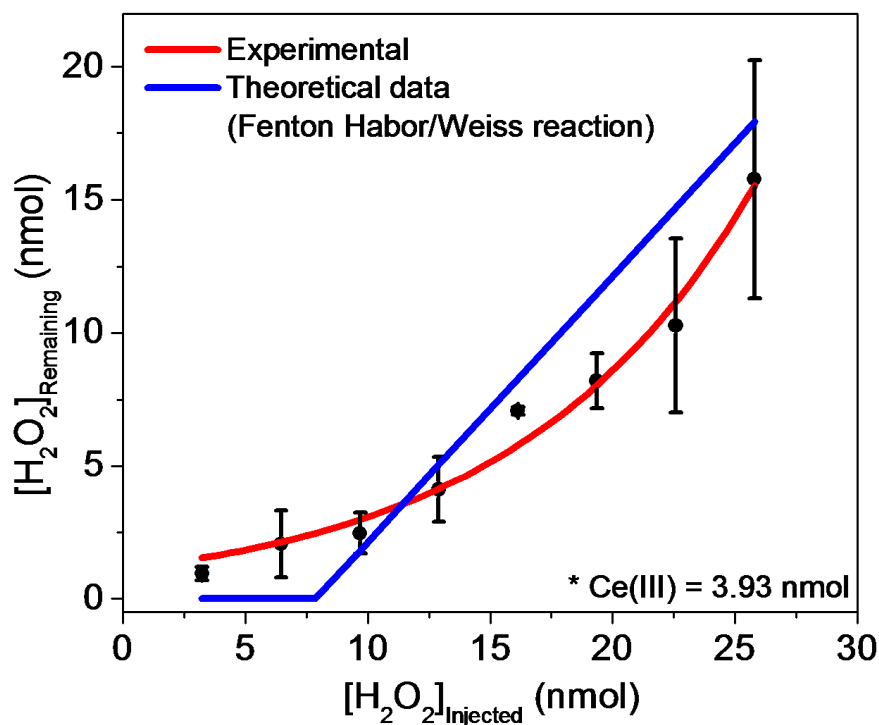


Figure 7.13 Quantitative analysis of H_2O_2 quenching of cerium oxide nanocrystals.

The remaining (un-reacted) H_2O_2 in a supernatant of nanoceria solution was measured by chemiluminescence from the reaction with luminol and peroxide after the separation of nanoceria using the ultracentrifugation method. 3.8 nm oleic acid coated cerium oxide was utilized with the increase in the injections of H_2O_2 . Based on the calibration curve (Supplemental Figure 7), the remaining molar H_2O_2 was obtained from the equation: $y = 9.0 \times 10^6 x$ (y = the intensity of luminescence, x = mole of H_2O_2). The theoretical data of the remaining H_2O_2 was obtained by the equation: $[H_2O_2]_{\text{remained}} = [H_2O_2]_{\text{injected}} - 2 \times 3.54$ (nmol of cerium (III)) in the solution; One molar cerium (III) decomposes 2 molar H_2O_2 in the Fenton-like reaction.

Figure 7.13 shows that the experimental curve obtained from the amount of unreacted peroxide fit well to the expectation of a Fenton-like reaction (the ratio between cerium ion and H_2O_2 is 1 to 2).⁵⁸ Moreover, we can correlate the shift in the absorption spectrum to the generation of oxygen through this process. As Ce(III) is converted to Ce(IV) the color of the solution changes roughly linearly with the amount of Ce(III) converted; Figure 7.11 shows that as more of this is converted you get more oxygen with a 0.0298

slope. Finally, consistent with this data is the observation that the reaction is pH dependent. Specifically at lower pH values it is more reactive (Figure 7.8).

7.3.2. Benchmarking of anti-oxidant capacity and trends with size and surface coating

A critical question to address is what the capacity is for different particles, with different sizes and coatings, to react with hydrogen peroxide through the Fenton-type chemistry described above. For the purposes of this discussion, we refer to this parameter as the antioxidant capacity so as to align our discussion with the literature on antioxidants.^{58, 139, 148a} One way convenient way to characterize this and compare it across samples is to use colorimetric data to indicate the amount of Ce(IV) produced. Here we defined the shift ($\Delta\lambda$) by measuring the wavelength of 0.3 optical density before and after peroxide addition. For example, 100 nmol of H₂O₂ led to only a 10 nm red shift in one case while 10 μ mol of H₂O₂ led to a shift of 50 nm absorbance wavelength. This data shows that adding more peroxide increases the shift of the spectrum as more Ce(IV) is produced. However, for all samples there is a saturation point at which further addition of peroxide leads to no change. For example, for the former samples the absorption shift remained the same between 10 and 15 μ mol of H₂O₂ addition. For these measurements all nanoparticle solutions were fixed at 2.78 μ M of ceria concentration (cerium (III) concentrations on the surfaces of the nanoparticles are 1 μ mol; see Figure 7.1). Note that the molecular weight of the nanoparticles varies sensitively with their diameter, but for a 3.8 nm nanocrystal the equivalent particle concentration is roughly 10 pmol.

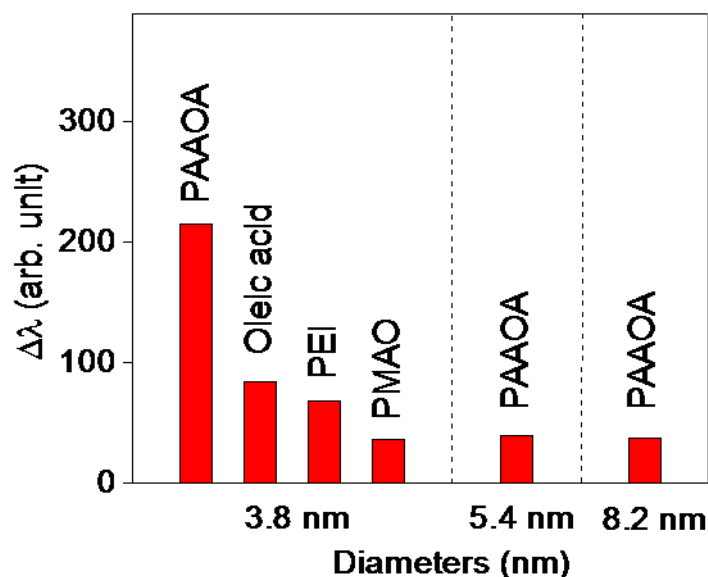


Figure 7.14 The different extents of H_2O_2 quenching capacity depending on various diameters and surface stabilizers on nanoceria.

To compare the surface polymer dependent H_2O_2 quenching efficiency of nanoceria, the extent of the band shift ($\Delta\lambda$) was measured at 0.30 absorbance after the injection of H_2O_2 from the control. For the diameter dependent H_2O_2 quenching, three different diameter CeO_2 suspensions were utilized ($d = 3.8, 5.4, 8.2$ nm; PAAOA coated CeO_2). Surface coating dependent H_2O_2 quenching was shown by 3.8 nm CeO_2 covered with four different polymers (PAAOA, oleic acid, PEI, and PMAO).

These colorimetric tests reveal that the smallest nanoceria has the largest absorption change after the addition of H_2O_2 and hence greatest antioxidant capacity (Figure 7.14). We attribute this to both the higher concentration of cerium (III) in these nanocrystals and the increased stability of the cerium (IV). The smallest particle has the greatest concentration of cerium (III) on the surface of nanoceria because of the increasing lattice expansion and the release of oxygen atoms.^{24-25, 124a} For example, we found that the cerium (III) concentrations from different diameter ceria samples were 43, 39 and 30 % from 3.8, 5.4, and 8.2 nm cerium oxide, respectively.^{32b} All of the various surface coatings showed similar trends: smaller nanocrystals had higher antioxidant capacities.

For example, PAAOA coated 3.8 nm CeO₂ after treatment with excess H₂O₂ had $\Delta\lambda$ of 215 as compared to 8.2 nm diameter nanoceria having only $\Delta\lambda$ of 37 nm.

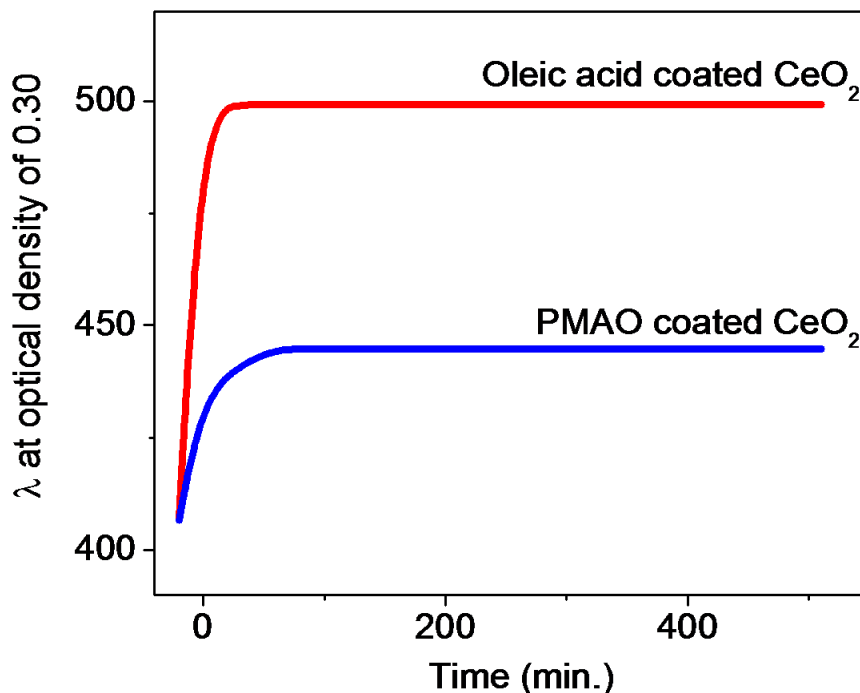


Figure 7.15 The magnitude of the red shift UV-Vis band of oleic acid and PMAO coated ceria nanocrystal suspension after H₂O₂ injection.

10 μmol of H₂O₂ was injected in 2.78 μM of ceria nanocrystal suspension and the wavelength at optical density of 0.30 was measured as a function of time (min). Oleic acid coated CeO₂ was saturated quickly with the higher red-shifted UV-Vis band as compared to PMAO coated one.

In addition to the diameter of the nanocrystalline ceria, the surface coating also played a significant role in defining the reactivity of the material. Specifically, when nanocrystals were coated with thicker polymers their antioxidant capacity diminished. Figure 7.14 shows the shift in the extents of H₂O₂ quenching capacity for four different polymer coating materials (oleic acid, PAAOA, PEI, and PMAO) for 3.8 nm diameter ceria cores. PAAOA coated nanoceria, as expected, had the largest red-shift

corresponding to the most reactivity towards hydrogen peroxide. The reactivity of other polymer coatings scaled well with their thickness as measured using dynamic light scattering (Figure 7.4). We speculate that the very thinnest surface coatings present small kinetic barriers to the interfacial reaction between H_2O_2 and cerium (III), while thicker polymer molecules block surfaces from H_2O_2 . While we generally gave the system enough time to react so our observations would reflect equilibrium, we did observe that the thinnest surface coating (e.g. oleic acid on CeO_2) became saturated within only 30 minutes as compared to the thicker polymer coated ceria (e.g. PMAO coated CeO_2) which required 60 minutes (Figure 7.15).

Absorption spectroscopy is an excellent method to compare relative quenching capacities among particles, but these data do not provide a benchmark against known anti-oxidant and radiation protection molecules already widely used. For this purpose, we applied a standard test, the oxygen-radical absorbance capacity (ORAC) assay,¹⁴⁰ to the best performing nanocrystalline ceria from the peroxide tests: nanocrystalline ceria with 3.8 nm core diameter coated with oleic acid. This test monitors how the fluorescence from a Fluorescein salt persists in the presence of an antioxidant which scavenges reactive oxygen species (ROS) generated by the radical initiator, AAPH. A fluorescence intensity that persists for a long time indicates a strong antioxidant.

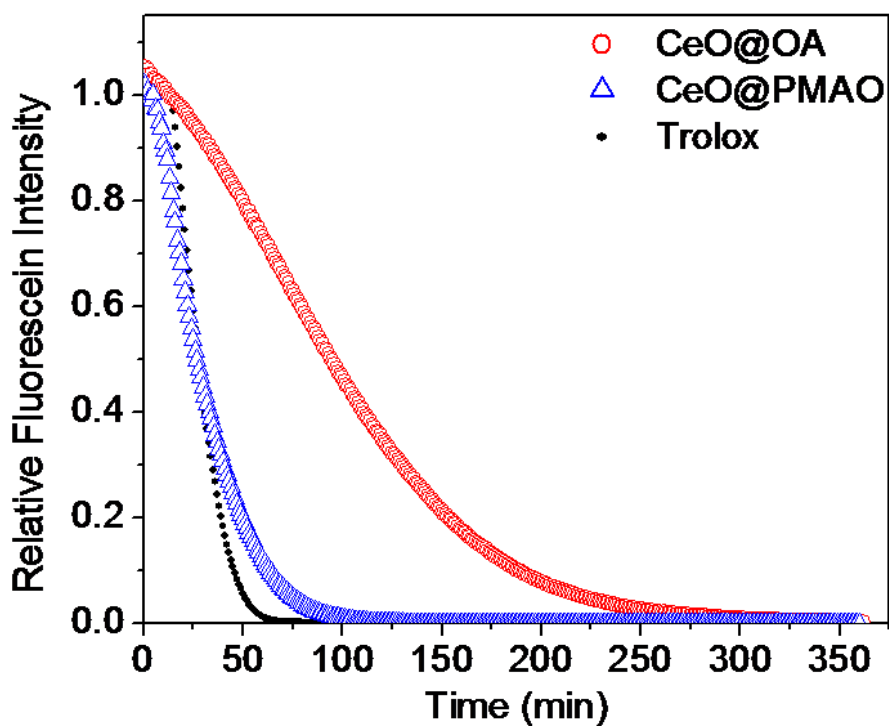


Figure 7.16 Oxygen-radical absorbance capacity (ORAC) assay of oleic acid coated – (red), PMAO coated – (blue) nanoceria and Trolox (black).

The concentration of cerium oxide nanocrystals (the number of nanocrystals in the suspension; see the experimental section) and Trolox ($C_{14}H_{18}O_4$; mass of trolox was divided by the molar mass of 250.29 g/mol) was $0.8 \mu\text{M}$. Fluorescence was measured every minute for 6 hrs. In order to characterize the percentage of the antioxidant capacity of given substances, the area under curve (AUC) was calculated from each graph and divided by the AUC of the blank sample (see the experimental section).

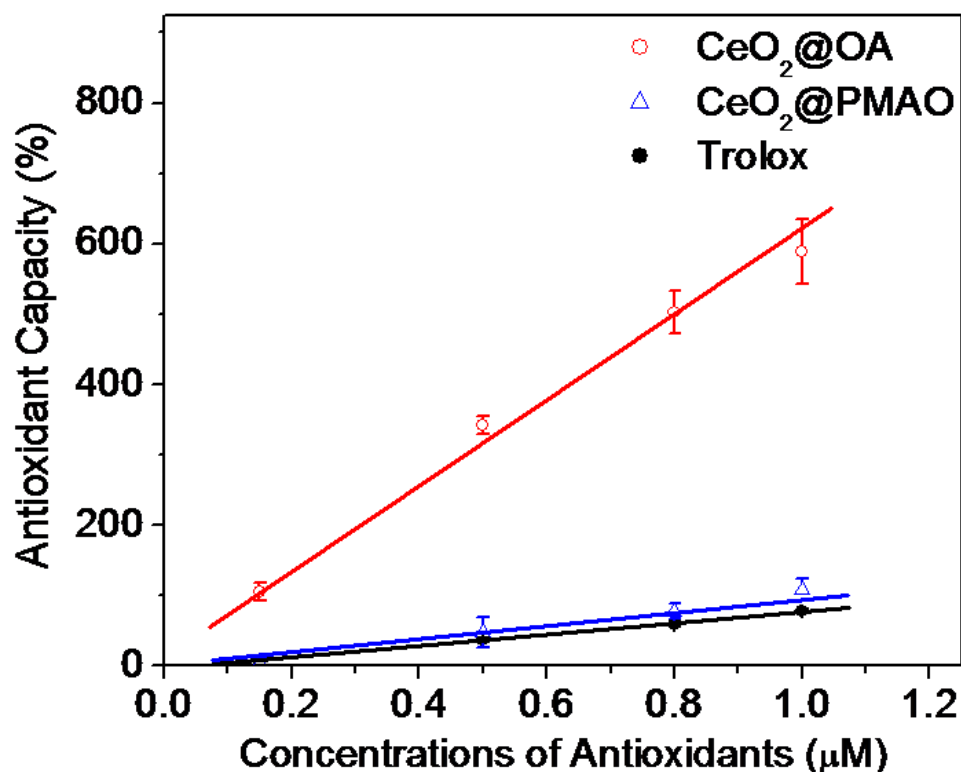


Figure 7.17 Antioxidant capacity of cerium oxide nanocrystals.

The capacity was calculated from the equation mentioned from Lucio et al.¹⁴³ The slopes of the trend lines from oleic acid coated- (red), PMAO coated- (blue), nanoceria and Trolox (black) are 616.02, 95.76, and 73.24, respectively. All measurements were repeated three times.

This ORAC assay revealed that the antioxidant capacity of oleic acid coated cerium oxide was 9 times higher than a water-soluble derivative of Vitamin E, Trolox (Figure 7.17). In this assay, all antioxidant samples (nanoceria and Trolox) were stored in PBS (pH = 7) from 0.1 to 1 μM and the fluorescence intensity was monitored after the injection of 45 mM of AAPH in every minute for 6 hours as shown in Figure 7.16. The thinnest surface coating (oleic acid) present on ceria nanocrystal allows more radical scavenging than the thickest polymer (PMAO) on the nanocrystal; PMAO coated nanoceria which has a very similar antioxidant capacity to Trolox. Furthermore, the

nanoceria showed efficacy at sub micromolar concentrations in ceria, and even nanomolar concentrations with regards to the entire particles. In comparison, standard concentrations of 1 to 10 micromolar vitamin E or single-walled carbon nanotubes are typically applied.^{139-140, 143} We also note that oleic acid coated ceria is non-toxic at these concentrations in an MTS assay using HDF cell line; LD₅₀ is 1.8 μ M as shown in Figure 7.18. These data suggest that the oleic acid coated nanoceria could be a potent antioxidant material with high radical scavenger capacity and low toxicity.

All of the prior benchmarks for anti-oxidant capacity were completed outside of cell culture; to understand how the results translated in a cellular system we examined the ability of nanocrystalline ceria to protect cells from hydrogen peroxide. We performed intracellular reactive oxygen species (ROS) measurements. In this measurement, a standard fluorescence dye molecule, Dihydrorhodamine 6G (DHR6G), was used for ROS analysis. As a standard oxidant we employed hydrogen peroxide. As peroxide levels, or associated ROS, increased in a cell DHR6G reacted with ROS and turned to Rhodamine 6G (R6G). Therefore, the higher fluorescence intensity of R6G indicates the more oxidative stress. To explore antioxidant capacity of cerium oxide nanocrystals toward H₂O₂ driven oxidative stress of fibroblasts, cells were cultured in the presence of cerium oxide nanocrystals at 37 °C for 1 day. Relatively high nanocrystal exposures (100 ppm of cerium), close to the LD₅₀ values, were employed (the LD₅₀ value for 3.8 nm was 94.9 ppm (1789.9 nM of nanocrystals); and for 8.2 nm cerium oxide nanocrystals, 87.7 ppm (87.2 nM of nanocrystals)) during the first exposure. The higher concentrations over LD₅₀ resulted in cell death. The cells were then washed, and the medium was then changed, and replaced with a fresh medium that contained a large 2 mM H₂O₂ dose. In

this experimental scheme, only ceria nanocrystals that were internalized could be responsible for any observed protective effect.

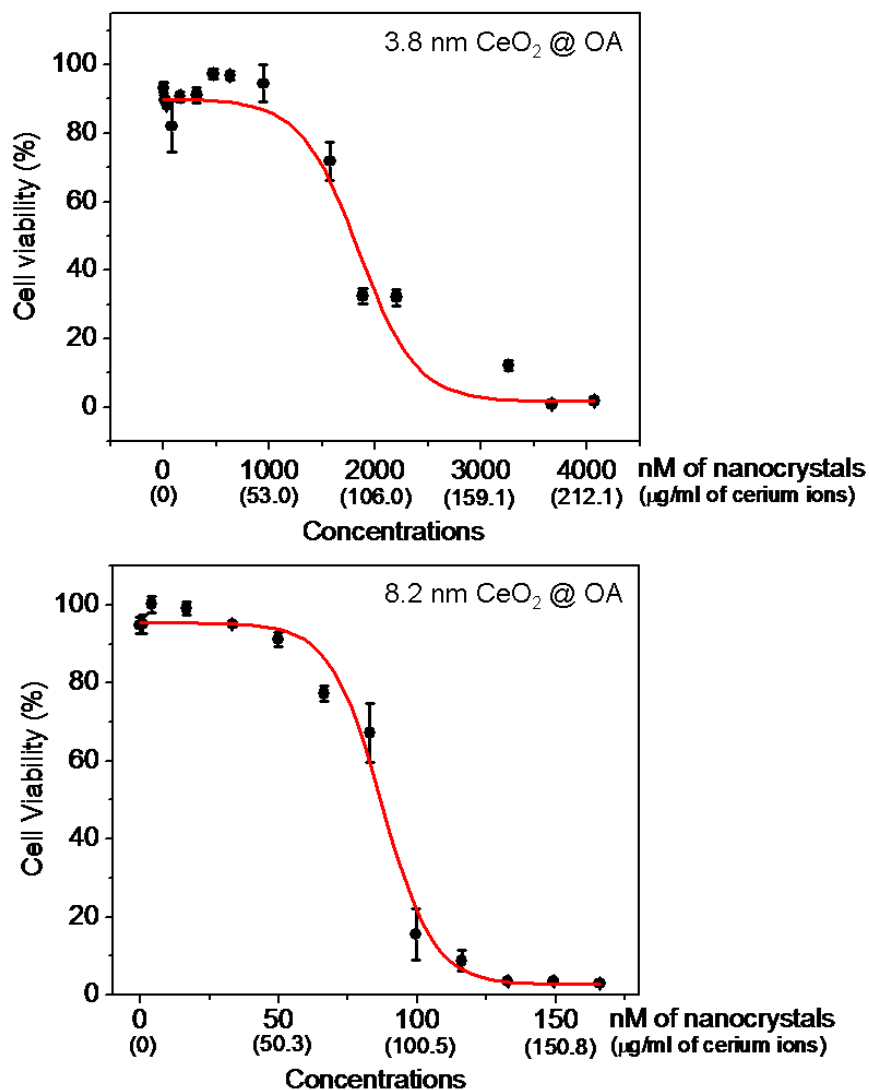


Figure 7.18 Cell viability of Human Dermal Fibroblast (HDF) cell line in the presence of 3.8 and 8.2 nm coated cerium oxide nanocrystals coated with oleic acid.

In the MTS analysis, HDF cells exhibited a decrease in viability as ceria nanocrystal concentration increased. A acute cell viability assay revealed that a LD₅₀ value for 3.8 nm cerium oxide nanocrystals coated with oleic acid was 1.8 μM (94.9 ppm), and for 8.2 nm cerium oxides, 87.2 nM (87.7 ppm). The ORAC assay using trolox and 3.8 nm cerium oxides in Figure 7 was treated under the concentration of 1000 nM (0.15, 0.5, 0.8, and 1 μM).

In all cases, prior exposure to cerium oxide nanocrystals led to a protective effect and less oxidative stress. Figure 7.19 shows the bar graphs of relative R6G fluorescence from the samples (untreated -, 3.8 nm cerium oxide -, 8.2 nm cerium oxide nanocrystal treated cells) as injected hydrogen peroxide increased. When fibroblasts were not treated with cerium oxides, oxidative stress increased up to 74 % when 2 mM of H_2O_2 was added. However, cerium oxide treated cells reduced oxidative stress of fibroblast cells (relative R6G fluorescence was -51 and -24 % from 3.8 and 8.2 nm cerium oxide treated cells, respectively.) In addition, significant reduction in oxidative stress occurred from fibroblasts treated with the smallest cerium oxide nanocrystals (3.8 nm) than the biggest cerium oxides (8.2 nm). The highest percentage of cerium (III) concentration from the smallest cerium oxide nanocrystal (43 % of Ce (III) from 3.8 nm cerium oxide) could scavenge ROS in the cells more effectively than the biggest cerium oxide nanocrystal (30 % of Ce (III) from 8.2 nm cerium oxide). This ROS measurement assay shows that the oleic acid coated cerium oxide nanocrystals are of interest in biological application especially to scavenge reactive oxygen species.

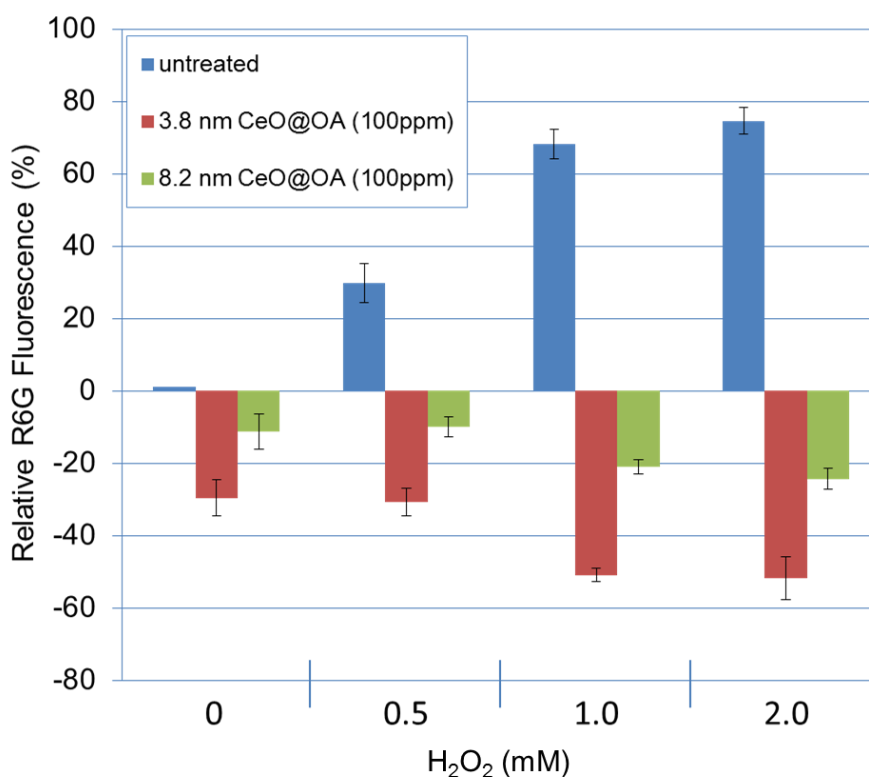


Figure 7.19 Intracellular ROS measurement.

Relative R6G fluorescence (%) was calculated by the equation mentioned in experimental details. Oxidative stress of fibroblasts (untreated, blue bars) increased as applied hydrogen peroxide amount increased. However, cerium oxide treated fibroblasts decreased oxidative stress of fibroblasts; 3.8 nm cerium oxide (red bar) more effectively scavenge ROS than 8.2 nm cerium oxide (green bar) in the media.

7.3.3. Recycling behavior of nanoscale ceria and its dependence on surface coating

One finding from this work is that nanoparticles may be reused as antioxidants because cerium (IV) can in some cases slowly recycle back to cerium (III). Das *et al.* demonstrated this feasibility of the redox cycling of cerium ions using nanoceria prepared by co-precipitation method; the pale yellow solution formed after hydrogen peroxide

reaction passively returned to its original position in a matter of days.³¹ (Figure 7.20 and Figure 7.21) As is apparent, many of these samples can be used again and again presumably after native donors present in water have converted the cerium (IV) back to cerium (III).

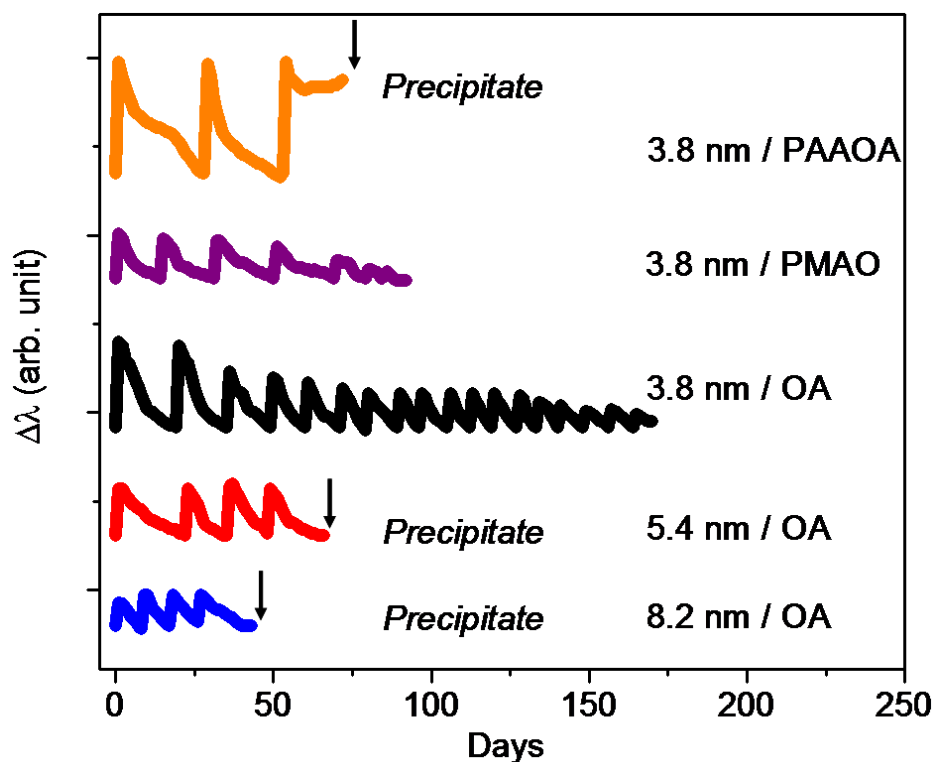


Figure 7.20 Antioxidant property of water-soluble nanoceria coated with bilayer surface structures. PAAOA, oleic acid (OA), and PMAO coated nanoceria in diameter of 3.8, 5.4, and 8.2 nm were utilized. All cerium oxide nanocrystal concentrations were $2.78 \mu\text{M}$ (Cerium (III) concentration on the surface of nanocrystal: $1 \mu\text{mol}$) and $10 \mu\text{mol}$ of H_2O_2 was injected in every cycle. The wavelength (λ) of the red-shifted UV-Vis band was monitored at optical density of 0.30 abs as a function of time. UV band was recovered as time goes on and the additional injections of H_2O_2 gave rise to the red-shift, again. However, the multiple injections of H_2O_2 led to the reduction in quenching property (the extent of $\Delta\lambda$) of nanoceria suspension. 3.8 nm PMAO and oleic acid (OA) coated cerium oxide did not show any visible precipitate but the H_2O_2 quenching property decreased by multiple injection of H_2O_2 . PAAOA coated cerium oxide was precipitated after 3rd injection of H_2O_2 and 5.4 and 8.2 nm OA coated CeO_2 was precipitated after 4th addition of H_2O_2 . PEI coated CeO_2 was never recovered from the 1st injection of H_2O_2 and lost its colloidal stability (Figure 7.21).

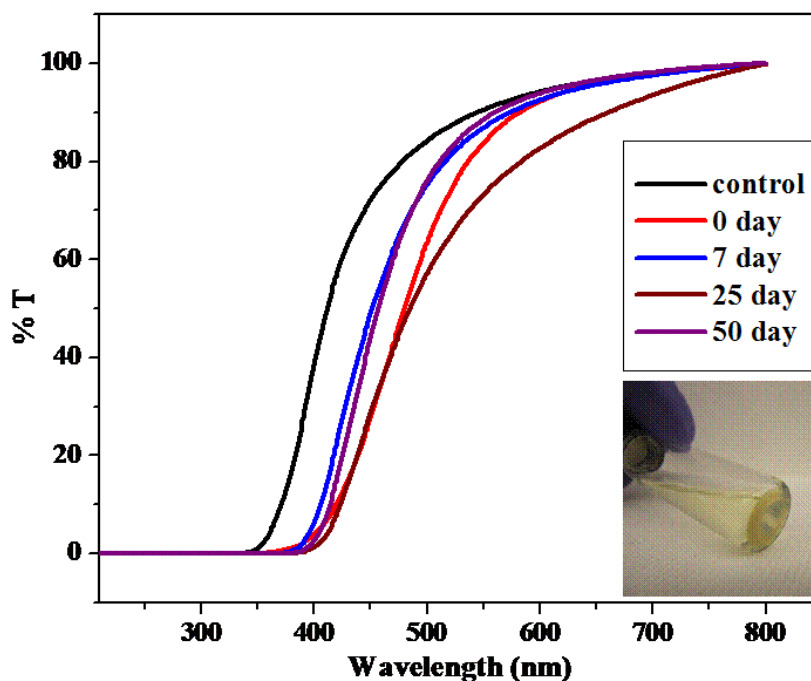


Figure 7.21 Loss of colloidal stability of PEI coated 3.8 nm nanoceria after H_2O_2 injection. UV-Vis band was monitored over time. The red-shift UV-Vis band was not recovered to the control. The inset photograph showed precipitates at the bottom of the sample containing PEI coated nanoceria in 50 days after the injection of H_2O_2 .

However, after multiple uses nanoparticles can either exhibit reduced reactivity towards hydrogen peroxide, or they can precipitate out of solution. In the data in Figure 7.20 this is shown with an arrow, after which no meaningful data could be collected. This phenomenon is analogous to a catalyst poisoning process. If particles are to be optimized for long-term redox cycling stability the factors that improve the ability to recycle the material must be identified. To compare across these materials, we calculated for these samples the total number of moles of peroxide per mole of cerium (III) (note: not per mole of nanocrystals) that could be reacted with the particles without resulting in precipitation.

From the perspective of multiple redox cycling, oleic acid coated nanoceria had the longest lifetime; oleic acid coated ceria did not lose its colloidal stability even after eighteen injections of H_2O_2 over six months (10 μmol of H_2O_2 injection per cycle, 18 cycles) for 6 months (Figure 7.20). This material can react with twenty times more peroxide for 18 cycles; CeO_2 suspension under the multiple H_2O_2 injections showed 21.6 μmol of H_2O_2 decomposition for 18 cycles based on the results from GC-MS and UV-Vis in Figure 7.11. We speculate that oleic acid not only forms the hydrophilic 2nd layer by hydrophobic-hydrophobic interaction with 18-carbon chain on oleylamine, but also makes the 1st layer more compact by the stronger interaction between oleic acid and ceria.^{3a} While very thin bilayer coating structures (oleic acid) resulted in the best antioxidant property with great colloidal stability, multiple injections of H_2O_2 gradually reduced the extent of the antioxidant property; after 18 cycles of the redox reaction, oleic acid coated nanoceria lose almost 90 % of the antioxidant property as compared to the 1st redox cycling. The surface coating may react with H_2O_2 with the introduction of the excess amount of H_2O_2 , yield nanocrystal aggregates and decrease the antioxidant property.¹⁴⁹ (Figure 7.22)

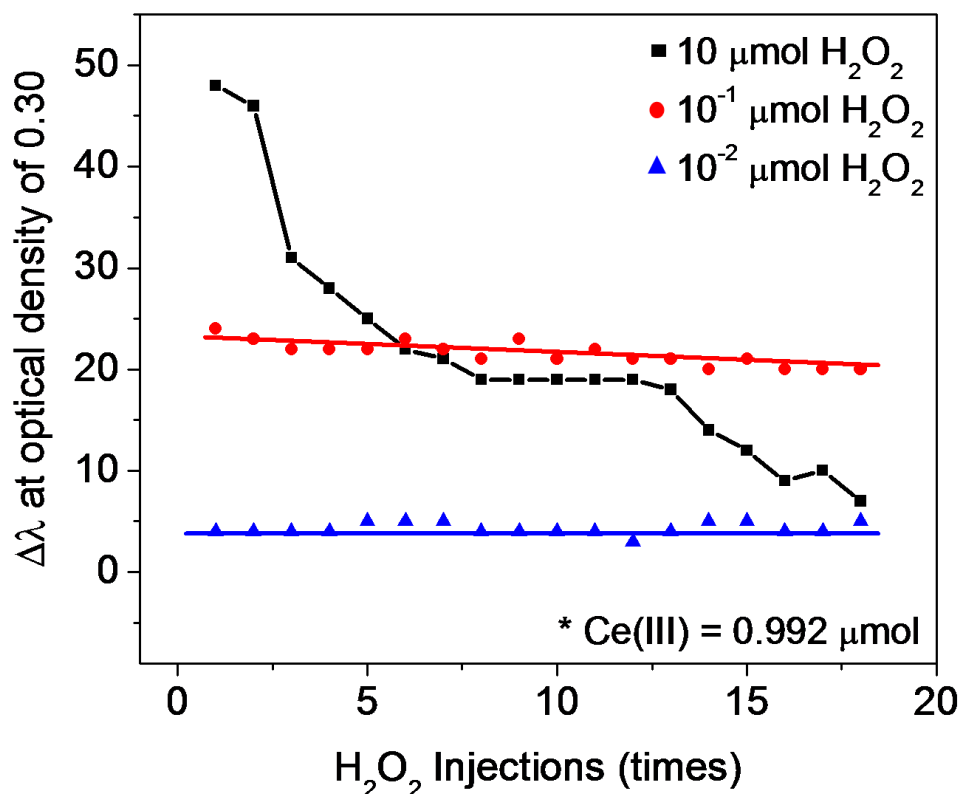


Figure 7.22 Antioxidant capacity of ceria nanocrystal suspension (2.78 μM of nanocrystal concentration: 1 μmol of cerium (III) concentration) depending on different amount of H_2O_2 injections for 18 cycles.

The excess H_2O_2 (black line) led to the decrease in the magnitude of the red shift of UV-Vis band from the control ($\Delta\lambda$) but the same (red line) and lower (blue line) amount of H_2O_2 injection than cerium (III) showed the consistency of the antioxidant capacity without losing the colloidal stability.

7.4. Conclusion

Monodisperse cerium oxide nanocrystals were synthesized with uniform diameters by the high temperature decomposition of cerium precursors in organic media. The resulting nanocrystals were phase transferred to water via a bilayer method using amphiphilic polymers (polyacrylic acid, oleic acid, and polymaleicanhydride-alt-1-octadecene) as well as a ligand exchange route by the addition of polyethylene imine. In the quantitative

analysis, the evolved O_2 and the remaining H_2O_2 concentration in the process of H_2O_2 quenching in nanoceria solution were monitored using GC-MS and luminol test; the ratio of the reacted H_2O_2 : cerium (III) : O_2 was almost 2 : 1 : 1. These illustrated that colloiddally stable oleic acid coated cerium oxide could quench H_2O_2 molecules through more likely Fenton-like reaction. The antioxidant capacity of ceria depends on cerium (III) concentration and the polymer shell thickness; 43 % cerium (III) formed by 3.8 nm cerium oxide nanocrystal coated with thinner surface stabilizer (such as, polyacrylic acid or oleic acid) quenches more H_2O_2 molecules than 30 % cerium (III) from 8.2 nm nanoceria covered with thicker polymer (polyethylene imine or polymaleicanhydride-alt-1-octadecene). In the ORAC assay, the antioxidant capacity of the thinnest surface coated nanoceria (3.8 nm CeO_2 coated with oleic acid) was found to have 9 times higher than that of the thickest polymer coated nanoceria (PMAO coated CeO_2) and Trolox in oxygen-radical absorbance capacity (ORAC) assay. Furthermore, these nanocrystals reduced oxidative stress of HDF cells. In the long term redox cycling, the oleic acid coated CeO_2 has the best colloidal stability in the presence of H_2O_2 ; the material showed good H_2O_2 quenching as well as recovery of cerium (III) after multiple injections of H_2O_2 . That is, the recovered water-soluble nanoceria can be reusable without loss of colloidal stability. Based on our data, the oleic acid coated nanoceria may be a potential antioxidant with a high radical scavenger capacity.

Conclusion

I have shown here that monodisperse iron oxide and cerium oxide nanocrystals are synthesized under high temperature metal precursor decomposition. The morphology of nanocrystals is transformed by various metal precursors, reaction temperature, time, cosurfactants, and molar ratio between metal salt and surfactant. To benchmark iron oxide and cerium oxide nanocrystals, I have examined high percentage of single walled CNT growth using iron oxide nanocrystals and antioxidant capacity of cerium oxide nanocrystals.

Vertically aligned CNT carpets with high quality were grown by iron oxide and aluminum ferrite nanocrystals. CNT carpet growth rates using these pre-synthesized aluminum ferrite and iron oxide nanocrystals were 10 times faster for the ferrites than for pure iron oxides. Furthermore, the highest percentage (60%) of single walled nanotube was formed from the smallest aluminum ferrite nanocrystals (4.0 nm). These data illustrate that aluminum in an iron oxide nanocrystal not only prevents catalyst poisoning, but slows the decomposition of the carbon source (acetylene) in the CNT growth process, leading to less amorphous carbon.

Finally, I demonstrated antioxidant capacity of cerium oxide nanocrystals. The surface passivation chemistry and cerium (III) content of nanocrystals can greatly influence their antioxidant properties. In the mechanistic study supported by colorimetric assay, GC-MS, and luminol test, cerium (III) is found to react with H_2O_2 with the ratio of 1:2 via Fenton-type mechanism. Furthermore, antioxidant capacity

of cerium oxide was 9 times higher than Trolox. These data suggest that appropriately derivatized cerium oxide could serve as a scavenger for radical species in biological media.

References

1. (a) Guardia, P.; Perez-Juste, J.; Labarta, A.; Batlle, X.; Liz-Marzan, L. M., Heating rate influence on the synthesis of iron oxide nanoparticles: the case of decanoic acid. *Chemical Communications* **2010**, 46 (33), 6108-6110; (b) Kim, J.; Lee, J. E.; Lee, J.; Yu, J. H.; Kim, B. C.; An, K.; Hwang, Y.; Shin, C. H.; Park, J. G.; Kim, J.; Hyeon, T., Magnetic fluorescent delivery vehicle using uniform mesoporous silica spheres embedded with monodisperse magnetic and semiconductor nanocrystals. *Journal of the American Chemical Society* **2006**, 128 (3), 688-689; (c) Bucak, S.; Jones, D. A.; Laibinis, P. E.; Hatton, T. A., Protein separations using colloidal magnetic nanoparticles. *Biotechnology Progress* **2003**, 19 (2), 477-484; (d) Oberteuffer, J., Magnetic Separation: A Review of Principles, Devices, and Applications. *Ieee Transactions on Magnetics* **1974**, 10 (2), 223-238; (e) Yu, H.; Gibbons, P. C.; Kelton, K. F.; Buhro, W. E., Heterogeneous seeded growth: A potentially general synthesis of monodisperse metallic nanoparticles. *Journal of the American Chemical Society* **2001**, 123 (37), 9198-9199; (f) Wang, Y. C.; Liu, Y. J.; Luehmann, H.; Xia, X. H.; Brown, P.; Jarreau, C.; Welch, M.; Xia, Y. N., Evaluating the Pharmacokinetics and In Vivo Cancer Targeting Capability of Au Nanocages by Positron Emission Tomography Imaging. *Acs Nano* **2012**, 6 (7), 5880-5888.
2. (a) Fu, Q.; Saltsburg, H.; Flytzani-Stephanopoulos, M., Active nonmetallic Au and Pt species on ceria-based water-gas shift catalysts. *Science* **2003**, 301 (5635), 935-938; (b) Kaspar, J.; Fornasiero, P.; Graziani, M., Use of CeO(2)-based oxides in the three-way catalysis. *Catal Today* **1999**, 50 (2), 285-298; (c) Park, J.; An, K. J.; Hwang, Y. S.; Park, J. G.; Noh, H. J.; Kim, J. Y.; Park, J. H.; Hwang, N. M.; Hyeon, T., Ultra-large-scale syntheses of monodisperse nanocrystals. *Nature Materials* **2004**, 3 (12), 891-895.
3. (a) Prakash, A.; Zhu, H. G.; Jones, C. J.; Benoit, D. N.; Ellsworth, A. Z.; Bryant, E. L.; Colvin, V. L., Bilayers as Phase Transfer Agents for Nanocrystals Prepared in Nonpolar Solvents. *Acs Nano* **2009**, 3 (8), 2139-2146; (b) Dubertret, B.; Skourides, P.; Norris, D. J.; Noireaux, V.; Brivanlou, A. H.; Libchaber, A., In vivo imaging of quantum dots encapsulated in phospholipid micelles. *Science* **2002**, 298 (5599), 1759-1762; (c) Murray, C. B.; Norris, D. J.; Bawendi, M. G., Synthesis and Characterization of Nearly Monodisperse Cde (E = S, Se, Te) Semiconductor Nanocrystallites. *Journal of the American Chemical Society* **1993**, 115 (19), 8706-8715; (d) Hyeon, T.; Lee, S. S.; Park, J.; Chung, Y.; Bin Na, H., Synthesis of highly crystalline and monodisperse maghemite nanocrystallites without a size-selection process. *Journal of the American Chemical Society* **2001**, 123 (51), 12798-12801; (e) Buffat, P.; Borel, J. P., Size Effect on Melting Temperature of Gold Particles. *Physical Review A* **1976**, 13 (6), 2287-2298; (f) Hai, H. T.; Yang, H. T.; Kura, H.; Hasegawa, D.; Ogata, Y.; Takahashi, M.; Ogawa, T., Size control and characterization of wustite (core)/spinel (shell) nanocubes obtained by decomposition of iron oleate complex. *Journal of Colloid and Interface Science* **2010**, 346 (1), 37-42; (g) Sun, S. H.; Zeng, H., Size-controlled synthesis of magnetite nanoparticles. *Journal of the American*

Chemical Society **2002**, 124 (28), 8204-8205; (h) Xie, J.; Peng, S.; Brower, N.; Pourmand, N.; Wang, S. X.; Sun, S. H., One-pot synthesis of monodisperse iron oxide nanoparticles for potential biomedical applications. *Pure and Applied Chemistry* **2006**, 78 (5), 1003-1014; (i) Yin, Y.; Alivisatos, A. P., Colloidal nanocrystal synthesis and the organic-inorganic interface. *Nature* **2005**, 437 (7059), 664-670; (j) Yu, W. W.; Falkner, J. C.; Yavuz, C. T.; Colvin, V. L., Synthesis of monodisperse iron oxide nanocrystals by thermal decomposition of iron carboxylate salts. *Chemical Communications* **2004**, (20), 2306-2307.

4. (a) Lamer, V. K.; Dinigar, R. H., Theory, Production and Mechanism of Formation of Monodispersed Hydrosols. *Journal of the American Chemical Society* **1950**, 72 (11), 4847-4854; (b) Overbeek, J. T. G., Monodisperse Colloidal Systems, Fascinating and Useful. *Advances in Colloid and Interface Science* **1982**, 15 (3-4), 251-277; (c) Sugimoto, T., Preparation of Monodispersed Colloidal Particles. *Advances in Colloid and Interface Science* **1987**, 28 (1), 65-108; (d) Wey, J. S.; Strong, R. W., Growth Mechanism of Agbr Crystals in Gelatin Solution. *Photographic Science and Engineering* **1977**, 21 (1), 14-18.

5. Burda, C.; Chen, X. B.; Narayanan, R.; El-Sayed, M. A., Chemistry and properties of nanocrystals of different shapes. *Chem Rev* **2005**, 105 (4), 1025-1102.

6. (a) Kahlweit, M., Ostwald Ripening of Precipitates. *Advances in Colloid and Interface Science* **1975**, 5 (1), 1-35; (b) Marqusee, J. A.; Ross, J., Theory of Ostwald Ripening - Competitive Growth and Its Dependence on Volume Fraction. *Journal of Chemical Physics* **1984**, 80 (1), 536-543; (c) Liu, Y.; Kathan, K.; Saad, W.; Prud'homme, R. K., Ostwald ripening of beta-carotene nanoparticles. *Physical Review Letters* **2007**, 98 (3); (d) Feldmann, G.; Fabrim, Z. E.; Hennig, G. L., Ostwald Ripening of precipitates and self similarity of size distributions in reaction controlled growth. *Journal of Materials Science* **2008**, 43 (2), 614-620.

7. Jun, Y. W.; Choi, J. S.; Cheon, J., Shape control of semiconductor and metal oxide nanocrystals through nonhydrolytic colloidal routes. *Angewandte Chemie-International Edition* **2006**, 45 (21), 3414-3439.

8. Cornell, R. M.; Schwertmann, U., *The Iron Oxides: Structure, Properties, Reactions, Occurrences and Uses*. WILEY-VCH: Weinheim, 2003.

9. (a) Awschalom, D. D.; Divincenzo, D. P., Complex Dynamics of Mesoscopic Magnets. *Phys Today* **1995**, 48 (4), 43-48; (b) LesliePelecky, D. L.; Rieke, R. D., Magnetic properties of nanostructured materials. *Chemistry of Materials* **1996**, 8 (8), 1770-1783; (c) Pankhurst, Q. A.; Connolly, J.; Jones, S. K.; Dobson, J., Applications of magnetic nanoparticles in biomedicine. *J Phys D Appl Phys* **2003**, 36 (13), R167-R181.

10. Hoare, T.; Santamaria, J.; Goya, G. F.; Irusta, S.; Lin, D.; Lau, S.; Padera, R.; Langer, R.; Kohane, D. S., A Magnetically Triggered Composite Membrane for On-Demand Drug Delivery. *Nano Letters* **2009**, 9 (10), 3651-3657.

11. (a) Babes, L.; Denizot, B.; Tanguy, G.; Le Jeune, J. J.; Jallet, P., Synthesis of iron oxide nanoparticles used as MRI contrast agents: A parametric study. *Journal of Colloid and Interface Science* **1999**, 212 (2), 474-482; (b) Papisov, M. I.; Bogdanov, A.; Schaffer, B.; Nossiff, N.; Shen, T.; Weissleder, R.; Brady, T. J., Colloidal Magnetic-

Resonance Contrast Agents - Effect of Particle Surface on Biodistribution. *Journal of Magnetism and Magnetic Materials* **1993**, *122* (1-3), 383-386.

12. Lee, J. H.; Jang, J. T.; Choi, J. S.; Moon, S. H.; Noh, S. H.; Kim, J. W.; Kim, J. G.; Kim, I. S.; Park, K. I.; Cheon, J., Exchange-coupled magnetic nanoparticles for efficient heat induction. *Nat Nanotechnol* **2011**, *6* (7), 418-422.

13. Kang, Y. S.; Risbud, S.; Rabolt, J. F.; Stroeve, P., Synthesis and characterization of nanometer-size Fe₃O₄ and gamma-Fe₂O₃ particles. *Chemistry of Materials* **1996**, *8* (9), 2209-2211.

14. Perez, J. A. L.; Quintela, M. A. L.; Mira, J.; Rivas, J.; Charles, S. W., Advances in the preparation of magnetic nanoparticles by the microemulsion method. *Journal of Physical Chemistry B* **1997**, *101* (41), 8045-8047.

15. (a) Das, M.; Dhak, P.; Gupta, S.; Mishra, D.; Maiti, T. K.; Basak, A.; Pramanik, P., Highly biocompatible and water-dispersible, amine functionalized magnetite nanoparticles, prepared by a low temperature, air-assisted polyol process: a new platform for bio-separation and diagnostics. *Nanotechnology* **2010**, *21* (12); (b) Ramirez, L. P.; Landfester, K., Magnetic polystyrene nanoparticles with a high magnetite content obtained by miniemulsion processes. *Macromol. Chem. Phys.* **2003**, *204* (1), 22-31.

16. Rockenberger, J.; Scher, E. C.; Alivisatos, A. P., A new nonhydrolytic single-precursor approach to surfactant-capped nanocrystals of transition metal oxides. *Journal of the American Chemical Society* **1999**, *121* (49), 11595-11596.

17. Caruntu, D.; Caruntu, G.; Chen, Y.; O'Connor, C. J.; Goloverda, G.; Kolesnichenko, V. L., Synthesis of variable-sized nanocrystals of Fe₃O₄ with high surface reactivity. *Chem Mater* **2004**, *16* (25), 5527-5534.

18. Park, J.; Lee, E.; Hwang, N. M.; Kang, M. S.; Kim, S. C.; Hwang, Y.; Park, J. G.; Noh, H. J.; Kini, J. Y.; Park, J. H.; Hyeon, T., One-nanometer-scale size-controlled synthesis of monodisperse magnetic iron oxide nanoparticles. *Angew Chem Int Edit* **2005**, *44* (19), 2872-2877.

19. Hou, Y. L.; Xu, Z. C.; Sun, S. H., Controlled synthesis and chemical conversions of FeO nanoparticles. *Angewandte Chemie-International Edition* **2007**, *46* (33), 6329-6332.

20. Sun, S. H.; Zeng, H.; Robinson, D. B.; Raoux, S.; Rice, P. M.; Wang, S. X.; Li, G. X., Monodisperse MFe₂O₄ (M = Fe, Co, Mn) nanoparticles. *J Am Chem Soc* **2004**, *126* (1), 273-279.

21. (a) Deluga, G. A.; Salge, J. R.; Schmidt, L. D.; Verykios, X. E., Renewable hydrogen from ethanol by autothermal reforming. *Science* **2004**, *303* (5660), 993-997; (b) Shido, T.; Iwasawa, Y., Regulation of Reaction Intermediate by Reactant in the Water Gas Shift Reaction on CeO₂, in Relation to Reactant-Promoted Mechanism. *J Catal* **1992**, *136* (2), 493-503.

22. (a) Tsunekawa, S.; Fukuda, T.; Kasuya, A., Blue shift in ultraviolet absorption spectra of monodisperse CeO_{2-x} nanoparticles. *J Appl Phys* **2000**, *87* (3), 1318-1321; (b) Tsunekawa, S.; Fukuda, T.; Kasuya, A., X-ray photoelectron spectroscopy of monodisperse CeO_{2-x} nanoparticles. *Surf Sci* **2000**, *457* (3), L437-L440.

23. Skorodumova, N. V.; Simak, S. I.; Lundqvist, B. I.; Abrikosov, I. A.; Johansson, B., Quantum origin of the oxygen storage capability of ceria. *Phys Rev Lett* **2002**, *89* (16).
24. Qiu, L. M.; Liu, F.; Zhao, L. Z.; Ma, Y.; Yao, J. N., Comparative XPS study of surface reduction for nanocrystalline and microcrystalline ceria powder. *Appl Surf Sci* **2006**, *252* (14), 4931-4935.
25. Deshpande, S.; Patil, S.; Kuchibhatla, S. V. N. T.; Seal, S., Size dependency variation in lattice parameter and valency states in nanocrystalline cerium oxide. *Appl Phys Lett* **2005**, *87* (13).
26. Zhou, Y. C.; Rahaman, M. N., Hydrothermal Synthesis and Sintering of Ultrafine CeO₂ Powders. *J Mater Res* **1993**, *8* (7), 1680-1686.
27. Han, W. Q.; Wu, L. J.; Zhu, Y. M., Formation and oxidation state of CeO_{2-x} nanotubes. *J Am Chem Soc* **2005**, *127* (37), 12814-12815.
28. Liao, X. H.; Zhu, J. M.; Zhu, J. J.; Xu, J. Z.; Chen, H. Y., Preparation of monodispersed nanocrystalline CeO₂ powders by microwave irradiation. *Chem Commun* **2001**, (10), 937-938.
29. Yang, S. W.; Gao, L., Controlled synthesis and self-assembly of CeO₂ nanocubes. *J Am Chem Soc* **2006**, *128* (29), 9330-9331.
30. Masui, T.; Fujiwara, K.; Machida, K.; Adachi, G.; Sakata, T.; Mori, H., Characterization of Cerium(IV) oxide ultrafine particles prepared using reversed micelles. *Chem Mater* **1997**, *9* (10), 2197-2204.
31. Das, M.; Patil, S.; Bhargava, N.; Kang, J. F.; Riedel, L. M.; Seal, S.; Hickman, J. J., Auto-catalytic ceria nanoparticles offer neuroprotection to adult rat spinal cord neurons. *Biomaterials* **2007**, *28* (10), 1918-1925.
32. (a) Gu, H.; Soucek, M. D., Preparation and characterization of monodisperse cerium oxide nanoparticles in hydrocarbon solvents. *Chem Mater* **2007**, *19* (5), 1103-1110; (b) Lee, S. S.; Zhu, H. G.; Contreras, E. Q.; Prakash, A.; Puppala, H. L.; Colvin, V. L., High Temperature Decomposition of Cerium Precursors To Form Ceria Nanocrystal Libraries for Biological Applications. *Chem Mater* **2012**, *24* (3), 424-432.
33. Yu, T. Y.; Joo, J.; Park, Y. I.; Hyeon, T., Large-scale nonhydrolytic sol-gel synthesis of uniform-sized ceria nanocrystals with spherical, wire, and tadpole shapes. *Angew Chem Int Edit* **2005**, *44* (45), 7411-7414.
34. Wang, D. S.; Xie, T.; Peng, Q.; Zhang, S. Y.; Chen, J.; Li, Y. D., Direct thermal decomposition of metal nitrates in octadecylamine to metal oxide nanocrystals. *Chem-Eur J* **2008**, *14* (8), 2507-2513.
35. Ahniyaz, A.; Sakamoto, Y.; Bergstrom, L., Tuning the aspect ratio of ceria nanorods and nanodumbbells by a face-specific growth and dissolution process. *Cryst Growth Des* **2008**, *8* (6), 1798-1800.
36. (a) Ebbesen, T. W.; Lezec, H. J.; Hiura, H.; Bennett, J. W.; Ghaemi, H. F.; Thio, T., Electrical conductivity of individual carbon nanotubes. *Nature* **1996**, *382* (6586), 54-56; (b) Kim, P.; Shi, L.; Majumdar, A.; McEuen, P. L., Thermal transport measurements of individual multiwalled nanotubes. *Physical Review Letters* **2001**, *87* (21), -; (c) Baughman, R. H.; Zakhidov, A. A.; de Heer, W. A., Carbon nanotubes -

- the route toward applications. *Science* **2002**, 297 (5582), 787-792; (d) Javey, A.; Shim, M.; Dai, H. J., Electrical properties and devices of large-diameter single-walled carbon nanotubes. *Applied Physics Letters* **2002**, 80 (6), 1064-1066; (e) O'Connell, M. J.; Bachilo, S. M.; Huffman, C. B.; Moore, V. C.; Strano, M. S.; Haroz, E. H.; Rialon, K. L.; Boul, P. J.; Noon, W. H.; Kittrell, C.; Ma, J. P.; Hauge, R. H.; Weisman, R. B.; Smalley, R. E., Band gap fluorescence from individual single-walled carbon nanotubes. *Science* **2002**, 297 (5581), 593-596; (f) Li, J.; Hu, L.; Wang, L.; Zhou, Y.; Gruner, G.; Marks, T. J., Organic light-emitting diodes having carbon nanotube anodes. *Nano Letters* **2006**, 6 (11), 2472-2477; (g) Avouris, P.; Freitag, M.; Perebeinos, V., Carbon-nanotube photonics and optoelectronics. *Nature Photonics* **2008**, 2 (6), 341-350.
37. (a) Chhowalla, M.; Teo, K. B. K.; Ducati, C.; Rupesinghe, N. L.; Amaratunga, G. A. J.; Ferrari, A. C.; Roy, D.; Robertson, J.; Milne, W. I., Growth process conditions of vertically aligned carbon nanotubes using plasma enhanced chemical vapor deposition. *Journal of Applied Physics* **2001**, 90 (10), 5308-5317; (b) Li, W. Z.; Wang, D. Z.; Yang, S. X.; Wen, J. G.; Ren, Z. F., Controlled growth of carbon nanotubes on graphite foil by chemical vapor deposition. *Chemical Physics Letters* **2001**, 335 (3-4), 141-149.
38. (a) Yamada, T.; Namai, T.; Hata, K.; Futaba, D. N.; Mizuno, K.; Fan, J.; Yudasaka, M.; Yumura, M.; Iijima, S., Size-selective growth of double-walled carbon nanotube forests from engineered iron catalysts. *Nature Nanotechnology* **2006**, 1 (2), 131-136; (b) Zhao, B.; Futaba, D. N.; Yasuda, S.; Akoshima, M.; Yamada, T.; Hata, K., Exploring Advantages of Diverse Carbon Nanotube Forests With Tailored Structures Synthesized by Supergrowth from Engineered Catalysts. *Acs Nano* **2009**, 3 (1), 108-114; (c) Ci, L.; Vajtai, R.; Ajayan, P. M., Vertically aligned large-diameter double-walled carbon nanotube arrays having ultralow density. *J Phys Chem C* **2007**, 111 (26), 9077-9080.
39. Lee, S. S.; Zhang, C. G.; Lewicka, Z. A.; Cho, M. J.; Mayo, J. T.; Yu, W. W.; Hauge, R. H.; Colvin, V. L., Control over the Diameter, Length, and Structure of Carbon Nanotube Carpets Using Aluminum Ferrite and Iron Oxide Nanocrystals as Catalyst Precursors. *J Phys Chem C* **2012**, 116 (18), 10287-10295.
40. Hafner, J. H.; Bronikowski, M. J.; Azamian, B. R.; Nikolaev, P.; Rinzler, A. G.; Colbert, D. T.; Smith, K. A.; Smalley, R. E., Catalytic growth of single-wall carbon nanotubes from metal particles. *Chemical Physics Letters* **1998**, 296 (1-2), 195-202.
41. (a) Li, Y.; Liu, J.; Wang, Y. Q.; Wang, Z. L., Preparation of monodispersed Fe-Mo nanoparticles as the catalyst for CVD synthesis of carbon nanotubes. *Chemistry of Materials* **2001**, 13 (3), 1008-1014; (b) Sato, S.; Kawabata, A.; Nihei, M.; Awano, Y., Growth of diameter-controlled carbon nanotubes using monodisperse nickel nanoparticles obtained with a differential mobility analyzer. *Chemical Physics Letters* **2003**, 382 (3-4), 361-366.
42. Cheung, C. L.; Kurtz, A.; Park, H.; Lieber, C. M., Diameter-controlled synthesis of carbon nanotubes. *Journal of Physical Chemistry B* **2002**, 106 (10), 2429-2433.
43. Hata, K.; Futaba, D. N.; Mizuno, K.; Namai, T.; Yumura, M.; Iijima, S., Water-assisted highly efficient synthesis of impurity-free single-walled carbon nanotubes. *Science* **2004**, 306 (5700), 1362-1364.

44. (a) Majumder, M.; Chopra, N.; Andrews, R.; Hinds, B. J., Nanoscale hydrodynamics - Enhanced flow in carbon nanotubes. *Nature* **2005**, *438* (7064), 44-44; (b) Futaba, D. N.; Hata, K.; Yamada, T.; Hiraoka, T.; Hayamizu, Y.; Kakudate, Y.; Tanaike, O.; Hatori, H.; Yumura, M.; Iijima, S., Shape-engineerable and highly densely packed single-walled carbon nanotubes and their application as super-capacitor electrodes. *Nature Materials* **2006**, *5* (12), 987-994; (c) Holt, J. K.; Park, H. G.; Wang, Y. M.; Stadermann, M.; Artyukhin, A. B.; Grigoropoulos, C. P.; Noy, A.; Bakajin, O., Fast mass transport through sub-2-nanometer carbon nanotubes. *Science* **2006**, *312* (5776), 1034-1037; (d) Peng, X.; Komatsu, N.; Bhattacharya, S.; Shimawaki, T.; Aonuma, S.; Kimura, T.; Osuka, A., Optically active single-walled carbon nanotubes. *Nature Nanotechnology* **2007**, *2* (6), 361-365.
45. Li, W. Z.; Xie, S. S.; Qian, L. X.; Chang, B. H.; Zou, B. S.; Zhou, W. Y.; Zhao, R. A.; Wang, G., Large-scale synthesis of aligned carbon nanotubes. *Science* **1996**, *274* (5293), 1701-1703.
46. (a) Pan, Z. W.; Xie, S. S.; Chang, B. H.; Wang, C. Y.; Lu, L.; Liu, W.; Zhou, M. Y.; Li, W. Z., Very long carbon nanotubes. *Nature* **1998**, *394* (6694), 631-632; (b) Ren, Z. F.; Huang, Z. P.; Xu, J. W.; Wang, J. H.; Bush, P.; Siegal, M. P.; Provencio, P. N., Synthesis of large arrays of well-aligned carbon nanotubes on glass. *Science* **1998**, *282* (5391), 1105-1107; (c) Gunjishima, I.; Inoue, T.; Yamamuro, S.; Sumiyama, K.; Okamoto, A., Growth of vertically aligned carbon nanotubes from highly active Fe-Ti-O nanoparticles prepared by liquid-phase synthesis. *Japanese Journal of Applied Physics Part 1-Regular Papers Brief Communications & Review Papers* **2007**, *46* (6A), 3700-3703; (d) Alvarez, N. T.; Hamilton, C. E.; Pint, C. L.; Orbaek, A.; Yao, J.; Frosinini, A. L.; Barron, A. R.; Tour, J. M.; Hauge, R. H., Wet Catalyst-Support Films for Production of Vertically Aligned Carbon Nanotubes. *Acs Appl Mater Inter* **2010**, *2* (7), 1851-1856.
47. Nishino, H.; Yasuda, S.; Namai, T.; Futaba, D. N.; Yamada, T.; Yumura, M.; Iijima, S.; Hata, K., Water-assisted highly efficient synthesis of single-walled carbon nanotubes forests from colloidal nanoparticle catalysts. *J Phys Chem C* **2007**, *111* (48), 17961-17965.
48. Moodley, P.; Loos, J.; Niemantsverdriet, J. W.; Thune, P. C., Is there a correlation between catalyst particle size and CNT diameter? *Carbon* **2009**, *47* (8), 2002-2013.
49. Tour, J. M.; Alvarez, N. T.; Li, F.; Pint, C. L.; Mayo, J. T.; Fisher, E. Z.; Colvin, V. L.; Hauge, R. H., Uniform Large Diameter Carbon Nanotubes in Vertical Arrays from Premade Near-Monodisperse Nanoparticles. *Chem Mater* **2011**, *23* (15), 3466-3475.
50. (a) Otsuka, K.; Wang, Y.; Sunada, E.; Yamanaka, I., Direct partial oxidation of methane to synthesis gas by cerium oxide. *J Catal* **1998**, *175* (2), 152-160; (b) Otsuka, K.; Ushiyama, T.; Yamanaka, I., Partial Oxidation of Methane Using the Redox of Cerium Oxide. *Chem Lett* **1993**, (9), 1517-1520.
51. (a) Liu, X. W.; Zhou, K. B.; Wang, L.; Wang, B. Y.; Li, Y. D., Oxygen Vacancy Clusters Promoting Reducibility and Activity of Ceria Nanorods. *J Am Chem Soc* **2009**, *131* (9), 3140-+; (b) Heckert, E. G.; Karakoti, A. S.; Seal, S.; Self, W. T., The role

of cerium redox state in the SOD mimetic activity of nanoceria. *Biomaterials* **2008**, 29 (18), 2705-2709.

52. Esch, F.; Fabris, S.; Zhou, L.; Montini, T.; Africh, C.; Fornasiero, P.; Comelli, G.; Rosei, R., Electron localization determines defect formation on ceria substrates. *Science* **2005**, 309 (5735), 752-755.

53. (a) Tabakova, T.; Boccuzzi, F.; Manzoli, M.; Sobczak, J. W.; Idakiev, V.; Andreeva, D., A comparative study of nanosized IB/ceria catalysts for low-temperature water-gas shift reaction. *Appl Catal a-Gen* **2006**, 298, 127-143; (b) Tsunekawa, S.; Sivamohan, R.; Ito, S.; Kasuya, A.; Fukuda, T., Structural study on monosize CeO_{2-x} nano-particles. *Nanostruct Mater* **1999**, 11 (1), 141-147; (c) Bensalem, A.; Muller, J. C.; Bozonverduraz, F., From Bulk CeO₂ to Supported Cerium Oxygen Clusters - a Diffuse Reflectance Approach. *J Chem Soc Faraday T* **1992**, 88 (1), 153-154.

54. (a) Mogensen, M.; Sammes, N. M.; Tompsett, G. A., Physical, chemical and electrochemical properties of pure and doped ceria. *Solid State Ionics* **2000**, 129 (1-4), 63-94; (b) Corma, A.; Atienzar, P.; Garcia, H.; Chane-Ching, J. Y., Hierarchically mesostructured doped CeO₂ with potential for solar-cell use. *Nat Mater* **2004**, 3 (6), 394-397; (c) Park, S. D.; Vohs, J. M.; Gorte, R. J., Direct oxidation of hydrocarbons in a solid-oxide fuel cell. *Nature* **2000**, 404 (6775), 265-267.

55. Karakoti, A.; Singh, S.; Dowding, J. M.; Seal, S.; Self, W. T., Redox-active radical scavenging nanomaterials. *Chem Soc Rev* **2010**, 39 (11), 4422-4432.

56. Rzigalinski, B. A.; Meehan, K.; Davis, R. M.; Xu, Y.; Miles, W. C.; Cohen, C. A., Radical nanomedicine. *Nanomedicine-Uk* **2006**, 1 (4), 399-412.

57. (a) Chaudhary, Y. S.; Panigrahi, S.; Nayak, S.; Satpati, B.; Bhattacharjee, S.; Kulkarni, N., Facile synthesis of ultra-small monodisperse ceria nanocrystals at room temperature and their catalytic activity under visible light. *J Mater Chem* **2010**, 20 (12), 2381-2385; (b) Perez, J. M.; Asati, A.; Nath, S.; Kaittanis, C., Synthesis of biocompatible dextran-coated nanoceria with pH-dependent antioxidant properties. *Small* **2008**, 4 (5), 552-556.

58. Heckert, E. G.; Seal, S.; Self, W. T., Fenton-like reaction catalyzed by the rare earth inner transition metal cerium. *Environ Sci Technol* **2008**, 42 (13), 5014-5019.

59. Imlay, J. A.; Chin, S. M.; Linn, S., Toxic DNA Damage by Hydrogen-Peroxide through the Fenton Reaction In vivo and In vitro. *Science* **1988**, 240 (4852), 640-642.

60. Xue, Y.; Luan, Q. F.; Yang, D.; Yao, X.; Zhou, K. B., Direct Evidence for Hydroxyl Radical Scavenging Activity of Cerium Oxide Nanoparticles. *J Phys Chem C* **2011**, 115 (11), 4433-4438.

61. (a) Tarnuzzer, R. W.; Colon, J.; Patil, S.; Seal, S., Vacancy engineered ceria nanostructures for protection from radiation-induced cellular damage. *Nano Lett* **2005**, 5 (12), 2573-2577; (b) Misra, M. K.; Sarwat, M.; Bhakuni, P.; Tuteja, R.; Tuteja, N., Oxidative stress and ischemic myocardial syndromes. *Med Sci Monitor* **2009**, 15 (10), Ra209-Ra219; (c) Kumar, B.; Koul, S.; Khandrika, L.; Meacham, R. B.; Koul, H. K., Oxidative stress is inherent in prostate cancer cells and is required for aggressive phenotype. *Cancer Res* **2008**, 68 (6), 1777-1785; (d) Emerit, J.; Edeas, A.; Bricaire, F., Neurodegenerative diseases and oxidative stress. *Biomed Pharmacother* **2004**, 58

- (1), 39-46; (e) Nyska, A.; Kohen, R., Oxidation of biological systems: Oxidative stress phenomena, antioxidants, redox reactions, and methods for their quantification. *Toxicol Pathol* **2002**, *30* (6), 620-650; (f) Finkel, T.; Holbrook, N. J., Oxidants, oxidative stress and the biology of ageing. *Nature* **2000**, *408* (6809), 239-247; (g) Niu, J. L.; Azfer, A.; Rogers, L. M.; Wang, X. H.; Kolattukudy, P. E., Cardioprotective effects of cerium oxide nanoparticles in a transgenic murine model of cardiomyopathy. *Cardiovasc Res* **2007**, *73* (3), 549-559.
62. Kim, C. K.; Kim, T.; Choi, I. Y.; Soh, M.; Kim, D.; Kim, Y. J.; Jang, H.; Yang, H. S.; Kim, J. Y.; Park, H. K.; Park, S. P.; Park, S.; Yu, T.; Yoon, B. W.; Lee, S. H.; Hyeon, T., Ceria Nanoparticles that can Protect against Ischemic Stroke. *Angew Chem Int Edit* **2012**, *51* (44), 11039-11043.
63. (a) Duan, H. W.; Kuang, M.; Wang, X. X.; Wang, Y. A.; Mao, H.; Nie, S. M., Reexamining the effects of particle size and surface chemistry on the magnetic properties of iron oxide nanocrystals: New insights into spin disorder and proton relaxivity. *Journal of Physical Chemistry C* **2008**, *112* (22), 8127-8131; (b) Yu, W. W.; Chang, E.; Falkner, J. C.; Zhang, J. Y.; Al-Somali, A. M.; Sayes, C. M.; Johns, J.; Drezek, R.; Colvin, V. L., Forming biocompatible and nonaggregated nanocrystals in water using amphiphilic polymers. *J Am Chem Soc* **2007**, *129* (10), 2871-2879.
64. Pint, C. L.; Pheasant, S. T.; Parra-Vasquez, A. N. G.; Horton, C.; Xu, Y. Q.; Hauge, R. H., Investigation of Optimal Parameters for Oxide-Assisted Growth of Vertically Aligned Single-Walled Carbon Nanotubes. *J Phys Chem C* **2009**, *113* (10), 4125-4133.
65. (a) de los Arcos, T.; Garnier, M. G.; Seo, J. W.; Oelhafen, P.; Thommen, V.; Mathys, D., The influence of catalyst chemical state and morphology on carbon nanotube growth. *J Phys Chem B* **2004**, *108* (23), 7728-7734; (b) Kayastha, V. K.; Wu, S.; Moscatello, J.; Yap, Y. K., Synthesis of vertically aligned single- and double-walled carbon nanotubes without etching agents. *J Phys Chem C* **2007**, *111* (28), 10158-10161; (c) Amama, P. B.; Pint, C. L.; McJilton, L.; Kim, S. M.; Stach, E. A.; Murray, P. T.; Hauge, R. H.; Maruyama, B., Role of Water in Super Growth of Single-Walled Carbon Nanotube Carpets. *Nano Letters* **2009**, *9* (1), 44-49; (d) Amama, P. B.; Pint, C. L.; Kim, S. M.; McJilton, L.; Eyink, K. G.; Stach, E. A.; Hauge, R. H.; Maruyama, B., Influence of Alumina Type on the Evolution and Activity of Alumina-Supported Fe Catalysts in Single-Walled Carbon Nanotube Carpet Growth. *Acs Nano* **2010**, *4* (2), 895-904; (e) Han, S. J.; Yu, T. K.; Park, J.; Koo, B.; Joo, J.; Hyeon, T.; Hong, S.; Im, J., Diameter-controlled synthesis of discrete and uniform-sized single-walled carbon nanotubes using monodisperse iron oxide nanoparticles embedded in zirconia nanoparticle arrays as catalysts. *Journal of Physical Chemistry B* **2004**, *108* (24), 8091-8095.
66. Karakoti, A. S.; Singh, S.; Kumar, A.; Malinska, M.; Kuchibhatla, S. V. N. T.; Wozniak, K.; Self, W. T.; Seal, S., PEGylated Nanoceria as Radical Scavenger with Tunable Redox Chemistry. *J Am Chem Soc* **2009**, *131* (40), 14144-+.
67. Asati, A.; Santra, S.; Kaittanis, C.; Nath, S.; Perez, J. M., Oxidase-Like Activity of Polymer-Coated Cerium Oxide Nanoparticles. *Angewandte Chemie-International Edition* **2009**, *48* (13), 2308-2312.

68. (a) West, A. R., *Basic solid state chemistry*. Wiley: Chichester West Sussex ; New York, 1988; p x, 415 p; (b) O'Handley, R. C., *Modern magnetic materials : principles and applications*. Wiley: New York, 2000; p xxvii, 740 p.
69. (a) Huang, J. H.; Parab, H. J.; Liu, R. S.; Lai, T. C.; Hsiao, M.; Chen, C. H.; Sheu, H. S.; Chen, J. M.; Tsai, D. P.; Hwu, Y. K., Investigation of the growth mechanism of iron oxide nanoparticles via a seed-mediated method and its cytotoxicity studies. *Journal of Physical Chemistry C* **2008**, *112* (40), 15684-15690; (b) Yavuz, C. T.; Mayo, J. T.; Yu, W. W.; Prakash, A.; Falkner, J. C.; Yean, S.; Cong, L. L.; Shipley, H. J.; Kan, A.; Tomson, M.; Natelson, D.; Colvin, V. L., Low-field magnetic separation of monodisperse Fe₃O₄ nanocrystals. *Science* **2006**, *314* (5801), 964-967.
70. Raj, K.; Moskowitz, R., Commercial Applications of Ferrofluids. *Journal of Magnetism and Magnetic Materials* **1990**, *85* (1-3), 233-245.
71. (a) Park, J.; Joo, J.; Kwon, S. G.; Jang, Y.; Hyeon, T., Synthesis of monodisperse spherical nanocrystals. *Angewandte Chemie-International Edition* **2007**, *46* (25), 4630-4660; (b) Carbone, L.; Cozzoli, P. D., Colloidal heterostructured nanocrystals: Synthesis and growth mechanisms. *Nano Today* **2010**, *5* (5), 449-493.
72. Kudlash, A. N.; Vorobyova, S. A.; Lesnikovich, A. I., Interphase synthesis and some characteristics of aqueous nickel dispersions. *J Phys Chem Solids* **2008**, *69* (7), 1652-1656.
73. Anisur, R. M.; Shin, J.; Choi, H. H.; Yeo, K. M.; Kang, E. J.; Lee, I. S., Hollow silica nanosphere having functionalized interior surface with thin manganese oxide layer: nanoreactor framework for size-selective Lewis acid catalysis. *Journal of Materials Chemistry* **2010**, *20* (47), 10615-10621.
74. Xu, J.; Zhu, Y. G.; Huang, H. T.; Xie, Z.; Chen, D.; Shen, G. Z., Zinc-oleate complex as efficient precursor for 1-D ZnO nanostructures: synthesis and properties. *Crystengcomm* **2011**, *13* (7), 2629-2635.
75. Bronstein, L. M.; Huang, X. L.; Retrum, J.; Schmucker, A.; Pink, M.; Stein, B. D.; Dragnea, B., Influence of iron oleate complex structure on iron oxide nanoparticle formation. *Chemistry of Materials* **2007**, *19* (15), 3624-3632.
76. Peng, X. G.; Wickham, J.; Alivisatos, A. P., Kinetics of II-VI and III-V colloidal semiconductor nanocrystal growth: "Focusing" of size distributions. *Journal of the American Chemical Society* **1998**, *120* (21), 5343-5344.
77. (a) Kodama, R. H.; Berkowitz, A. E.; McNiff, E. J.; Foner, S., Surface spin disorder in NiFe₂O₄ nanoparticles. *Phys Rev Lett* **1996**, *77* (2), 394-397; (b) Schiessl, W.; Potzel, W.; Karzel, H.; Steiner, M.; Kalvius, G. M.; Martin, A.; Krause, M. K.; Halevy, I.; Gal, J.; Schafer, W.; Will, G.; Hillberg, M.; Wappling, R., Magnetic properties of the ZnFe₂O₄ spinel. *Phys Rev B* **1996**, *53* (14), 9143-9152; (c) Liu, C.; Zou, B. S.; Rondinone, A. J.; Zhang, J., Chemical control of superparamagnetic properties of magnesium and cobalt spinel ferrite nanoparticles through atomic level magnetic couplings. *J Am Chem Soc* **2000**, *122* (26), 6263-6267; (d) Liu, C.; Zou, B. S.; Rondinone, A. J.; Zhang, Z. J., Reverse micelle synthesis and characterization of superparamagnetic MnFe₂O₄ spinel ferrite nanocrystallites. *J Phys Chem B* **2000**, *104* (6), 1141-1145; (e) Chinnasamy, C. N.; Narayanasamy, A.; Ponpandian, N.; Chattopadhyay, K.; Shinoda, K.; Jeyadevan, B.; Tohji, K.; Nakatsuka, K.; Furubayashi,

T.; Nakatani, I., Mixed spinel structure in nanocrystalline NiFe₂O₄. *Phys Rev B* **2001**, 6318 (18), -; (f) Ashiq, M. N.; Iqbal, M. J.; Gul, I. H., Effect of Al-Cr doping on the structural, magnetic and dielectric properties of strontium hexaferrite nanomaterials. *J Magn Magn Mater* **2011**, 323 (3-4), 259-263; (g) Kang, E.; Park, J.; Hwang, Y.; Kang, M.; Park, J. G.; Hyeon, T., Direct synthesis of highly crystalline and monodisperse manganese ferrite nanocrystals. *J Phys Chem B* **2004**, 108 (37), 13932-13935; (h) Hyeon, T.; Chung, Y.; Park, J.; Lee, S. S.; Kim, Y. W.; Park, B. H., Synthesis of highly crystalline and monodisperse cobalt ferrite nanocrystals. *J Phys Chem B* **2002**, 106 (27), 6831-6833; (i) Zeng, H.; Rice, P. M.; Wang, S. X.; Sun, S. H., Shape-controlled synthesis and shape-induced texture of MnFe₂O₄ nanoparticles. *J Am Chem Soc* **2004**, 126 (37), 11458-11459; (j) Chinnasamy, C. N.; Narayanasamy, A.; Ponpandian, N.; Chattopadhyay, K.; Shinoda, K.; Jeyadevan, B.; Tohji, K.; Nakatsuka, K.; Furubayashi, T.; Nakatani, I., Mixed spinel structure in nanocrystalline NiFe₂O₄. *Phys Rev B* **2001**, 63 (18); (k) Schiessl, W.; Potzel, W.; Karzel, H.; Steiner, M.; Kalvius, G. M.; Martin, A.; Krause, M. K.; I, H.; Gal, J.; Schafer, W.; Will, G.; Hillberg, M.; Wappling, R., Magnetic properties of the ZnFe₂O₄ spinel. *Phys Rev B* **1996**, 53 (14), 9143-9152.

78. (a) Jordan, A.; Scholz, R.; Wust, P.; Fahling, H.; Felix, R., Magnetic fluid hyperthermia (MFH): Cancer treatment with AC magnetic field induced excitation of biocompatible superparamagnetic nanoparticles. *J Magn Magn Mater* **1999**, 201, 413-419; (b) Kim, D. K.; Zhang, Y.; Kehr, J.; Klason, T.; Bjelke, B.; Muhammed, M., Characterization and MRI study of surfactant-coated superparamagnetic nanoparticles administered into the rat brain. *J Magn Magn Mater* **2001**, 225 (1-2), 256-261.

79. (a) Neveu, S.; Bee, A.; Robineau, M.; Talbot, D., Size-selective chemical synthesis of tartrate stabilized cobalt ferrite ionic magnetic fluid. *J Colloid Interf Sci* **2002**, 255 (2), 293-298; (b) Fried, T.; Shemer, G.; Markovich, G., Ordered two-dimensional arrays of ferrite nanoparticles. *Adv Mater* **2001**, 13 (15), 1158-+; (c) Liu, Q.; Huang, H.; Lai, L.; Sun, J.; Shang, T.; Zhou, Q.; Xu, Z., Hydrothermal synthesis and magnetic properties of NiFe₂O₄ nanoparticles and nanorods. *J Mater Sci* **2009**, 44 (5), 1187-1191; (d) Zhang, Z. J.; Wang, Z. L.; Chakoumakos, B. C.; Yin, J. S., Temperature dependence of cation distribution and oxidation state in magnetic Mn-Fe ferrite nanocrystals. *J Am Chem Soc* **1998**, 120 (8), 1800-1804; (e) Tang, Z. X.; Sorensen, C. M.; Klabunde, K. J.; Hadjipanayis, G. C., Preparation of Manganese Ferrite Fine Particles from Aqueous-Solution. *J Colloid Interf Sci* **1991**, 146 (1), 38-52; (f) Hong, C. Y.; Jang, I. J.; Horng, H. E.; Hsu, C. J.; Yao, Y. D.; Yang, H. C., Ordered structures in Fe₃O₄ kerosene-based ferrofluids. *J Appl Phys* **1997**, 81 (8), 4275-4277; (g) Moumen, N.; Pileni, M. P., Control of the size of cobalt ferrite magnetic fluid. *J Phys Chem-U* **1996**, 100 (5), 1867-1873.

80. (a) Bao, N. Z.; Shen, L. M.; An, W.; Padhan, P.; Turner, C. H.; Gupta, A., Formation Mechanism and Shape Control of Monodisperse Magnetic CoFe₂O₄ Nanocrystals. *Chem Mater* **2009**, 21 (14), 3458-3468; (b) Moriya, M.; Ito, M.; Sakamoto, W.; Yogo, T., One-Pot Synthesis and Morphology Control of Spinel Ferrite (MFe₂O₄), M = Mn, Fe, and Co) Nanocrystals from Homo- and Heterotrimetallic

Clusters. *Cryst Growth Des* **2009**, *9* (4), 1889-1893; (c) Baruwati, B.; Manorama, S. V., Monodispersed NiFe₂O₄ nanoparticles: Nonaqueous synthesis and characterization. *Mater Chem Phys* **2008**, *112* (2), 631-636.

81. (a) Namai, A.; Sakurai, S.; Nakajima, M.; Suemoto, T.; Matsumoto, K.; Goto, M.; Sasaki, S.; Ohkoshi, S., Synthesis of an Electromagnetic Wave Absorber for High-Speed Wireless Communication. *J Am Chem Soc* **2009**, *131* (3), 1170-1173; (b) Wolska, E.; Wolniewicz, A., On the Aluminium-Substituted Magnetites. *Phys Status Solidi A* **1987**, *104* (2), 569-574; (c) Gillot, B.; Rousset, A., On the Limit of Aluminum Substitution in Fe₃O₄ and Gamma-Fe₂O₃. *Phys Status Solidi A* **1990**, *118* (1), K5-K8.

82. (a) Afsar, M. N.; Korolev, K. A.; Namai, A.; Ohkoshi, S. I., Millimeter-Wave Ferromagnetic Absorption of Epsilon Aluminum Iron Oxide Nano Ferrites. *Ieee T Magn* **2011**, *47* (10), 2588-2591; (b) Wang, X.; Krommenhoek, P. J.; Bradford, P. D.; Gong, B.; Tracy, J. B.; Parsons, G. N.; Luo, T. J. M.; Zhu, Y. T., Coating Alumina on Catalytic Iron Oxide Nanoparticles for Synthesizing Vertically Aligned Carbon Nanotube Arrays. *Acs Appl Mater Inter* **2011**, *3* (11), 4180-4184.

83. (a) Dehe, G.; Seidel, B.; Melzer, K.; Michalk, C., Determination of a Cation Distribution Model of Spinel System Fe₃-Al_xO₄. *Phys Status Solidi A* **1975**, *31* (2), 439-447; (b) Jentsch, T. L.; Chun, C. L.; Gabor, R. S.; Penn, R. L., Influence of aluminum substitution on the reactivity of magnetite nanoparticles. *J Phys Chem C* **2007**, *111* (28), 10247-10253; (c) Prasad, N. K.; Panda, D.; Singh, S.; Bahadur, D., Preparation of cellulose-based biocompatible suspension of nano-sized gamma-Al_xFe_{2-x}O₃. *Ieee T Magn* **2005**, *41* (10), 4099-4101.

84. Vigneau, E.; Loisel, C.; Devaux, M. F.; Cantoni, P., Number of particles for the determination of size distribution from microscopic images. *Powder Technol* **2000**, *107* (3), 243-250.

85. Smith, A. M.; Nie, S., Minimizing the hydrodynamic size of quantum dots with multifunctional multidentate polymer ligands. *J Am Chem Soc* **2008**, *130* (34), 11278-+.

86. (a) Zhang, X. M.; Neiner, D.; Wang, S. Z.; Louie, A. Y.; Kauzlarich, S. M., A new solution route to hydrogen-terminated silicon nanoparticles: synthesis, functionalization and water stability. *Nanotechnology* **2007**, *18* (9); (b) Wang, K. T.; Iliopoulos, I.; Audebert, R., Viscometric Behavior of Hydrophobically Modified Poly(Sodium Acrylate). *Polym Bull* **1988**, *20* (6), 577-582.

87. (a) Smith, G. H.; Pomeroy, H. H.; Mcgee, C. G.; Mysels, K. J., Preparation of Aluminum Di-Soaps. *J Am Chem Soc* **1948**, *70* (3), 1053-1054; (b) Mehrotra, R. C., Preparation of Aluminium Tri-Soaps. *Nature* **1953**, *172* (4367), 74-74; (c) Woods, D. E.; Taylor, A. J., The preparation of aluminium soaps by a continuous process. I. Aluminium laurate. *J Appl Chem* **1958**, *8* (4), 237-246; (d) Marks, B. M.; Howard, H. C., The catalytic decomposition of oleic acid. *J Phys Chem-U.S* **1928**, *32*, 1040-1048.

88. (a) Raghavender, A. T.; Pajic, D.; Zadro, K.; Milekovic, T.; Rao, P. V.; Jadhav, K. M.; Ravinder, D., Synthesis and magnetic properties of NiFe_{2-x}Al_xO₄ nanoparticles. *J Magn Magn Mater* **2007**, *316* (1), 1-7; (b) Suryawanshi, S. S.; Deshpande, V. V.; Deshmukh, U. B.; Kabur, S. M.; Chaudhari, N. D.; Sawant, S. R., XRD analysis and bulk

magnetic properties of Al³⁺ substituted Cu-Cd ferrites. *Mater Chem Phys* **1999**, *59* (3), 199-203.

89. Mozaffari, M.; Aboalizadeh, Z.; Amighian, J., Investigation of magnetic properties of Al substituted nickel ferrite nanopowders, synthesized by the sol-gel method. *J Magn Magn Mater* **2011**, *323* (23), 2997-3000.

90. Kairdolf, B. A.; Smith, A. M.; Nie, S., One-pot synthesis, encapsulation, and solubilization of size-tuned quantum dots with amphiphilic multidentate ligands. *J Am Chem Soc* **2008**, *130* (39), 12866-+.

91. Murakami, K.; Chan, S. Y.; Routtenberg, A., Protein-Kinase-C Activation by Cis-Fatty Acid in the Absence of Ca²⁺ and Phospholipids. *J Biol Chem* **1986**, *261* (33), 5424-5429.

92. (a) Cherukuri, P.; Bachilo, S. M.; Litovsky, S. H.; Weisman, R. B., Near-infrared fluorescence microscopy of single-walled carbon nanotubes in phagocytic cells. *Journal of the American Chemical Society* **2004**, *126* (48), 15638-15639; (b) Shvedova, A. A.; Kisin, E. R.; Porter, D.; Schulte, P.; Kagan, V. E.; Fadeel, B.; Castranova, V., Mechanisms of pulmonary toxicity and medical applications of carbon nanotubes: Two faces of Janus? *Pharmacology & Therapeutics* **2009**, *121* (2), 192-204; (c) Yue, G. Z.; Qiu, Q.; Gao, B.; Cheng, Y.; Zhang, J.; Shimoda, H.; Chang, S.; Lu, J. P.; Zhou, O., Generation of continuous and pulsed diagnostic imaging x-ray radiation using a carbon-nanotube-based field-emission cathode. *Applied Physics Letters* **2002**, *81* (2), 355-357.

93. (a) Nikolaev, P.; Bronikowski, M. J.; Bradley, R. K.; Rohmund, F.; Colbert, D. T.; Smith, K. A.; Smalley, R. E., Gas-phase catalytic growth of single-walled carbon nanotubes from carbon monoxide. *Chemical Physics Letters* **1999**, *313* (1-2), 91-97; (b) Edgar, K.; Spencer, J. L., Aerosol-based synthesis of carbon nanotubes. *Current Applied Physics* **2004**, *4* (2-4), 121-124.

94. (a) Anderson, P. E.; Rodriguez, N. M., Influence of the support on the structural characteristics of carbon nanofibers produced from the metal-catalyzed decomposition of ethylene. *Chemistry of Materials* **2000**, *12* (3), 823-830; (b) Baker, R. T. K.; Barber, M. A.; Waite, R. J.; Harris, P. S.; Feates, F. S., Nucleation and Growth of Carbon Deposits from Nickel Catalyzed Decomposition of Acetylene. *Journal of Catalysis* **1972**, *26* (1), 51-&; (c) Kukovitsky, E. F.; L'vov, S. G.; Sainov, N. A.; Shustov, V. A.; Chernozatonskii, L. A., Correlation between metal catalyst particle size and carbon nanotube growth. *Chemical Physics Letters* **2002**, *355* (5-6), 497-503; (d) Kim, M. S.; Rodriguez, N. M.; Baker, R. T. K., The Interaction of Hydrocarbons with Copper Nickel and Nickel in the Formation of Carbon Filaments. *Journal of Catalysis* **1991**, *131* (1), 60-73; (e) Kiang, C. H.; Goddard, W. A.; Beyers, R.; Salem, J. R.; Bethune, D. S., Catalytic Synthesis of Single-Layer Carbon Nanotubes with a Wide-Range of Diameters. *Journal of Physical Chemistry* **1994**, *98* (26), 6612-6618; (f) Kiang, C. H.; Goddard, W. A.; Beyers, R.; Salem, J. R.; Bethune, D. S., Catalytic effects of heavy metals on the growth of carbon nanotubes and nanoparticles. *Journal of Physics and Chemistry of Solids* **1996**, *57* (1), 35-39; (g) Lee, C. J.; Park, J.; Yu, J. A., Catalyst effect on carbon nanotubes synthesized by thermal chemical vapor deposition. *Chemical Physics Letters* **2002**, *360* (3-4), 250-255; (h) An, L.; Owens, J.

- M.; McNeil, L. E.; Liu, J., Synthesis of nearly uniform single-walled carbon nanotubes using identical metal-containing molecular nanoclusters as catalysts. *Journal of the American Chemical Society* **2002**, *124* (46), 13688-13689.
95. Pint, C. L.; Nicholas, N.; Pheasant, S. T.; Duque, J. G.; Nicholas, A.; Parra-Vasquez, G.; Eres, G.; Pasquali, M.; Hauge, R. H., Temperature and gas pressure effects in vertically aligned carbon nanotube growth from Fe-Mo catalyst. *J Phys Chem C* **2008**, *112* (36), 14041-14051.
96. (a) Fan, S. S.; Chapline, M. G.; Franklin, N. R.; Tomblor, T. W.; Cassell, A. M.; Dai, H. J., Self-oriented regular arrays of carbon nanotubes and their field emission properties. *Science* **1999**, *283* (5401), 512-514; (b) Li, Y. M.; Kim, W.; Zhang, Y. G.; Rolandi, M.; Wang, D. W.; Dai, H. J., Growth of single-walled carbon nanotubes from discrete catalytic nanoparticles of various sizes. *Journal of Physical Chemistry B* **2001**, *105* (46), 11424-11431.
97. (a) Sinnott, S. B.; Andrews, R.; Qian, D.; Rao, A. M.; Mao, Z.; Dickey, E. C.; Derbyshire, F., Model of carbon nanotube growth through chemical vapor deposition. *Chemical Physics Letters* **1999**, *315* (1-2), 25-30; (b) Dal, H. J.; Rinzler, A. G.; Nikolaev, P.; Thess, A.; Colbert, D. T.; Smalley, R. E., Single-wall nanotubes produced by metal-catalyzed disproportionation of carbon monoxide. *Chemical Physics Letters* **1996**, *260* (3-4), 471-475.
98. (a) Mudimela, P. R.; Nasibulin, A. G.; Jiang, H.; Susi, T.; Chassaing, D.; Kauppinen, E. I., Incremental Variation in the Number of Carbon Nanotube Walls with Growth Temperature. *J Phys Chem C* **2009**, *113* (6), 2212-2218; (b) Shibuta, Y.; Watanabe, Y.; Suzuki, T., Growth and melting of nanoparticles in liquid iron: A molecular dynamics study. *Chem Phys Lett* **2009**, *475* (4-6), 264-268; (c) Auffan, M.; Rose, J.; Bottero, J. Y.; Lowry, G. V.; Jolivet, J. P.; Wiesner, M. R., Towards a definition of inorganic nanoparticles from an environmental, health and safety perspective. *Nature Nanotechnology* **2009**, *4* (10), 634-641.
99. Ducati, C.; Alexandrou, I.; Chhowalla, M.; Amaratunga, G. A. J.; Robertson, J., Temperature selective growth of carbon nanotubes by chemical vapor deposition. *Journal of Applied Physics* **2002**, *92* (6), 3299-3303.
100. (a) Lee, J.; Lee, J.; Tanaka, T.; Mori, H., In situ atomic-scale observation of melting point suppression in nanometer-sized gold particles. *Nanotechnology* **2009**, *20* (47), -; (b) Mattevi, C.; Wirth, C. T.; Hofmann, S.; Blume, R.; Cantoro, M.; Ducati, C.; Cepek, C.; Knop-Gericke, A.; Milne, S.; Castellarin-Cudia, C.; Dolafi, S.; Goldoni, A.; Schloegl, R.; Robertson, J., In-situ X-ray photoelectron spectroscopy study of catalyst-support interactions and growth of carbon nanotube forests. *J Phys Chem C* **2008**, *112* (32), 12207-12213.
101. Roy, S. K.; Coble, R. L., Solubilities of Magnesia Titania and Magnesium Titanate in Aluminum Oxide. *J Am Ceram Soc* **1968**, *51* (1), 1-&.
102. Zhang, H.; Cao, G. P.; Wang, Z. Y.; Yang, Y. S.; Shi, Z. J.; Gu, Z. N., Influence of ethylene and hydrogen flow rates on the wall number, crystallinity, and length of millimeter-long carbon nanotube array. *J Phys Chem C* **2008**, *112* (33), 12706-12709.

103. (a) Jorio, A.; Pimenta, M. A.; Souza, A. G.; Saito, R.; Dresselhaus, G.; Dresselhaus, M. S., Characterizing carbon nanotube samples with resonance Raman scattering. *New Journal of Physics* **2003**, *5*, -; (b) Duesberg, G. S.; Loa, I.; Burghard, M.; Syassen, K.; Roth, S., Polarized Raman spectroscopy on isolated single-wall carbon nanotubes. *Physical Review Letters* **2000**, *85* (25), 5436-5439.
104. Murakami, Y.; Chiashi, S.; Miyauchi, Y.; Hu, M. H.; Ogura, M.; Okubo, T.; Maruyama, S., Growth of vertically aligned single-walled carbon nanotube films on quartz substrates and their optical anisotropy. *Chem Phys Lett* **2004**, *385* (3-4), 298-303.
105. Puretzky, A. A.; Geohegan, D. B.; Jesse, S.; Ivanov, I. N.; Eres, G., In situ measurements and modeling of carbon nanotube array growth kinetics during chemical vapor deposition. *Applied Physics a-Materials Science & Processing* **2005**, *81* (2), 223-240.
106. Burt, D. P.; Whyte, W. M.; Weaver, J. M. R.; Glidle, A.; Edgeworth, J. P.; Macpherson, J. V.; Dobson, P. S., Effects of Metal Underlayer Grain Size on Carbon Nanotube Growth. *J Phys Chem C* **2009**, *113* (34), 15133-15139.
107. Nasibulin, A. G.; Moisala, A.; Jiang, H.; Kauppinen, E. I., Carbon nanotube synthesis from alcohols by a novel aerosol method. *Journal of Nanoparticle Research* **2006**, *8* (3-4), 465-475.
108. (a) Maruyama, S.; Einarsson, E.; Murakami, Y.; Edamura, T., Growth process of vertically aligned single-walled carbon nanotubes. *Chem Phys Lett* **2005**, *403* (4-6), 320-323; (b) Einarsson, E.; Kadowaki, M.; Ogura, K.; Okawa, J.; Xiang, R.; Zhang, Z. Y.; Yamamoto, T.; Ikuhara, Y.; Maruyama, S., Growth Mechanism and Internal Structure of Vertically Aligned Single-Walled Carbon Nanotubes. *J Nanosci Nanotechno* **2008**, *8* (11), 6093-6098.
109. Dillon, A. C.; Jones, K. M.; Bekkedahl, T. A.; Kiang, C. H.; Bethune, D. S.; Heben, M. J., Storage of hydrogen in single-walled carbon nanotubes. *Nature* **1997**, *386* (6623), 377-379.
110. (a) Lebedkin, S.; Schweiss, P.; Renker, B.; Malik, S.; Hennrich, F.; Neumaier, M.; Stoermer, C.; Kappes, M. M., Single-wall carbon nanotubes with diameters approaching 6 nm obtained by laser vaporization. *Carbon* **2002**, *40* (3), 417-423; (b) Kiang, C. H., Growth of large-diameter single-walled carbon nanotubes. *J Phys Chem A* **2000**, *104* (11), 2454-2456; (c) Yang, Q. H.; Bai, S.; Sauvajol, J. L.; Bai, J. B., Large-diameter single-walled carbon nanotubes synthesized by chemical vapor deposition. *Adv Mater* **2003**, *15* (10), 792-+; (d) Zhou, W. W.; Ding, L.; Yang, S.; Liu, J., Synthesis of High-Density, Large-Diameter, and Aligned Single-Walled Carbon Nanotubes by Multiple-Cycle Growth Methods. *Acs Nano* **2011**, *5* (5), 3849-3857.
111. (a) Benedict, L. X.; Chopra, N. G.; Cohen, M. L.; Zettl, A.; Louie, S. G.; Crespi, V. H., Microscopic determination of the interlayer binding energy in graphite. *Chem Phys Lett* **1998**, *286* (5-6), 490-496; (b) Chopra, N. G.; Benedict, L. X.; Crespi, V. H.; Cohen, M. L.; Louie, S. G.; Zettl, A., Fully Collapsed Carbon Nanotubes. *Nature* **1995**, *377* (6545), 135-138; (c) Elliott, J. A.; Sandler, J. K. W.; Windle, A. H.; Young, R. J.; Shaffer, M. S. P., Collapse of single-wall carbon nanotubes is diameter dependent. *Phys Rev Lett* **2004**, *92* (9); (d) Gao, G. H.; Cagin, T.; Goddard, W. A., Energetics,

structure, mechanical and vibrational properties of single-walled carbon nanotubes. *Nanotechnology* **1998**, *9* (3), 184-191; (e) Liu, B.; Yu, M. F.; Huang, Y. G., Role of lattice registry in the full collapse and twist formation of carbon nanotubes. *Phys Rev B* **2004**, *70* (16); (f) Liu, H. J.; Cho, K. J., A molecular dynamics study of round and flattened carbon nanotube structures. *Appl Phys Lett* **2004**, *85* (5), 807-809; (g) Pantano, A.; Parks, D. M.; Boyce, M. C., Mechanics of deformation of single- and multi-wall carbon nanotubes. *J Mech Phys Solids* **2004**, *52* (4), 789-821; (h) Tang, T.; Jagota, A.; Hui, C. Y.; Glassmaker, N. J., Collapse of single-walled carbon nanotubes. *J Appl Phys* **2005**, *97* (7); (i) Xiao, J.; Liu, B.; Huang, Y.; Zuo, J.; Hwang, K. C.; Yu, M. F., Collapse and stability of single- and multi-wall carbon nanotubes. *Nanotechnology* **2007**, *18* (39); (j) Zhang, S. L.; Khare, R.; Belytschko, T.; Hsia, K. J.; Mielke, S. L.; Schatz, G. C., Transition states and minimum energy pathways for the collapse of carbon nanotubes. *Phys Rev B* **2006**, *73* (7).

112. (a) Chang, T. C.; Guo, Z. R., Temperature-Induced Reversible Dominoes in Carbon Nanotubes. *Nano Lett* **2010**, *10* (9), 3490-3493; (b) Crespi, V. H.; Chopra, N. G.; Cohen, M. L.; Zettl, A.; Louie, S. G., Anisotropic electron-beam damage and the collapse of carbon nanotubes. *Phys Rev B* **1996**, *54* (8), 5927-5931; (c) Hertel, T.; Walkup, R. E.; Avouris, P., Deformation of carbon nanotubes by surface van der Waals forces. *Phys Rev B* **1998**, *58* (20), 13870-13873; (d) Qian, W. Z.; Wei, F.; Liu, T.; Wang, Z. W.; Li, Y. D., What causes the carbon nanotubes collapse in a chemical vapor deposition process. *J Chem Phys* **2003**, *118* (2), 878-882; (e) Ruoff, R. S.; Tersoff, J.; Lorents, D. C.; Subramoney, S.; Chan, B., Radial Deformation of Carbon Nanotubes by Van-Der-Waals Forces. *Nature* **1993**, *364* (6437), 514-516; (f) Sun, D. Y.; Shu, D. J.; Ji, M.; Liu, F.; Wang, M.; Gong, X. G., Pressure-induced hard-to-soft transition of a single carbon nanotube. *Phys Rev B* **2004**, *70* (16); (g) Wang, Z. W., Formation of a quenchable dense carbon form by compression of double-walled carbon nanotubes. *J Phys Chem B* **2004**, *108* (47), 18192-18194; (h) Yakobson, B. I.; Campbell, M. P.; Brabec, C. J.; Bernholc, J., High strain rate fracture and C-chain unraveling in carbon nanotubes. *Comp Mater Sci* **1997**, *8* (4), 341-348; (i) Yu, M. F.; Lourie, O.; Dyer, M. J.; Moloni, K.; Kelly, T. F.; Ruoff, R. S., Strength and breaking mechanism of multiwalled carbon nanotubes under tensile load. *Science* **2000**, *287* (5453), 637-640; (j) Zhang, X. H.; Sun, D. Y.; Liu, Z. F.; Gong, X. G., Structure and phase transitions of single-wall carbon nanotube bundles under hydrostatic pressure. *Phys Rev B* **2004**, *70* (3).

113. (a) Chang, T., Dominoes in Carbon Nanotubes. *Phys Rev Lett* **2008**, *101* (17); (b) Shklyae, O. E.; Mockensturm, E.; Crespi, V. H., Modeling Electrostatically Induced Collapse Transitions in Carbon Nanotubes. *Phys Rev Lett* **2011**, *106* (15).

114. (a) Crespi, V. H.; Chopra, N. G.; Cohen, M. L.; Zettl, A.; Radmilovic, V., Site-selective radiation damage of collapsed carbon nanotubes. *Appl Phys Lett* **1998**, *73* (17), 2435-2437; (b) Giusca, C. E.; Tison, Y.; Silva, S. R. P., Atomic and electronic structure in collapsed carbon nanotubes evidenced by scanning tunneling microscopy. *Phys Rev B* **2007**, *76* (3); (c) Lammert, P. E.; Zhang, P. H.; Crespi, V. H., Gapping by squashing: Metal-insulator and insulator-metal transitions in collapsed carbon nanotubes. *Phys Rev Lett* **2000**, *84* (11), 2453-2456; (d) Martel, R.; Schmidt,

- T.; Shea, H. R.; Hertel, T.; Avouris, P., Single- and multi-wall carbon nanotube field-effect transistors. *Appl Phys Lett* **1998**, *73* (17), 2447-2449.
115. Yu, M. F.; Dyer, M. J.; Chen, J.; Qian, D.; Liu, W. K.; Ruoff, R. S., Locked twist in multiwalled carbon-nanotube ribbons. *Phys Rev B* **2001**, *64* (24).
116. (a) Bourgeois, L. N.; Bursill, L. A., High-resolution transmission electron microscopy and energetics of flattened carbon nanoshells. *Chem Phys Lett* **1997**, *277* (5-6), 571-578; (b) Motta, M.; Moisala, A.; Kinloch, I. A.; Windle, A. H., High performance fibres from 'Dog bone' carbon nanotubes. *Adv Mater* **2007**, *19* (21), 3721-+; (c) Yu, M. F.; Kowalewski, T.; Ruoff, R. S., Investigation of the radial deformability of individual carbon nanotubes under controlled indentation force. *Phys Rev Lett* **2000**, *85* (7), 1456-1459; (d) Yu, M. F.; Kowalewski, T.; Ruoff, R. S., Structural analysis of collapsed, and twisted and collapsed, multiwalled carbon nanotubes by atomic force microscopy. *Phys Rev Lett* **2001**, *86* (1), 87-90.
117. Kiang, C. H.; Goddard, W. A.; Beyers, R.; Bethune, D. S., Structural modification of single-layer carbon nanotubes with an electron beam. *J Phys Chem-Us* **1996**, *100* (9), 3749-3752.
118. Alvarez, N. T.; Li, F.; Pint, C. L.; Mayo, J. T.; Fisher, E. Z.; Tour, J. M.; Colvin, V. L.; Hauge, R. H., Uniform Large Diameter Carbon Nanotubes in Vertical Arrays from Premade Near-Monodisperse Nanoparticles. *Chem Mater* **2011**, *23* (15), 3466-3475.
119. Kong, J.; Soh, H. T.; Cassell, A. M.; Quate, C. F.; Dai, H. J., Synthesis of individual single-walled carbon nanotubes on patterned silicon wafers. *Nature* **1998**, *395* (6705), 878-881.
120. Bernholc, J.; Brabec, C.; Nardelli, M. B.; Maiti, A.; Roland, C.; Yakobson, B. I., Theory of growth and mechanical properties of nanotubes. *Appl Phys a-Mater* **1998**, *67* (1), 39-46.
121. (a) Li, W. Z.; Yan, X.; Kempa, K.; Ren, Z. F.; Giersig, M., Structure of flattened carbon nanotubes. *Carbon* **2007**, *45* (15), 2938-2945; (b) Liu, S. W.; Yue, J.; Wehmschulte, R. J., Large thick flattened carbon nanotubes. *Nano Lett* **2002**, *2* (12), 1439-1442.
122. Yu, M. F.; Dyer, M. J.; Ruoff, R. S., Structure and mechanical flexibility of carbon nanotube ribbons: An atomic-force microscopy study. *J Appl Phys* **2001**, *89* (8), 4554-4557.
123. Kroto, H. W.; Heath, J. R.; O'Brien, S. C.; Curl, R. F.; Smalley, R. E., C-60 - Buckminsterfullerene. *Nature* **1985**, *318* (6042), 162-163.
124. (a) Campbell, C. T.; Peden, C. H. F., Chemistry - Oxygen vacancies and catalysis on ceria surfaces. *Science* **2005**, *309* (5735), 713-714; (b) Tsai, Y. Y.; Oca-Cossio, J.; Agering, K.; Simpson, N. E.; Atkinson, M. A.; Wasserfall, C. H.; Constantinidis, I.; Sigmund, W., Novel synthesis of cerium oxide nanoparticles for free radical scavenging. *Nanomedicine-Uk* **2007**, *2* (3), 325-332; (c) Mattos, L. V.; Rodino, E.; Resasco, D. E.; Passos, F. B.; Noronha, F. B., Partial oxidation and CO₂ reforming of methane on Pt/Al₂O₃, Pt/ZrO₂, and Pt/Ce-ZrO₂ catalysts. *Fuel Process Technol* **2003**, *83* (1-3), 147-161.
125. (a) Colon, J.; Hsieh, N.; Ferguson, A.; Kupelian, P.; Seal, S.; Jenkins, D. W.; Baker, C. H., Cerium oxide nanoparticles protect gastrointestinal epithelium from

radiation-induced damage by reduction of reactive oxygen species and upregulation of superoxide dismutase 2. *Nanomed-Nanotechnol* **2010**, *6* (5), 698-705; (b) Hirst, S. M.; Karakoti, A. S.; Tyler, R. D.; Sriranganathan, N.; Seal, S.; Reilly, C. M., Anti-inflammatory Properties of Cerium Oxide Nanoparticles. *Small* **2009**, *5* (24), 2848-2856; (c) Karakoti, A. S.; Monteiro-Riviere, N. A.; Aggarwal, R.; Davis, J. P.; Narayan, R. J.; Self, W. T.; McGinnis, J.; Seal, S., Nanoceria as antioxidant: Synthesis and biomedical applications. *Jom-Us* **2008**, *60* (3), 33-37; (d) Chen, J. P.; Patil, S.; Seal, S.; McGinnis, J. F., Rare earth nanoparticles prevent retinal degeneration induced by intracellular peroxides. *Nat Nanotechnol* **2006**, *1* (2), 142-150; (e) Ivanov, V. K.; Usatenko, A. V.; Shcherbakov, A. B., Antioxidant activity of nanocrystalline ceria to anthocyanins. *Russ J Inorg Chem+* **2009**, *54* (10), 1522-1527; (f) D'Angelo, B.; Santucci, S.; Benedetti, E.; Di Loreto, S.; Phani, R. A.; Falone, S.; Amicarelli, F.; Ceru, M. P.; Cimini, A., Cerium Oxide Nanoparticles Trigger Neuronal Survival in a Human Alzheimer Disease Model By Modulating BDNF Pathway. *Curr Nanosci* **2009**, *5* (2), 167-176; (g) Singh, N.; Cohen, C. A.; Rzigalinski, B. A., Treatment of neurodegenerative disorders with radical nanomedicine. *Neuroprotective Agents: Eighth International Neuroprotection Society Meeting* **2007**, *1122*, 219-230; (h) Qi, X. P.; Lewin, A. S.; Sun, L.; Hauswirth, W. W.; Guy, J., Suppression of mitochondrial oxidative stress provides long-term neuroprotection in experimental optic neuritis. *Invest Ophth Vis Sci* **2007**, *48* (2), 681-691; (i) Schubert, D.; Dargusch, R.; Raitano, J.; Chan, S. W., Cerium and yttrium oxide nanoparticles are neuroprotective. *Biochem Bioph Res Co* **2006**, *342* (1), 86-91.

126. (a) Zhang, L.; He, R.; Gu, H. C., Synthesis and kinetic shape and size evolution of magnetite nanoparticles. *Materials Research Bulletin* **2006**, *41* (2), 260-267; (b) Park, J.; Lee, E.; Hwang, N. M.; Kang, M.; Kim, S. C.; Hwang, Y.; Park, J. G.; Noh, H. J.; Kim, J. Y.; Park, J. H.; Hyeon, T., One-nanometer-scale size-controlled synthesis of monodisperse magnetic iron oxide nanoparticles. *Angew Chem Int Ed Engl* **2005**, *44* (19), 2873-7; (c) Sun, S.; Zeng, H.; Robinson, D. B.; Raoux, S.; Rice, P. M.; Wang, S. X.; Li, G., Monodisperse MFe₂O₄ (M = Fe, Co, Mn) nanoparticles. *J Am Chem Soc* **2004**, *126* (1), 273-9; (d) Jana, N. R.; Chen, Y. F.; Peng, X. G., Size- and shape-controlled magnetic (Cr, Mn, Fe, Co, Ni) oxide nanocrystals via a simple and general approach. *Chem Mater* **2004**, *16* (20), 3931-3935; (e) Sun, S.; Zeng, H., Size-controlled synthesis of magnetite nanoparticles. *J Am Chem Soc* **2002**, *124* (28), 8204-5.

127. (a) Zhou, H. P.; Zhang, Y. W.; Mai, H. X.; Sun, X.; Liu, Q.; Song, W. G.; Yan, C. H., Spontaneous organization of uniform CeO₂ nanoflowers by 3D oriented attachment in hot surfactant solutions monitored with an in situ electrical conductance technique. *Chem-Eur J* **2008**, *14* (11), 3380-3390; (b) Yu, T.; Park, Y. I.; Kang, M. C.; Joo, J.; Park, J. K.; Won, H. Y.; Kim, J. J.; Hyeon, T., Large-scale synthesis of water dispersible ceria nanocrystals by a simple sol-gel process and their use as a chemical mechanical planarization slurry. *Eur J Inorg Chem* **2008**, (6), 855-858.

128. Niederberger, M.; Garnweitner, G., Organic reaction pathways in the nonaqueous synthesis of metal oxide nanoparticles. *Chem-Eur J* **2006**, *12* (28), 7282-7302.

129. Ould-Ely, T.; Prieto-Centurion, D.; Kumar, A.; Guo, W.; Knowles, W. V.; Asokan, S.; Wong, M. S.; Rusakova, I.; Luttge, A.; Whitmire, K. H., Manganese(II) oxide nanohexapods: Insight into controlling the form of nanocrystals. *Chem Mater* **2006**, *18* (7), 1821-1829.
130. (a) Kar, S.; Patel, C.; Santra, S., Direct Room Temperature Synthesis of Valence State Engineered Ultra-Small Ceria Nanoparticles: Investigation on the Role of Ethylenediamine as a Capping Agent. *J Phys Chem C* **2009**, *113* (12), 4862-4867; (b) Natile, M. M.; Boccaletti, G.; Glisenti, A., Properties and reactivity of nanostructured CeO₂ powders: Comparison among two synthesis procedures. *Chem Mater* **2005**, *17* (25), 6272-6286; (c) Korsvik, C.; Patil, S.; Seal, S.; Self, W. T., Superoxide dismutase mimetic properties exhibited by vacancy engineered ceria nanoparticles. *Chem Commun* **2007**, (10), 1056-1058.
131. (a) Hailstone, R. K.; DiFrancesco, A. G.; Leong, J. G.; Allston, T. D.; Reed, K. J., A Study of Lattice Expansion in CeO₂ Nanoparticles by Transmission Electron Microscopy. *J Phys Chem C* **2009**, *113* (34), 15155-15159; (b) Patil, S.; Seal, S.; Guo, Y.; Schulte, A.; Norwood, J., Role of trivalent La and Nd dopants in lattice distortion and oxygen vacancy generation in cerium oxide nanoparticles. *Appl Phys Lett* **2006**, *88* (24).
132. Vonhoene, J.; Charles, R. G.; Hickam, W. M., Thermal Decomposition of Metal Acetylacetonates Mass Spectrometer Studies. *J Phys Chem-U*s **1958**, *62* (9), 1098-1101.
133. (a) Svenson, S.; Tomalia, D. A., Commentary - Dendrimers in biomedical applications - reflections on the field. *Adv Drug Deliver Rev* **2005**, *57* (15), 2106-2129; (b) Parak, W. J.; Gerion, D.; Pellegrino, T.; Zanchet, D.; Micheel, C.; Williams, S. C.; Boudreau, R.; Le Gros, M. A.; Larabell, C. A.; Alivisatos, A. P., Biological applications of colloidal nanocrystals. *Nanotechnology* **2003**, *14* (7), R15-R27; (c) Cohen, H.; Levy, R. J.; Gao, J.; Fishbein, I.; Kousaev, V.; Sosnowski, S.; Slomkowski, S.; Golomb, G., Sustained delivery and expression of DNA encapsulated in polymeric nanoparticles. *Gene Ther* **2000**, *7* (22), 1896-1905.
134. Deshpande, S.; Patil, S.; Kuchibhatla, S. V. N. T.; Seal, S., Size dependency variation in lattice parameter and valency states in nanocrystalline cerium oxide. *Appl Phys Lett* **2005**, *87* (13), -.
135. (a) Park, E. J.; Choi, J.; Park, Y. K.; Park, K., Oxidative stress induced by cerium oxide nanoparticles in cultured BEAS-2B cells. *Toxicology* **2008**, *245* (1-2), 90-100; (b) Lin, W. S.; Huang, Y. W.; Zhou, X. D.; Ma, Y. F., Toxicity of cerium oxide nanoparticles in human lung cancer cells. *Int J Toxicol* **2006**, *25* (6), 451-457; (c) Limbach, L. K.; Li, Y. C.; Grass, R. N.; Brunner, T. J.; Hintermann, M. A.; Muller, M.; Gunther, D.; Stark, W. J., Oxide nanoparticle uptake in human lung fibroblasts: Effects of particle size, agglomeration, and diffusion at low concentrations. *Environ Sci Technol* **2005**, *39* (23), 9370-9376; (d) Horie, M.; Nishio, K.; Fujita, K.; Endoh, S.; Miyauchi, A.; Saito, Y.; Iwahashi, H.; Yamamoto, K.; Murayama, H.; Nakano, H.; Nanashima, N.; Niki, E.; Yoshida, Y., Protein Adsorption of Ultrafine Metal Oxide and Its Influence on Cytotoxicity toward Cultured Cells. *Chem Res Toxicol* **2009**, *22* (3), 543-553.

136. Kuchibhatla, S. V. N. T.; Karakoti, A. S.; Seal, S., Colloidal stability by surface modification. *Jom-U*s **2005**, *57* (12), 52-56.
137. (a) Cory, A. H.; Owen, T. C.; Barltrop, J. A.; Cory, J. G., Use of an Aqueous Soluble Tetrazolium Formazan Assay for Cell-Growth Assays in Culture. *Cancer Commun* **1991**, *3* (7), 207-212; (b) Mosmann, T., Rapid Colorimetric Assay for Cellular Growth and Survival - Application to Proliferation and Cyto-Toxicity Assays. *J Immunol Methods* **1983**, *65* (1-2), 55-63.
138. (a) Pagliari, F.; Mandoli, C.; Forte, G.; Magnani, E.; Pagliari, S.; Nardone, G.; Licocchia, S.; Minieri, M.; Di Nardo, P.; Traversa, E., Cerium Oxide Nanoparticles Protect Cardiac Progenitor Cells from Oxidative Stress. *Acs Nano* **2012**, *6* (5), 3767-3775; (b) Asati, A.; Santra, S.; Kaittanis, C.; Perez, J. M., Surface-Charge-Dependent Cell Localization and Cytotoxicity of Cerium Oxide Nanoparticles. *Acs Nano* **2010**, *4* (9), 5321-5331.
139. Cao, G. H.; Alessio, H. M.; Cutler, R. G., Oxygen-Radical Absorbency Capacity Assay for Antioxidants. *Free Radical Bio Med* **1993**, *14* (3), 303-311.
140. Lucente-Schultz, R. M.; Moore, V. C.; Leonard, A. D.; Price, B. K.; Kosynkin, D. V.; Lu, M.; Partha, R.; Conyers, J. L.; Tour, J. M., Antioxidant Single-Walled Carbon Nanotubes. *J Am Chem Soc* **2009**, *131* (11), 3934-3941.
141. (a) Qin, Y.; Lu, M.; Gong, X. G., Dihydrorhodamine 123 is superior to 2,7-dichlorodihydrofluorescein diacetate and dihydrorhodamine 6G in detecting intracellular hydrogen peroxide in tumor cells. *Cell Biol Int* **2008**, *32* (2), 224-228; (b) Carlson, C.; Hussain, S. M.; Schrand, A. M.; Braydich-Stolle, L. K.; Hess, K. L.; Jones, R. L.; Schlager, J. J., Unique Cellular Interaction of Silver Nanoparticles: Size-Dependent Generation of Reactive Oxygen Species. *J Phys Chem B* **2008**, *112* (43), 13608-13619.
142. Wu, L. M.; Shen, X. M.; Liu, D. Q., A novel GC-MS method for rapid determination of headspace oxygen in vials of pharmaceutical formulations. *J Pharmaceut Biomed* **2008**, *48* (1), 8-12.
143. Lucio, M.; Nunes, C.; Gaspar, D.; Ferreira, H.; Lima, J. L. F. C.; Reis, S., Antioxidant Activity of Vitamin E and Trolox: Understanding of the Factors that Govern Lipid Peroxidation Studies In Vitro. *Food Biophys* **2009**, *4* (4), 312-320.
144. Binns, C., *Introduction to nanoscience and nanotechnology*. Wiley: Hoboken, N.J., 2010; p xvii, 301 p.
145. Djuricic, B.; Pickering, S., Nanostructured cerium oxide: Preparation and properties of weakly-agglomerated powders. *J Eur Ceram Soc* **1999**, *19* (11), 1925-1934.
146. Scholes, F. H.; Hughes, A. E.; Hardin, S. G.; Lynch, P.; Miller, P. R., Influence of hydrogen peroxide in the preparation of nanocrystalline ceria. *Chem Mater* **2007**, *19* (9), 2321-2328.
147. Pirmohamed, T.; Dowding, J. M.; Singh, S.; Wasserman, B.; Heckert, E.; Karakoti, A. S.; King, J. E. S.; Seal, S.; Self, W. T., Nanoceria exhibit redox state-dependent catalase mimetic activity. *Chem Commun* **2010**, *46* (16), 2736-2738.
148. (a) Yildiz, G.; Demiryurek, A. T.; Sahin-Erdemli, I.; Kanzik, I., Comparison of antioxidant activities of aminoguanidine, methylguanidine and guanidine by

luminol-enhanced chemiluminescence. *Brit J Pharmacol* **1998**, *124* (5), 905-910; (b) King, D. W.; Lounsbury, H. A.; Millero, F. J., Rates and Mechanism of Fe(II) Oxidation at Nanomolar Total Iron Concentrations. *Environ Sci Technol* **1995**, *29* (3), 818-824.

149. (a) Turnwald, S. E.; Lorier, M. A.; Wright, L. J.; Mucalo, M. R., Oleic acid oxidation using hydrogen peroxide in conjunction with transition metal catalysis. *J Mater Sci Lett* **1998**, *17* (15), 1305-1307; (b) Swern, D.; Billen, G. N.; Findley, T. W.; Scanlan, J. T., Hydroxylation of Monounsaturated Fatty Materials with Hydrogen Peroxide. *J Am Chem Soc* **1945**, *67* (10), 1786-1789; (c) Nouredini, H.; Kanabur, M., Liquid-phase catalytic oxidation of unsaturated fatty acids. *J Am Oil Chem Soc* **1999**, *76* (3), 305-312.